Flood Extent and Volume Estimation using Multi-Temporal Synthetic Aperture Radar.

Miles Adam Clement

A thesis submitted to Newcastle University in partial fulfilment of the requirements for the degree of Doctor of Philosophy within the School of Engineering and the Faculty of Science, Agriculture and Engineering

Initial Submission: September 2019

Examination: November 2019

Final Submission: January 2020

Acknowledgements

I would like to thank my supervisors, Prof. Phil Moore and Prof. Chris Kilsby, for their excellent support, encouragement and advice throughout the course of my PhD. I always enjoyed our meetings, and it has been a privilege to have the guidance of such well-renowned and knowledgeable supervisors.

Thanks go to NERC and the organisers of the Data, Risk and Environmental Analytical Methods (DREAM) CDT for funding the studentship. Thanks to my fellow Newcastle 'Dreamers' - Fergus, Ben, Grant, Jess and Amy - for making the symposia and challenge weeks enjoyable.

I am very appreciative of Prof. Jon Mills and Dr. Guy Schumann for examining the thesis. I really enjoyed the viva, in large part due to you both for making me feel comfortable during the exam, and for providing thought-provoking and challenging conversation.

My thanks to David Boorman of CEH for supplying COSMOS-UK data, and to NPAS Carr Gate for agreeing to the use of their aerial imagery.

I have thoroughly enjoyed the PhD experience, in a large part to the brilliant people I have shared my work environment with. Thanks go to the various residents of G19, in particular Chris P, Pippa, Craig, Neil, Beth, Kat and James, for providing excellent daily conversation (mostly about sport). This is alongside the wider Geospatial Engineering and Water research community at Newcastle, who provided interesting seminars, research meetings, and varied morning coffee conversations.

Away from the university my time in Newcastle has been equally rewarding, including playing for most of the local korfball teams –Tyneside Titans, Northern Storm and Newcastle University – providing a much-needed release from the PhD. The early Sunday morning road-trips to Edinburgh were made bearable by Fran, Chris R and Kerry. Thanks to Elizabeth, Adam and Willow for the Northumberland walks and pub lunches.

I consider myself lucky to have such amazing, supportive friends away from Newcastle. Cottage, walking and sport-watching weekends away with Jonny, Felicity, Joe, Lara, Gareth, Claire, Rosi and Ben have always been something to look forward to. Thank you for always showing interest and for providing much-needed breaks from studying.

Thanks go to Mum, Leon, Geoff and the rest of my family for their support and encouragement throughout my studies. It was always a relaxing break to head back to Flitcham for some peace and quiet! The Carver family have been very supportive throughout my studies, with plenty of advice, roast dinners and countryside walks, something which I am very grateful for.

Finally, a massive thank you to my wonderful girlfriend Amelia. Your never-ending support, patience and encouragement have been a blessing. You were there to pick up the pieces during the tough times, and to celebrate the better times, something which I'll forever be grateful for. Thank you for being my rock.

Abstract

Satellite imagery has the potential to monitor flooding across wide geographical regions. Recent launches have improved the spatial and temporal resolution of available data, with the European Space Agency (ESA) Copernicus programme providing global imagery at no end-user cost. Synthetic Aperture Radar (SAR) is of particular interest due to its ability to map flooding independent of weather conditions. Satellite-derived flood observations have real-world application in flood risk management and validation of hydrodynamic models.

This thesis presents a workflow for estimating flood extent, depth and volume utilising ESA Sentinel-1 SAR imagery. Flood extents are extracted using a combination of change detection, variable histogram thresholding and object-based region growing. An innovative technique has been developed for estimating flood shoreline heights by combining the inundation extents with high-resolution terrain data. A grid-based framework is used to derive the water surface from the shoreline heights, from which water depth and volume are calculated.

The methodology is applied to numerous catchments across the north of England that suffered from severe flooding throughout the winter of 2015-16. Extensive flooding has been identified throughout the study region, with peak inundation occurring on 29th December 2015. On this date, over 100 km^2 of flooding is identified in the Ouse catchment, equating to a water volume of 0.18 km^3. The SAR flood extents are validated against satellite optical imagery, achieving a Total Accuracy of 91% and a Critical Success Index of 77%. The derived water surfaces have an average error of 3 cm and an RMSE of 98 cm compared to river stage measurements.

The methods developed are robust and globally applicable, shown with an additional study along the Mackenzie River in Australia. The presented methodology, alongside the increased temporal resolution provided by Sentinel-1, highlights the potential for accurate, reliable mapping of flood dynamics using satellite imagery.

Keywords: Flooding, Sentinel-1, Synthetic Aperture Radar, Change Detection, Terrain Analysis

Key Acronyms

ALOS	Advanced Land Observing Satellite
ASTER	Advanced Spaceborne Thermal Emission and Reflection Radiometer
ASTER GDEMv2	ASTER Global DEM Second Version
AW3D30	ALOS World 3D Global 30 m DSM
CDAT	Change Detection and Thresholding
CEMS	Copernicus Emergency Management Service
Cκ	Cohen's Kappa Coefficient
CSI	Critical Success Index
DEM	Digital Elevation Model
DSM	Digital Surface Model
DTM	Digital Terrain Model
EA	UK Environment Agency
ESA	European Space Agency
FMP	Environment Agency Flood Maps for Planning
GEE	Google Earth Engine
GlobCover	Global Land Cover Map
GRD	Ground Range Detected
GSWE	Global Surface Water Explorer
HAND	Height Above Nearest Drainage
IW	Interferometric Wide Swath
LiDAR	Light Detection and Ranging
MNDWI	Modernised Normalised Difference Water Index
MP	Minimum-Point Threshold
NPAS	National Police Aire Service
OS	Ordnance Survey
PA_f	Producer's Accuracy
RADAR	Radio Detection and Ranging
RMSE	Root Mean Squared Error
SAR	Synthetic Aperture Radar
SNAP	Sentinel Applications Platform
SRTM	Shuttle Radar Topography Mission

SRTM WBD	Shuttle Radar Topography Mission Water Body Dataset
TA	Total Accuracy
TOPSAR	Terrain Observations with Progressive Scans SAR
UA_f	User's Accuracy

Contents

Figures

Tables

Chapter 1. Introduction

1.1. Background

Understanding the nature of flood events at a location is paramount for mitigating and adapting to the risk presented by the hazard (Rahman and Di, 2017). The exposure of populations and economic assets to flood risk has increased over the past decades, primarily due to expanding urbanisation alongside an increase in event magnitude and occurrence due to climate change (IPCC, 2012; Garschagen and Romero-Lankao, 2015). Between 1980 and 2013, global flood events caused over 220,000 fatalities and economic losses exceeding $1 trillion (Winsemius *et al.*, 2016). Reducing future flood risk in the context of increasing extreme events is vital for developing a more sustainable society (Wang *et al.*, 2015).

However, reliable data on the spatial occurrence of historical flood events can be difficult to obtain (Cunha *et al.*, 2011). This is exacerbated by the variable nature of flooding. There are numerous sources of inundation, including pluvial (surface water), fluvial, groundwater, coastal (such as storm surges and tsunamis) and snowmelt events, each with different characteristics, including speed of onset, duration, predictability and scale of impacted locations. Flooding is a global phenomenon, underlined by the range of source mechanisms, and is widely considered the most common natural hazard (Stefanidis and Stathis, 2013; Below and Wallemacq, 2018). The Dartmouth Flood Observatory (DFO) collates and maps inundation events, with Figure 1.1 showing flood occurrence since 2000, totalling 3,129 events. Given the global nature of flooding, sufficient in-situ monitoring is considered geographically impractical and likely to be expensive, whilst nominally providing point measurements that have questionable use for understanding the dynamics of an event (Maheu *et al.*, 2003; Alsdorf *et al.*, 2007). Hydrodynamic models have been developed for most types of flooding, and simulations can output flood extent, depth and velocity information (Teng *et al.*, 2017). However, there are natural and epistemic uncertainties with the development of hydrodynamic models that can reduce confidence in their outputs (Merz and Thieken, 2005).

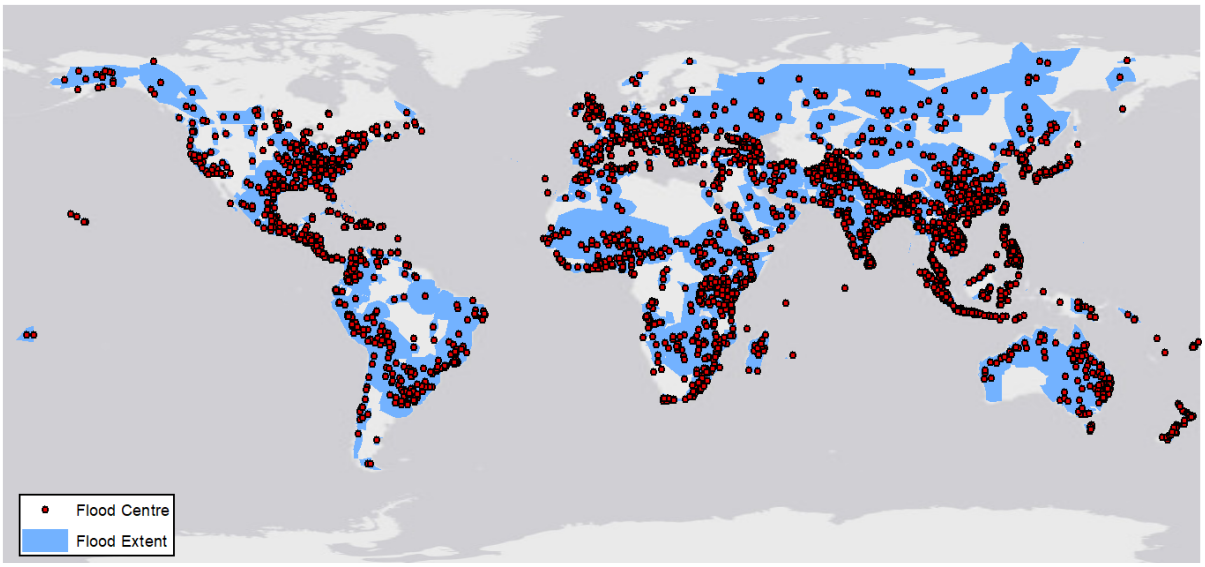

Figure 1.1. Centroid locations and impacted regions for floods between 2000 and 2018 (n = 3129) recorded in the Dartmouth Flood Observatory (DFO) database. DFO records suggest there were over 390,000 fatalities from flooding during this period, with approximately 350 million people displaced.

Earth observation satellites provide data suitable for mapping a wide variety of environmental variables. Within a hydrological context, remote sensing imagery has been used to monitor surface water extent (Huang *et al.*, 2018), soil moisture (Gao *et al.*, 2017), wetlands (Muro *et al.*, 2016) and snow cover (Snapir *et al.*, 2019). Compared to in-situ measurements, the geographical coverage provided by satellite imagery significantly improves the potential for mapping wide-scale flooding. There are two types of satellite imagery, passive (for example multispectral, often referred to as optical) and active (such as Synthetic Aperture Radar (SAR)), both of which can delineate flooding. The ability of SAR to acquire imagery irrespective of weather conditions makes it the preferred choice for flood mapping (Alsdorf *et al.*, 2007). Recent satellite launches have increased the quantity and quality of available data, improving the potential of monitoring the intricacies of dynamic environmental variables from space. A prime example is the European Space Agency (ESA) Copernicus programme, including the Sentinel-1 SAR satellite constellation, which provides global imagery every 1-3 days at no cost to the end user.

Numerous algorithms have been developed for deriving flood extent from both optical and SAR imagery. For optical imagery, methods of detecting water normally involve indices using two or more spectral bands (McFeeters, 1996; Xu, 2006). SAR flood mapping is based around the identification of the specular reflection of the radar

signal off the theoretically flat water surface (Henderson and Lewis, 2008). Common techniques include histogram thresholding (Matgen *et al.*, 2011), active contour models (Horritt *et al.*, 2001) and change detection (Long *et al.*, 2014). Despite the successes of SAR flood mapping using the above techniques, there are ongoing challenges in accurately and reliably delineating inundation in urban and woodland locations (Giustarini *et al.*, 2013; Schumann and Moller, 2015).

Alongside data on flood extent, information on water depth is important for managing flood risk during an event. Satellite altimetry can provide surface water height measurements, albeit with limited coverage and temporal resolution (Alsdorf *et al.*, 2007). Subsequently, flood depths are normally indirectly calculated based on combining the observed flood extents with terrain data (Cian *et al.*, 2018a). The merging of two different sources of data often increases the uncertainty, accounting for which is shown to be vital for producing viable depths (Grimaldi *et al.*, 2016).

The successful delineation of multiple flood parameters has many uses within the flood management cycle. Near real-time flood mapping, such as that performed by the Copernicus Emergency Management Service (European Commission, 2019), provides valuable information to emergency services during an event. Satellite products are regularly used for validating hydrodynamic model results, alongside the potential for data assimilation to improve forecasting during an event (Grimaldi *et al.*, 2016). Additionally, satellite data has been used for post-event damage assessments and has helped inform flood risk mitigation and adaptation strategies (Bovolo and Bruzzone, 2007; Rahman and Di, 2017).

The motivation behind this study is to make use of new satellite datasets to provide an improved understanding of flood dynamics. The increase in temporal resolution provided by Sentinel-1 will allow for improved mapping of changes in flood extent. Algorithms will be developed for estimating water depths that sufficiently account for the uncertainty produced by SAR flood mapping. The addition of water volume to the more commonly reported flood extent and water depth will provide greater insight into the evolution of longer duration flood events, whilst providing additional parameters for validating hydrodynamic models.

1.2. Aims and Objectives

The overall aim of the project is to develop innovative algorithms for estimating flood dynamics using satellite SAR imagery and ancillary geospatial datasets. The multi-temporal analysis of the results will highlight the improved understanding of flood extent, depth and volume throughout an event that recent satellite launches can provide, further advancing the capability of mapping and monitoring inundation. The work will thus provide:

- An initial assessment of imagery from the recently launched Sentinel-1 SAR satellites for mapping inundation across large geographical areas.
- Development of novel techniques for delineating water depth and volume based on the observed flood extent and terrain data.
- Establish the potential for greater insight into the flood dynamics of an event with the increase in the temporal resolution of imagery.
- Validation of results against multiple data sources to determine the strengths and limitations of the methodology.

There are a number of objectives that will help the project aim to be achieved, detailed below.

Objective 1: Delineating Flood Extent from SAR Imagery (Chapters 4 and 5)

Flood extents will be extracted from Sentinel-1 SAR imagery using a hybrid approach. The goal is to utilise the relative strengths of various established processing algorithms to reduce the number of misclassifications in the final flood delineation. This will include an assessment of the available Sentinel-1 polarisations, both as single images for flood mapping, as well as the potential for a combined classification. A number of validation sources will be used to confirm the accuracy of the results, including Sentinel-1 optical imagery, aerial imagery and flood classifications from other SAR data.

Objective 2: Calculating Water Surface, Depth and Volume (Chapter 6)

The derived flood extents will be combined with high-resolution LiDAR terrain data to allow for an estimation of the water surface. From this, water depths and flood volumes will be calculated. This will allow for the multi-temporal analysis of flood dynamics to be undertaken. Some of the key challenges are how to account for uncertainty when combining the different datasets, including under-prediction of the

SAR flood extent and the difference in data resolution. Novel algorithms and concepts will be employed to account for the inherent uncertainty of the datasets and methodology. Water surfaces will be compared to in-situ gauge records to determine accuracy.

Objective 3: Assess the Potential for Improved Understanding of Flood Dynamics (Chapters 4, 5, 6 and 8)

The combination of improved temporal resolution provided by Sentinel-1 and the multiple flood characteristics calculated in Objectives 1 and 2 will allow for greater insight into the changing dynamics of a flood event. The methodologies will be applied to the extensive, prolonged flooding associated with 2015-16 UK winter storm season. Results will be compared to in-situ gauge data and precipitation records. The improved understanding of the temporal changes in flood hydrology will be assessed, providing answers to questions of whether the improved Sentinel-1 acquisition rate is sufficient, or if multi-satellite constellations are required to fully monitor and understand the life-cycle of a flood.

Objective 4: Confirm the Global Applicability of Algorithms (Chapters 7 and 8)

One of the advantages of satellite data is the ability to monitor the environment anywhere on the planet. Subsequently, flood mapping algorithms should be geographically robust and produce similar levels of accuracy irrespective of the flood location. This will be tested by applying the final algorithms to an additional case study away from the main UK event analysed for the other objectives. This includes the assessment of globally available terrain datasets within the context of estimating water depths and volumes using the workflow developed for Objective 2.

1.3. Thesis Structure

Following this introduction, Chapter 2 will provide a review of the current academic literature, including a brief overview of flood hazards, remote sensing platforms and sensors, before more detail is given on SAR processing for flood extent mapping and current algorithms for deriving water depth. Chapter 3 provides details on SAR acquisition parameters, introduces the Sentinel-1 data acquisition, and describes the SAR pre-processing undertaken to produce analysis-ready data. Chapter 4 provides an initial assessment of Sentinel-1 based flood mapping, analysing the changing

inundation extents throughout the winter of 2015-16 for a small region south of York, UK. This chapter has been published in the Journal of Flood Risk Management. Chapter 5 expands and improves on the methodology used in the previous chapter, before mapping flood extents across numerous catchments in northern England over a three month period. Chapter 6 presents an algorithm for estimating water surfaces, depths and volumes based on satellite-derived flood extent and high-resolution LiDAR terrain data, with results presented for the Ouse and Aire catchments in the UK. Chapter 7 presents an international application of the algorithms from Chapters 5 and 6, analysing the inundation caused by Tropical Cyclone Debbie along the Mackenzie River in Queensland, Australia. Lower-resolution global terrain models are used in place of the LiDAR dataset used in Chapter 6, providing an understanding of how the algorithms perform across multiple resolutions of terrain data. Finally, Chapter 8 provides commentary on the dynamics of the 2015-16 UK winter floods, discusses the strengths and limitations of the developed algorithms and SAR flood mapping, before highlighting potential avenues for future work.

Chapter 2. Satellite Remote Sensing and Flooding

2.1. Introduction to Flooding: Sources and Impacts

Many natural hazards, such as earthquakes and volcanoes, only occur in certain locations due to their geological setting. Floods, however, are a global hazard, driven by the numerous different source mechanisms that can cause an event. The Intergovernmental Panel on Climate Change (IPCC) defines flooding as *"The overflowing of the normal confines of a stream or other body of water or the accumulation of water over areas that are not normally submerged"* (IPCC, 2012). The Centre for Research on the Epidemiology of Disasters (CRED) publishes annual reports analysing the occurrence and impact of natural disasters. Figure 2.1 shows how disasters in 2017 compared to the average from the previous decade (Below and Wallemacq, 2018). The data shows that between 2007 and 2016, floods were the most common natural disaster with an average of 162 major events recorded per year. Impacts include an average of 5,553 deaths per year, whilst affecting 85 million people per annum, more than any other hazard. Average economic losses from flood events are shown to be in the region of $36.7 billion per year.

There are numerous different sources of flooding, each with its own characteristics in terms of flashiness (speed of onset), magnitude, duration, predictability and monitoring potential. The primary focus will be fluvial, surface water (pluvial) and groundwater events, due to their prevalence both in the UK and globally. Heavy or prolonged precipitation is often the main cause of these types of event, which can result in multi-source flooding, where two or more of these sources are active at a single time. Fluvial flood events occur when the stage of a river rises above the height of the banks that normally constrain it, resulting in the inundation of the floodplain. Surface water flooding occurs when the precipitation inputs are greater than the land surface's potential to store or transport the water, resulting in localised inundation. Groundwater inundation is common after prolonged rainfall which leads to an increase in the height of the water table, which upon reaching the surface causes flooding as the water pools. Other types of flooding, such as those from snowmelt, storm surges and tsunamis, or from a reservoir or dam failure, can often be challenging to manage due to events being unpredictable, large in magnitude, and in some cases located in remote regions.

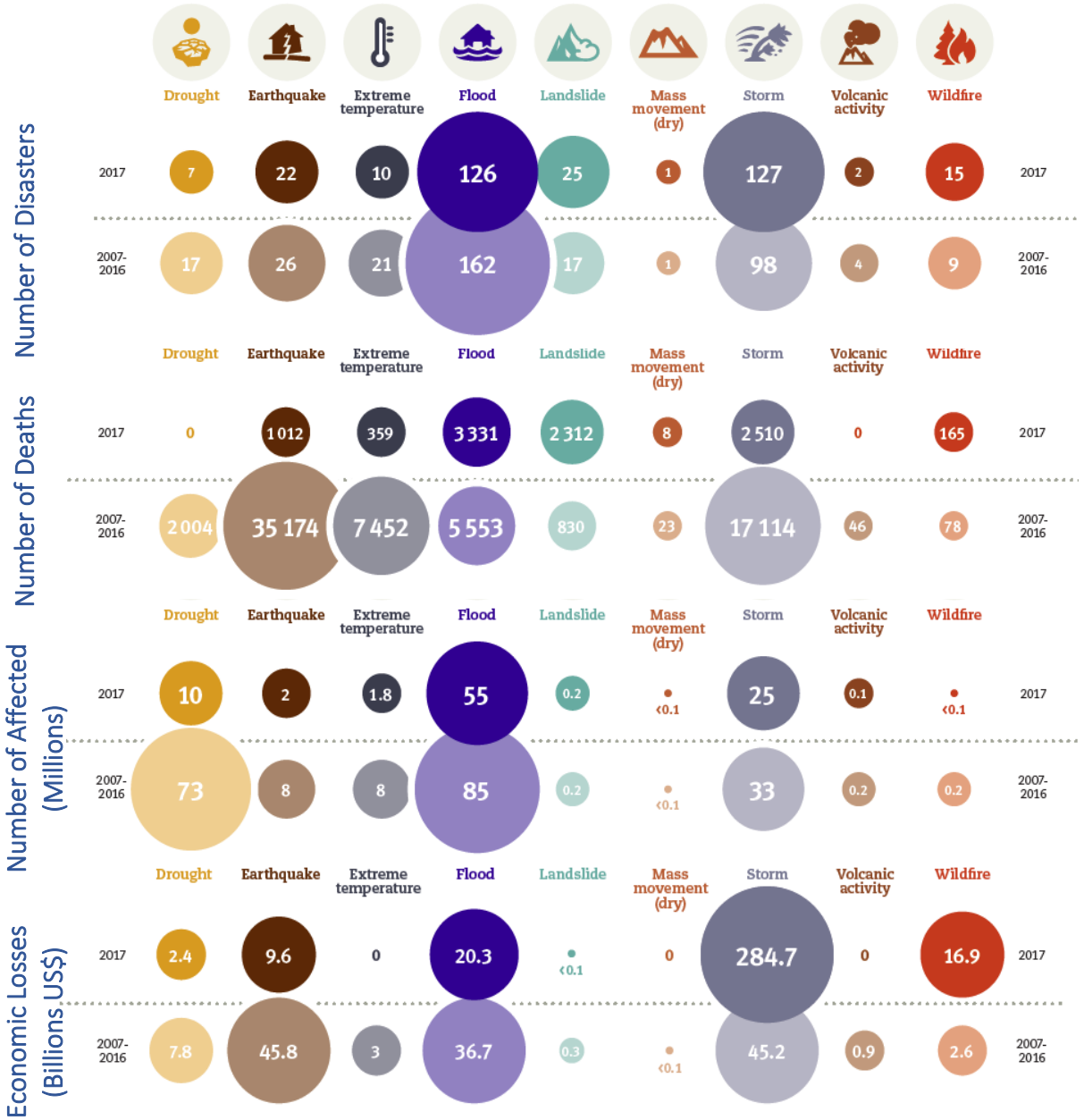

Figure 2.1. CRED statistics comparing the impacts of different natural hazards. From top, disaster occurrence, fatalities, people impacted (millions) and economic losses (billions US$). Data is shown for 2017, and a yearly average from data between 2007 and 2016. Adapted from Below and Wallemacq (2018).

As well as the characteristics of the precipitation event, the size, gradient and land cover of a river catchment can also impact flood event characteristics. Anthropogenic land-use change can often increase the frequency and magnitude of an event. Deforestation in upper catchments can decrease infiltration rates and water storage potential, whilst creating faster transport pathways (Owrangi *et al.*, 2014). Urbanisation and the replacement of natural land cover with impenetrable surfaces alter the storage and runoff properties by reducing infiltration and increasing surface

runoff (Miller *et al.*, 2014). Both mechanisms result in water moving faster into the river network, either by overland flow or via man-made culverts and sewer systems, which subsequently increases the peak flows whilst reducing the lag time (Huang *et al.*, 2008; Braud *et al.*, 2013).

Flood risk is made up of three components; the probability and characteristics of a flood event, the exposure of a population and assets to the hazard, and the vulnerability of the community and its ability to cope with the impacts during and after the event (Jongman *et al.*, 2012). Urbanisation can increase exposure to flooding by locating a population, services and businesses in flood-prone regions (Güneralp *et al.*, 2015). However, attempts to mitigate flood risk by engineering resilience into urban areas and infrastructure makes the concept of risk a complex one to quantify (Winsemius *et al.*, 2016). Figure 2.2 shows exposure to flood events for selected countries, both in terms of people and economic assets, expressed as absolute values compared to relative proportions (Peduzzi *et al.*, 2009; Kundzewicz *et al.*, 2014). The relationship between relative cost and the absolute cost is not linear (Winsemius *et al.*, 2016). For example, in China the absolute costs for both people and GDP are high, but as a relative percentage for the country as a whole the values look less severe. Conversely, in Guyana, the absolute totals are lower, but the proportion affected is higher (Kundzewicz *et al.*, 2014). Generally, the more economically developed a country is, the greater it's potential to mitigate against flood risk. In Japan, 9% of the landmass is flood-prone, and due to urbanisation 41% of the country's population and 65% of their national assets are located in these regions. However, flood defences mean that exposure is low (Kundzewicz *et al.*, 2014).

2.1.1. Floods and Climate Change

A commonly highlighted likely impact of climate change is the increase in extreme weather events, including prolonged temperature extremes and more intense rainfall events (Orlowsky and Seneviratne, 2012; Fischer and Knutti, 2015). There is evidence to suggest that this may subsequently increase the occurrence and severity of hydrological hazards, such as droughts and floods (Trenberth, 2011; Arnell and Gosling, 2016). A special report was produced in 2012 by the IPCC, titled "*Managing the Risks of Extreme Events and Disasters to Advance Climate Change Adaption*" (IPCC, 2012). The report, summarised by Kundzewicz *et al.* (2014), evaluated the

previous research in the literature linking climate change to the spatial and temporal pattern of extreme weather and flood events. The authors provide analysis and conclusions on the likelihood of climate change-induced alterations in extreme weather and subsequent hydrological hazards.

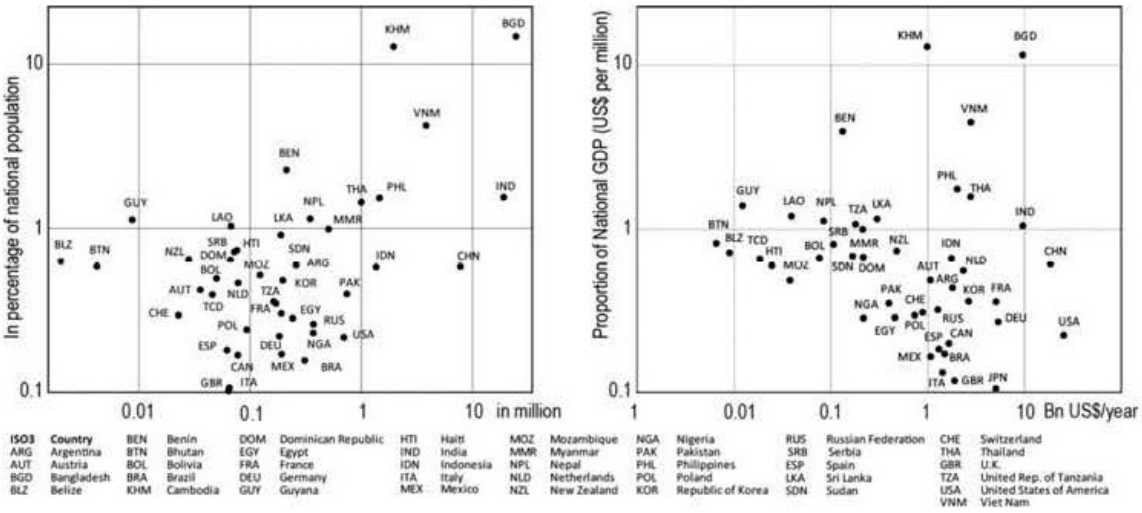

Figure 2.2. The number of people (left) and assets (right) exposed to flooding each year for selected countries, expressed as absolute values against relative values. Originally published in Kundzewicz *et al.* (2014), using data from Peduzzi *et al.* (2009).

One of the main challenges when assessing climate change impacts is accounting for a large amount of uncertainty within the analysis and predictions (Kay *et al.*, 2009; Arnell and Gosling, 2016). For example, translating any observed trends in precipitation into river flow and changes in flood characteristics is difficult due to the lack of in-situ data to substantiate any such relationship, both spatially and temporally (Kundzewicz *et al.*, 2014). Based on the evidence the IPCC considered, they report that some regions have seen a significant increase in extreme precipitation events, concluding that it is likely that this trend will continue, particularly in high latitudes and northern mid-latitudes during winter (Trenberth, 2011; IPCC, 2012). Despite the predicted increase in extreme events, mean precipitation appears likely to decrease, continuing the trend of reducing streamflow into the oceans over the past 60 years (Dai *et al.*, 2009; Trenberth, 2011; Madsen *et al.*, 2014). This has the potential to create complex water management issues, with regions being exposed to both flood events and water scarcity (Prudhomme *et al.*, 2014; Schewe *et al.*, 2014). The report also notes that there has been an increase in reported flood disasters and associated social and economic impacts over the last 20 years (Milly *et al.*, 2002). However, a

portion of this change can likely be attributed to improved reporting of events, as well as increased risk to people and infrastructure caused by the urbanisation of flood-prone regions (Peduzzi *et al.*, 2009; Güneralp *et al.*, 2015). Assessing how climate change is going to impact flood risk means combining the uncertainties that come from climate change projections with those from predicting future patterns in population movement and economic growth (Jongman *et al.*, 2012).

2.2. Remote Sensing and Environmental Monitoring

Remote sensing can be defined as the acquisition of data for the analysis of the environment using a device that is not in contact with the object or region being studied (Lillesand *et al.*, 2008). Platforms that provide remote sensing datasets include satellites, aircraft, unmanned aerial vehicles (UAVs) and ground-based monitoring. The types of data produced are numerous, many of which are available across all platforms. These include: multispectral (often referred to as optical) imagery; thermal imagery; microwave radar (Radio Detection and Ranging) and LiDAR (Light Detection and Ranging), both of which can be used for height estimation (altimetry) or image creation (Synthetic Aperture Radar); positional data such as GPS; and measurements of earth's gravity and magnetic fields. The wide variety of remote sensing data types available allow for aspects of the atmosphere, biosphere, cryosphere, hydrosphere, marine environments and urban areas to be monitored and researched. As well as analysing environmental conditions, remote sensing data has also been used to help create, calibrate and validate physical models of the environment.

2.2.1. Sensor Platform

Two of the main parameters which determine a sensor's ability to successfully monitor the environment are the spatial resolution of the data and the temporal coverage provided. Based purely on these, it can be argued that aerial and UAV imagery provides greater reliability for environmental mapping and analysis due to the high resolution provided, and the ability to schedule acquisition (Yu and Lane, 2006; Yan *et al.*, 2015). However, data collection can be expensive and weather dependent (Grimaldi *et al.*, 2016). Satellites can provide moderate to high spatial resolution data, often at no cost to the end-user. Temporal and spatial resolutions vary and are strongly linked, with higher spatial resolution available at the expense of temporal coverage (Di Baldassarre *et al.*, 2011; Yan *et al.*, 2015). This has led to the

development and launch of satellite constellations, with multiple satellites allowing for improved temporal coverage whilst maintaining higher spatial resolutions (Martinis and Rieke, 2015; Yan *et al.*, 2015). Compared to aerial imagery, satellites provide coverage across a wider geographical area, with swaths up to hundreds of kilometres in length and width. Furthermore, data is readily available over the internet, reducing the requirements for expertise in planning data acquisition from aerial platforms. Due to the operational advantage of satellite data, only datasets captured on these platforms will be discussed henceforth.

2.2.2. ESA Copernicus Programme and the Sentinels

In 2014 the European Commission (EC) and the European Space Agency (ESA) started the Copernicus programme as a natural successor to the Global Monitoring for Environment and Security (GMES) programme. The aim for Copernicus was to launch and operate a series of earth observation satellites, known as the Sentinels, providing timely and easily accessible data for the monitoring of the natural and built environment. Services are designed to support activities across six key thematic areas: land, marine, atmosphere, climate, emergency and security (Copernicus, 2019). Within these themes, Copernicus data has been used to support a wide variety of research and services undertaken by policymakers, public authorities and academia.

Currently, there are six operational or planned missions, all of which contain multiple satellites. Data types from these missions include SAR imagery (Sentinel-1), multispectral imagery (Sentinel-2), radar altimetry (Sentinel-3 and 6) and atmospheric monitoring (Sentinel-4 and 5). The first of the satellites was launched in April 2014 (Sentinel-1a), with two satellite constellations currently in orbit for Sentinel-1, 2 and 3, and a single satellite for both Sentinel-5 and 6. The current long-term goal for Copernicus is to have up to four satellites in orbit for each of the Sentinel missions, totalling 20 satellites across Copernicus, providing regular acquisitions for each of the different data types (Copernicus, 2019).

All of the data produced by the Copernicus programme is free to use, and can be downloaded by the Copernicus Scihub portal. In their annual report for 2018, Copernicus state that there are 185,000 registered users, with 23,000 new products made available each day, resulting in a total of 13 million products available

(Copernicus, 2018). The provision of freely available Earth observation data has wide-ranging benefits across multiple sectors; It is estimated that between €16.2 and €21.3 billion has been generated as economic benefits from the Copernicus programme since 2008, far eclipsing the €8.2 billion invested by the European Commission (Copernicus, 2019). Amongst the societal and environmental impacts championed are the reduction in casualties from natural disasters, improvements in food security, and higher accuracy when monitoring environmental protection compliance (Copernicus, 2019). A Web of Science search shows the number of articles with either Sentinel-1, 2 or 3 in their title totals 1,307 between 2014 and 2019, showing a high usage of Sentinel data within academia. Furthermore, this is increasing annually, from 75 publications in 2015 to 459 in 2018.

2.2.3. Satellite Imagery and Flood Monitoring

There are two main classes of sensor that acquire satellite imagery: passive sensors, which includes multispectral, hyperspectral (both often referred to as optical) and thermal imagery; and active sensors, such as Synthetic Aperture Radar (SAR). A comparison between multispectral and SAR imagery is provided in Figure 2.3. A list of multispectral and SAR imaging satellites, along with the main acquisition parameters, can be found in Table 2.1.

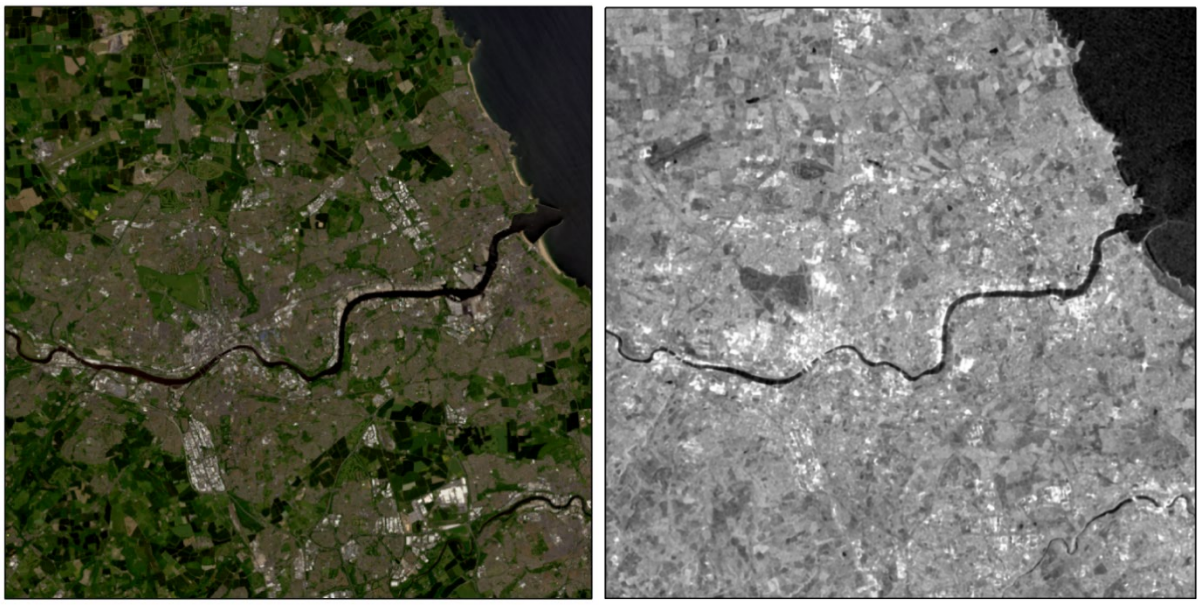

Figure 2.3. Comparison between multispectral (Sentinel-2, left) and SAR (Sentinel-1, right) satellite imagery for Newcastle-upon-Tyne, UK.

Synthetic Aperture Radar (SAR)								
Satellite	Agency	Years Active	Ground Resolution (m)	Revisit (Days	Polarisation	Band	Cost/Scene (US$) - Archive	Cost/Scene (US$) - New
ERS-1	ESA	1991 - 2000	25	35	VV	C	Free	---
ERS-2	ESA	1995 - 2011	25	35	VV	C	Free	---
JERS 1	JAXA	1992 - 1998	18	44	HH	L	Free	---
RADARSAT-1	CSA	1995 - 2013	8 - 100	24	HH	C	1,155 (pre-2008), 2,770 - 3,465 (post-2008)	---
RADARSAT-2	CSA	2007 onwards	3 - 100	24	Full	C	2,770 - 6,000	2,770 - 6,000
ENVISAT-ASAR	ESA	2002 - 2012	30 - 1000	35	Single/Dual	C	Free	---
ALOS-PALSAR	JAXA	2006 - 2012	10 - 100	46	Single/Dual	L	Free - 44	---
ALOS-PALSAR-2	JAXA	2014 onwards	3 - 100	14	Single/Dual	L	1,335 - 4,450	2,670 - 5,785
COSMO-SkyMED	ASI	2007 onwards	15 - 100	16 (<1-4 at full constellation)	Single/Dual	X	730 - 2,655	1,460 - 5,310
TerraSAR-X	DLR	2007 onwards	1 - 16	11	Full	X	1,216 - 2,985	2,430 - 5,970
TANDEM-X	DLR	2010 onwards	3.00	11	Full	X	1,216 - 2,985	2,430 - 5,970
Kompsat-5	KARI	2013 onwards	1 - 20	28	Full	X	800 - 1,650	1,600 - 3,300
Sentinel-1A	ESA	2014 onwards	5 - 100	12 (1-6 at full constellation	Dual	C	Free	Free
Sentinel-1B	ESA	2016 onwards	5 - 100	13 (1-6 at full constellation	Dual	C	Free	Free

Multispectral (Optical)						
Satellite	Agency	Year Active	Ground Resolution (m)	Revisit (Days)	Cost/km^2 (US$) - Archive	Cost/km^2 (US$) - New
World-View 2, 3	Digital Globe	2009 & 2014 onwards	1.84, 1.24	1.1	20 (min 25 km^2)	31.5 (min 500 km^2)
SPOT 5, 6, 7	AIRBUS	2002, 2012 & 2014 onwards	10, 6, 6	5 - 26	1.2 (min 500 km^2)	1.75 (min 100 km^2)
Landsat 5, 7, 8	NASA	1984 - 2013, 1999 & 2013 onwards	30	16	Free	Free
MODIS (TERRA, AQUA)	NASA	1999 & 2002 onwards	500	0.5	Free	Free
Sentinel-2A, 2B	ESA	2015 & 2017 onwards	10	5	Free	Free

[14]

Table 2.1. Past and current SAR (top) and major multispectral (bottom) imaging satellites, with main acquisition parameters. Costs, where provided, are an estimate and may be inaccurate. Adapted from Grimaldi *et al.* (2016).

Multispectral sensors are passive, relying on solar energy to illuminate the ground and recording the naturally reflected energy (Lillesand *et al.*, 2008). They produce a series of image bands capturing the reflectance from different portions of the electromagnetic spectrum, such as the visible (red, green, blue), near-infrared and short-wave infrared wavelengths (Figure 2.4). The range of spectral bands available allows for classification based on the varying reflectance of the feature of interest at different wavelengths. A common approach is to use indices or decision trees that utilise two or more selected spectral bands which display high or low reflectance for the particular feature. Examples include the Normalised Difference Vegetation Index (NDVI (Huete *et al.*, 2002)), the Modernised Normalised Difference Water Index (MNDWI (Xu, 2006)), the Automated Water Extraction Index (AWEI (Feyisa *et al.*, 2014)) and F-Mask, used to identify regions affected by cloud cover and shadow (Zhu and Woodcock, 2012). Equations for common indices used to identify water, based on its strong reflectance in the green band and weaker responses in the near- and shortwave-infrared wavelengths, can be found in Table 2.2.

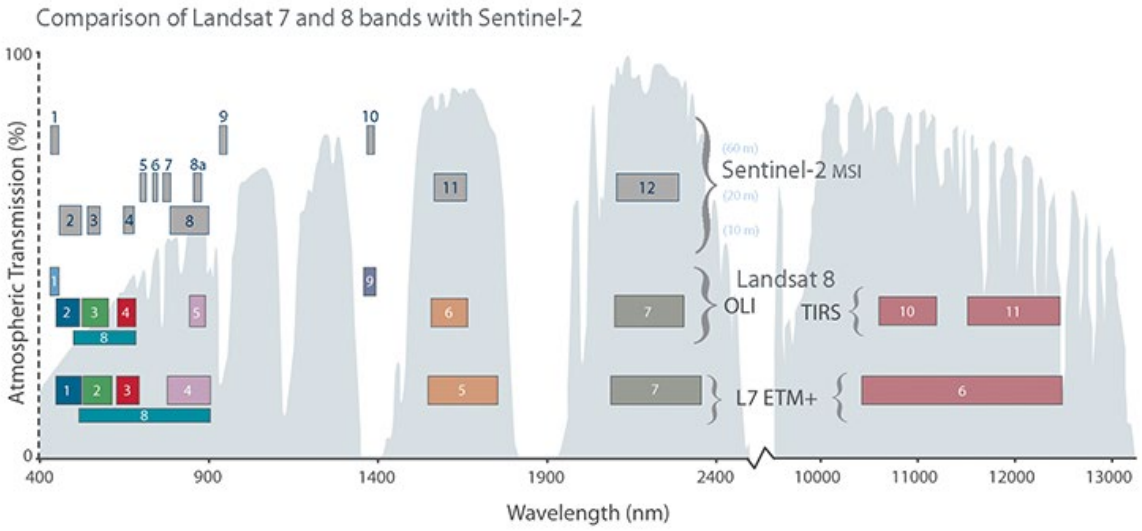

Figure 2.4. The portion of the electromagnetic spectrum utilised by multispectral imagery. Spectral band designations for Landsat-7, Landsat-8 and Sentinel-2 are shown. Originally published online by NASA (last accessed 07th Jan 2019), available at https://landsat.gsfc.nasa.gov/sentinel-2a-launches-our-compliments-our-complements/.

The quantity and variety of data contained within multispectral imagery, including both the acquired image bands and derived information such as the indices outlined in Table 2.2, means the datatype generally produces good results when machine learning classification techniques are used to classify an image. Algorithms have a range of complexities and can either be supervised or unsupervised. Images are

classified into regions of similar spectral responses across all bands, representing different land covers (Lillesand *et al.*, 2008). Machine learning algorithms can be used to identify either a single land cover, such as surface water extent, or to classify a full image. Holloway and Mengersen (2018) classed machine learning algorithms into four main types: Classification algorithms, including support vector machines and random forest, which aim to allocate objects to predefined classes based on user-defined training samples; Clustering algorithms, such as k-means, which use target parameters, such as the number of classes and how distinct these are, to combine objects into unlabelled classes without the need for training data; Regression algorithms, including neural networks and spectral angle classifications, which estimate a continuous response based on previously defined training input variables; and Dimension Reduction techniques, such as principal component analysis, which reduce the number of variables within an image to define new variables that contain the majority of the key information required to classify the data. Examples of algorithms used to identify surface water include neural networks (Li *et al*., 2015; Isikdogan *et al*., 2017), support vector machines (Nandi *et al.* 2017), random forests (Feng *et al*., 2015) and k-means clustering (Molleri *et al.*, 2010). In their study of mapping surface water in Nepal using a variety of machine learning techniques, Archarya *et al.* (2019) found that all algorithms provided accuracies above 90%, with random forest producing the greatest reliability. The authors note that accuracy is reduced in all algorithms when applied to scenes containing snow. Paul *et al*. (2018) noted that many machine learning algorithms only require a small number of training samples to provide accurate results.

Although multispectral imagery is commonly and successfully used within the literature for a range of environmental studies, there are some challenges that need acknowledging. As a passive sensor, the features shown in an optical image are those which first interact with the solar radiation. This means multispectral sensors are unable to penetrate cloud cover, which restricts the imaging of ground features if present (Alsdorf *et al.*, 2007; Gan *et al.*, 2012). Clouds are intrinsically linked to precipitation, and by association cause inundation, which can create the common situation of flood events being obscured due to persistent cloud cover. Similarly, data captured during the night will suffer from insufficient illumination (Mason *et al.*, 2014). Shadows, either from clouds or from tall ground features, can further mask the

image, limiting analysis in urban and woodland areas even on clear days (Alsdorf *et al.*, 2007; Zhu and Woodcock, 2012).

SAR satellites operate in the microwave portion of the electromagnetic spectrum, transmitting a radar pulse towards the earth's surface and recording the backscattered signal that is returned to the satellite (Lillesand *et al.*, 2008). Images display the intensity of this return, which is influenced by surface roughness, object orientation and the dielectric properties (water content) of the imaged surface (Brivio *et al.*, 2002; Henderson and Lewis, 2008). Identification and analysis of specific features within SAR images can often be more challenging than multispectral data, with a particular backscatter response observed within a SAR image, whether weak or strong, potentially corresponding to a number of ground features depending on the satellite acquisition parameters and environmental conditions (Esch *et al.*, 2011). However, because SAR satellites are an active sensor and produce their own source of illumination, they can collect data independent of weather conditions or time of day, providing an operational advantage over multispectral satellites for regular monitoring the environment (Schumann *et al.*, 2009a; Huang *et al.*, 2018). The focus of the remainder of this literature review is on how flooding has been mapped using SAR imagery, with more detail provided in Section 2.3.

2.2.4. Information Requirements and Usage

With regards to flood management and response, remote sensing data has previously been used for two main purposes; by emergency personnel during and after an event to identify regions affected, and by the hydrodynamic modelling community to help improve confidence in model outputs. Both of these require similar observations from remote sensing imagery, namely flood extent and depth. This information during a flood event allows for emergency personnel to identify which population centres and infrastructure are at risk from inundation, allowing for buildings to be protected and the safe evacuation of at-risk people (Yulianto *et al.*, 2015; Cian *et al.*, 2018b). Important in this stage of management is the timely creation of the flood data, with the improved temporal resolution of current satellites increasing the probability of a flood event being imaged, allowing for near real-time monitoring (Martinis *et al.*, 2009, 2015a). Furthermore, high-resolution imagery can be used to map flood damage after large events, assisting in post-event recovery (van der Sande *et al.*, 2003; Bovolo and Bruzzone, 2007).

Index Name		Equation	Reference
Normalised Difference Water Index	NDWI	(Green - NIR)/(Green + NIR)	McFeeters, 1996
Modernised Normalised Difference Water Index	MNDWI	(Green - SWIR)/(Green + SWIR)	Xu, 2006
Automated Water Extraction Index (No Shadow)	$AWEI_{nsh}$	4 x (Green - SWIR[5]) - (0.25 x NIR + 2.75 x SWIR[7])	Feyisa et al., 2014
Automated Water Extraction Index (Shadow)	$AWEI_{sh}$	Blue + 2.5 x Green - 1.5 x (NIR + SWIR[5]) - 0.25 X SWIR[7]	Feyisa et al., 2014

Table 2.2. Examples of spectral indices used to identify water from optical imagery. Note the AWEI indices are developed using Landsat-5, which has multiple SWIR bands (numbers 5 and 7), with the number in square brackets depicting which is used.

Date	Author	Technique	Data	Location	Reported Accuracy & Validation Source
1995	Hess et al.	Supervised Classification Tree	SIR-C	Amazon, Brazil	**99%** In-Field Observations
1997	Oberstadler et al.	Visual Interpretation	ERS-1	Rhine, Germany	*Visual Comparison to Aerial Imagery*
1999	De Roo et al.	Maximum Likelihood Supervised Classification	ERS-1	Rivers Oder & Meuse	**74-82%** Aerial Imagery
2001	Townsend	Supervised Classification Tree	RADARSAT-1	North Carolina, USA	**94%** Wells on Floodplain *
2005	Bonn & Dixon	Supervised Classification	RADARSAT-1	Manitoba, Canada	*Not Reported*
2006	Matgen et al.	Principal Component Analysis	ERS-1	Alzette, Luxembourg	*Not Reported* **
2011	Pulvirenti et al.	Fuzzy Classification	COSMO-SkyMED	Shkodër, Albania	**85%** Histogram Thresholding Result ***
2013	Westerhoff et al.	Multi-Temporal Probability Distribution	ENVISAT-ASAR	Pakistan & Thailand	**90-97%** HAND and SAR Statistics **
2014	Mason et al.	Double Bounce Scattering Modelling	TerraSAR-X	Severn, UK	**91%** Known Flood Locations
2014	Pradhan et al.	Texture Analysis	TerraSAR-X	Terengganu, Malaysia	**84%** No Source Given
2015	Martinis et al.	Tile-Based Thresholding & Fuzzy Classification	TerraSAR-X	Various	**87-99%** Aerial and Optical Imagery
2015	Schlaffer et al.	Multi-Temporal Harmonic Analysis	ENVISAT-ASAR	Severn, UK	**>80% Rural** Aerial Imagery
2018	Amitrano et al.	Texture Analysis & Fuzzy Classification	Sentinel-1, COSMO-SkyMED, RADARSAT-2	Various	**93-95%** Coperinucus EMS ****

[18]

Table 2.3. Selected additional SAR flood mapping methodologies found within the literature.

Notes on validation and accuracy reporting:

** 13 points used as validation instead of more continuous data.*

*** No accuracy reported, but results used in further hydrodynamic modelling analysis.*

**** Validation dataset derived from same SAR scene used for main analysis, and subsequently likely correlated.*

***** No mention is given of what methods used by the Copernicus Emergency Management Service (EMS) to derive flood extent.*

Physically-based hydrodynamic models provide an understanding of how water flows through a catchment during the course of a rainfall event, including identifying areas of inundation. Common outputs include flood extent, depth, and water velocities. Retrieval of extent and depth from satellite imagery allows for model calibration and validation, helping to identify when models are working below requirements (Musa *et al.*, 2015; Grimaldi *et al.*, 2016). Furthermore, it is possible to assimilate information from satellite images directly into flood models during an event, reducing the uncertainty of the model predictions by correcting the model state at the time of the satellite pass (Matgen *et al.*, 2010; Giustarini *et al.*, 2011). However, care is needed when comparing remote sensing data to model outputs, as inaccuracies in the flood extents or depths from the imagery can result in false confidence in the hydrodynamic model, or lead to over-parameterisation of the model to match the validation dataset (Giustarini *et al.*, 2011; Musa *et al.*, 2015).

2.3. Determining Flood Extent from SAR

SAR sensors have a side-looking geometry instead of the nadir viewing angle typically found onboard multispectral satellites, which results in the microwave pulse specularly reflecting away from the satellite when it interacts with a flat surface, such as water (Henderson and Lewis, 2008). In a SAR image, these locations are synonymous with low backscatter values and can be identified as dark areas compared to lighter, stronger backscatter responses that are associated with land features (Zhou *et al.*, 2000). The clear difference in backscatter from water and land has led to algorithms being developed based on the delineation of the boundary between flood and dry land, and the subsequent extraction of the inundated areas. Identification of the flood shoreline is normally possible to an accuracy of one pixel (Bates *et al.*, 2014; Grimaldi *et al.*, 2016).

Type of algorithms are often divided into pixel-based processes, where each individual pixel is classified as its own entity, or object-based algorithms, which look to class groups of pixels as a single object based on the probability of them being related (Lu *et al.*, 2015; Martinis *et al.*, 2015a). Some of the more common processes (image histogram thresholding, active contour models and region growing, and change detection) are described in detail below, with Table 2.3 containing information on additional techniques used within the wider research community. There is no clear consensus within the literature as to the most accurate and robust method for

identifying flood areas, and it is common for multiple techniques to be used in conjunction within a hybrid workflow (Di Baldassarre *et al.*, 2011; Matgen *et al.*, 2011). Each technique has examples where it has accurately delineated flood extents, with the geographical location, satellite acquisition parameters and environmental conditions all varying between studies and potentially impacting accuracy (Grimaldi *et al.*, 2016). Additional in-depth reviews on flood mapping from SAR imagery can be found in Grimaldi *et al.* (2016), Schumann *et al.* (2009a) and Yan *et al.* (2015).

Some SAR acquisition parameters and geographical properties can impact the success of the flood mapping algorithms. The specifics of these mechanisms and how they impact flood detection are discussed in detail in Chapter 3. However, some are briefly mentioned within in the following sections, so definitions are given here to assist the reader. Polarisation refers to the orientation that the radar pulse is transmitted and received in relation to the satellite antenna. Normally this will be either Vertical (V) or Horizontal (H), resulting in four common polarisations (VV, VH, HH and HV). The wavelength and frequency of a SAR signal is the portion of the electromagnetic spectrum that the sensor is operating in. Common bands used in satellite SAR systems are X, C and L, equating to 2.5-3.75 cm, 3.75-7.5 cm, and 15-30 cm wavelengths respectively. The size of the wavelength determines the size of the object that can be imaged.

Speckle in a SAR image is random noise caused by multiple scattering objects within a pixel space. For example, two adjacent pixels covering the same field of a crop can have different backscatter values due to variations in the individual crops affecting the signal pathways. Over a large area, this can cause a ‘salt and pepper’ effect over a homogeneous land cover. Due to the side-looking geometry of a SAR sensor, tall features, such as mountains or buildings, can impact the microwaves ability to image and extract information in urban and woodland regions. This can cause geometric artefacts, with the most paramount for flood monitoring being radar shadow, which occurs when the feature blocks the radar pulse from imaging the ground immediately behind it. These locations show up as dark regions within a SAR image, similar to the specularly reflected response from a water surface. The double bounce effect is common in flooded urban and woodland locations, and describes the reflection of the radar signal off multiple surfaces, in this case the water surface and the protruding

feature. This diverts the signal back to the satellite, producing increased backscatter instead of the low returns expected with specular reflection.

2.3.1. Histogram Thresholding

The simplest and quickest method for differentiating between land and water in an image is histogram thresholding (Di Baldassarre *et al.*, 2011). The difference between the expected water and land backscatter responses can be clearly highlighted by plotting the density histogram of the backscatter intensity, with an example shown in Figure 2.5 (Matgen *et al.*, 2011). The distribution is theoretically bimodal, which allows for a threshold to be determined, and the subsequent segmentation of areas of water. Although thresholds can be determined manually (Brown *et al.*, 2016), this can often be subjective, time-consuming, and requires technical knowledge and experience to be performed successfully (Matgen *et al.*, 2011; Westerhoff *et al.*, 2013). Therefore the research community commonly utilises automated thresholding algorithms, allowing for more timely and consistent classification of flood and non-flood regions. Examples include Otsu's algorithm (Otsu, 1979) and the Kittler and Illingworth (KI) algorithm (Kittler and Illingworth, 1986). Both methods have been successfully used for identifying flooding from SAR images, with Schlaffer *et al.* (2015) and Schumann *et al.* (2009b) utilising Otsu's algorithm, and Bazi *et al.* (2005) and Twele *et al.* (2016) applying the KI algorithm, all within a multi-algorithm flood detection frameworks. Landuyt *et al.* (2018) compared the two algorithms, reporting that Otsu's algorithm has a tendency to overestimate flood extent, whilst KI inherently underestimates.

Although flood mapping using a single histogram threshold is common, the variability in SAR backscatter responses under variable environmental conditions, alongside possible bias with each thresholding algorithm, means there is the potential of under or over-prediction of the flood extent. Hostache *et al.* (2009) provide an example where multiple thresholds are calculated from the SAR histogram to account for uncertainty, allowing for the classification of the flood map based on the likelihood of a region being inundated. Separate gamma distributions are calculated for land and water backscatter, with thresholds defined at the minimum land (T_{min}) and the maximum water (T_{max}) backscatter values. Based on these thresholds, the SAR image is classified in certainty flooded (backscatter below T_{min}), potentially flooded (between the two thresholds) and unflooded (above T_{max}).

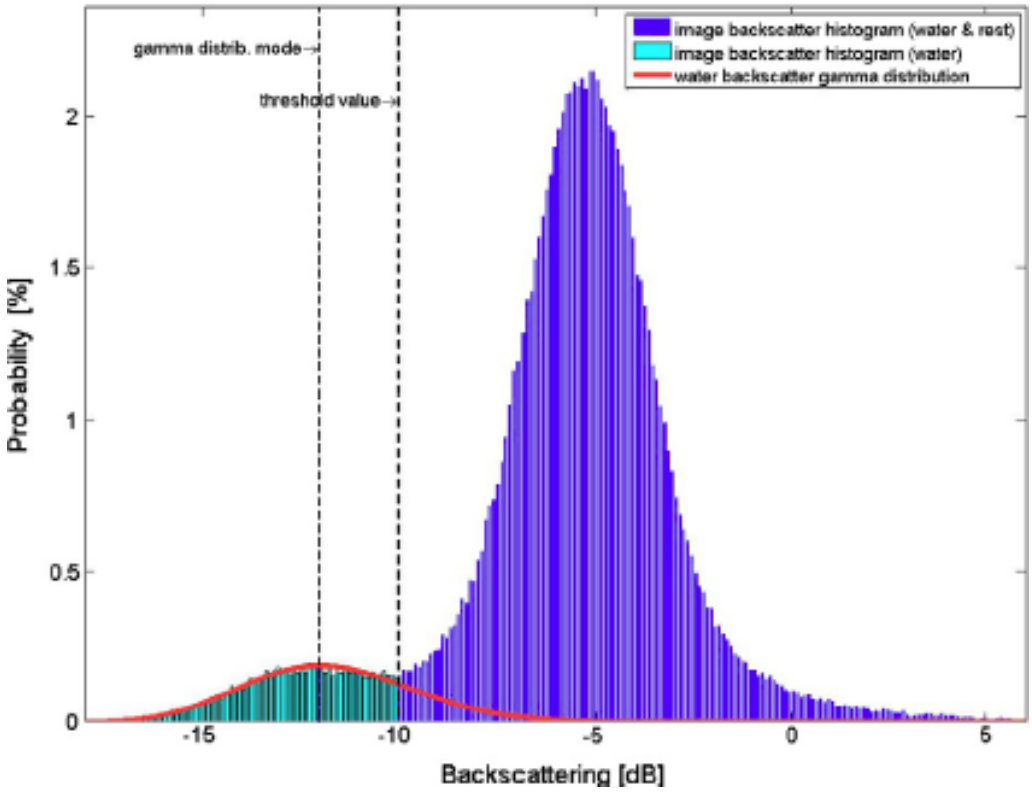

Figure 2.5. Image histogram showing differences in backscatter for water (cyan) and land (blue). The ideal threshold is shown as the low density point between the gamma distributions for water and land. Originally published in Matgen *et al.* (2011).

Applying global thresholding across a whole SAR scene can be challenging. Large differences in the number of pixels within each class are common, and can result in the loss of the bimodality of the histogram which can cause an inaccurate threshold value being determined (Martinis *et al.*, 2009; Landuyt *et al.*, 2018). Splitting an image into smaller regions allows for more reliable identification of the threshold value by ensuring the water and land classes have a similar number of pixels (Bovolo and Bruzzone, 2007). Martinis *et al*. (2009) developed a tiling method to identify regions that had a clear bimodal histogram, allowing for more reliable determination of threshold values using the KI algorithm. The split-based algorithm (SBA) divides a scene into non-overlapping tiles. Each tile is further divided into four sub-tiles, then for each tile, the coefficient of variation (ratio between the mean and standard deviation) of the sub-tiles is calculated. Tiles that are sufficiently bimodal and present a lower mean pixel value compared to the whole scene are selected as suitable for helping determine the final threshold. The global threshold is calculated from either the summed histograms of the tiles selected, or as the median of the individual thresholds calculated for each chosen tile. A further development of the SBA, the hierarchical split-based algorithm (HSBA), works on a similar premise, but searches

for non-uniform tiles to determine the distribution of individual histograms (Chini *et al.*, 2017). This allows for the inclusion of a greater number of local histograms that may have been missed in the SBA algorithm due to the fixed tiling process. The result is a series of different sized and shaped tiles, each with an associated histogram and threshold. Similar to the SBA, these can be averaged, or the histograms summed to find a global threshold if required (Chini *et al.*, 2017). Landuyt *et al.* (2018) found that application of Otsu and KI thresholding algorithms within the SBA framework resulted in improved accuracy. In particular, Otsu's algorithms showed a 30% increase in overall accuracy with the inclusion of image tiling prior to thresholding.

2.3.2. Active Contour Models and Region Growing

Active contour models (ACM), often referred to as a 'Snake', use image statistics to settle on a smooth shoreline contour (Horritt *et al.*, 2001). Start locations for the algorithm need to be defined, and within the literature have either been chosen manually, determined by river locations, or selected based on low backscatter responses within the SAR image of interest (Horritt, 1999; Chan and Vese, 2001; Landuyt *et al.*, 2018). The ACM is controlled by an energy function, which dynamically grows towards the object edge by creating a series of nodes along the current water boundary and assessing the adjacent non-flooded pixels for the likelihood of belonging to the shoreline contour (Horritt *et al.*, 2001). Whether a pixel belongs within the ACM is determined by a goodness function, which is calculated by comparing the pixel value to the mean and variance of the pixels already in the Snake boundary (Horritt *et al.*, 2001). Other constraints, such as tension and curvature, ensure that the flood boundary is smooth and remove the possibility of the Snake overlapping itself; in these situations the algorithm develops sub-snakes, allowing for multiple flood regions or unflooded locations within the flood boundary to be delineated. A Snake will stop growing once all of the adjacent pixels to the nodes suggest non-flood conditions, resulting in a flood boundary where minimal energy is required to travel along (Horritt *et al.*, 2001). An adaption on the traditional Snake algorithm was developed by Mason *et al.* (2007), with additional constraints based on underlying terrain information implemented. The inclusion of height information within the energy function resulted in a flood boundary that better followed the edge of the topographic floodplain, with the Snake finding a smooth low-energy solution for both the terrain and the SAR data.

A similar method to ACM is region growing, with the main difference being the selection of the flooded area being pixel-based, instead of the more object-based operation of the ACM (Matgen *et al.*, 2011). Like an ACM, start locations for the algorithm are required, with similar sampling strategies utilised as with a Snake. Region growing expands the area of flooding from the starting location to include pixels that are homogeneous with the backscatter values of the already identified flood region. This continues until a pre-defined threshold is met at the flood boundary, which in previous studies have been based on the statistics and distributions found within the histogram (Matgen *et al.*, 2011; Giustarini *et al.*, 2013).

Studies using ACMs have produced good results when identifying the flood boundary. Horritt *et al.* (2001) suggested that the algorithm, once properly calibrated, will locate the edge of the flood to within one pixel. Their study of flooding along the River Thames in 1992 produced a 75% accuracy when compared to aerial imagery, with errors mostly coming from the inability of SAR to map inundated vegetation. Matgen *et al.* (2007) found that the ACM identified slightly more flooding (an increase of 1-2 pixels) when compared to a histogram threshold classification for their study of the floods along the River Alzette in 2003. Matgen *et al.* (2011) applied a region growing based algorithm to delineate flooding for the 2007 River Severn flood event. Start locations were determined by thresholding, based on the gamma distributions of the land and water classes within the bimodal histogram. Comparing their results to 181 aerial imagery defined ground control points, an RMSE of 2.00 pixels was found for the flood boundary location. The authors highlight the advantages of using SAR derived start positions for ACM and region growing algorithms, instead of the river locations commonly used in earlier research, as this allows for improved delineation of inundation away from permanent water bodies. Giustarini *et al.* (2013) presented the same methodology, with adjustments made to make the process fully automated. The algorithm produces an accuracy of 82% when compared to manually derived flood boundaries from aerial photography. A further iteration of this algorithm is presented by Lu *et al.* (2014). They add more robust processing for determining a threshold in the absence of a clear bimodal histogram. The updated algorithm is applied to RADARSAT images covering the 1997 floods of Ottawa, and compared to the previous algorithm iterations and a manually thresholded water extent, with all methods validated against water extents derived from aerial imagery. The three iterations of the classification algorithm produce total accuracies ranging between

93% and 96%. The updated region growing algorithm outperformed the previous iterations, with reduced under-prediction of the flood extent.

In their review of SAR flood mapping, Di Baldassarre *et al.* (2011) noted that although results are often good from Snakes, drawbacks include the requirement to fine-tune numerous parameters and long processing times when applied over large areas. These conclusions are collaborated by Landuyt *et al.* (2018), who compared ACM flood maps to those produced by thresholding and change detection algorithms. They note that ACMs have the ability to produce flood maps with increased accuracy, albeit often with the requirement for location-specific parameterisation.

2.3.3. Change Detection

The algorithms discussed in the preceding sections are all based on identifying flooding from a single SAR image. However, the increased number of operational satellites in recent years has resulted in a large volume of past data being available. Satellites that operate on a fixed orbit, such as Sentinel-1, have a back catalogue of images that can be compared to highlight any changes in environmental conditions. When used in flood detection, this involves comparing a dry, non-flood image to one taken when inundation is present. The aim when doing this is to identify those regions that are showing the specular reflection of the radar signal, indicative of surface water, instead of a stronger backscatter response from unflooded land. By subtracting the reference image from the flood image, pixels with a negative shift in backscatter are distinguishable from areas that have had minimal change or an increase in backscatter between scenes, allowing for flood mapping (Giustarini *et al.*, 2013; Schlaffer *et al.*, 2015).

To undertake change detection a reference image is required. Poor selection can result in false classifications due to the variations in image acquisition parameters, or land cover conditions independent of the flood event (Lunetta *et al.*, 2004; Matgen *et al.*, 2011). With the potential for hundreds of images to choose from, selecting a suitable image can be a time-consuming process. Hostache *et al.* (2012) proposed a series of guidelines to help with reference image selection. Firstly, satellite acquisition parameters should match. Previously this would mean that the exact same satellite would need to be used. However, as constellations of satellites carrying the same payload are becoming more common, it is enough that the sensor

collecting and recording the data are the same, thus allowing a greater number of images to be considered. By using a reference image from the same sensor as the flooded scene, SAR specific parameters such as wavelength and polarisation will match. Additionally, radar look angles should correspond as closely as possible, ensuring minimal misclassifications due to different geometric effects caused by topographic features (such as radar shadow, foreshortening and overlaying) that can come from different viewing geometries. For fixed orbit satellites (including Sentinel-1), this means selecting images from the same orbital track. When planning on-demand acquisition during an event (such as Cosmo-SkyMED and RADARSAT-2), this involves ensuring look direction and angle are equivalent to any reference images available for the location. Finally, it is suggested that the reference image should come from a similar time period as the flooded image to minimise any large changes in backscatter caused by non-flood land cover changes. For example, the backscatter characteristics of a bare field in winter will differ from one at the full crop height in summer.

Two methods can be employed to ensure the timing of the reference image is consistent with flood image acquisition. The first involves creating a composite image from numerous scenes captured during the same time period in previous years, with the mean or median pixel value extracted to represent average backscatter (Cian *et al.*, 2018b). This has the advantage of producing an image without speckle due to temporal smoothing of the pixel values. However, the requirement for a number of images to be processed and stored can limit the use of composite images within real-time situations without the prior creation of the reference image. Care is also needed to ensure none of the scenes used to create the composite contain flooding, particularly in regions prone to annual events. An alternative method is to use a single image, commonly the last scene acquired pre-flood (O'Grady *et al.*, 2011). Hostache *et al.* (2012) developed an algorithm for selecting the most suitable reference image from numerous candidates based on the spread of land backscatter responses. Direct comparison between two SAR images can be subject to differences in pixel values caused by speckle, and before undertaking change detection each image requires the application of a suitable filter to ensure textual consistency of features. Land covers should produce relatively similar levels of backscatter away from areas of inundation, particularly if there is a short temporal baseline between images.

The output from the change detection is an image where each pixel represents the difference in backscatter between the reference and flood images. A negative value will indicate potential flooding, but the process on its own does not produce a deterministic map that is often required in flood management situations. Because of this, further processes are normally applied to the difference image, with thresholding commonly used to segment regions showing of the greatest negative shift in backscatter (Bazi *et al.*, 2005; Moser and Serpico, 2005). Long *et al.* (2014), in their study of multi-year flooding in Namibia, thresholded their difference images based on the mean and standard deviation. When compared to Landsat imagery, percentage errors ranged between 8.3% and 22.9%. They suggest sources of error come from cloud shadow in the reference dataset, differences in SAR image resolutions and emergent vegetation obscuring flooding, along with poor reference image selection in some situations.

However, it should be noted that having pre-processed the flood image for the change detection algorithm, it would be prudent to further classify the data using an additional single image technique. Hybrid processing frameworks, utilising two or more of the above approaches, have become common as a means of reducing some of the sources of misclassifications found when using a single method. Matgen *et al.* (2011) noted that accuracy was improved when a change detection element was added to a hybrid processing flow containing histogram thresholding and region growing, with RMSE reduced from 2.00 pixels to 1.27 when compared to aerial imagery. Chini *et al.* (2017) used an HSBA framework to apply a change detection and region growing algorithm to the 2007 floods near Tewkesbury, with a total accuracy of 89% when compared to aerial photography.

2.3.4. Machine Learning Algorithms

Alongside the more commonly utilised techniques described above, there are numerous studies that use machine learning algorithms to identify flood extent from SAR imagery. Skakun (2010) applied an artificial neural network algorithm to extract flood extent from ERS-2, Envisat and Radarsat-2 images, achieving accuracies ranging between 85% and 98%. Insom *et al.* (2015) used Support Vector Machines (SVM) to accurately map inundation in Thailand, noting the superior mapping achieved by SVMs when there is a small number of training samples compared to other machine learning algorithms. Geng *et al.* (2017) note the challenges speckle

noise can provide when classifying features in a SAR image, before proposing a neural network algorithm combined with a spatial smoothing process to limit misclassifications. Recent work has showcased machine learning algorithms based on a combination of both multispectral and SAR imagery, with particular improvements in the quality of training samples used within the classification. Benoudjit and Guida (2019) used a stochastic gradient descent supervised classification algorithm to delineate flooding based on automatically extracted pre-flood training samples. They note there is a compromise between the size of training samples, the subsequent classification accuracy, and the computational time. The authors conclude there are challenges in automatically defining training samples due to spatial resolution deficiencies and cloud cover within the optical images, both of which result in incorrect labelling of samples or insufficient open water training data. Bangira *et al*. (2019) compared the performance of various machine learning algorithms (including SVM, Random Forest (RF) and k-nearest neighbour) when mapping complex water in South Africa using training samples from both types of imagery, with accuracies ranging between 79.5% for RF and 91.7% for SVM. The authors note that the combined thresholding of the SAR and NDWI classified multispectral images produced similar accuracy levels to the machine learning algorithms, at a lower computational cost.

The application of machine learning algorithms for extracting surface water from SAR imagery is relatively unexplored, and although some of the results to date are promising, challenges remain with the reliability of automatic selection of training samples, and the accurate classification of the flood image at a low computational cost. Frameworks that account for these challenges are required before the more widespread application of machine learning techniques are used for SAR flood detection.

2.3.5. Ongoing Challenges

Despite the proven utility of SAR to map flooding in open, rural areas, there are still challenges in deriving flood extent in other geographical situations. Both urban and woodland regions prohibit accurate flood mapping due to the high number of vertical structures (buildings or trees) that intercept the radar signal. Higher spatial resolution can reduce some of the uncertainty of flood mapping in urban locations, however, even images captured at 3 meter resolution can be severely impeded (Giustarini *et*

al., 2013). SAR simulators have been used to mathematically model the radar signal's interaction with urban features to identify the locations likely impacted by radar shadow (Mason *et al.*, 2012a). Further analysis of the radar backscatter pathways can be used to determine where double bouncing of the radar signal is likely to have occurred, allowing for flood identification (Mason *et al.*, 2014). However, this method requires high-resolution terrain and surface models, datasets which are not available for many locations. Giustarini *et al.* (2013) used change detection to identify and remove any false classifications caused by radar shadow, with an accuracy of 82% when validated against aerial photographs. They found that around 2% of the flooding within the validation dataset was found in regions affected by radar shadow.

Recent research has shown that Interferometric SAR (InSAR) coherence has the potential to identify flooding in urban locations (Pulvirenti *et al.*, 2016; Chini *et al.*, 2019; Li *et al.*, 2019). Coherence is a measure of similarity between the phase and amplitudes of two SAR images. In dry conditions, urban areas are typically coherent due to the fixed geometry of the ground features, which produce highly correlated backscatter signals when imaged from the same satellite position (Figure 2.6). The coherence is lost when the urban area is flooded due to variations in the relative spatial locations of the scattering surfaces, which subsequently alter the radar pathways (Li *et al.*, 2019). Chini *et al.* (2019) used the coherence between Sentinel-1 datasets to map inundation in Houston during Hurricane Harvey. They initially map buildings to represent locations where double bouncing of the SAR signal is likely, before assessing changes between the pre-flood and co-flood coherence in these regions to identify inundation. The authors note that the small temporal baseline and fixed orbit of Sentinel-1 lends itself to InSAR based flood detection, despite the moderate resolution of the data. Li *et al.* (2019) mapped the urban flooding from the same event using higher resolution TerraSAR-X data, utilising multi-temporal SAR intensity and coherence within a neural network framework. The authors note that accuracy was improved with the addition of coherence to the classification.

Identifying flooding in vegetated areas brings the additional challenge of the variability in plant structure depending on the season, particularly when using methods that require a temporal analysis like change detection (Pulvirenti *et al.*, 2016). This limits the application of InSAR for identifying flooded vegetation due to

the lack of coherence in dry conditions. Algorithms developed to identify flooded vegetation include decision trees (Martinez and Le Toan, 2007; Betbeder *et al.*, 2014), fuzzy classifications (Pierdicca *et al.*, 2008; Pulvirenti *et al.*, 2013) and supervised classifications (Hess *et al.*, 1995; Voormansik *et al.*, 2014). Tsyganskaya *et al.* (2018) developed a time-series based approach for identifying temporarily flooded vegetation in Namibia using the ratio between cross- and co-polarised data, which displays a marked increase in value when compared to non-flooded images for the same region (Figure 2.7). Results are obtained using a k-means clustering algorithm and thresholding, with an overall accuracy of 85% compared to the visual interpretation of optical imagery. They note that this methodology has the potential for highlighting flooding in urban areas.

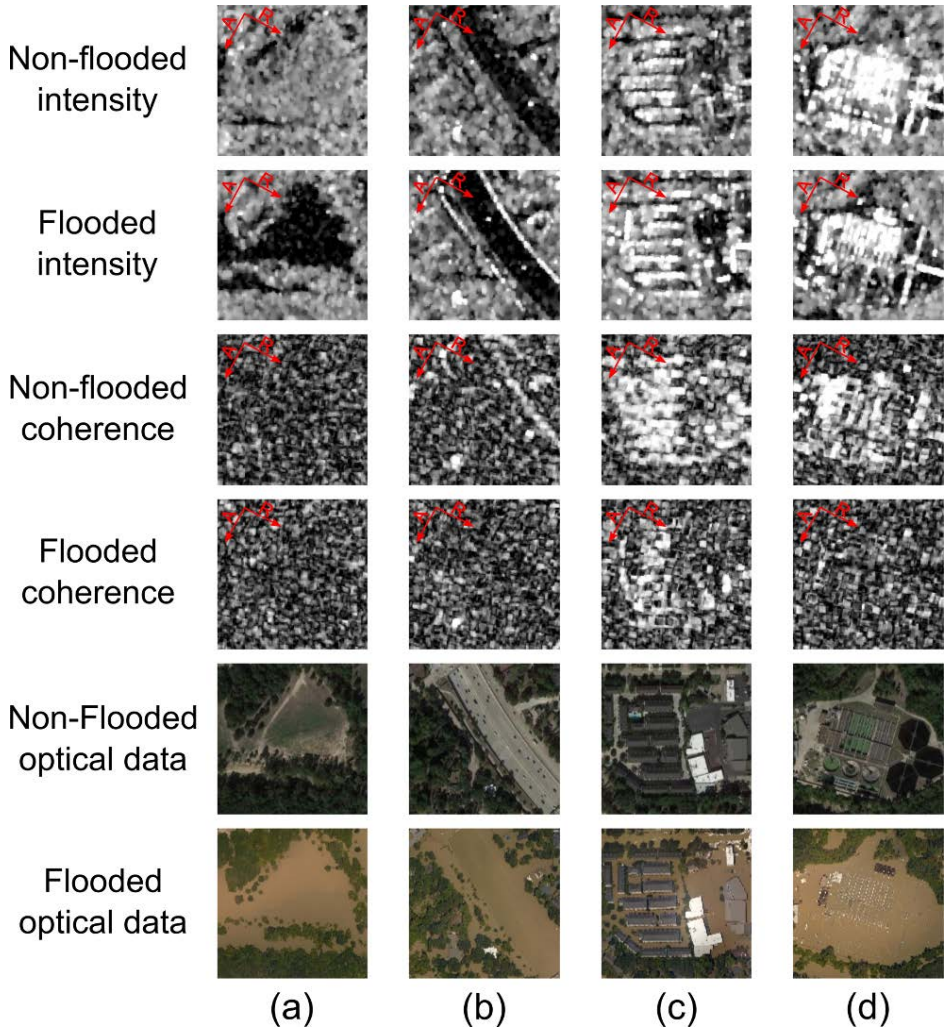

Figure 2.6. SAR backscatter intensity and coherence for different levels of urbanisation, in flooded and non-flooded conditions. Columns show grassland (a), roads (b), buildings with low-level flooding (c), and buildings with high-level flooding (d). In particular, note the lack of coherence in vegetated and flat land covers during non-flood (columns (a) and (b), 3rd row), and the loss of coherence in more built-up locations when flooded (columns (c) and (d), 4th row). Originally published in Li *et al.* (2019).

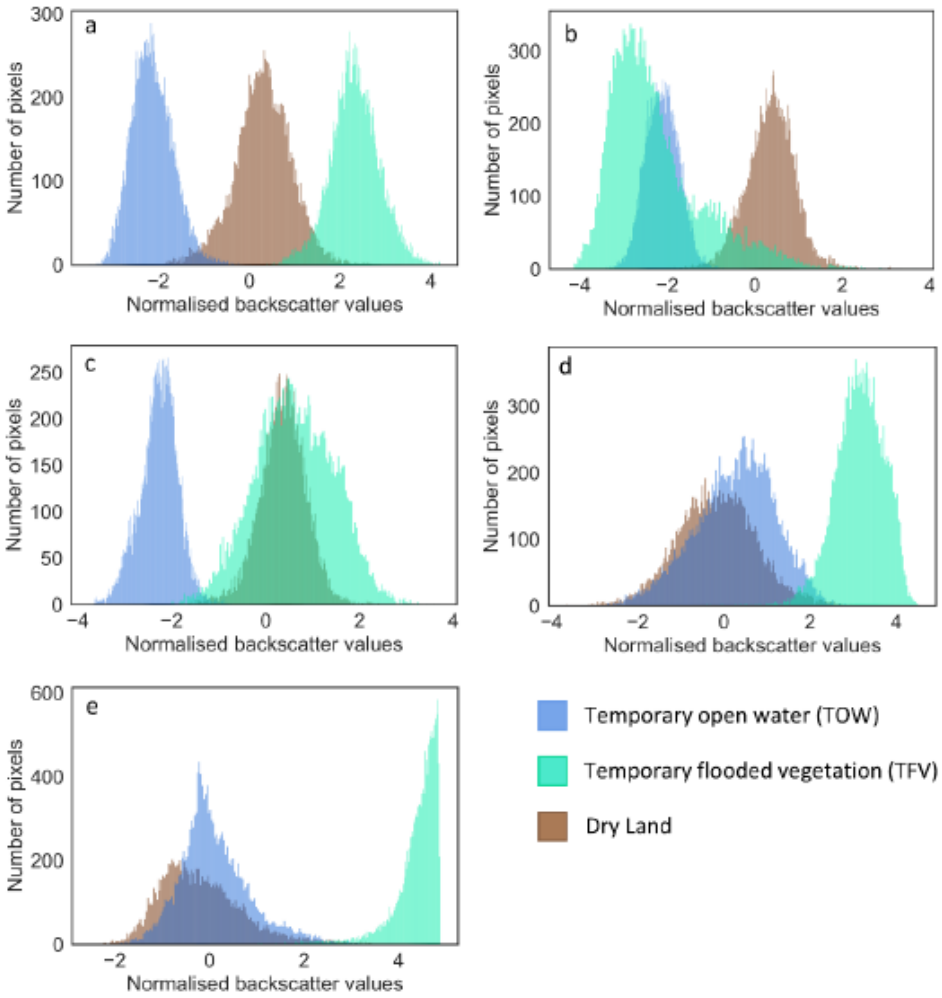

Figure 2.7. Variation in normalised backscatter values for VV (a) and VH (b) polarisations and derivatives (VV + VH (c), VV – VH (d) and VV / VH (e)) for open water, dry land and flooded vegetation. Originally published in Tsyganskaya *et al.* (2018).

With the improvements made in satellite data and flood mapping algorithms, near real-time inundation monitoring is possible. Although the temporal resolution is improving for fixed orbit SAR satellite, it is still unlikely that any images will be captured for short-term events, unless a satellite is specifically tasked to acquire data (Grimaldi *et al.*, 2016). The use of constellations of satellites can improve revisit times, however, there will still be situations where flood events are insufficiently imaged.

Along with the improved imagery provided by recent satellites launches, the infrastructure for delivering and processing the data has also been enhanced. For example, data from the Sentinel satellites is often transmitted through the European Data Relay System (EDRS), a series of geostationary satellites that allow faster delivery of data by removing the requirement for acquisition satellites to have line-of-

sight with the ground receiver stations (Torres *et al.*, 2012; ESA-ARTES, 2017). The result is that Sentinel data is often available within an hour of acquisition. Advances in computing infrastructure, such as cloud computing, allows for image pre-processing and classification to be completed in a timely manner, increasing the opportunities for results being used by emergency personnel or assimilated into flood forecasting models. Examples of automated flood classification algorithms include those developed by Lu *et al*. (2014), Martinis *et al.* (2015b), Mason *et al.* (2012a), Twele *et al.* (2016) and Westerhoff *et al.* (2013). Ensuring that these algorithms are robust across different SAR satellites and acquisition parameters, geographical location, size of the study area and environmental conditions should be the next steps undertaken. Current examples of on-demand, real-time operational flood detection services include the Copernicus Emergency Management System (CEMS) and the Dartmouth Flood Observatory (DFO), which acquire and process satellite imagery for emergency services during an event.

2.4. Deriving Flood Surfaces, Depths and Volumes

Previous studies have proposed a number of methodologies for estimating the height of the water surface, either via direct measurement or indirect estimation. Direct methods involve using sensors which are primarily designed to measure the height of the Earth's surface, such as LiDAR and altimeters, or InSAR processing from the SAR datasets used to derive flood extent. Indirect techniques focus on combining the derived flood extents with terrain models to estimate the shoreline heights and interpolating these to form a water surface. The depth and volume of the flood can subsequently be calculated by subtracting the elevation data from the water surface.

2.4.1. Water Surfaces: Direct Measurements

InSAR has been used to create numerous globally available DEMs, such as SRTM (Shuttle Radar Topography Mission), and is commonly used to measure the deformation of the Earth's surface (Chen *et al.*, 2016). To determine any change in surface height over time, two overlapping SAR images are co-registered for locational accuracy before analysing the temporal differences in phase and amplitude of coherent microwave signals to derive any changes (Refice *et al.*, 2014). Due to the specular reflection of the radar signal over water, there is minimal backscatter from which to determine coherence between signals, limiting water height estimation via InSAR (Alsdorf *et al.*, 2001). However, the lack of coherence itself has previously

been used to map flood extent, provided there is a small temporal baseline between the two images (Refice *et al.*, 2014). Estimations of height variation are possible at the edge of the flood where emergent vegetation or buildings protruding the water surface, particular for longer duration events, where there is an increase in temporally coherent backscatter caused by the double bounce effect (Pulvirenti *et al.*, 2016). An example is provided by Jung *et al.* (2010), who characterised the floodplains of the Amazon and Congo Rivers using InSAR, before using measurements of height variation to identify temporal flood dynamics.

Radar altimeters are another form of active microwave sensing. Working as a profiling tool, altimeters transmit a nadir, short-wavelength radar pulse towards the earth and recording the time taken for the signal echoes to return to the sensor, which can then be used to determine the height of the surface in relation to the satellite altitude (Kouraev *et al.*, 2004; Crétaux and Birkett, 2006; Tarpanelli *et al.*, 2013). Originally designed for monitoring the sea surface height, previous studies have shown that altimetry data can be applied for monitoring terrestrial hydrology, such as lakes and rivers (Berry *et al.*, 2005; Jarihani *et al.*, 2013; Birkinshaw *et al.*, 2014; Villadsen *et al.*, 2015). Waveforms are averaged over the altimeter footprint to provide water level heights estimates with an accuracy in the range of 0.3-0.6 m (Smith, 1997; Coe and Birkett, 2004; Crétaux and Birkett, 2006). Birkinshaw *et al.* (2014) used ERS-2 and ENVISAT datasets to determine river stage, subsequently used to estimate discharge for the Mekong and Ob Rivers when combined with Landsat derived water extents. Jarihani *et al.* (2013) compared the accuracy of five different altimetry missions when observing the height of Lake Argyle, Australia. They found RMSEs ranging between 0.04 m (ICESat, a laser altimeter) and 1.5 m (TOPEX/Poseidon), noting that results were more accurate on newer satellites that had improved onboard retracking algorithms for terrestrial water bodies.

There are many challenges when monitoring terrestrial water bodies using altimeters. Waveform shape of the return signal varies with land cover. Over oceans, echoes from the water surface produce waveforms following the Brown model (Berry *et al.*, 2005). Waveforms models from terrestrial water bodies are often referred to as flat-patch or quasi-specular, and comprise of a more pronounced signal peak compared to ocean waveforms (Berry *et al.*, 2005). However, data over land is often more complex due to additional contamination, either from land and off-nadir water bodies,

and extracting the water body signal can often be a difficult process. Homogenous water footprints are only available on reaches over 1 km, and the use of retracking algorithms is required to extract the water surface signal from the complex waveforms that can be produced from terrestrial geographies (Berry *et al.*, 2005). Deriving accurate water heights is generally only possible when the river or lake width exceeds 200-400 m (Tarpanelli *et al.*, 2013). Furthermore, tracking onboard the altimeter instruments can lose surface lock in areas of highly variable topography, causing a loss of data for water bodies located in mountainous regions (Kouraev *et al.*, 2004). Satellite altimeters provide limited spatial coverage, with many parts of the Earth's surface not covered. Altimeter footprints are normally over several kilometres, with an along-track spacing between 300 m to 6-7 km, and orbit-to-orbit spacing of tens to hundreds of kilometres (Fu, 2001). Revisit times are normally in the order of 10 to 35 days. The reduced spatial and temporal coverage for satellite altimeters increases the possibility of a flood event being missed (Alsdorf *et al.*, 2007). Furthermore, when combining flood extent and water height measurements from different satellites, there is likely to be a mismatch in acquisition timing. In these situations, care is needed to ensure any changes in flood characteristics between acquisitions are accounted for within the data analysis.

2.4.2. Water Surfaces: Indirect Estimation

Many of the satellites used to directly measuring water surfaces suffer from limitations with their spatial and temporal coverage, as well as requiring technical knowledge and complex processing techniques to determine water heights from the data. As an alternative, methods for indirectly estimating the water surface have been developed based on combining the derived flood extent with widely available terrain information. Indirect methods reduce the requirement for additional real-time data, allowing for quicker analysis and lower costs, whilst limiting the uncertainty propagating from mismatched acquisition timings. However, it can be assumed that any estimate of a water surface determined by an indirect method is unlikely to have the same level of accuracy as a direct measurement. Differences in dataset resolution between the satellite imagery and terrain model, classification inaccuracies when deriving the flood extent, accuracy of the terrain model, and the algorithms developed to interpolate the shoreline heights into a surface can all produce errors within the derived water surface (Schumann *et al.*, 2009a; Zwenzner and Voigt, 2009; Cohen *et al.*, 2018).

Digital Terrain Models (DTM) and Digital Elevation Models (DEM) provide elevation data at a variety of geographical scales, spatial resolutions and vertical accuracies (Figure 2.8). The freely available Shuttle Radar Topography Mission (SRTM) DEM is available across the globe at 30-90 m resolution. LiDAR data is available covering much smaller geographical areas and can provide high-resolution data as low as 25 cm. As well as selecting an appropriate spatial resolution when indirectly measuring a water surface, the level of height accuracy needs to be acknowledged. A comprehensive assessment of SRTM for hydrological purposes was undertaken by Ludwig and Schneider (2006). Comparing SRTM to a local reference terrain model (DGM25), they report height errors ranging between -5 and 10 m for slopes less than 5°, with the error increasing up to 30 m for slopes above 50°. Rodriguez *et al.* (2006) assessed SRTM performance across different continents, finding absolute height errors ranging between 5.6 m and 9 m. LiDAR data normally comes at a vertical accuracy of +/- 15 cm RMSE (Data.Gov.UK, 2017).

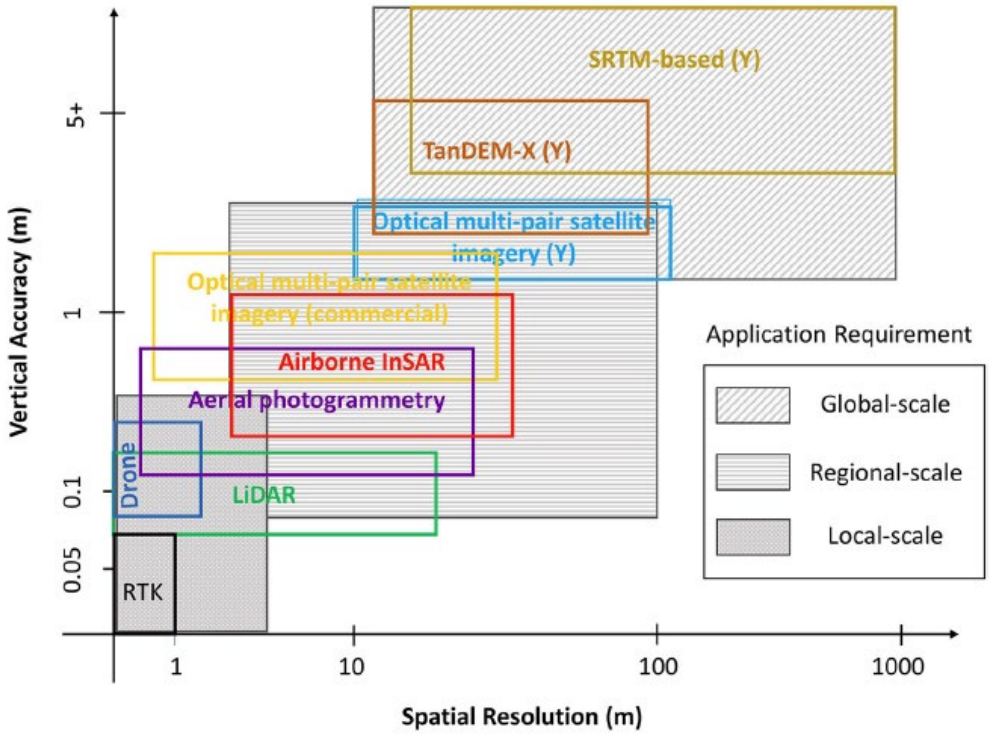

Figure 2.8. Spatial resolution and vertical accuracy for sources of topographic information and DEMs at local, regional and global scale. Originally published in Schumann and Bates (2018).

A key principle when estimating a water surface is ensuring it is hydraulically coherent. Raclot (2006) states that hydraulic energy decreases as a flood wave moves downstream, resulting in a reduction in water level. Additionally, Mason *et al.*

(2007) suggest that the decline in flood shoreline height should be smooth. When combining SAR flood extents with terrain data, shoreline heights are inherently noisy and often do not follow these principles. It is unlikely that the spatial resolution of the imagery and DTM will match, which means that the true topographic flood boundary may differ from those created from the SAR data (Schumann *et al.*, 2009a; Cohen *et al.*, 2018). Locational inaccuracies can often be by a number of pixels depending on the differences in resolutions of the datasets. This can be further exacerbated by flood detection algorithms failing to identify the full extent of inundation due to emergent vegetation at the flood boundary, or classification inaccuracy in woodland and urban locations (Horritt, 2003). This can result in an underestimation of the shoreline height when the flood extents are combined with the DTM. Subsequently, flood boundary heights are often edited to remove any potentially erroneous data points located near urban and woodland regions, and in areas of steeper slope (Hostache *et al.*, 2009; Mason *et al.*, 2012b).

A number of algorithms have been developed in the literature to estimate a water surface whilst addressing the uncertainties described above. Matgen *et al.* (2007) generated a series of cross-sections perpendicular to the flood, allowing for comparison of the shoreline heights on each bank, with adjustments to the flood orientation and location to ensure correlation. A moving average filter is applied to the updated height values along each bank, before a water surface is interpolated using a variety of techniques. The authors find that surfaces created by Multiple Linear Regression provide superior results compared to Triangular Irregular Network (TIN) and Spline water surfaces, which are more impacted by erroneous shoreline heights. Schumann *et al.* (2007) further develop the algorithm to create the Regression and Elevation-based Flood Information eXtraction (REFIX) model. Waterline heights are extracted from flood cross-sections, before being smoothed using linear regression. A TIN surface is subsequently created from the shoreline heights, allowing for improved water surface representation in complex hydrological situations. Schumann *et al*. (2008a) go on to test terrain datasets at various resolutions using the REFIX model, achieving RMSE values ranging between 0.35 m (LiDAR) and 1.07 m (SRTM). A similar approach is proposed by Zwenzner and Voigt (2009), who utilise a dense network of cross-sections, each of which is individually adjusted until height agreement is found on both sides of the flood. This accounts for potential uncertainties from the satellite observations, resulting in an updated flood

extent mask. Shoreline heights are smoothed using a moving average filter, before a TIN of the water surface is created. The authors highlight the potential for poor estimation in locations of steep terrain, where a small change in extent can result in a large variation in water height. The above methods assume flat water across the plane of the flood when adjusting the cross-sections, which may be over-generalising the hydrology occurring during the flood.

Both Schumann *et al*. (2008b) and Hostache *et al.* (2009) attempt to account for the inherent uncertainty of indirect flood level estimation by producing multiple water depth maps to highlight different probabilities of inundation. Schumann *et al*. (2008b) classified a flooded SAR image using numerous thresholds to account for classification uncertainty, alongside adjusting the geolocation of the resultant flood regions to resolve positional uncertainty, such as that caused by emergent vegetation. Fixed cross-sections are subsequently used to extract shoreline height values from all flood classifications, allowing for statistical measures (mean, median, percentiles etc.) to be used to derive a range of TIN water surfaces and depth maps, providing a measure of probability. Hostache *et al.* (2009) produced two thematic flood maps using histogram thresholding to represent the likely minimum and maximum flood extent, which are in turn used to produce a range of waterline height values. Hydraulic coherence principles are applied to numerous flood cross-sections to force decreasing heights downstream, resulting in a reduced range of possible height values at each location. Prior to this, any cross-sections located near urban or woodland areas, or that intersect steep terrain, are removed due to the uncertainty in the flood extent classification. The results are subsequently used to validate hydrodynamic model results.

As well as the cross-section based techniques described above, there are algorithms based on individually evaluating points along the flood boundary. Mason *et al.* (2012b) present an algorithm for selecting distributed edge points in both rural and urban locations. Uncertain rural shoreline points are removed from locations of high slope, before a geospatial dilation and erosion operation is applied, with points without locational consistency before and after the process being removed as potentially suspect. Remaining points are adjusted for emergent vegetation based on local SAR backscatter variances, a technique noted as having a high error margin by the authors. Shoreline heights are extracted in urban areas from locations unaffected

by radar shadow. All points are subsequently thinned to limit spatial clustering, reducing those with similar location and observed heights using Principal Component Analysis. Brown *et al.* (2016) created points every 100 m along the flood boundary, before extracting height values from a high-resolution LiDAR DTM and creating a water surface TIN utilising those points not found on steep slopes.

A common assumption when estimating water surfaces is that they can be considered flat across smaller regions. Based on this, Huang *et al.* (2014) estimated water surfaces for numerous subsets of a large flood in the Murray-Darling basin, Australia, by iteratively filling a terrain dataset until the locations of water depth matched the satellite observed extent. A similar technique was used by Matgen *et al.* (2016), who produced water surface maps under the assumption of consistent water depth for each section of a flood. The Height Above Nearest Drainage (HAND) dataset (described in Section 3.4.2.1) is repeatedly thresholded until an optimal fit is found to the satellite observed flood extents. Cian *et al.* (2018a) created water surfaces for each individual flood polygon by finding stability in the percentile values of the boundary heights. The methodology first removes likely over and underestimation of flood heights via the 5^{th} and 95^{th} percentiles. The algorithm then checks the gaps between every 5^{th} percentile, looking for similarity. The flood surface is selected by the largest percentile pair with less than 10 cm difference between them, with the final height being the median of the two values. Cohen *et al.* (2018) presented the Floodwater Depth Estimation Tool (FwDET), which interpolates unedited shoreline heights using a pixel-based nearest neighbour algorithm, concluding that the technique overestimates the water surface in steep terrain and urban areas.

Indirectly derived flood surfaces are often validated against in-situ river stage, high water marks, hydrodynamic models or aerial photography (Di Baldassarre *et al.*, 2011). Reported accuracies range from tens of centimetres (Matgen *et al.*, 2007; Hostache *et al.*, 2009) through to meters (Oberstadler *et al.*, 1997; Zwenzner and Voigt, 2009). Vertical accuracy for many LiDAR DTMs is in the region of 10 to 15 cm (West *et al.*, 2018; Zhang *et al.*, 2019a), and many studies produce accuracies within this. Sources of error, as previously mentioned, are commonly attributed as the mismatch in resolution between the SAR and DTM data, and the underestimation of the SAR flood extent due to emergent vegetation (Zwenzner and Voigt, 2009; Cian *et*

al., 2018a). The second of these is systemic in the prevalent trend of under-predicting the water surface when using indirect methodologies when compared to direct measurements (Mason *et al.*, 2012b).

2.4.3. Depth and Volume Calculation

Once a water surface has been created, it is possible to calculate the flood depths by subtracting the DTM, as demonstrated by Cian *et al.* (2018a) and Cohen *et al.* (2018). Depths can subsequently be used to calculate the water volume, which can provide vital information for emergency planners during an event, particularly if water pumping is being undertaken (Brown *et al.*, 2016). An example is presented for the Chao Phraya River in Thailand by Rakwatin *et al.* (2013). Their methodology uses river levels to create daily water surfaces over a 2 month period. These are subsequently clipped to locations identified as flooded in RADARSAT imagery, and used to calculate the volume. The research produces a dense time-series of water volumes, with sub-catchment water movements analysed via segmentation of the study area. This highlights the potential for the monitoring of flood dynamics at multiple scales. However, the methodology is limited by the requirement for a dense river gauge network to reliably create the water surfaces, data that is commonly available more sparsely.

2.5. Big Data Computing and Analytics

The term “Big Data” became common in the late 2000s as a result of the increase in data volume brought on by the internet age (Li *et al*., 2016). Big data is defined as the requirement for state-of-the-art hardware, software and database technologies to allow for the capture, storage, manipulation, analysis and presentation of a dataset (Ma *et al*., 2015; Li *et al*., 2016). Big data can come in many forms, including social media metrics, electronic communications, transaction data, and infrastructure monitoring, as well as the geospatial datasets used within this thesis (Li *et al*., 2016). With the continuing launch of new Earth Observation satellites, the quantity of openly available imagery is rapidly expanding. These increases in data pose significant challenges, and the computing infrastructure required for the storage, analysis and dissemination of the data similarly requires advancing, highlighting that satellite remote sensing resides within the big data domain (Ma *et al.*, 2015).

There are a number of ways in which a dataset can be “big”. The three Vs of big data, namely volume, velocity and variety, further describe some of the challenges associated with big data (Li *et al*., 2016). If the volume of a dataset is such that the use of scalable computer systems, such as clusters and cloud computing, provide a cost, time or performance benefit compared to traditional IT infrastructure, then it is typically classed as big data (Sun and Scanlon, 2019). Velocity within a big data context can refer to the speed of data acquisition, as well as the required timeline for data analysis (Sun and Scanlon, 2019). There are numerous types of spatial data, both satellite acquired or otherwise, all of which require different data formats, processing and levels of uncertainty. Additional big data Vs have been proposed, including veracity, visualisation and value, highlighting the breadth of challenges associated with processing complex datasets (Li *et al*., 2016). All of the Vs are relevant to remote sensing of the environment. Some of the main challenges include: the large volume of data produced by earth observation satellites (as highlighted in Section 2.2.2. (Copernicus, 2018)); time-critical remote sensing applications that require fast acquisition, transmission and processing of data in near real-time (Sun and Scanlon, 2019); varying levels of accuracy from different data sources, making uncertainties within analysis hard to quantify (Li *et al*., 2016); and the visualisation of large, multi-temporal datasets, results and uncertainty (Li *et al*., 2016). Solving these challenges will allow for the near real-time, large scale environmental analysis utilising the global, multi-temporal and multi-sensor datasets currently available (Ma *et al.*, 2015; Sun and Scanlon, 2019).

There are a number of technologies that provide solutions to the challenges of big data. Scalable high-performance computing (HPC) infrastructures, including both clusters and cloud computing, allow for agile processing of large datasets by increasing the number of processors, memory and disk space (Ma *et al.*, 2015). The increased processing power available through HPC allows for improved processing speed and greater algorithm complexity, allowing for the further development of near real-time applications and machine learning frameworks (Ma *et al.*, 2015; McCabe *et al*., 2017). With the ability to scale the number of processors to match the desired application, raw processing power is no longer the limiting factor when analysing a large volume of data (Ma *et al*., 2015). Typically, one of the more time-consuming stages are data input-output operations, and one of the key principles within HPC is the idea of moving the code to the data across parallel processors. This results in

operations that are computationally heavy with limited data transfer, ultimately reducing processing time (Ma *et al.*, 2015; Li *et al.*, 2016).

Improvements have been made in storage of remote sensing datasets with the application of NoSQL databases and Data Cubes. NoSQL (Not Only Structured Query Language) is a distributed database technique designed to store non-relational data within a scaleable framework, which utilises key-value pairings to allow for fast data retrieval upon request (Ma *et al*., 2015). Data cubes store information within a multi-dimensional array (typically latitude, longitude and time), allowing for simplified access to multi-temporal data for the user (Augustin *et al*., 2019). The Australian Geoscience Data Cube (Lewis *et al*., 2017) was one of the first major implementations of data cube technology, with subsequent frameworks developed across many countries and regions based on the open-source technology (Augustin *et al*., 2019). One of the principles behind data cubes is the production of Analysis Ready Data (ARD), where the majority of the pre-processing is undertaken by the institutions that acquire that data (such as satellite agencies) due to their greater accessibility to HPC facilities (Augustin *et al*., 2019). This allows data to become more accessible to a wider variety of end-users by reducing the knowledge and infrastructure requirements to complete analysis.

There are services that combine many of the above technologies into user-friendly tools, allowing for processing and analysis of large volumes of satellite imagery. Examples include Google Earth Engine (GEE) and Amazon Web Services (AWS). These services both provide ARD from a number of satellites whilst being supported by cloud computing infrastructure, allowing the user to undertake fast, complex analysis of multi-temporal satellite datasets (Gorelick *et al*., 2017; McCabe *et al*., 2017). The availability of a back-catalogue of historical satellite data stored on these platforms can allow for improved training of machine learning algorithms (McCabe *et al*., 2017). An example of historical hydrological analysis is presented by Pekel *et al*. (2016), who produced the Global Surface Water Explorer using GEE by analysing the multi-temporal Landsat imagery to identify surface water, allowing for analysis of changes in water occurrence and seasonality through time.

2.6. Summary and Research Opportunities

Recent satellite launches have ushered in a new, data-rich era of earth observation. Temporal coverage has been improved for sensors providing medium to high-resolution imagery through the development of satellite constellations. Whilst data from some on-demand satellites can be costly, the Copernicus Sentinel programme provides data from a variety of sensors free of charge. Advancements in computing allow for processing algorithms and image analysis to be completed faster, opening up the possibility of near real-time monitoring. For flooding, remote sensing can help improve our understanding of the changing dynamics of an event. It is now possible to get multiple images of the same flood event, allowing for analysis of how the extent, depth, slope and water volume change through flood onset, peak and recession.

SAR provides an operational advantage when mapping flooding due to its ability to penetrate cloud cover. Flood mapping from SAR imagery is a well-researched topic. Both pixel and object-based algorithms have been developed to identify open water from images, highlighting the specular reflection of the radar signal. Hybrid frameworks, combining multiple traditional processing techniques, have become common and help to reduce false classifications. Challenges remain, primarily when identifying inundation under vegetation and within the urban environment. Due to the high impact of flood events in urban areas, improving sensing in these locations has become a high priority for research.

Data fusion of the SAR derived flood extents and terrain models allow for estimation of the water surface, and subsequently water depth and volume. Key within this process is accounting for uncertainty, with inaccurate flood extents and the mismatch in resolution between datasets likely to introduce errors. Various methods have been developed for identifying the true topographic edge of the flood extent, however, these have the potential for over-generalising the shoreline heights. Further research is needed into how best to identify locations of accurate flood delineation to allow for subsequent water surface interpolation.

Research has shown that automated, global, near real-time flood monitoring is achievable using some of the algorithms currently developed. Operational flood monitoring allows for derived flood maps to be used by emergency personnel or

assimilated into hydrodynamic models. However, there is no clear consensus as which methodology is the most reliable and accurate. Most studies focus on singular flood events or source of satellite data, with no consideration of robustness across different acquisition parameters or environmental conditions. Furthermore, good validation datasets are often hard to find, resulting in a lack of consistency and confidence in the reported accuracies. Ensuring algorithms are scalable for global applications, adaptable for different satellite parameters and robust to accurately identify flooding in various environmental settings is important for new research going forward.

Chapter 3. SAR Acquisition and Pre-Processing

3.1. SAR Image Acquisition

Radio detection and ranging, more commonly known as radar, was first utilised as a source of imagery by the military in the late 1940s. Seasat, the first civilian satellite carrying a radar instrument, was launched in 1978, and since then there have been numerous spaceborne platforms collecting radar imagery (major radar satellite missions are summarised in Table 2.1), alongside aerial and ground-based systems. Radar imaging systems are active, meaning they provide their own source of illumination, and work by transmitting a microwave pulse towards the earth's surface and recording the reflected signal returned to the sensor (Lillesand *et al.*, 2008). As an active sensor, they can image during the night and independent of weather conditions (Alsdorf *et al.*, 2007).

There are two common types of imaging radar, side-looking radar (SLR or SLAR) and synthetic aperture radar (SAR). SLR has deficiencies in spatial resolution (discussed in Section 3.1.1.) that led to the development of SAR. Figure 3.1 gives an overview of how a SAR system operates. As it travels along its orbit, a SAR instrument is constantly alternating between transmitting a microwave pulse and recording the returning echoes (Lillesand *et al.*, 2008). Ground features are imaged by multiple pulses, with advanced processing and merging of the signals resulting in an increased illumination time for ground objects. The frequency of the returned signal from a feature will differ based on the location of the object in relation to the satellite, known as the Doppler shift. Within the radar beam, target features ahead of the sensor will have an upshift in frequency, whilst those behind will have a downshift (Rees, 2013). Correcting the returned signals for their Doppler shifts allows for the merging of pulses, improving the signal-to-noise ratio and spatial resolution of the resulting image (Lillesand *et al.*, 2008).

Radars are normally side-looking, and transmit microwave signals at angles typically ranging between 15° and 50° from nadir. The side-looking imaging geometry of SAR satellites results in a number of key angle descriptors used to explain the location of the data collected in relation to the satellite (Figure 3.2). These include the look angle (sometimes referred to as the elevation angle), which is the angle from nadir that the

radar signal is transmitted along (Mather and Koch, 2011). Complementary to the elevation angle is the depression angle, the angle from 90° horizontal at the satellite to the region of interest. The incidence angle describes the angle between the radar beam and nadir at the point of intersection with the ground surface, whereas the local incidence angle describes the relationship between the radar signal and the ground surface once local land slope has been taken into account (Mather and Koch, 2011). The distance between the radar and the point of interest on the ground is known as the slant-range, with the ground-range being the corresponding distance from the on-ground satellite position to the target (Lillesand *et al.*, 2008).

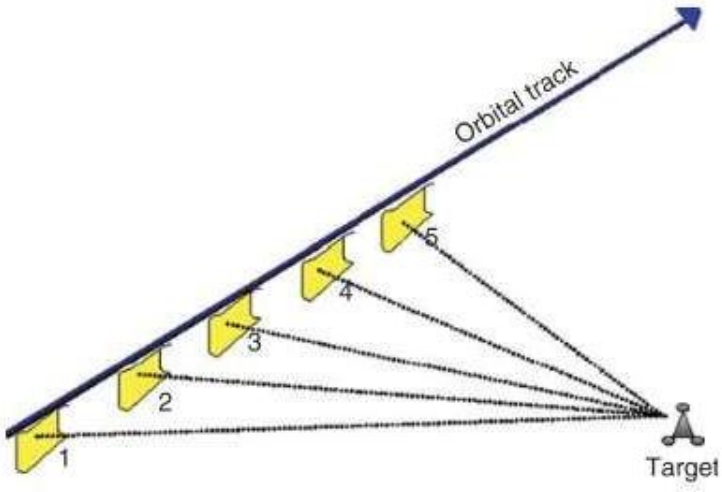

Figure 3.1. Conceptual diagram of how a Synthetic Aperture Radar system acquires data. Multiple pulses of the SAR beam illuminate the ground target as the satellite travels along its orbit. Signals have different Doppler shifts depending on the target position in relation to the satellite. Adjusting for Doppler frequencies and signal merging allows for imaging of the target using the synthetic aperture, which is equivalent to the distance travelled whilst imaging the target. In the image shown, the synthetic aperture is the distance between 1 and 5, compared to the physical antenna shown in yellow. Published in Mather and Koch (2011).

Numerous aspects of the return signal are recorded at the satellite, including the amplitude of the return, the phase of the wavelength, and the time taken for the signal to return (Lillesand *et al.*, 2008). Slant-range distance to a reflector can be calculated based on the time for the return signal to reach the satellite and the speed of sound. The data displayed within a radar image is known as backscatter and represents a measure of the amount of the transmitted radar microwaves returned to the satellite from the Earth's surface (Lillesand *et al.*, 2008). Commonly the strength of the signal is displayed in decibels (dB), which represents the log-transform of the signal power returned to the satellite. Images are normally displayed in greyscale,

with white pixels representing areas where a large proportion of the radar signal is returned to the sensor and dark pixels are where minimal signal backscatter has occurred.

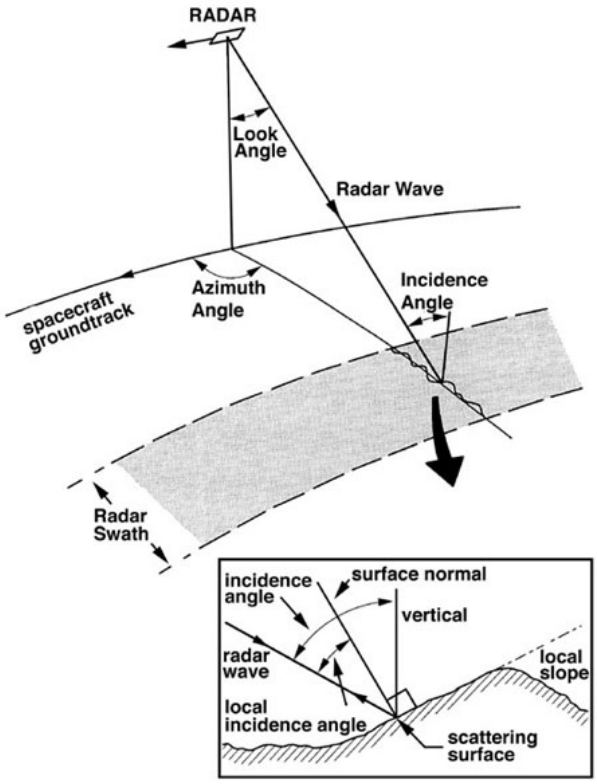

Figure 3.2. Synthetic Aperture Radar (SAR) imaging geometry, showing key angle descriptors including look angle, incidence angle and local incidence angle. Published online at http://satftp.soest.hawaii.edu/space/hawaii/vfts/kilauea/radar_ex/page1.html (last accessed 03/03/2019).

The main component which dictates backscatter strength is surface roughness, which is itself a function of land cover, object shape and size (Lillesand *et al.*, 2008; Grimaldi *et al.*, 2016). Figure 3.3 gives examples of how the scattering of the microwave signal varies with land cover, between non-flooded and flooded situations. Water is theoretically flat, and will specularly reflect the radar signal resulting in minimal signal return to the satellite (Henderson and Lewis, 2008; Jung *et al.*, 2010). This is in contrast to the higher amounts of backscatter produced by other land surfaces. For example, a region of vegetation will produce more backscatter due to the greater number of irregular objects for the signal to interact with, causing an increase in surface roughness and volume scattering of the radar signal (Schumann and Moller, 2015; Twele *et al.*, 2016). In an urban area, the radar signal often interacts with more than one feature due to the close proximity of high reflectance

targets. Known as double bouncing, the microwave signal can interact with the ground followed by a building (or vice-versa), resulting in a large proportion of the transmitted radar signal being returned to the satellite (Schumann and Moller, 2015). When mapping surface water, double bouncing of the SAR signal in urban and woodland regions masks the specular reflectance from the water surface, often leading to an underestimation of the water extent (Zwenzner and Voigt, 2009). Depending on the orientation of the double bounce feature this can result in a stronger return signal compared to dry conditions (Horritt *et al.*, 2001; Giustarini *et al.*, 2013).

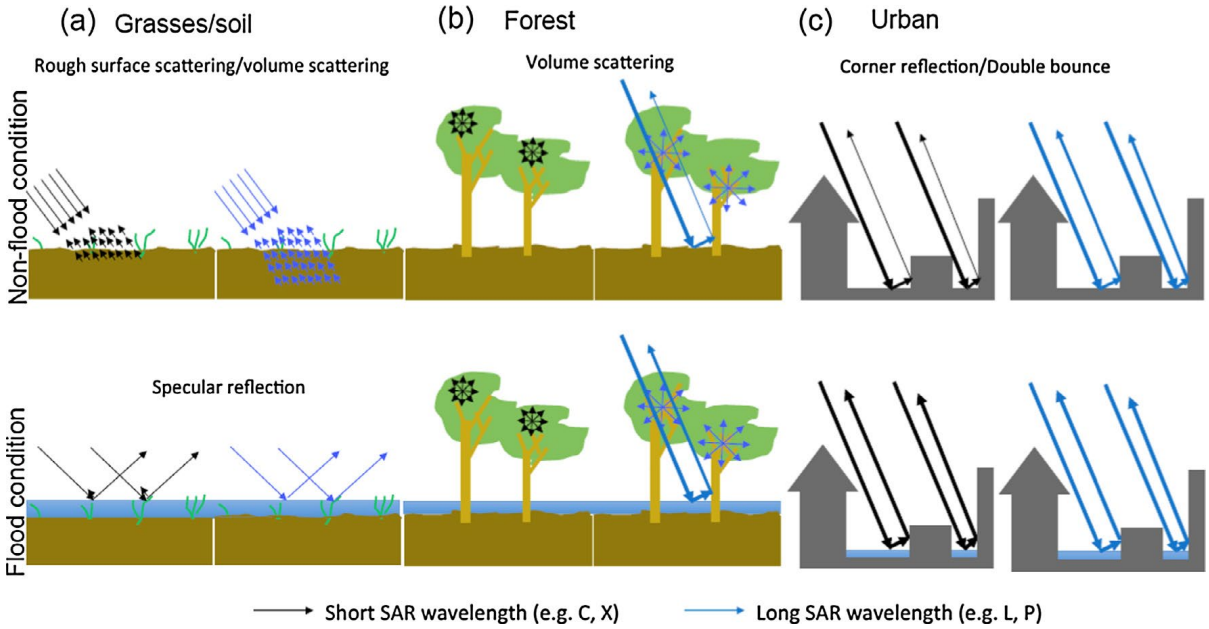

Figure 3.3. Backscattering characteristics for different land covers (from left, grassland, forest and urban environments) in dry (top) and wet (bottom) conditions. Expected responses from both short and long wavelength SAR systems shown. Mechanisms to note include; the specular reflection of the radar signal from open water (bottom left), the volume scattering of shorter wavelengths in forest canopies irrespective of flood conditions (middle), and the double bounce of the radar signal from tree trunks and buildings in urban and forest environments, an effect which strengthens if water is present (middle and right). Originally published in Schumann and Moller (2015).

The dielectric properties, or water content, of the feature being imaged can influence the amount of backscatter produced. Microwaves are unable to penetrate water, a relationship that can result in two effects depending on the environmental situation (Liang *et al.*, 2012). The first is the reflection of the radar signal from open water, either specularly if the surface is flat, or more scattered if there is wind roughening of the surface (Alsdorf *et al.*, 2007). The second mechanism occurs when the land

cover has high water content, such as saturated vegetation or soil. In drier conditions, some of the radar signals are reflected into these surfaces, reducing backscatter within an image (Jackson, 2002; Liang *et al.*, 2012). However, when saturated the radar signal fully reflects off the complex surface, increasing scattering in all directions, including towards the satellite (Saatchi and van Zyl, 1995; Lillesand *et al.*, 2008). In the case of soil, backscatter will increase with soil wetness up until surface water forms, at which point specular reflectance will occur and the signal returned to the satellite will decrease to almost zero (Baghdadi *et al.*, 2008; Mitchell *et al.*, 2014). As well as the environmental conditions being imaged, certain acquisition parameters can also impact backscatter, as discussed in the following sections.

3.1.1. Image Resolution

The spatial resolution of radar data is made up of two components: range resolution, which describes the cell size in the direction of the radar pulse; and azimuth resolution, which defines the cell dimension parallel to the orbit of the satellite. The two resolution aspects are determined by different physical acquisition parameters and can vary in size from each other.

Range resolution is determined by the length of the pulse of the transmitted signal. For objects to be distinguishable in range direction they have to be at least half a pulse length removed from one another. If the objects are closer, then the return signals will overlap and the radar system will be unable to differentiate between them (Rees, 2013). When considered in the slant-range domain, range resolution is consistent with the distance from the instrument. However, the ground-range resolution is inversely proportional to the cosine of the depression angle, meaning the data resolution increases with increasing distance from the instrument (Lillesand *et al.*, 2008).

Azimuth resolution is dependent on the beamwidth, which is proportional to the wavelength of the transmitted microwaves and sensor altitude, and inversely proportional to the antenna length. In real-aperture SLR systems, the transmitted beam width increases with slant-range distance, creating a decrease in azimuth resolution at far-range (Rees, 2013). Short-range resolution can be improved by utilising smaller wavelengths or a longer antenna, or by flying the instrument at a

lower altitude. However, often these requirements are impractical and fail to resolve the worsening of the azimuth resolution with range, restricting real-aperture surveys to aerial platforms and imaging small study areas at a short-range distance (Lillesand *et al.*, 2008).

SAR systems are designed to overcome the degradation in spatial resolution with distance from the instrument and the loss of resolution with sensor altitude. A short physical antenna is still found on the instrument, however, a longer synthetic aperture is created from the motion of the instrument over the time, creating an array of antennae that can mathematically be considered a single entity (Lillesand *et al.*, 2008). The far-range is imaged for a longer time period than the near-range, resulting in an increase in effective antenna length with slant-range distance, which can result in synthesised apertures several kilometres in length at far-ranges. Ground objects are imaged with numerous radar pulses, encompassing the full range of Doppler shifts as the satellite travels from behind to ahead of the object. Processing and correcting these signals to the centroid Doppler frequency allows for narrow effective beamwidths to be determined, subsequently creating a constant azimuth resolution (Lillesand *et al.*, 2008). SAR azimuth resolution is calculated as being approximately half of the physical antenna length, with shorter antenna lengths producing a finer resolution (Rees, 2013).

3.1.2. SAR Wavelength and Frequency

SAR data is collected within the microwave region of the electromagnetic spectrum, which is segmented into several bands of specific wavelengths and frequencies that sensors commonly operate within (Table 3.1). Satellite SAR systems normally operate at C-band (RADARSAT-2 and Sentinel-1, frequency 5.405 GHz, wavelength 5.6 cm) or X-band (COSMOS-SkyMED and TerraSAR-X, frequency 9.65 GHz, wavelength 3.11 cm) frequencies, although occasionally longer wavelength L-band instruments (ALOS-2, frequency 1.27 GHz, wavelength 23.5 cm) are used. The wavelength of a signal has a direct impact on which ground features contribute to the backscatter return within an image (Mather and Koch, 2011). The smaller the wavelength, the smaller the object that the SAR signal will interact with. This can create a more varied response from vegetation and bare soil as the true nature of the surface roughness is captured within the image, instead of a more generalised return captured by longer wavelengths (Lillesand *et al.*, 2008).

Band Designation	Frequency (MHz)	Wavelength (cm)
P	300 - 1,000	30 - 100
L	1,000 - 2,000	15 - 30
S	2,000 - 4,000	7.5 - 15
C	4,000 - 8,000	3.75 - 7.5
X	8,000 - 12,000	2.5 - 3.75
K_u	12,000 - 18,000	1.667 - 2.5
K	18,000 - 27,000	1.111 - 1.667
K_a	27,000 - 40,000	0.75 - 1.111

Table 3.1. Radar band designations, frequency and wavelength. Adapted from Mather and Koch (2011).

Both long and short wavelength systems can have situational advantages where the imagery provides superior mapping of surface water (Martinis and Rieke, 2015). For open water bodies, shorter wavelengths provide better delineation of the shoreline, particularly if the land surrounding the water body is flat (Voormansik *et al.*, 2014). However, shorter wavelengths are also more susceptible to increased backscatter from surface water waves (Grimaldi *et al.*, 2016). Images from longer wavelength sensors provide increased canopy penetration, allowing for water identification in forested areas via analysis of the backscatter to identify where double bouncing between the flood surface and the tree trunks has occurred (Voormansik *et al.*, 2014; Chapman *et al.*, 2015). Manavalan (2018) suggested that overall, longer wavelength L-band sensors are the preferential choice for flood monitoring due to their applicability across a greater variety of geographical settings. However, the choice of wavelength is normally determined by the availability of satellites and images, instead of the optimal parameters based on thematic need. The prevalence of shorter wavelength satellites in orbit means most research and operational flood monitoring is completed using C- or X-band images, despite potentially improved mapping in certain situations using L-band sensors.

3.1.3. SAR Polarisation

The polarisation of SAR data refers to the orientation of the transmitted and received signal in relation to the satellite antenna (Lillesand *et al.*, 2008). Typically, the radar signal is transmitted either vertically (V) or horizontally (H), with one of the vertical (V) or horizontal (H) components of the backscattered response recorded (Figure 3.4). This results in four common polarisations: HH (Horizontally transmitted – Horizontally

recorded), HV (Horizontally transmitted – Vertically recorded), VH (Vertically transmitted – Horizontally recorded) and VV (Vertically transmitted – Vertically recorded). HH and VV polarisations are often referred to as co-polarised imagery, whilst HV and VH are cross-polarised. Land covers can produce varying backscatter responses depending on the image polarisation, making it a key consideration when analysing an image for a particular thematic area. An example of how backscatter varies between VH and VV polarisations is shown in Figure 3.5.

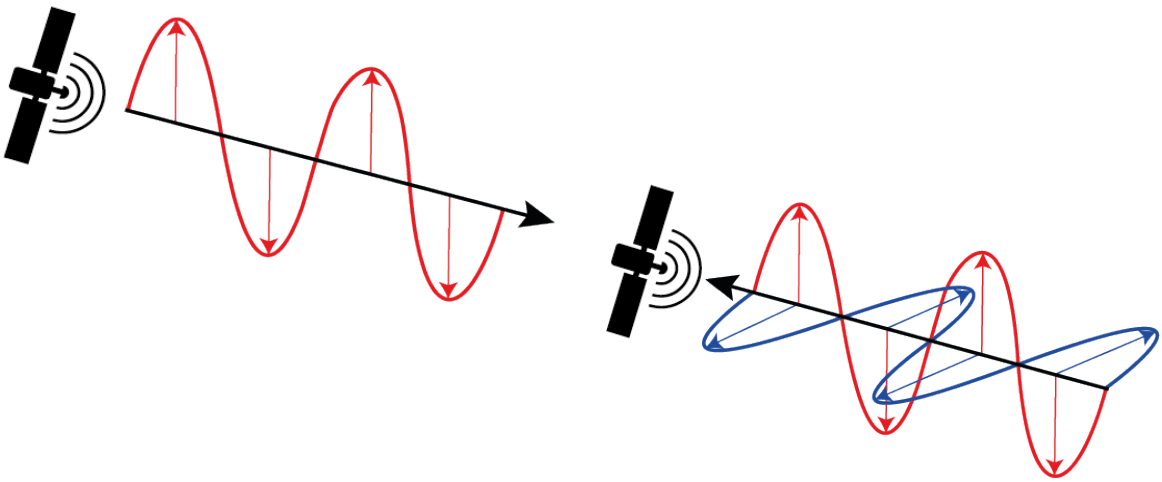

Figure 3.4. Polarisation within Sentinel-1, which is transmitted vertically (V, shown left), and received both vertically (V) and horizontally (H, shown right). Other SAR systems often transmit horizontally instead of, or alongside, the vertical signal.

As with other land covers, image polarisation can have an impact on how successfully a water classification algorithm performs. The consensus is that HH polarised data achieve the greatest accuracy in identifying open water (Henry *et al.*, 2006; Manjusree *et al.*, 2012). However, data from Sentinel-1, which forms the basis of the research presented in the following chapters, is only available in VH and VV polarisations. In their comparison between the available Sentinel-1 polarisations, Twele *et al.* (2016) found that VV imagery provided better flood boundary delineation due to the preservation of the vertical component of the radar signal when interacting with protruding vegetation (the double bounce effect), allowing for a clearer definition of the flood shoreline. However, VV imagery is more susceptible to increased backscattering from surface roughening of the water surface, often caused by wind or heavy rain (Brisco *et al.*, 2008). Cross-polarised data is less affected by roughening, and has been shown to have high accuracy when mapping open water, but can suffer from falsely classifying land as water (Manjusree *et al.*, 2012). This is due to

the higher amount of volume scattering and depolarization of the radar signal caused by vegetation, resulting in a highly variable land response to the radar signal, including regions of lower backscatter similar to water (Jin and Xu, 2013; Twele *et al.*, 2016). Due to the differences in classification accuracy with each polarisation, the use of multiple polarisations when available is recommended, with improved flood delineation achieved by the removal of misclassifications caused by polarisation specific mechanisms (Henry *et al.*, 2006; Brisco *et al.*, 2008; Manjusree *et al.*, 2012).

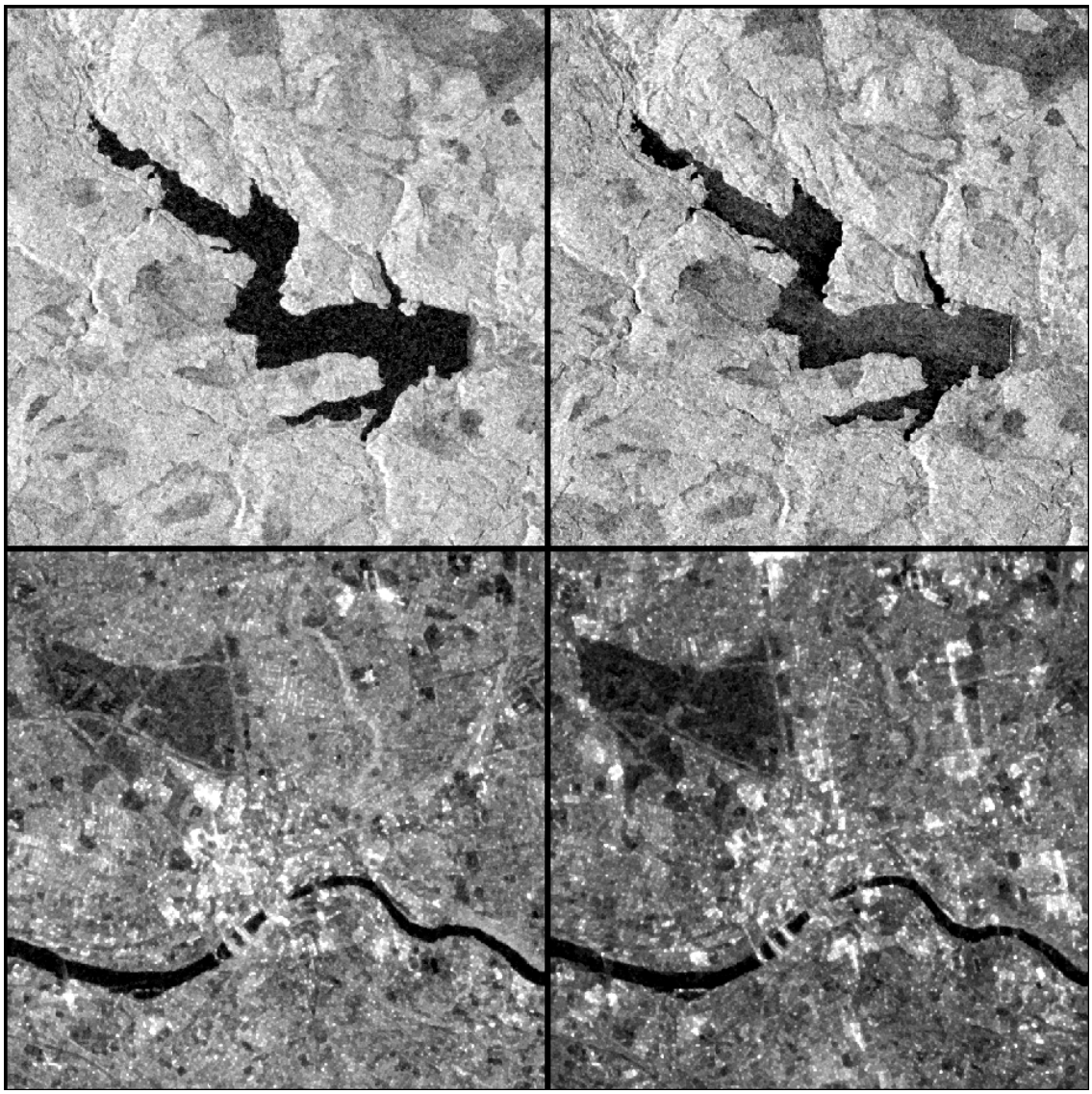

Figure 3.5. Comparison between VH (left) and VV (right) polarised images for water (Kielder reservoir, UK (Top)) and urban (Newcastle upon Tyne, UK (Bottom)) settings. The VV data shows a higher susceptibility for noisier returns from water bodies, caused by wind roughening of the water surface. Note the improved detail shown for urban features in VV polarisation. Each panel is scaled to the extent shown to allow for clearer showcasing of image differences. Backscatter values vary considerably between the top and bottom panels despite the similar colour scales displayed. Images from 1st January 2016.

3.1.4. Speckle

A common aspect of SAR imagery is speckle, caused by multiple sources of scattering within a pixel feature space that produce variable backscatter responses (Brivio *et al.*, 2002). This results in a 'salt and pepper' effect on the image, with pixels from the same land cover having inconsistent backscatter values. Speckle can be reduced by applying a local adaptive filter, with the aim of smoothing out homogeneous surfaces whilst preserving object edges (Lillesand *et al.*, 2008). Numerous filters have been applied in the literature when pre-processing a SAR image, including Median (Pradhan *et al.*, 2014; Martinis *et al.*, 2015b); Frost (Matgen *et al.*, 2007; Schumann *et al.*, 2008a); Gamma MAP (Manjusree *et al.*, 2012; Long *et al.*, 2014); Lee (Brivio *et al.*, 2002; Chung *et al.*, 2015); Refined Lee (Nakmuenwai *et al.*, 2017; Martinis *et al.*, 2018); and Lee Sigma (Zwenzner and Voigt, 2009; Brown *et al.*, 2016) filtering. As well as the type of filter, other parameters such as the number of looks, window size and sigma can all impact the amount of smoothing achieved by a filter. There is no qualitative method for determining the best technique for speckle suppression, with filter selection often decided based on the subjective judgement of the researcher.

3.1.5. Radar Shadow, Foreshadowing, Layover and Foreshortening

As previously mentioned, SAR sensors are side-looking, which can result in geometric distortions within an image at locations where the radar signal interacts with tall features, such as mountains or buildings (Rees, 2000; Huang *et al.*, 2017). There are three main types of these terrain effects; radar shadow, foreshadowing and layover (Figure 3.6). Radar shadow refers to the inability of the radar signal to illuminate the land immediately behind a large obscuring feature (Rees, 2000). Accounting for shadowing is particularly important when mapping surface water, as these areas show up as dark regions within a SAR image, similar to locations of low backscatter (Giustarini *et al.*, 2013; Huang *et al.*, 2017). Foreshadowing in a SAR image is the increase in backscatter from the side of a mountain facing the satellite, and is caused by the decrease in local incidence angle due to the slope of the terrain (Mather and Koch, 2011). Foreshortening often occurs when mountainous regions are imaged at lower radar look angles, resulting in the compression of the depicted ground distance in the range direction caused by different signal travel times between the top and base of a mountain (Lillesand *et al.*, 2008). Similar to foreshortening is layover, which is the complete overlapping of the upper part of a

feature with its base due to the signal interacting with the mountain top first, and tends to occur when feature slopes are steeper (Lillesand *et al.*, 2008).

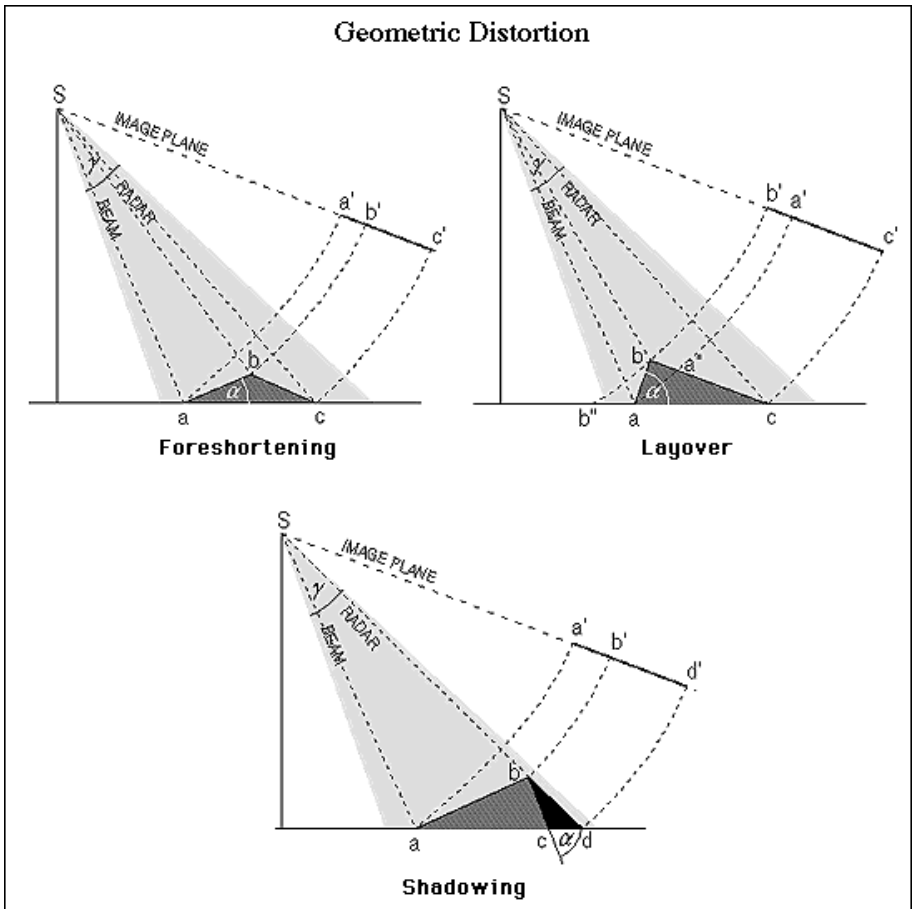

Figure 3.6. Common geometric errors found within SAR data caused by regions of high topography. Shadowing is of particular interest for water body mapping studies due to its similarity to the low backscatter response from water. Image published online by ESA, available at https://earth.esa.int/handbooks/asar/CNTR1-1-2.html (last accessed 03/03/2019).

3.2. Sentinel-1 SAR

Sentinel-1 is a constellation of two satellites, both carrying the same payload of a C-band SAR instrument. Both satellites nominally fly opposite each other along the same orbit, providing conflict-free data acquisition allowing the creation of a consistent archive of imagery on a global scale (Geudtner *et al.*, 2014). The regular orbit and freely available medium-high resolution imagery provided by Sentinel-1 has allowed improved insight and monitoring of environmental processes. A search of recent publications shows a range of thematic areas utilising Sentinel-1 data, including surface water, wetlands, soil moisture and flood monitoring (Boni *et al.*, 2016; Muro *et al.*, 2016; Twele *et al.*, 2016); land deformation studies, including

earthquakes, landslides and land subsidence (Barra *et al.*, 2016; Dai *et al.*, 2016; Sowter *et al.*, 2016); volcano monitoring (González *et al.*, 2015; Lau *et al.*, 2018); cryosphere science (Mouginot *et al.*, 2017; Karvonen, 2018; Lemos *et al.*, 2018); sea ice, ocean wave, ship and oil spill detection (Muckenhuber *et al.*, 2016; Shao *et al.*, 2016; Velotto *et al.*, 2016); agricultural and forestry studies (Minh *et al.*, 2017; Rüetschi *et al.*, 2017; Torbick *et al.*, 2017); and urban change monitoring (Cao *et al.*, 2018; Corbane *et al.*, 2018; García *et al.*, 2018).

3.2.1. SAR Instrument

The Sentinel-1 satellites carry a payload of a C-Band SAR instrument, which operates at a central frequency of 5.405 GHz, and a central wavelength of 5.547 cm. The instrument has an antenna 12.3 m in length, a beam width of 0.23°, and a pulse width ranging between 5-100 μs (ESA, 2018a). Sentinel-1 comes with the ability to move the transmitted radar beam in both range (-13.0° to 12.3°) and azimuth (-0.9° to 0.9°) directions, allowing for the collection of images via the Terrain Observations with Progressive Scans SAR (TOPSAR) methodology (De Zan and Guarnieri, 2006). Sentinel-1 can operate in single or dual polarisation modes, with a switchable transmit chain and two simultaneously operating receiver chains allowing this. The instrument contains an internal calibration scheme, ensuring that there is a high degree of radiometric stability by monitoring the differences in amplitude and phase between the transmitted and received signals (ESA, 2018a). Each Sentinel-1 satellite has a data storage capacity of 1.4 Gb, and the ability to transmit data at a rate of 520 Mbit/s (ESA, 2018a).

3.2.2. Orbit Information and Coverage

Sentinel-1 operates along a polar sun-synchronous orbit, with each satellite circling the Earth 175 times throughout a 12 day repeat period (ESA, 2018b). The two Sentinel-1 satellites fly opposite each other along the same orbit track, reducing the repeat period for the constellation to 6 days. Revisit frequency for the constellation, or how often a point on the ground is imaged independent of orbit track, is around 3 days at the equator, and less than 1 day at high latitudes (Figure 3.7). Satellites are kept within a target drift RMS of fewer than 50 m from the intended flight path, allowing for improved reliability for change detection analysis and SAR interferogram creation (Geudtner *et al.*, 2014).

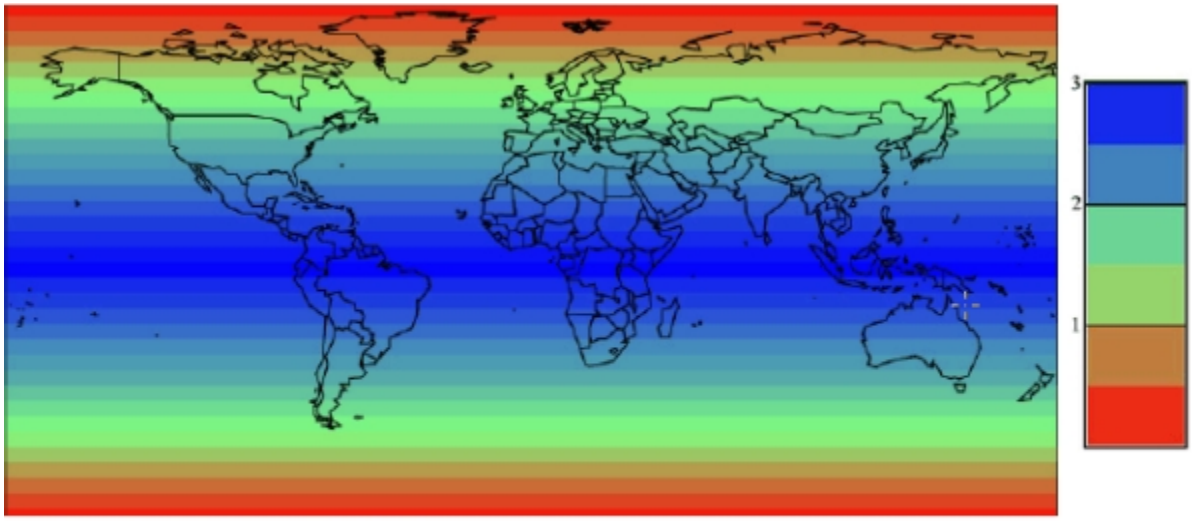

Figure 3.7. Sentinel-1 revisit frequency for the two satellite constellation. Coverage at the equator is approximately every 3 days, with sub-daily at the poles. Image published online by ESA (2018b).

3.2.3. Acquisition Modes

Sentinel-1 has four available acquisition modes: Extra Wide Swath (EW), Interferometric Wide Swath (IW), Stripmap (SM) and Wave (WV). Each mode is designed for different imaging situations, with the satellite automatically switching mode depending on the geographical location targeted during acquisition. An overview of SM, EW and WV is given here, with a more detailed explanation of IW supplied, as this is the default acquisition mode over land. Figure 3.8 provides a diagrammatic overview of how each acquisition mode works.

The main application for EW data is in marine monitoring, including sea-ice tracking and oil spill detection. Images are dual-polarised, and available across 410 km swaths, with incidence angle ranging between 18.9° and 47.0°. The spatial resolution of EW data is 20 x 40 m (range x azimuth) (ESA, 2018c). Sentinel-1 rarely operates in SM mode, with its use restricted to the imaging of small islands, and when requested for assistance for real-time disaster monitoring and management. Despite its limited use, the acquisition parameters of SM mode are designed to match those of the ERS and ENVISAT missions. A single swath of 80 km is acquired at a fixed range of incidence angles, which is chosen from 6 predefined overlapping swaths. Data is dual-polarised and supplied at 5 m ground resolution (ESA, 2018d). Wave

mode (WV) is the default conflict-free acquisition mode over the oceans. Data is collected as a series of 20 x 20 km vignettes, providing continuity with ERS and ENVISAT. Vignettes are spaced 100 km apart, and alternate incidence angle between 23° and 36°. Images are provided at 5 m spatial resolution, and in VV polarisation (ESA, 2018e).

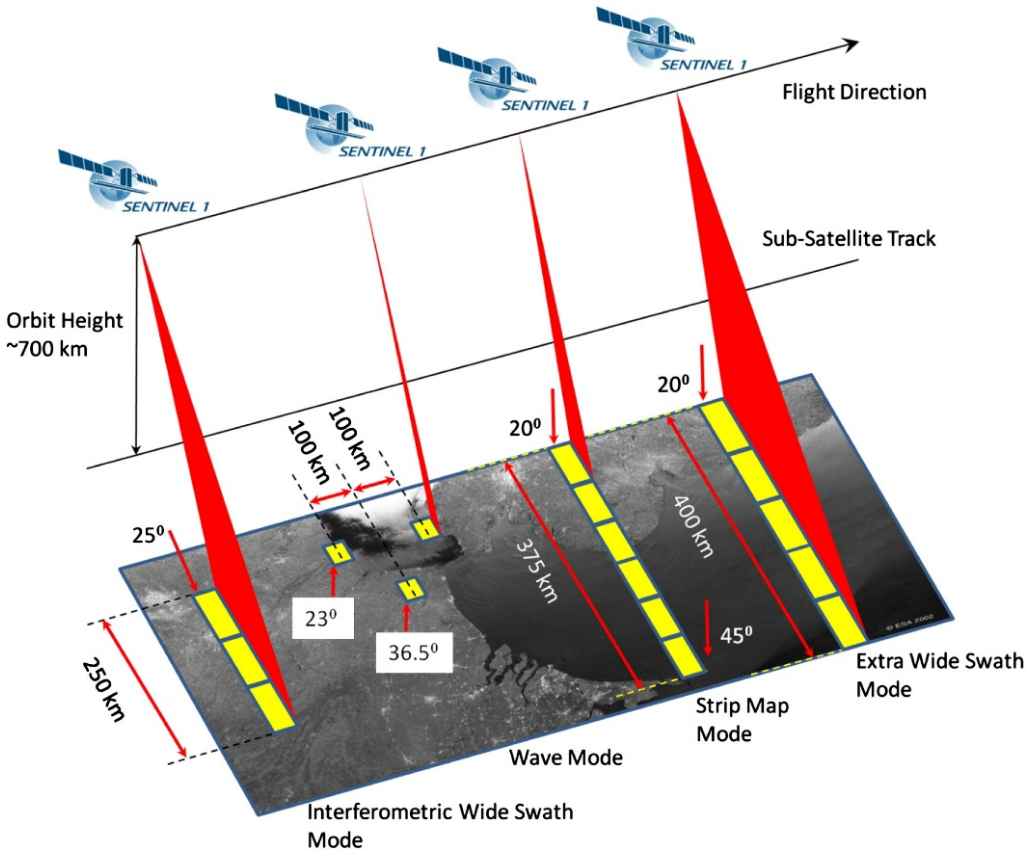

Figure 3.8. Sentinel-1 acquisition modes. Interferometric Wide Swath (IW) is the default mode over land. Image published online by ESA, available online at https://sentinel.esa.int/web/sentinel/missions/sentinel-1/instrument-payload (last accessed 03/03/2019).

3.2.3.1. IW and TOPSAR Acquisition

IW is the default acquisition mode over land and is acquired using the Terrain Observation with Progressive Scans SAR (TOPSAR) technique. Developed by De Zan and Guarnieri (2006), TOPSAR corrects for some of the radiometric errors that come from traditional SAR scanning techniques (such as ScanSAR) whilst providing data at a higher resolution. Scalloping is the light and dark banding in the range direction of a SAR image and is caused by inaccurate estimation of the Doppler centroid mean frequency due to the full range of possible Doppler shifts not being captured (Meta *et al.*, 2008). Although it is possible to remove this with post-

processing, methods often result in a reduction of resolution and cause decorrelation of the data, limiting interferometric studies (De Zan and Guarnieri, 2006). TOPSAR removes the effects of scalloping without the requirement of post-processing and is currently in use onboard TerraSAR-X and Sentinel-1 (D'aria *et al.*, 2007; Meta *et al.*, 2008). TOPSAR works by additionally steering the radar beam in the azimuth direction as well as continuing to steer in the range direction, as shown in Figure 3.9 (De Zan and Guarnieri, 2006). The resulting image has improved signal to noise ratio (SNR) due to each ground feature being illuminated by the full range of Doppler frequencies within the azimuth antenna pattern (Meta *et al.*, 2008; Geudtner *et al.*, 2014). The improved consistency in the SNR with azimuth almost entirely removes any scalloping in the data, with TerraSAR-X showing a decrease in scalloping from 1.2 dB to 0.3 dB when comparing TOPSAR to ScanSAR (Meta *et al.*, 2008).

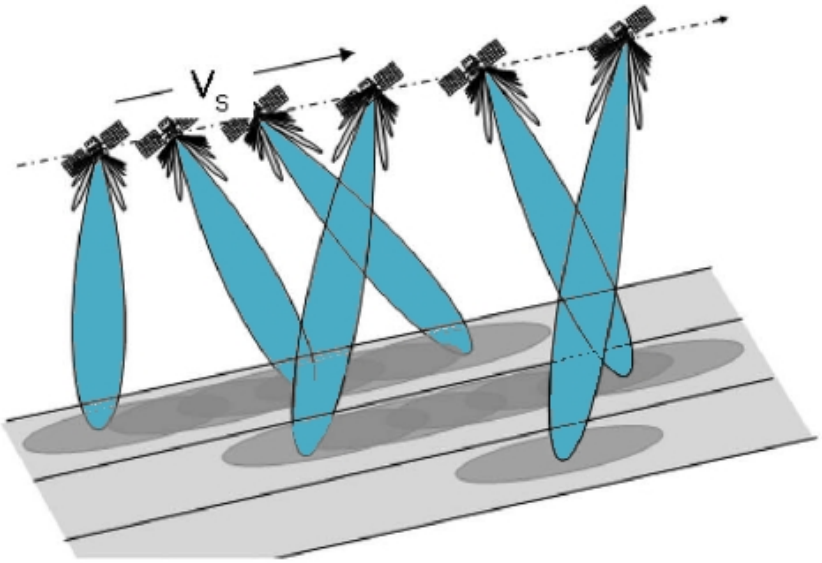

Figure 3.9. TOPSAR, the acquisition method used in Sentinel-1 IW mode. The antenna scans in both range and azimuth direction as the instrument travels along its orbit (De Zan and Guarnieri, 2006).

For Sentinel-1 IW data acquisition, three overlapping image sub-swaths are combined to create an image with an overall swath width of 250 km. Each sub-swath contains six bursts, which are processed individually as a single-look complex (SLC) scene prior to merging, shown in Figure 3.10 (ESA, 2018f). Data is collected at a spatial resolution of 5 m (range) by 20 m (azimuth), before being resampled to pixels of 10 m. Incidence angles across the swath range between 18.9° and 47.0° (ESA, 2018f).

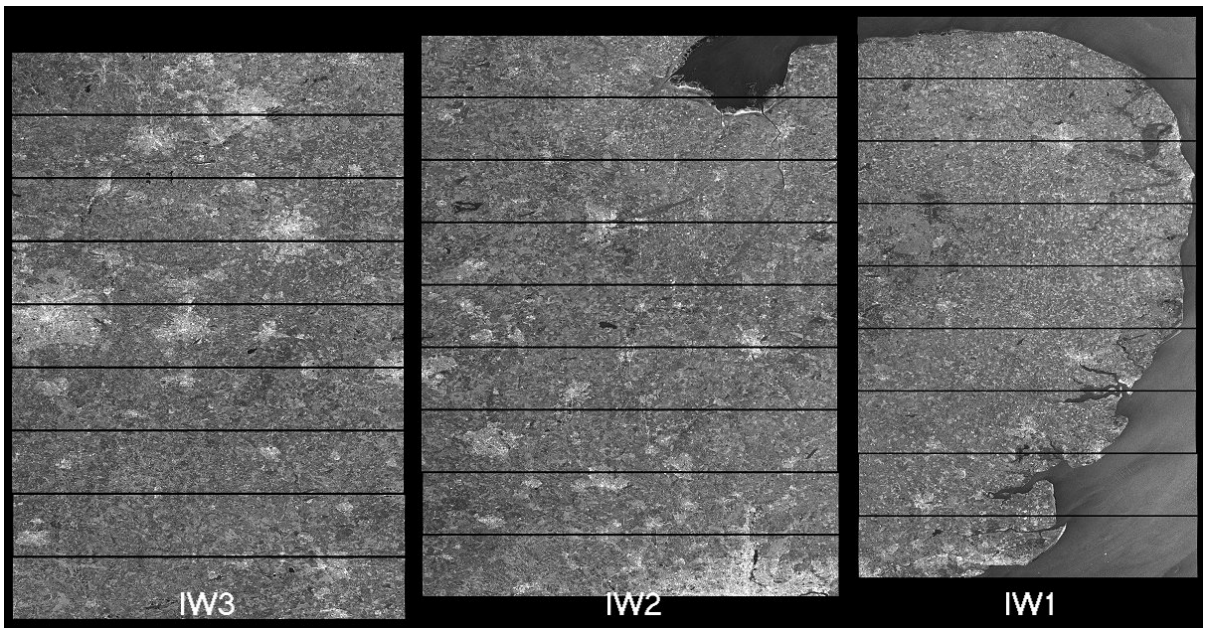

Figure 3.10. An example of the separate TOPSAR bursts prior to merging into the final GRD Sentinel-1 product. Note the six bursts for each of the three sub-swaths, each with enough overlap to ensure a consistent product once merged. Image published online by ESA (2018f).

3.2.4. Sentinel-1 Data Products

Sentinel-1 data is available from the Copernicus database in a number of different formats, with the intended application dictating which is most appropriate for the user to download. The data products can be split into three levels: Level-0, which describes the raw data; Level-1, which includes Single Look Complex (SLC) and Ground Range Detected (GRD) datasets; and Level-2, which are products specifically created for analysing oceans, including Ocean Wind Field (OWI), Ocean Swell Spectra (OSW) and Surface Radial Velocity (RVL) (ESA, 2018g).

The Level-1 products, SLC and GRD, are the most commonly used data types for terrestrial applications. A number of processing steps are applied to the raw data to create either product, summarised in Figure 3.11. Although both are classed as Level-1 products, SLC can be considered as the input dataset for the creation of GRD data. SLC provides data in slant-range geometry, with the phase of the backscattered signal preserved alongside amplitude (ESA, 2018h). Phase information is needed for the creation of interferograms, meaning SLC data is required as an input when creating terrain datasets and for ground deformation studies. GRD data, as the name suggests, is delivered in ground-range geometry,

having been projected onto a WGS84 ellipsoid. The phase information is lost during the multi-looking of the SLC data, used to create square pixels and reduce noise within the GRD products. Pixel values represent the amplitude of the returned signal (ESA, 2018h). Despite the disadvantage of reduced information, GRD data is arguably delivered in a more user-friendly format, allowing for image analysis without the requirement for technical knowledge of complex SAR processing.

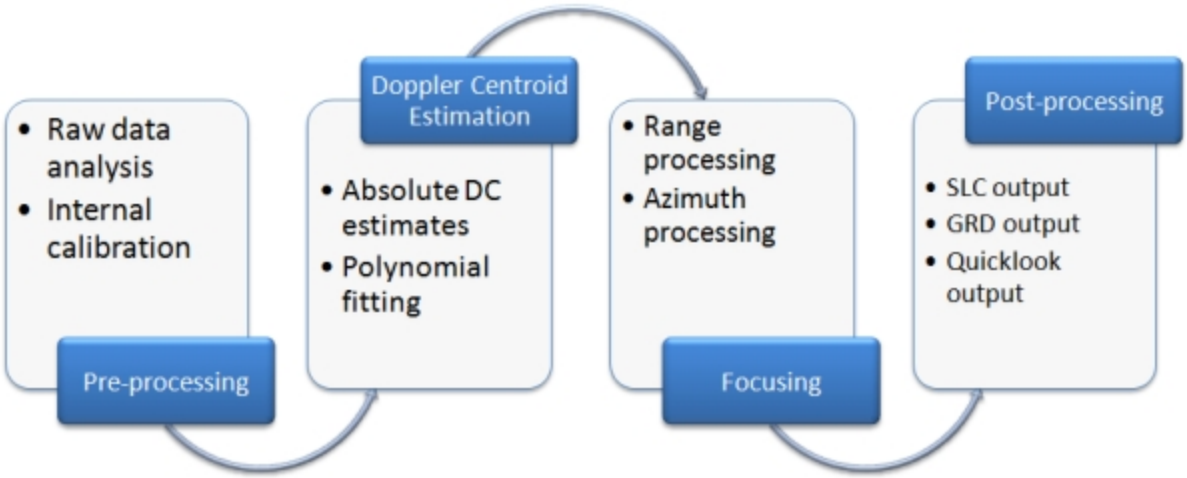

Figure 3.11. Processing flow used to produce SLC and GRD deliverables from raw Sentinel-1 data. Image published online by ESA (2018h).

3.3. Sentinel-1 Pre-Processing

The following sections briefly describe the processing steps undertaken to transform a GRD image, downloaded from the Copernicus Open Access Hub (https://scihub.copernicus.eu/), into the SAR image used for identifying flood extent in the following chapters. Processing was completed using the Sentinel Applications Platform (SNAP) Sentinel-1 Toolbox and the Python library that utilises the software tools. Within the SNAP software, help notes are available to provide guidance on how each tool operates, with information from these sources referenced as *SNAP (2018)* henceforth.

3.3.1. Applying Orbit Information

The orbit information within the metadata of a downloaded Sentinel-1 GRD product is likely to contain inaccuracies. The relevant information, namely satellite position and velocity information, can be updated using either precise or restituted orbit data, correcting the orbit state vectors within the metadata (SNAP, 2018). Precise orbits provide the optimal level of accuracy, however, these can take days-to-weeks to

produce, resulting in the restituted orbits often being used for near real-time applications (SNAP, 2018).

3.3.2. Thermal Noise Removal and Radiometric Calibration

SAR images can be subject to random additive thermal noise caused by the motion of electrons in the satellite circuitry due to temperature differences. With Sentinel-1 utilising the TOPSAR acquisition method, thermal noise can become particularly apparent between image sub-swaths due to the difference in timing between acquisitions (Park *et al.*, 2018). The thermal noise is removed using SNAP software, which use product-specific noise Look-up Tables (LUT) to deduce and apply corrections to the data, creating continuous intensity profiles across sub-swaths (SNAP, 2018).

The Level-1 GRD images have no correction applied to account for any radiometric bias across the scene. It is possible to assess data quality using uncalibrated data, however, to allow for further thematic analysis the data needs normalising to represent the scattering coefficient, which compares the observed signal strength to the backscatter intensity expected for a defined area (SNAP, 2018). This allows for the direct comparison between images collected from different dates, satellite tracks, operational modes and sensors. Data is normally calibrated to either Beta Nought (β^0), Sigma Nought (σ^0) or Gamma Nought (γ^0), with the different backscatter conversions determining the orientation of the reference area used to calibrate the data (Figure 3.12).

β^0 represents the backscatter brightness across a reference frame in slant range geometry, defined as:

$$\beta^0 = \beta / A_\beta. \quad (1)$$

where β is the radar backscatter, and A_β is the reference rectangle (Small, 2011). β^0 is often determined as a precursor to terrain flattening, which calibrates the data in relation to the local terrain instead of the WGS84 ellipsoid (SNAP, 2018).

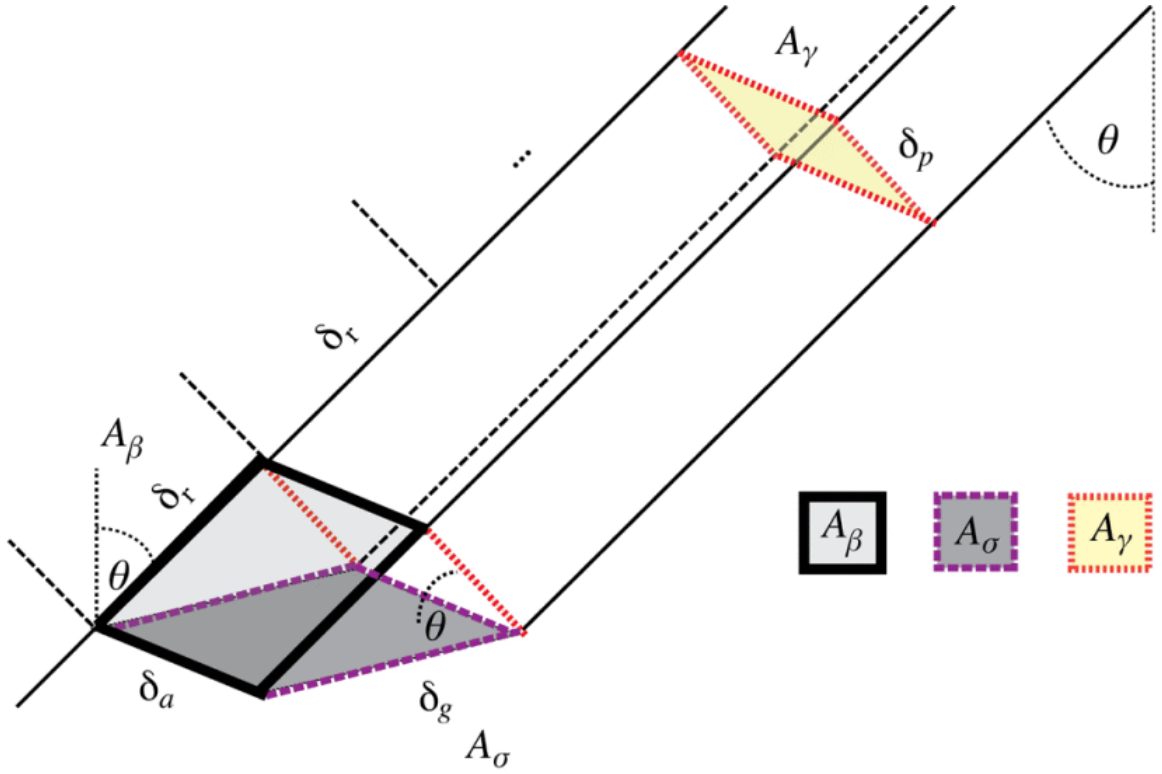

Figure 3.12. The different reference frames (in relation to the satellite slant-range geometry) used to calibrate SAR backscatter (Small, 2011). In the research presented data has been calibrated to A_σ, shown by the purple square, representing the scattering coefficient in relation to the ground ellipsoid.

σ^0 describes the scattering coefficient within a horizontal plane of the ground surface (A_σ), with σ_E^0 in the below equation referring to the σ^0 in relation to the ellipsoid model (Small, 2011).

$$\sigma_E^0 = \beta^0 . \frac{A_\beta}{A_\sigma} = \beta^0 . sin\theta_E. \quad (2)$$

γ^0 represents the backscatter intensity for a reference frame perpendicular to the radar line of sight (A_γ). As above, γ_E^0 depicts gamma nought in relation to the local ellipsoid (Small, 2011).

$$\gamma_E^0 = \beta^0 . \frac{A_\beta}{A_\gamma} = \beta^0 . tan\theta_E. \quad (3)$$

For the case of Sentinel-1, three Look-up Tables (LUT) are available within SNAP software, which converts the observed data to either β^0, σ^0 or γ^0 (SNAP, 2018).

Firstly, the scaling applied to the data in the initial level 1 pre-processing is removed, before the LUT is used to calibrate the data using the following equation:

$$value(i) = \frac{|DN_i|^2}{{A_i}^2} \quad (4)$$

where i is the relative pixel value in β^0, σ^0 or γ^0 based on DN_i (the input image pixel value), and A_i, the corresponding betaNought(i), sigmaNought(i) or gammaNought(i) from the LUT (SNAP, 2018). Where pixels fall between the values within the LUT, bi-linear interpolation is used to determine the new pixel value (SNAP, 2018).

For the research presented in this study, data is calibrated to σ^0. Previous studies have shown that using σ^0 provides improved land-water separation within the image histogram (Bioresita *et al.*, 2018; Giordan *et al.*, 2018). Some studies have recommended the use of calibrations that take local terrain into consideration, as opposed to using a local ellipsoid (Small, 2011; Huang *et al.*, 2018). In the SNAP software, this would comprise calibrating to β^0, and terrain flattening to γ^0. However, due to the unlikelihood of flooding occurring in high terrain regions, it was decided that calibrating to σ^0 would be sufficient.

3.3.3. Speckle Filtering

Speckle filtering removes the effects of local variations in backscatter, resulting in a smoother image that can be more accurately used in classifications. For the initial study of flood mapping in Yorkshire, a median filter was applied to the SAR images. A median speckle filter works by comparing the pixel of interest to those in its immediate neighbourhood and replacing the cell value with the median value of these pixels. A user-defined grid shape and size determines the number of pixels used in the calculation, with a rectangular neighbourhood with an odd number of pixels along the grid edges (5 x 5, 7 x 7 etc.) commonly used, ensuring the pixel being filtered is located in the centre of the neighbourhood. A median filter with a neighbourhood of 5 x 5 pixels was applied to the images for the initial study. The median filter has been widely used in the literature, and often provides good results when removing speckle in regions of land cover with minimal variation in baseline backscatter. However, it can result in over-smoothing of the data in locations where there is a wide range of

backscatter values, such as at the flood boundary (Mansourpour *et al.*, 2006; Lee *et al.*, 2009).

After the initial study, a comprehensive visual comparison was made of various speckle filters to ascertain if further improvement can be achieved in maintaining edge features whilst continuing to sufficiently filter homogenous areas. Superior filtering is achieved by the Refined Lee filter. The Refined Lee filter is an adaption of the Lee filter, which uses the local statistics to minimise the mean square error (MMSE) of the pixel value in relation to its neighbours (Lee, 1983). However, similar to the median filter the original iteration of the Lee filter struggled to maintain edges and highly reflective points within an image (Lee *et al.*, 2009). This lead to the development of the Refined Lee filter. The filter uses edge-aligned non-square neighbourhood windows to help maintain edges, whilst continuing to use MMSE to reduce noise in homogenous areas (Lee *et al.*, 2009). Edges are identified by assessing the local image variance, with the neighbourhood subdivided and filtered individually if an edge or point feature is detected (Lee *et al.*, 2009). High pixels values are maintained if a defined number of neighbouring pixels are above the 98th percentile for the image (Lee *et al.*, 2009). For the SAR image processing completed in this research, it was found that the default parameters in the SNAP software (7 x 7 window size) provided good speckle suppression (Figure 3.13).

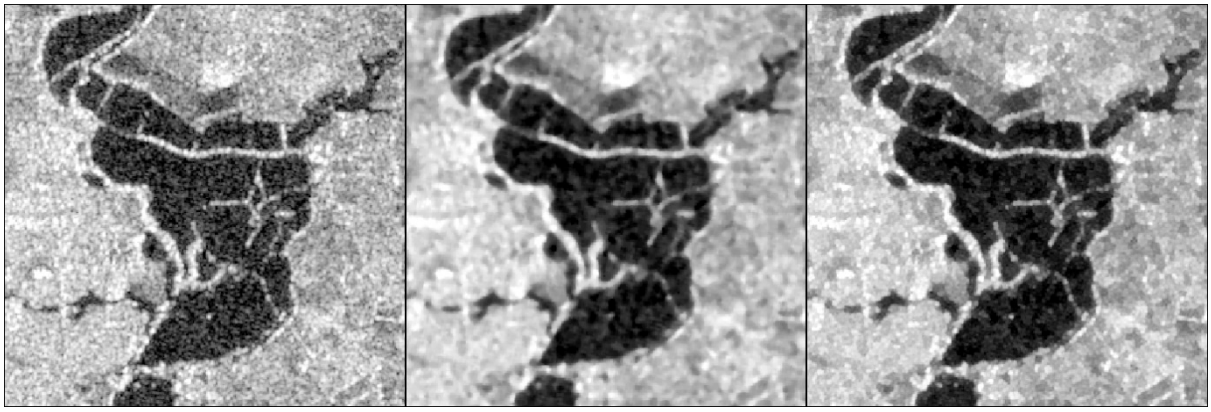

Figure 3.13. Speckle filtering used within the research presented in the following chapters. From left to right, unfiltered data, Median speckle filter (5 x 5 window), and Refined Lee speckle filter (7 x 7 window). Images are VH polarisation.

3.3.4. Terrain Correction

Topographic features are often distorted in SAR images due to the side-looking geometry of the instrument. To create an image that accurately represents the true

ground locations of features terrain correction is applied, which adjusts the input image based on the satellite orbit, look angle and underlying topography (SNAP, 2018). Terrain correcting allows for comparison between scenes independent of satellite source and viewing geometry. The Range Doppler orthorectification methodology (Small and Schubert, 2008) is applied, utilising the module built within the SNAP software. Along with the input image, precise orbit and timing information, a reference Digital Elevation Model (DEM), by default the Shuttle Radar Topography Mission (SRTM) 3 arc-second dataset, are used to transform the image (SNAP, 2018). Once the data has been terrain corrected, it is resampled to a user-defined pixel spacing, which by default is 10 m, before all images are co-registered to ensure locational accuracy between orbits. Due to the large range of backscatter values in an image, pixel intensity values are converted to decibels (dB) via log scaling ($10*\log_{10}\sigma°$), a dimensionless unit that allows for direct comparison between scenes from different satellite sources. Sentinel-1 images contain border noise (seen as very low values) as an artefact of the pre-processing used to create GRD products (SNAP, 2018). Although this can be removed earlier in the processing, it was found the SNAP tool for this ("S-1 GRD Border Noise Removal") provided inconsistent results. For each orbit, a minimum value mosaic is created from the processed images to identify locations of border noise, before all images are masked to remove these locations.

3.4. Digital Terrain Data

Digital terrain data (DTD) is commonly used to provide additional information for environmental analysis, often through the calculation of topographic parameters such as surface slope, curvature or watershed delineation. DTDs provide a numerical representation of the vertical distance between the ground terrain and a reference surface, such as mean sea level (Li *et al.*, 2004; Hirt, 2014). Terrain information can be acquired using a variety of platforms, including ground-based, airborne and satellite surveying methods, and derived from imagery (using photogrammetry), LiDAR point clouds and radar (using InSAR) datasets (Li *et al.*, 2004; Maune, 2007; Hirt, 2014). The resultant DTDs are available across a range of geographical extents (from local to global), spatial resolutions (cm to km) and with varying vertical accuracies (as shown in Figure 2.8 (Schumann and Bates, 2018)). Representation of terrain information can be in a number of formats, including contours, continuous raster grids (where the cell value represents the centroid terrain height), irregularly

distributed points and triangulated irregular networks (TINs) (Maune, 2007; Hirt, 2014).

There are two main data types described by the term DTD, Digital Surface Models (DSM) and Digital Terrain Models (DTM). DSMs represent the topographic height including surface features, such as vegetation and buildings, whilst DTMs describe the ground terrain without the inclusion of surface features (Hirt, 2014). An additional term, Digital Elevation Models (DEM), is commonly used, although less well defined. Some authors describe DEMs as being synonymous with DTMs as they represent the bare earth terrain (Maune, 2007; Hirt, 2014), however, many acquisition and processing techniques utilised to create global DEMs result in a DSM representation of terrain due to the inclusion (or lack of removal) of man-made and vegetative structures (Proietti *et al*., 2017). Authors have suggested that DTMs have a higher degree of accuracy than DEMs, with data collection targeted at representing complex topographic features, such as steeper slopes and ridges, sometimes missed by more general acquisition techniques (Li *et al.*, 2004; Maune, 2007). In these situations, DTMs provide a better depiction of the ground terrain when displayed as contours or discrete points, however, this additional detail is usually lost when converted to raster format (Maune, 2007). Another common definition of DEM is that it represents a general term for DTD, incorporating both DSM and DTM when no additional dataset specifics are provided by the publishing body (Maune, 2007; Hirt, 2014).

Within a satellite flood mapping context, terrain data is commonly used to refine observations by identifying regions that are unlikely to be inundated but may be susceptible to false classifications, such as radar shadow, helping improve the accuracy of the flood maps produced (Long *et al*., 2014; Twele *et al*., 2016). In Chapters 4, 5 and 6 of this thesis, three terrain models are used; the Ordnance Survey (OS) Terrain 5 m DTM, the Shuttle Radar Topography Mission (SRTM) DEM, and the Environment Agency LiDAR Composite DTM. Information on these datasets provided below. Further global terrain models are used in Chapter 7, with details on the creation and accuracy of these datasets provided at the start of that chapter.

3.4.1. Ordnance Survey (OS) Terrain 5m DTM

The OS terrain datasets cover the whole of Great Britain, and are available at 5 m or 50 m spatial resolutions. The source terrain data is created from aerial imagery,

which is automatically processed to create a TIN, providing an accurate representation of intricate topographic features (Ordnance Survey, 2017). Surface features, such as buildings and vegetation, are removed from the source TIN to create the resultant DTM, which is smoothed to remove any spikes or wells. For the OS Terrain 5 dataset, information is available as either a 5 m raster or as contours with 5 m spacing, both of which are interpolated from points extracted from the source TIN (Ordnance Survey, 2017). The contours provide an improved representation of the feature edges and height changes in steep locations, whilst the raster provides a continuous grid of height values. The dataset is updated quarterly based on a rolling 3-5 year acquisition pattern (Ordnance Survey, 2017). Accuracy is assessed by comparing the height values to GPS measurements. Reported accuracy for the OS Terrain 5 is 1.5 m RMSE in urban environments, and 2.5 m RMSE in rural locations (Ordnance Survey, 2017). The higher accuracy in urban environments allows for greater confidence for customers when undertaking modelling and analysis in complex environments, supporting a variety of activities including urban infrastructure planning and development, flood risk assessments, and environmental analysis (Ordnance Survey, 2017).

3.4.2. Shuttle Radar Topography Mission (SRTM)

SRTM is a near-global DEM acquired between the 11th and 22nd of February 2000 using separate C- and X-band radar instruments flown onboard the Space Shuttle Endeavour (Farr *et al.*, 2007). Interferometric processing of the C-SAR data is used to create a 90 m (3 arc-second) DEM, whilst the X-SAR data, with some smoothing and gap-filling from the C-SAR, forms the basis of a 30 m (1 arc-second) dataset (Farr *et al.*, 2007). The data is freely available, with coverage provided between 56°S and 60°N.

The aim of the SRTM mission was to provide data with a horizontal accuracy of 20 m, and an absolute vertical accuracy of 16 m (Kolecka and Kozak, 2014). Reported accuracies from the Jet Propulsion Laboratory (JPL) for the C-SAR DEM is 8.8 m absolute geolocation error and 6.2 m absolute elevation error. Further publications suggest that values do not exceed 20 m horizontal error, less than the pixel size of the DEM, and 12.6 m vertical error (Rodriguez *et al.*, 2006; Kolecka and Kozak, 2014; Satgé *et al.*, 2015). Studies have shown that vertical accuracy is improved in flat regions, with an increasing error in forested regions and locations with a higher

gradient (Sun *et al.*, 2003). Absolute errors ranging between 5 and 10 m have been reported on slopes below 10°, increasing up to approximately 18 m on slopes above 10° (Gorokhovich and Voustianiouk, 2006; Satgé *et al.*, 2015).

Within this research project, the 30 m X-SAR SRTM product is used due to its higher resolution. A comprehensive assessment of the use of this DEM for hydrological purposes was undertaken by Ludwig and Schneider (2006). They compare SRTM to a local reference terrain model (DGM25), along with 31 surveyed Ground Control Points (GCP). As with other studies, the greatest difference occurs in high slope regions and forested areas. The study shows for slopes less than 5°, there is an error in the SRTM ranging between -5 and 10 m, within the SRTM target absolute vertical error value of 16 m. This error increases to up to 30 m for slopes above 50°. It should be noted that the authors recognise that the reference data set may also contain errors and that the assessment of SRTM accuracy may be imprecise.

Both the OS Terrain 5 m DTM (in Chapter 4) and the SRTM DEM (in Chapter 5) are used to help filter out the regions of higher topography where flooding is unlikely and false-positive misclassifications from radar shadow are likely. The DEM derived filter is made up of two components, using the topographic slope and the Height Above Nearest Drainage (HAND) metric. The slope dataset is thresholded at 3°, using the assumption that any area with a slope higher than this is unlikely to be inundated. However, there are exceptions to this, such as taller features located on the floodplain, like river banks, which can be submerged despite their high slope. The HAND part of the filter is designed to remove the exclusion of features such as these, with a threshold of 20 m used.

3.4.2.1. Height Above Nearest Drainage (HAND)

Developed by Rennó *et al.* (2008) and Nobre *et al.* (2011), HAND is a measure of the relative height difference between a location and its point of entry into the river network. The algorithm takes inputs of a terrain model and the river network (which itself can be derived from the topographic data (Ozdemir and Bird, 2009)), before calculating the flow paths surface water would take from each pixel to its hydrologically related river or stream. The output is a raster dataset, with the Z-value for each pixel referring to the vertical height difference between the start location and the river.

Since its development, HAND has been used in numerous studies using SAR to map surface water or flooding, primarily as a filter to identify and remove regions susceptible to radar shadow (Martinis *et al.*, 2015a; Schlaffer *et al.*, 2015; Twele *et al.*, 2016; Bhatt *et al.*, 2017). Of particular interest is the study by Bioresita *et al.* (2018), which investigated the stage within the processing that HAND based terrain filtering should occur to optimise the SAR flood mapping accuracy. They conclude that application before segmenting the image into flood and non-flood regions provided more accurate results than filtering post-classification. The removal of areas of foreshadowing and radar shadow prior to performing histogram thresholding reduces the chance of artificial skewing of the data histogram, allowing for greater confidence in the accuracy of the chosen threshold (Long *et al.*, 2014). When compared to other hydrological indices, such as Topographic Wetness Index (TWI) and the Multi-Resolution Valley Bottom Flatness (MrVBF), HAND has been shown to improve accuracy when mapping surface water (Huang *et al.*, 2017; Rahmati *et al.*, 2018).

Despite the positive applications of HAND outlined above, it should be noted that the success of HAND, like any other DEM derived dataset, is dependent on the quality and resolution of the underlying terrain data (Gharari *et al*., 2011; McGrath *et al*., 2018; Loritz *et al*., 2019). Hydrological indices, such as HAND and TWI, often produce poorer results in flat, low-lying regions due to DEM errors and the often strong surface slope component within the respective algorithm. Huang *et al*. (2017) highlight the increased variance when using the MrVBF algorithm in locations where HAND produces scores of 0 m, suggesting that in certain situations the MrVBF may be preferable for removing false surface water classifications delineated by remote sensing. When utilising HAND within flood mapping studies, additional consideration is needed towards the type of flooding being identified. HAND is intrinsically linked to the hydrological network, and likely to be more capable at confirming inundation caused by fluvial sources, particularly if a low threshold value is chosen. There is the possibility that other sources of flooding, such as pluvial and snowmelt, will cause inundation on flat ground vertically removed from the river network, locations that will have a high HAND value and subsequently may be flagged as suspect.

3.4.3. UK Environment Agency LiDAR Composite

The 2 m LiDAR composite DTM, produced for England and Wales by the Environment Agency (EA), is used in Chapter 6. The raw dataset is updated annually via aerial LiDAR survey, with the composite made up of approximately 10,000 individually surveys (Environment Agency, 2019). Each new survey is merged with the existing composite using a feathered buffer approach (for example, the 2 m composite uses a 30 m buffer) to ensure the seamless surface integration, with greater weighting given to heights produced by newer surveys or those with finer resolutions (Environment Agency, 2019). Data is available to download as either a raw point cloud containing all the LiDAR returns, or in raster format as a DSM or DTM. The data is natively a DSM due to the sensors inability to penetrate foliage, and the strong return of buildings and infrastructure. Filtering removes any permanent (trees, buildings) or temporary (vehicles, livestock) features, resulting in a DTM of the underlying topography (Data.Gov.UK, 2017). The DTM has a vertical accuracy of +/- 15 cm RMSE and a spatial accuracy of 40 cm, and is available at 25 cm, 50 cm, 1 m and 2 m spatial resolutions (Data.Gov.UK, 2017; Environment Agency, 2019). Datasets are freely available, and currently cover approximately 75% of England, primarily located around the river network and the surrounding floodplains. However, the cm-scale datasets provide reduced coverage compared to the meter scale DTMs. The EA have recently announced their aim to cover the whole of England with 1 m LiDAR by 2020 (UK Authority, 2018). The 2 m composite is used to help estimate flood surface and volume (Chapter 6), with the spatial resolution chosen as it is the closest match to Sentinel-1.

3.5. Summary

This chapter has provided a detailed introduction to the main satellite dataset used throughout the following thesis, Sentinel-1 SAR imagery. This includes an overview of SAR acquisition terminology and parameters, such as wavelength, polarisation and speckle, with examples of how these may impact the detection of surface water from SAR imagery. As a continuation of Section 2.2.2, which introduced the ESA Copernicus programme, Section 3.2 provided a detailed overview of Sentinel-1, including the instrument payload, orbit information, and the TOPSAR data acquisition mode used to acquire the IW imagery used to derive flooding in Chapters 4 and 5. Sentinel-1 GRD products require a number of pre-processing steps prior to thematic analysis, primarily, radiometric calibration, speckle filtering and terrain correction. The

theory and application of each of these processes have been provided. In particular, Figure 3.13 provides an example of the noise attenuation achieved by the different speckle filtering applied in Chapters 4 (Median filter) and 5 (Refined Lee filter). Finally, this chapter has defined the different types of digital terrain data commonly used in geospatial analysis, before introducing the three main terrain datasets used within this thesis, OS Terrain, SRTM and EA Composite LiDAR. The acquisition methods and reported accuracies are provided for each of these, alongside a brief outline of their use in later chapters, including a description of the application, strengths and limitations of the HAND index.

Chapter 4. Determining Flood Extent from SAR: Initial Assessment

The following chapter is adapted from the paper “Multi-temporal Synthetic Aperture Radar Flood Mapping using Change Detection” which has been published in the Journal of Flood Risk Management. The full reference details are:

> Clement, M.A., Kilsby, C.G. and Moore, P. (2018) Multi-temporal Synthetic Aperture Radar Flood Mapping using Change Detection. *Journal of Flood Risk Management.* **11**(2):152-168. DOI: 10.1111/jfr3.12303

The aim of this chapter is to develop an initial workflow for extracting flood extent from Sentinel-1 SAR imagery. This has been undertaken for a small, flood-prone region south of York, which suffered from significant inundation during the 2015-16 UK winter floods. Results from this preliminary study will be used to inform adjustments to the initial methodology, which is subsequently applied in Chapter 5 to delineate the widespread flooding that occurred across many catchments in the north of England during the winter of 2015-16.

4.1. 2015-16 UK Winter Floods

The work presented in Chapters 4, 5 and 6 will focus on the analysis of the flooding caused by the 2015-16 UK winter storms. The UK Meteorological Office introduced the naming of storms ahead of the 2015-16 winter season as part of an initiative to improve public safety via clearer media and governmental communication of upcoming windstorms (Met Office, 2015). A total of eleven storms were named between November 2015 and March 2016, with a summary of these storms and their main impacts provided in Table 4.1.

The winter of 2015-16 set numerous meteorological and hydrological records. A summary is provided here, with a more in-depth analysis presented in Barker *et al.* (2016), Burt (2016) and McCarthy *et al.* (2016). In terms of rainfall, there were new monthly and seasonal rainfall accumulation records for locations across Scotland, Wales and northern England. It was the second wettest winter (December-January-February) on record (since 1850) for the UK, with 159% of normal rainfall accumulation (1981-2010) for the time period (McCarthy *et al.*, 2016). December

2015 was the wettest month on record since 1910, with rainfall across Wales, Scotland and northern England 2-4 times what is normally seen for the time of year.

Name	Dates Active	Max. Wind Gust (mph)	Rainfall	Affected Region	Impacts
Abigail	12-13 Nov 2015	84	Heavy Rainfall	North-West Scotland	20,000 homes without power.
Barney	17-18 Nov 2015	85	---	Central-West England, Wales	6,000 homes without power; Travel disruptions.
Clodagh	29 Nov 2015	97	---	Republic of Ireland, Northern England, Scotland	3,500 homes without power; Travel disruptions.
Desmond	5-6 Dec 2015	81	Max. Rainfall Total (48 hours): 405 mm	Northern England	Flooding of 5,200 homes; 61,000 homes without power; Travel disruptions.
Eva	24 Dec 2015	72	Additional Rain on Saturated Ground	North-West UK	Flooding.
Frank	29-30 Dec 2015	85	Additional Rain on Saturated Ground	Western UK	Flooding; Travel disruptions.
Gertrude	29 Jan 2016	105	---	Scotland, Northern England	Travel disruptions.
Henry	1-2 Feb 2016	90	Heavy Rainfall	North-East England	13,000 homes without power; Travel disruptions.
Imogen	8 Feb 2016	96	---	Wales, Southern England	3,000 homes without power; Travel disruptions.
Jake	2 Mar 2016	83	---	South Wales, South-West England	Some building damage; Road closures.
Katie	27-28 Mar 2016	106	---	Southern England	100,000 homes without power; Travel disruptions.

Table 4.1. List of named storms during the 2015-16 winter storm season. Adapted from Met Office information (https://www.metoffice.gov.uk/barometer/uk-storm-centre/2015-16) (last accessed 7th March 2019)

As expected with the observed record-setting precipitation, the hydrological response during the winter of 2015-16 was similarly extreme in terms of its spatial extent, duration and frequency. Various rivers exceeded their record peak flows on numerous occasions throughout the winter, as successive storms brought heavy, prolonged rainfall to saturated catchments. An overview of the mean seasonal flow, as a percentage of the 30-year average, is provided in Figure 4.1. A new record for daily outflow across all of Great Britain was set on the 5th Dec in the aftermath of Storm Desmond, surpassing the previous record by 30% (Barker *et al.*, 2016). In December 2015 new records for monthly mean river flow were established for

numerous catchments, including the Eden, Tees, Tyne and Wharfe, where flows were over 3 times what would normally be expected (Barker *et al.*, 2016).

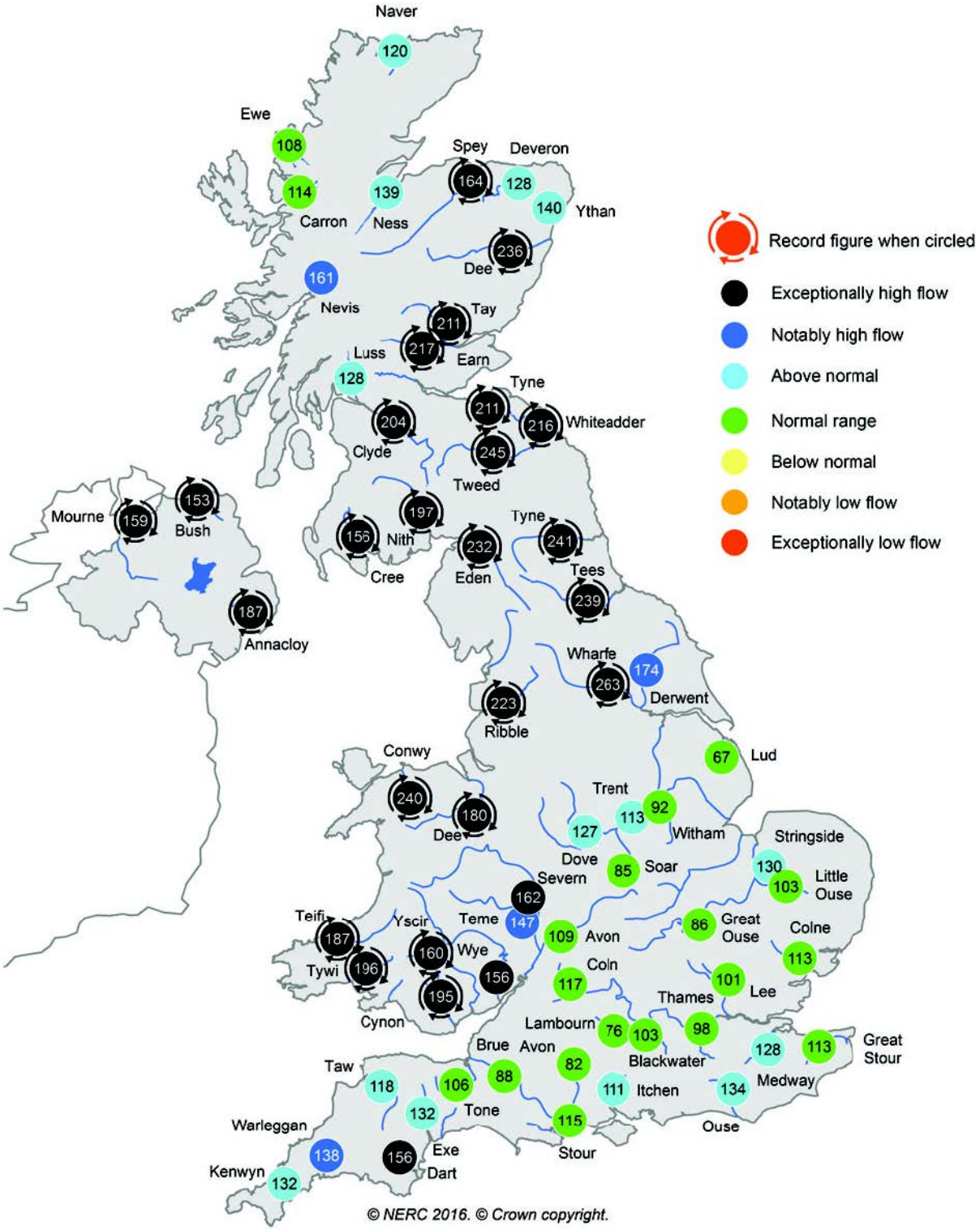

Figure 4.1. Mean river flows for November 2015 to January 2016 for major rivers throughout the UK, expressed as a percentage of long term average flows (1981-2010). Circled values represent those where a new record river flows occurred. Originally published in Barker *et al.* (2016).

The high river flows led to widespread flooding across much of northern UK and Scotland. The first severe flood warnings and property evacuations occurred in Cumbria on the 14th Nov, and by the passage of Storm Eva on 26th Dec over 500 flood warnings were in effect across northern England and Wales. It has been estimated that in some catchments peak flows reached those expected for 1-in-200 year return periods (Barker *et al.*, 2016). Impacts from the flooding include; a large numbers of households and businesses becoming inundated, including 16,000 properties in England during December 2015 (Hansard, 2016), with 5,000 business reporting being affected by the flooding; disruption and failure of transport networks, including bridges at Pooley Bridge and Tadcaster being washed away; the loss of agricultural crops and livestock, including 2,000 sheep in Cumbria; and disruption to utilities supply such as water and electricity, with 23,000 homes without power in Northumberland during Storm Desmond (Barker *et al.*, 2016). Over £200 million has been provided by the government to assist the recovery of impacted regions, and to implement adaptation and mitigation strategies to reduce future flood risk (Barker *et al.*, 2016). It is also estimated that over £1.3 billion has been paid out by insurance companies to cover damages sustained during the flooding (ABI, 2016). Despite the wide range of impacts, it is estimated the current flood defences performed well, protecting 20,000 properties from becoming inundated (Hansard, 2016).

4.2. Methodology

4.2.1. Location

A 400 km^2 study area in Yorkshire, UK, was selected for an initial assessment of the ability of satellite SAR to delineate flooding. The region, shown in Figure 4.2, stretches from the south of York down to Selby, and west beyond Tadcaster. The area is largely agricultural rural, with two major rivers flowing through it: the Wharfe and Ouse. The region suffered from spatially and temporally variable flooding during December 2015 and January 2016, when Storms Desmond (5-6th Dec), Eva (24th Dec) and Frank (29-30th Dec) brought widespread rainfall across the north of the UK.

4.2.2. Datasets

The main aim of the chapter is to assess the ability of Sentinel-1 SAR data to monitor flooding. A review of methods previously used to delineate surface water from SAR imagery is provided in Chapter 2. There are thirteen Sentinel-1 SAR images acquired over the study region between the 5th Dec and 10th Jan, listed in Table 4.2.

Radiometrically calibrated and terrain corrected Sentinel-1 images are available from Google Earth Engine (GEE), which provides free cloud computing facilities for research (GEE, 2015). The pre-processing steps undertaken on the imagery matches those described in Chapter 3 (GEE, 2015). The availability of pre-processed satellite imagery within GEE makes it a valuable tool for remote sensing practitioners, removing the requirement for this initial processing to be completed locally upon download. The cloud infrastructure also allows for wide-scale analysis, both spatially and temporally, to be completed with ease. The initial scene selection and change detection processing were completed using the GEE infrastructure.

Figure 4.2. The 400 km^2 study region, shown by the red box, for which flood extents have been determined between December 2015 and January 2016.

The polarisation of a SAR image can impact the accuracy of flood delineation algorithms, as highlighted in Chapter 3. Sentinel-1 is available in two polarisations, VH and VV, both of which have different sources of potential false classifications. VH data produces a wider range of backscatter values from vegetated land surfaces, leading to potential overlap with the low backscatter values associated with water (Manjusree *et al.*, 2012). VV polarised images are more susceptible to increased backscatter from roughening of the water surface, often caused by wind or heavy rain, resulting in inundation not being identified (Manjusree *et al.*, 2012). The limitations of each polarisation as environmental conditions vary requires acknowledgement when using Sentinel-1 for flood mapping. Previous research concluded that VV provides a slight advantage when identifying flooding when using Sentinel-1 data (Twele *et al.*, 2016). To allow for further comparison both polarisations have been processed using the same methods within this study.

Sentinel-1 Image	Date	Footprint %	Track ID	Num. Ref. Images
SIA_IW_GRDH_1SDV_20151205T061404_20151205T061429_008903_00CBC9_2323	05/12/2015	100	81	18
SIA_IW_GRDH_1SDV_20151208T174942_20151208T175007_008954_00CD3E_349B	08/12/2015	100	132	4
SIA_IW_GRDH_1SDV_20151210T062205_20151210T062230_008976_00CDE1_1951	10/12/2015	100	154	10
SIA_IW_GRDH_1SDV_20151213T175808_20151213T175833_009027_00CF27_4F38	13/12/2015	68.1	30	7
SIA_IW_GRDH_1SDV_20151217T061404_20151217T061433_009078_00D09B_ECA6	17/12/2015	100	81	18
SIA_IW_GRDH_1SDV_20151220T174947_20151220T175012_009129_00D20A_C0F7	20/12/2015	100	132	4
SIA_IW_GRDH_1SDV_20151222T062204_20151222T062229_009151_00D2AF_17F0	22/12/2015	100	154	10
SIA_IW_GRDH_1SDV_20151225T175803_20151225T175828_009202_00D428_9464	25/12/2015	68.2	30	7
SIA_IW_GRDH_1SDV_20151229T061403_20151229T061428_009253_00D59B_CC2A	29/12/2015	100	81	18
SIA_IW_GRDH_1SDV_20160101T174941_20160101T175006_009304_00D70A_60DE	01/01/2016	100	132	4
SIA_IW_GRDH_1SDV_20160103T062204_20160103T062229_009326_00D7AC_C9F2	03/01/2016	100	154	10
SIA_IW_GRDH_1SDV_20160106T175807_20160106T175832_009377_00D920_8394	06/01/2016	68.4	30	7
SIA_IW_GRDH_1SDV_20160110T061404_20160110T061433_009428_00DA93_B5C5	10/01/2016	100	81	18

Table 4.2. List of Sentinel-1 scenes used, with acquisition date, percentage of study area covered, satellite track ID and the number of images used to calculate the reference image.

Within the methodology, a terrain filter is applied to remove areas where the topographical location suggests that flooding is unlikely, but where SAR image acquisition may result in misclassification. For this, the Ordnance Survey 5 m Digital Terrain Model (DTM) was used to create Height above Nearest Drainage (HAND) and slope datasets. The slope aspect of the filter is required to remove areas of radar shadow, found when large vertical structures limit the ability of the SAR system to record data from the lee of the feature. The minimal radar response in these areas is similar to that of flat water. The HAND dataset represents the topographic difference

between a pixel and its hydrologically determined nearest watercourse (Rennó *et al.*, 2008; Nobre *et al.*, 2011). The addition of HAND reduces the impact of the slope filter in the lowlands by including features such as river banks, which would be otherwise removed. For this project, a HAND threshold of 20 m, along with 3° slope, were combined to create the terrain filter.

4.2.3. Validation Datasets and Accuracy Descriptors

A cloud-free satellite optical image was collected by Sentinel-2 on the 29th Dec, 12 hours after a Sentinel-1 image was acquired. The use of optical imagery to validate SAR water extractions has become common practice, despite the potential errors in classifying water using optical indices. However, the lack of in-situ data to act as a reference means the Sentinel-2 image has been used to validate the SAR flood extents. To extract the water bodies from the optical image the Modified Normalised Difference Water Index (MNDWI) was applied, defined by (Xu, 2006) as:

$$MNDWI = \frac{Green - SWIR}{Green + SWIR} \tag{5}$$

with band 3 and band 11 representing the Green and Shortwave-Infrared (SWIR) wavelengths within the Sentinel-2 instrumentation. The MNDWI highlights the strong absorption of SWIR radiation by water bodies, improving on other water extraction indices, notably the Normalised Difference Water Index (NDWI) (McFeeters, 1996), by providing better separation between water and urban areas. The MNDWI dataset can theoretically be segmented at zero to identify areas of water, however, differences in sensor acquisition parameters and geographical image characteristics can create a differing range of potential threshold values, necessitating the need for individual image thresholding. To achieve this Otsu's method was employed, maximising the variance between the water and land classes (Otsu, 1979).

		Reference Flood Extents	
		Flooded	**Non-Flooded**
SAR Derived Flood Extents	**Flooded**	A	B
	Non-Flooded	C	D

Table 4.3. Example of a contingency table used to validate SAR flood extents against a reference dataset.

The SAR and MNDWI flood extents have been compared using a contingency matrix, an example of which is shown in Table 4.3. This method of relating spatial data is regularly used to determine the accuracy of satellite-derived flood extents (Gan et al., 2012; Giustarini et al., 2015; Schlaffer et al., 2015). A number of accuracy metrics are reported when comparing the data this way, including Producer's Accuracy (PA_f), or the amount of inundation in the reference (optical) image that has been correctly identified as flooding in the SAR image, instead of being misclassified as land. This is determined by:

$$PA_f = \frac{A}{A + C} \tag{6}$$

User's Accuracy (UA_f) describes the amount of land in the reference image that has been misclassified as flooding in the SAR data, and is defined as:

$$UA_f = \frac{A}{A + B} \tag{7}$$

Furthermore, the Total Accuracy (TA) of the SAR flood extents in relation to the optical inundation maps can be determined with:

$$TA = \frac{A + D}{A + B + C + D} \tag{8}$$

One of the issues with reporting TA when assessing flood extents is the over-sensitivity towards correctly identified non-flooded regions, which can often take up a large proportion if the study region compared to the areas of flooding (Stephens *et al.*, 2014). This can result in an overestimation of the accuracy of the derived flood extents. An additional statistic that can be calculated is the Critical Success Index (CSI), which removes the correctly identified non-flooded pixels from the calculation, leaving:

$$CSI = \frac{A}{A + B + C} \tag{9}$$

This result still has the potential to misrepresent the results, producing an improved result with larger floods, or when the result has over-predicted the flood extent as opposed to under-predicting (Stephens *et al.*, 2014). The combination of CSI, UA_f and PA_f can adequately describe the accuracy of the flood classification, whilst identifying where any potential errors have occurred. The final statistic that is commonly reported is Cohen's kappa coefficient (C*κ*), which describes the likelihood that the relationship between the two extents is due to chance (Foody, 2006). This is scaled between 0 and 1, with 0 meaning completely due to chance. C*κ* is calculated by:

$$C\kappa = \frac{TA - Pe}{1 - Pe} \tag{10}$$

Pe is the proportion of correct classifications that may be attributed to chance, calculated from false-positive and false-negative results (Foody, 2006; Hunt *et al.*, 2010). Although there are no set guidelines for what defines a good agreement, it is generally considered that values above 0.7 are optimal for producing confidence in the relationship between the two datasets (O'Grady *et al.*, 2013).

The Environment Agency (EA) Flood Maps for Planning (FMP) contain modelled indicative results of areas likely to be inundated during a 100 year river or 200 year sea flood event (known as Zone 3, referred as 100 year event henceforth), as well as a 1000 year event from either source (Zone 2) (Porter and Demeritt, 2012). The extents have been modelled using a DTM with the flood defences removed, allowing for a subsequent dataset highlighting the areas protected by the current flood defences during a 100-year event. A further map showing the areas designated for storage areas is available, with these locations used to attenuate the flood peak in vulnerable areas. The SAR derived flood extents have been compared to the EA FMP, providing an evaluation of the correlation between the remote sensing data and modelled results. Within the study region, a 100-year flood would inundate 53.4 km^2 of the area (13.4% of the study region), including 10.4 km^2 classed as water storage areas (2.6%), with an additional 24.9 km^2 being actively protected by defences (6.2%).

An aerial photograph, taken on the 27th Dec by the National Police Air Service (NPAS) Carr Gate helicopter (twitter @NPAS_CarrGate), has been used in Figure 4.8 to provide supplementary information about the hydrological conditions in the region prior to the satellite crossing. The image was taken as the helicopter was to the west of the study region, close to Tadcaster on the River Wharfe. The image looks eastwards, towards the confluence of the Ouse and the Wharfe.

4.2.4. Flood Mapping Workflow

A Change Detection and Thresholding (CDAT) methodology, adapted from Long et al. (2014), was used to determine the flooding extent. Figure 4.3 provides a diagrammatic overview of the workflow. The first step requires a non-flood reference image for change detection. Selection of this image can influence the outcome, with seasonal differences in land use and variances in satellite acquisition parameters (e.g. orbit direction and incidence angle) requiring consideration (Hostache *et al.*, 2012). The reference images in this study were calculated using a collection of 39 previous Sentinel-1 images, dated between 3rd Jul 2015 and the 5th Nov 2015. Ideally, the time period used to create the reference collection would be similar to that of the flooding. However, due to the relatively short time Sentinel-1 has been operational, the majority of winter images suffer from either flooding or poor pre-processing within GEE, leading to the inclusion of summer images to ensure coverage for each satellite track. For each flood scene analysed, the images from the same satellite track are selected, with the median value from this subset taken for each pixel to create the final reference image. Four different satellite tracks provide coverage over the study area, with the number of images in each reference image collection ranging from 4 to 18, as summarised in Table 4.2.

As discussed in Chapter 3, SAR suffers from speckle due to the variation in the radar return within a pixel caused by multiple scattering sources. This results in a salt and pepper effect across homogenous land covers, which can be removed by applying a local adaptive filter (Esch *et al.*, 2011). For this initial study, both the flood and reference images had a median 5 x 5 filter applied to attenuate the speckle, allowing for clearer regions of water for delineation. The difference between the flood and the reference image is calculated under the premise that change detection highlights variations in the radar return to the satellite, and by proxy changes in land cover or conditions. It is expected that flooding will cause a large negative difference due to

the specular reflection of the radar signal by water, compared to the normal, stronger land backscatter response.

The difference image is subsequently masked based on terrain, with composition and parameters of the filter described previously. The application of the filter removes just over 8 km^2, or 2%, of the study region. A threshold approach is applied to the difference image to extract the largest negative change in backscatter, thus highlighting the area's most likely to be inundated. Long *et al.* (2014) determined the ideal threshold to be:

$$P_F < (\{\mu[D] - f_c * \{\sigma[D]\}) \quad (11)$$

where P_F is the pixels identified as flooded, μ and σ the mean and standard deviation of D, the difference image, and f_c is a coefficient. Optimal f_c was found to be 1.5 (Long *et al.*, 2014).

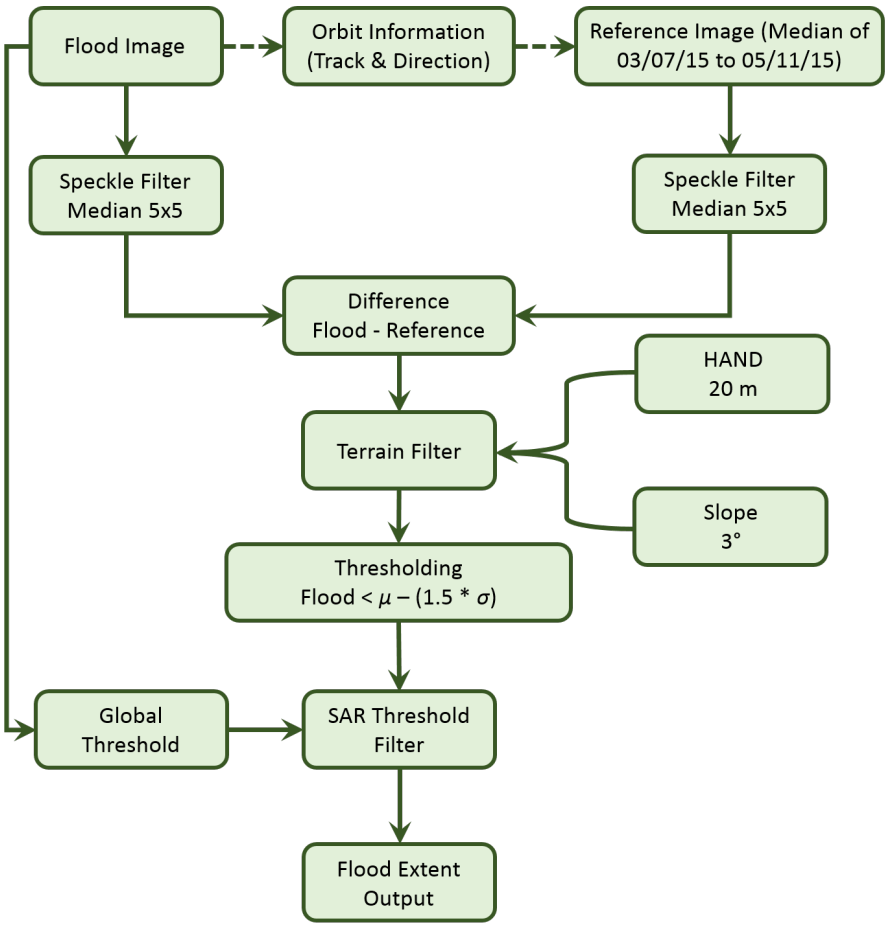

Figure 4.3. Workflow used to extract the flood extents from SAR imagery for this study. μ and σ represent the mean and standard deviation.

It was determined that an additional processing step was required compared to the original CDAT methodology. This is due to seasonal changes in land cover occasionally producing similar decreases in backscatter as flooding within the difference image, such as when an agricultural field has crops during the summer months to when the field is bare once the field has been harvested. For this filter, a global threshold defining the land-water boundary was determined by applying Otsu's algorithm (Otsu, 1979) to the histograms of the flooded SAR images used in the study, with only the areas identified as inundated by both the SAR threshold and the CDAT process used as the final flood extent.

The results are mapped, allowing direct comparisons between the two polarisations, as well as flooding identified from the Sentinel-2 optical imagery and the EA FMP. An estimate is also made of the number of days each pixel was inundated during the 37 day study period. Each satellite image has been allocated a number of days, calculated as an even distribution of the time between the preceding and following satellite passes. For each pixel, the image scores for the dates when flooding has been identified are summed to provide an estimate for the number of days the pixel was inundated. The study area has been sub-divided for this purpose, with different weightings required when the images do not cover the full region.

4.3. Results

4.3.1. Polarisation Comparison

Both polarisations display a similar sequence for the amount of flooding throughout the study period (Figure 4.4). The image collected on the 29th Dec provides the maximum flood extent for both polarisations, showing the aftermath of Storms Eva and Frank. On this date, 6.7% and 6.1% of the study region was inundated for VH and VV respectively. Preceding this date is a slight downward trend in flood extent from the initial image on 5th Dec, with extents of 2.3% (VH) and 2.0% (VV), to 25th Dec, with 0.7% (VH) and 1.0% (VV) of the region inundated. A decrease in flood extent is observed following 29th Dec, before an increase on 10th Jan to 4.9% (VH) and 4.2% (VV), the second greatest extent observed.

Both VH and VV polarisations are available for all images, allowing a comparison of their ability to delineate flooding. The observed time-series between the two datasets are similar, as seen in Figure 4.4. The satellite crossing on 17th Dec provides a match

in the extent of flooding between the two polarisations, although only 80.4% of the identified areas correspond. All other images provide differing flooding extents between VH and VV, with an even split for the greatest estimator. Figure 4.5 shows the relationship between the two datasets. A strong linear distribution is observed, with an R^2 value of 0.87. At lower extents of flooding, VV identifies a greater area of inundation, with the polarisations matching at 1.6%. As the extent of flooding grows, VH identifies an increasingly greater proportion of the region as inundated compared to VV, with 6.0% in VH equating to 5.1% in VV.

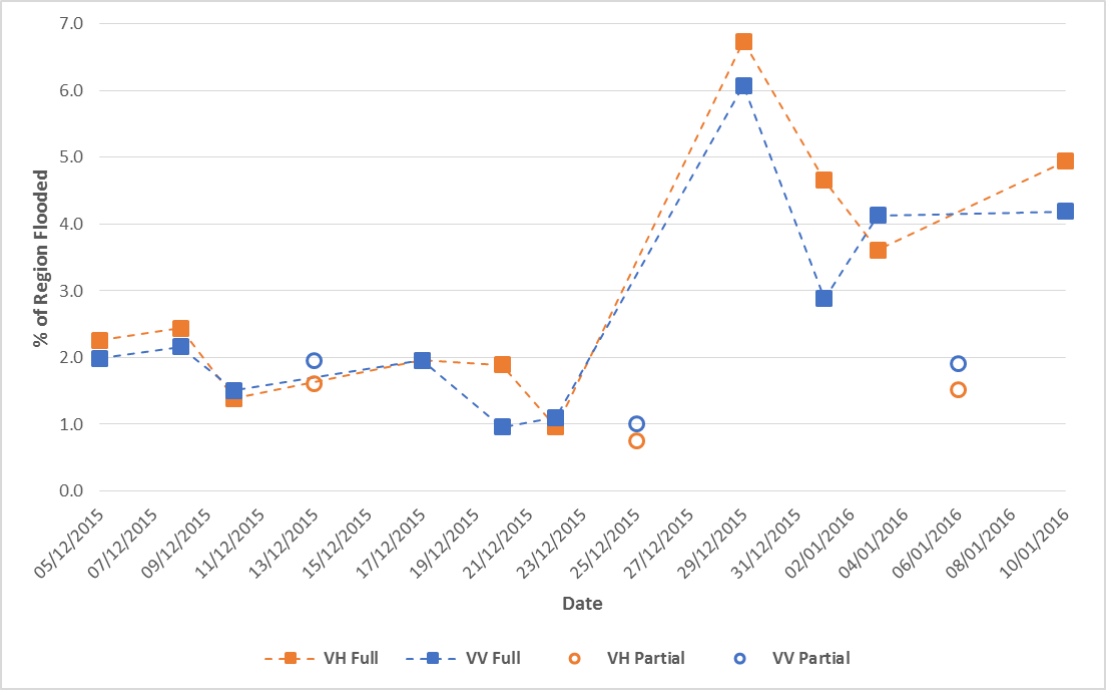

Figure 4.4. Percentage of the region identified as flooded for the VH and VV polarisations. Dates with full satellite coverage are joined to show the approximate sequence of flooding. Other data points, labelled as partial, have 68% of the region covered by Sentinel-1 and are likely to underestimate the extent of flooding.

Two dates show a considerable difference between the two polarisations. On the 20th Dec, the flood extent from VH (1.9%) is almost double that of VV (1.0%), with the VH identifying potential pluvial flooding that is missed by the VV. Similarly, on 1st Jan, VV (2.9%) identifies just 61.7% of the flood extent as estimated from VH (4.7%). On this date, the difference is largely within the main body of flooding, with the VH identifying a uniform water surface compared to the smaller separate areas seen in the VV (Figure 4.6). It can be hypothesised that the lack of consistency in the VV backscatter response is caused by the wind roughening of the water surface.

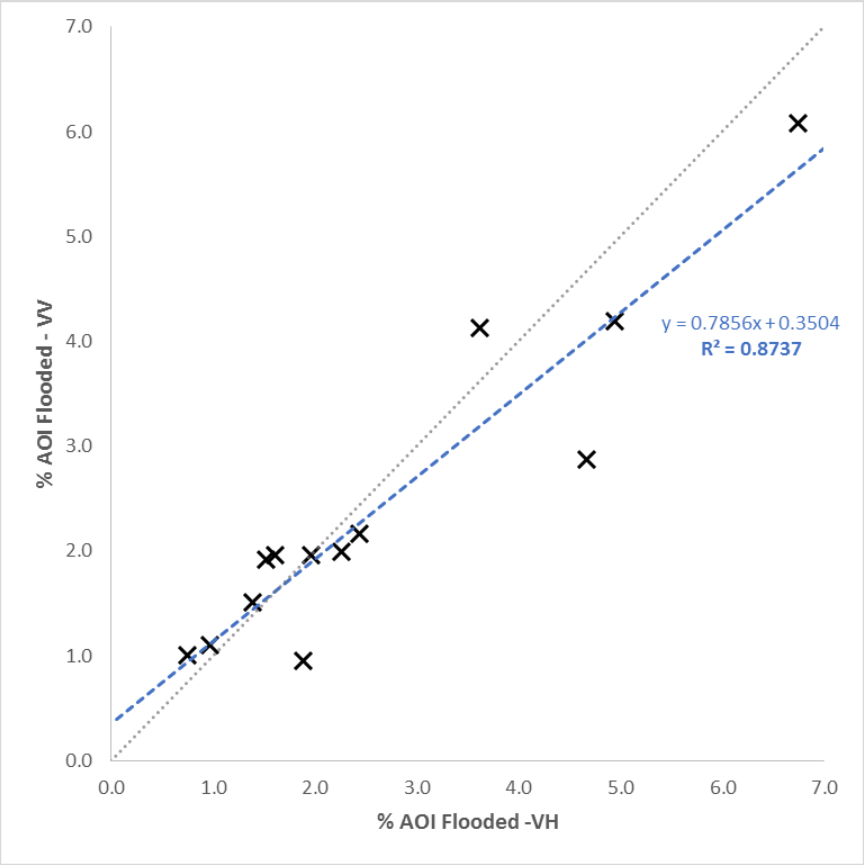

Figure 4.5. The relationship between the percentages of the study region identified as flooded for the VH and VV polarisations. Grey line represents *y=x* as a reference.

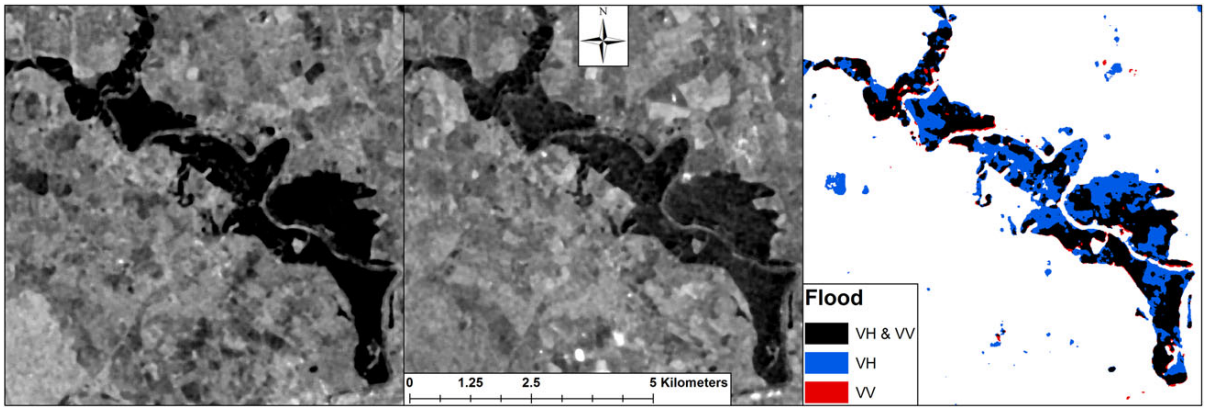

Figure 4.6. Comparison of the flood extents from the 1st Jan. VH SAR image (Left), VV SAR image (Middle), and derived flood extents (Right). Note VV shows an inconsistent body of water compared to VH due to increased backscatter on the water surface in the SAR image, likely caused by wind roughening of the water.

4.3.2. Validation

The MNDWI water extent of the Sentinel-2 optical image of the 29th Dec has been used to validate the flood extents from the two polarisations of the SAR image collected on the same day. The accuracy descriptors for both polarisations are

shown in Table 4.4. Producer's accuracy for identifying flooded pixels is slightly better with VH, showing a greater inclusion of Sentinel-2 identified water pixels in the flood extent. However, VV produces 94.3% user's accuracy compared to 87.0% for VH, showing less misclassification of land as water using this polarisation. Overall the total accuracies and CSI are similar, with 0.4% and 2.7% difference respectively, with VV producing stronger scores for both. The kappa coefficient (κ) varies from 0.778 for VH to 0.799 for VV, showing a good relationship between the optical result and the two polarisations, with minimal correlation caused by chance.

VH	Reference - Sentinel-2			
SAR - Sentinel-1	No Flood	Flood	SAR Total	**User's %**
No Flood	364.4	8.7	373.1	97.7
Flood	3.5	23.4	26.9	87.0
Ref. Total	367.9	32.1	400.0	
Producer's %	99.0	73.0		

VV	Reference - Sentinel-2			
SAR - Sentinel-1	No Flood	Flood	SAR Total	**User's %**
No Flood	366.5	9.2	375.7	97.6
Flood	1.4	22.9	24.3	94.3
Ref. Total	367.9	32.1	400.0	
Producer's %	99.6	71.5		

Table 4.4. Contingency tables showing the accuracy of the methodology for both polarisations. The MNDWI computed from a Sentinel-2 scene acted as a reference dataset. Black values represent km^2, red values are percentages. Total accuracy for VH was 97%, with a Cohen's Kappa of 0.778 and a CSI of 65.7%. Total accuracy for VV was 97.4%, with a Kappa of 0.799 and a CSI of 68.4%.

Figure 4.7 provides a mapped comparison between flood extents from the SAR and optical datasets. There is a good correlation between the three datasets for the large area of water which represents the inundated floodplain next to the Wharfe and Ouse Rivers. The differences between the datasets can be characterised in four ways: permanent water bodies identified in the optical image but not in the SAR, misclassification of shadow areas as water within the optical image, extraction of the edges of flat man-made features within the SAR, and potential misclassification of land within the VH SAR image.

Both VH and VV polarisations have identified the edges of some urban features as flooded. This is most notable with the flat tarmac associated with an airport,

highlighted in Figure 4.7, which provides a similar specular reflectance as water. There are matching flood extents between the Sentinel-2 validation dataset and the VV polarisation in these areas on the 29th Dec. The VH polarisation identifies additional sections of the runway edges as inundated compared to the other imagery. The suggested flooding may be correct, however, caution is required due to the potential for misclassification around these features.

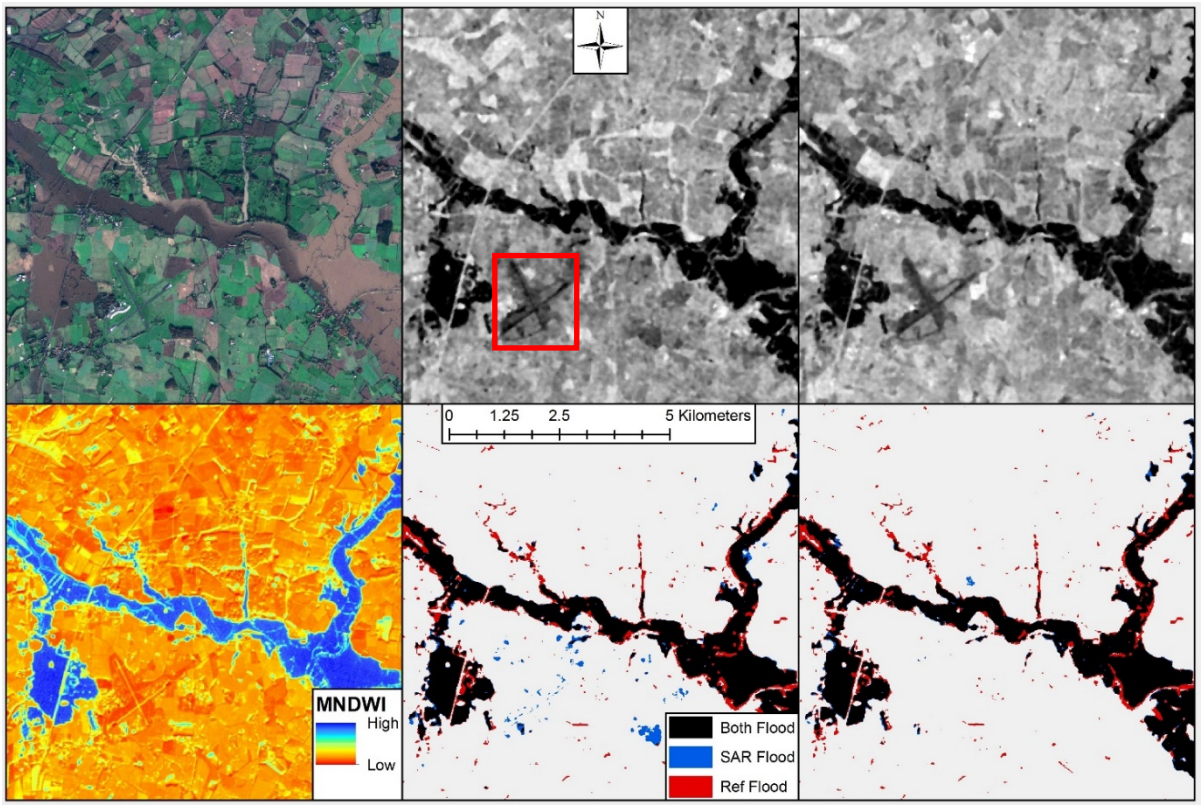

Figure 4.7. Validation of the results for a subset of the region against the Sentinel-2 image. (Top left) True colour composite Sentinel-2 satellite image for the 29th Dec. (Top middle) Sentinel-1 SAR image for the 29th Dec, VH polarisation. The location of the described airport is shown by the red box. (Top right) VV polarised SAR image. (Bottom left) MNDWI, calculated from the Sentinel-2 image, with blue representing water. (Bottom middle) Comparison of extracted flood extents, with blue representing those from VH SAR, red from optical and black represents areas identified in both. (Bottom right) VV flood extents compared to reference dataset.

Areas of pluvial flooding are highlighted in locations away from the floodplains. These areas are likely to be agricultural fields that have become inundated. Both polarisations identify smaller fields not classed as water in the MNDWI, with VH also extracting some larger areas. The VV flood extents provide a better match to the MNDWI dataset, suggesting the additional flood areas identified with the VH are

unlikely to be accurate. However, the misclassification of shadows as water within the reference dataset can complicate the accuracy assessment of the SAR derived flood maps when using optical data as a reference.

An aerial image from the 27th Dec, captured by the NPAS Carr Gate police helicopter, has been used to provide secondary validation of the results (Figure 4.8). The image has been geolocated based on road and railway locations, visible above the flood water in both datasets. Although the image is two days before the satellite crossing, the similarities are good, with the main flooded regions showing a match. Despite the lack of statistical metrics, there is still benefit in comparing the satellite data with other sources of imagery to confirm the results.

4.3.3. Flood Dynamics

The multiple satellite images of the region over the study period enabled tracking of the advance and retreat of the floodwaters. A good example is the recession of the peak event on 29th Dec, through two satellite passes on 1st Jan and 3rd Jan (Figure 4.9). At first inspection, the polarisations show a similar pattern of recession, particularly where the main body of flooding is concerned. There are three main areas where waters recede during the five day period: to the east of the image on the Wharfe, towards the north of the image below York, and downstream of the confluence of the two rivers. However, as mentioned previously, VV polarisation produces an erroneously reduced flood extent for 1st Jan, with areas of flooding likely missing from this analysis.

The other main bodies of flooding around the Wharfe and Ouse display a minimal change in surface area. However, it can be observed that the 3rd Jan locations along the river reach are being classed as land rather than flooded. This suggests a reduction in the depth of water, allowing features such as river banks to protrude the water surface.

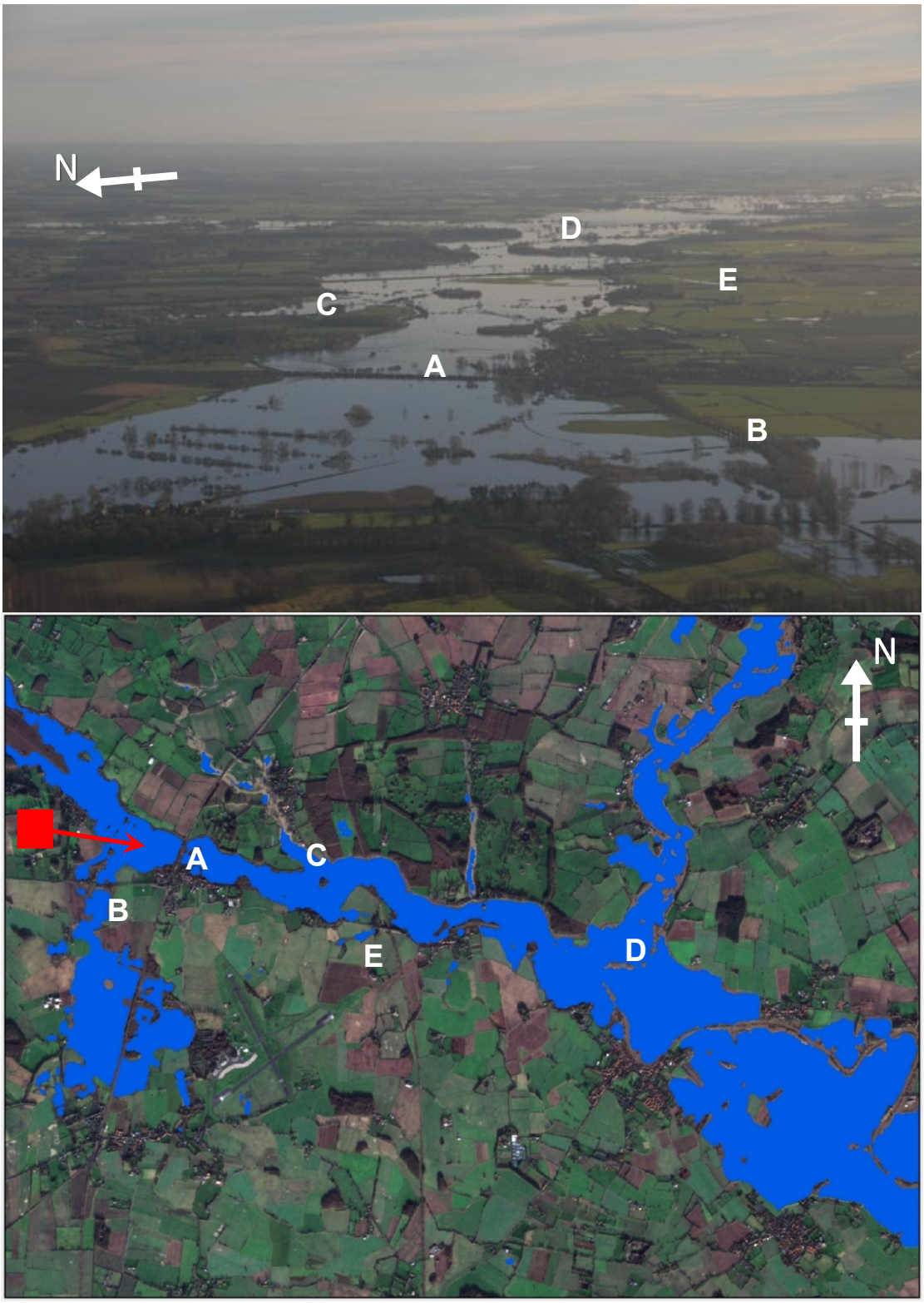

Figure 4.8. Comparison between an aerial photograph from Dec 27th (from *@NPAS_CarrGate*) (top), and the identified flood areas from VV polarised SAR on the 29th Dec (bottom). Red square and arrow show approximate location and viewing direction of the helicopter. Locations **A** (railway embankment) and **B** (B1223) provide georeferencing examples. Point **C** shows The Foss joining the River Wharfe, and point **D** shows the confluence of the Wharfe and the Ouse Rivers. Field level flooding is visible in both datasets, with an example given at **E**. Differences in flood extent are potentially caused by the 2-day time gap between the images.

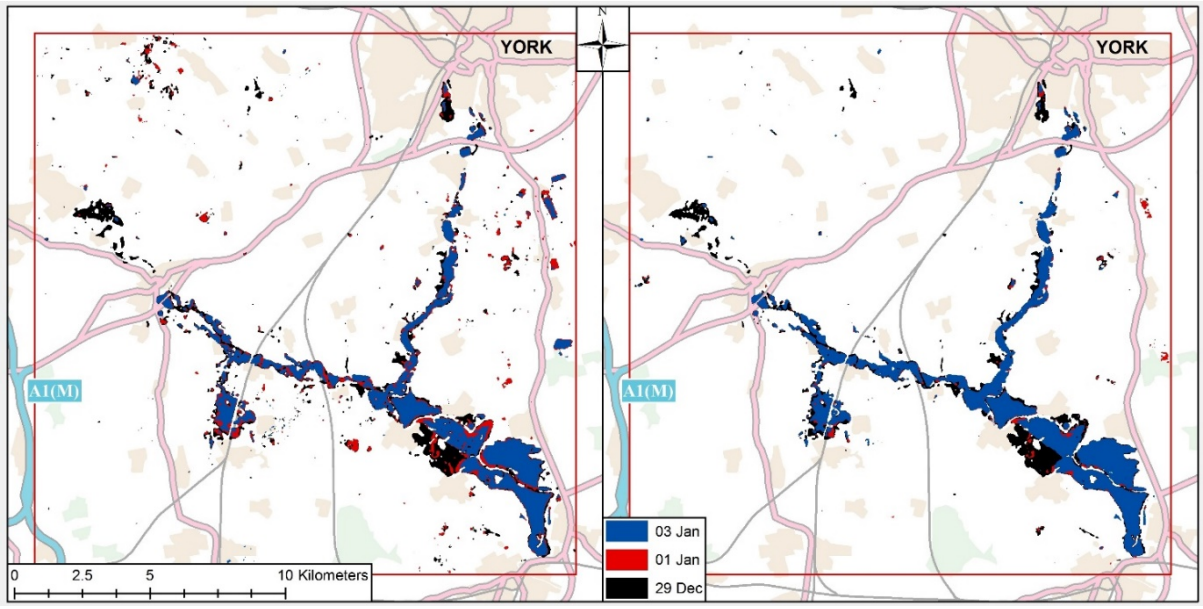

Figure 4.9. The retreat of flood waters during the aftermath of Storms Eva and Frank. VH (left) and VV (right) polarisations for satellite orbits on the 29th Dec, 1st Jan and 3rd Jan are shown.

To provide an overview of the most flood-prone areas in the region an estimate has been made for the number of days each pixel was flooded during the 37 day study period (Figure 4.10). Both polarisations display a similar pattern along the course of the rivers, with the greatest inundation located within the floodplains of the Wharfe and Ouse before the confluence. Some of these areas are shown to have flooded for the whole study period. Downstream of the confluence flooding only occurred after the extreme rainfall experienced during Storm Eva, when the peak flood extents are found. There are major differences with the mapping of inundated fields, with some areas identified as flooded for most of the study period within the VH map, whilst only being minimally highlighted by VV.

4.3.4. Comparison with EA FMP

It has been reported that some rivers in the UK exceeded their 100 or 200 year return period during the winter 2015-2016 floods (Barker *et al.*, 2016; NHMP, 2016). Accordingly, the SAR derived inundation extents have been compared to the EA FMP 100 year flood zone, as well as the areas designated for storage of floodwater and protected by flood defences (Figure 4.11).

An area of 53.4 km^2 of the 100-year flood area is undefended, and at risk of flooding during such an event. At peak flood, 49.2% (VH) and 48.0% (VV) of these regions

were inundated, suggesting the flooding was not a 100-year event in this area at the time of the satellite passes (Figure 4.12). Within the 100-year flood boundary, 10.4 km^2 has been designated as water storage areas. At maximum, 79.3% and 79.1% of these areas were inundated for VH and VV respectively, with Figure 4.11 suggesting the area downstream of the confluence was close to capacity. Arguably the most important information within the EA FMP is the areas protected from the 100-year event by the flood defences. At peak flood, a total of 2.3 km^2 became inundated using the VH data, with 2.2 km^2 for VV, under 10% of the protected areas in the region (Figure 4.13). This is largely to the west of Figure 4.11. Overall, the time-series for flooding for each designated area closely follows the overall flood sequence observed in Figure 4.4.

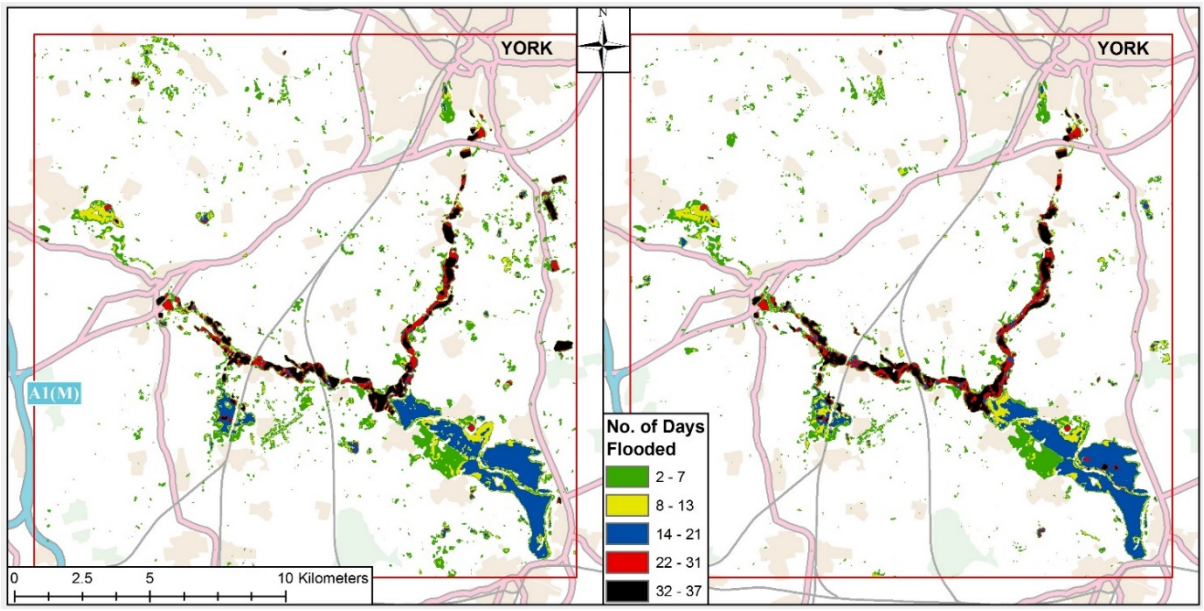

Figure 4.10. The estimated number of days each pixel is inundated for VH (left) and VV (right) polarisations. The total number of days in the study period is 37. Each image is assigned a number of days representing an even distribution of the time to the preceding and following satellite passes. For each pixel, the images identified as flooded have been summed to provide an estimate total days flooded.

The EA FMP largely encompass the main bodies of flooding identified in the satellite data. The percentage of the flooding that occurred outside any of the designated FMP areas has been calculated for each date (Figure 4.14), with mean percentages of 18.0% (VH) and 9.5% (VV). There are some dates where identified flood outside of the FMP prediction is high. The 5th Dec (VH and VV), 20th Dec (VH) and 22nd Dec (VH) have less than 75% of identified flooding within the FMP areas, with the SAR data all showing a large amount of pluvial flooding on these dates.

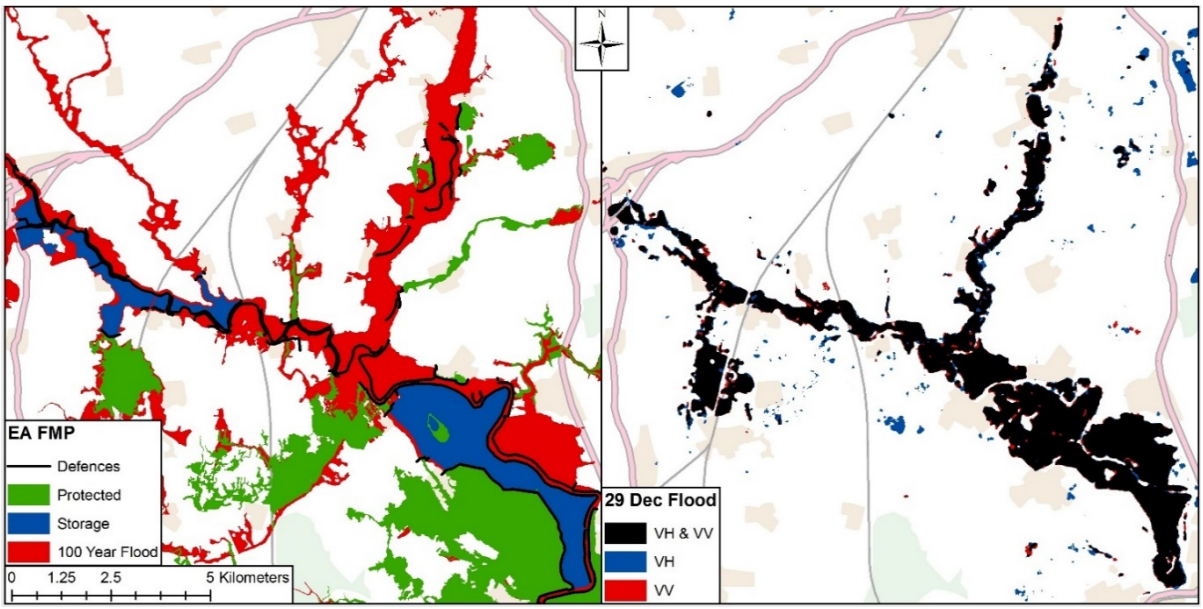

Figure 4.11. The EA FMP for a subset of the study region (left), showing 1 in 100-year flood, areas protected by flood defences, and flood storage areas. Extracted flood extents for VH, VV and where they overlap for the 29th Dec (right) for comparison.

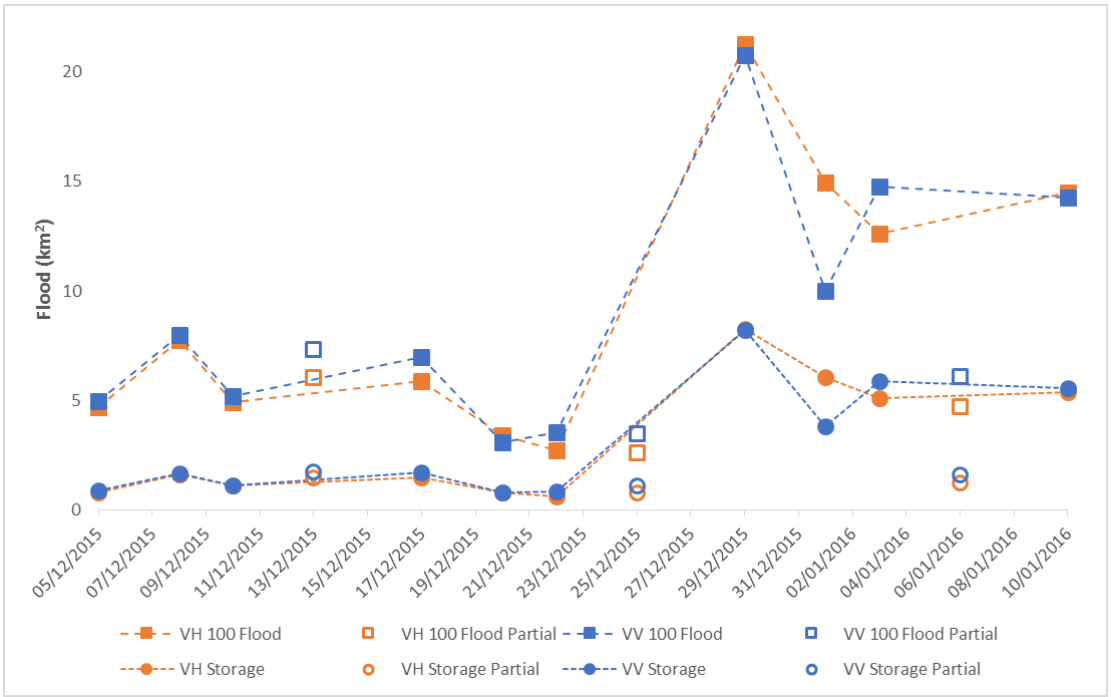

Figure 4.12. Area of flooding identified within the EA FMP 100 year flood boundary, and the proportion located in a designated flood storage area. Partial data points represent those without full satellite coverage. Total area for the 100-year flood region is 53.4 km^2 (13.4% of the study area), including 10.4 km^2 designated as flood storage areas.

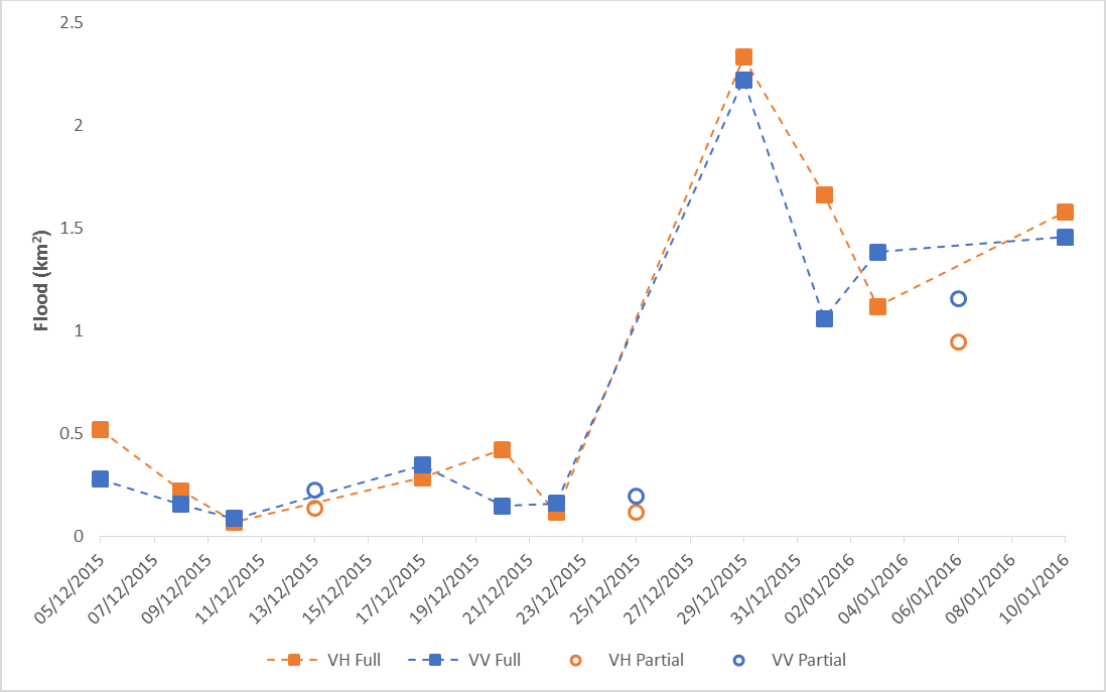

Figure 4.13. Amount of flooding within the protected areas identified in the EA FMP. Partial data points represent those without full satellite coverage. Protected areas cover 24.9 km^2, or 6.2%, of the study region.

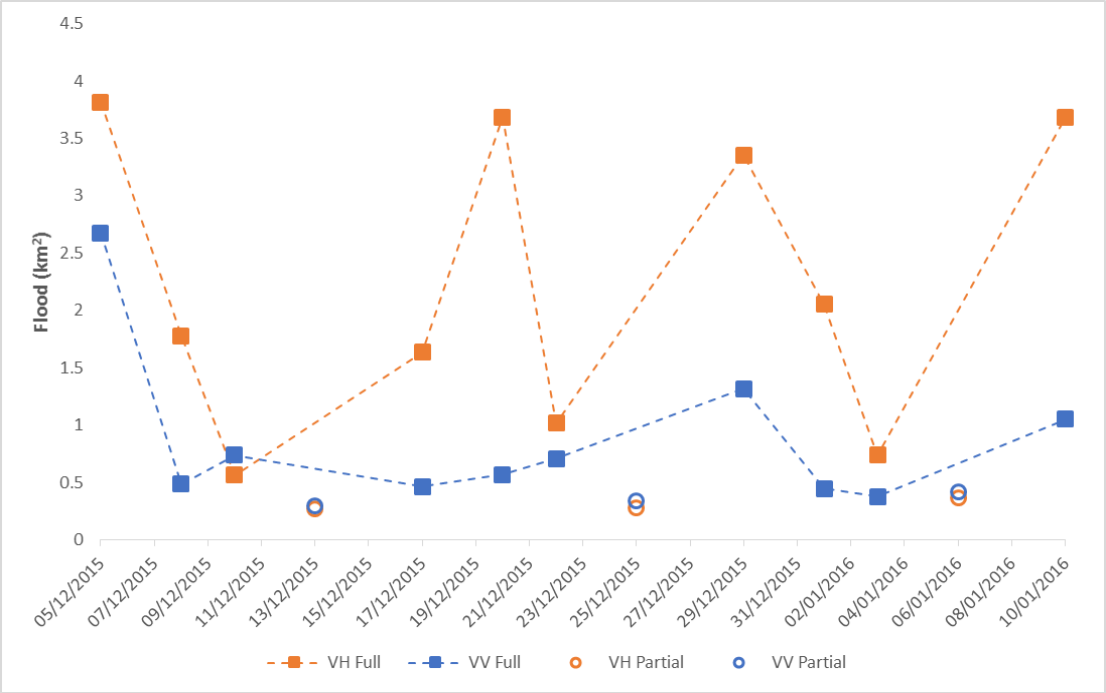

Figure 4.14. Amount of flooding identified that is not found within the boundaries of the EA FMP. Partial data points represent those without full satellite coverage. 80.4% of the area of interest, or 321.7 km^2, is not included in any of the EA FMP zones.

4.4. Discussion

The following section provides a brief discussion on the results produced from the presented initial flood mapping study. Further in-depth conclusions regarding the dynamics of the 2015-16 floods and the use of satellite SAR to map and monitor flood extent will be provided in Chapter 8, incorporating results and discussion points from applying the adjusted flood mapping algorithm across the north of England.

The validation of the SAR results against the Sentinel-2 MNDWI dataset provides good correlation for both polarisations. Long *et al.* (2014) completed a similar comparison with optical imagery to determine the total accuracy of the original CDAT method, achieving accuracies ranging between 77.1% and 91.7%. The 97.0% and 97.4% total accuracies for the VH and VV polarisations achieved in this study suggests the adaption applied to the original method provides an improvement. Producer's and user's accuracies, and Cohen's kappa coefficient (κ) all provide good results, with sources of misclassification identified in both the SAR and the optical imagery classification. CSI values are similar for both polarisations, with 65.7% for VH and 68.4% for VV. These compare favourably to CSI values calculated from the contingency table reported in Long *et al.* (2014), which range from 9.6% to 28.5%.

Similar to the results presented by Twele *et al.* (2016), the VV polarisation provided a slight improvement in accuracy compared to VH. However, both polarisations produce similar validation results in this study, and considering the inaccuracies associated with identifying inundation using SAR, it is still unclear which of the two Sentinel-1 polarisations is the preferential choice for delineating flooding.

The largest source of inaccuracy comes from the SAR flood extents failing to classify areas of water identified within the validation dataset (cell "B" within Table 4.3). It should be noted that the optical validation dataset is fundamentally different from the SAR flood extents as it represents the surface water extent, whereas the change detection processing removes permanent water bodies within the SAR workflow.

There are some caveats that require acknowledging when using optical data to validate the SAR flood extents. It should be noted that optical imagery, as a satellite product, potentially suffers from inaccuracies within the water identification process. Therefore, it cannot be considered as a definitive measure of flood extent accuracy.

Furthermore, a single reference image was used in this study, when ideally multiple images would be available to confirm the accuracy of the flood extents from each polarisation. However, the limitations of optical imagery, namely its inability to penetrate cloud cover, restricts the number of available scenes. Within this study, the VV flood extents on 1st Jan appear inadequate when compared to the preceding and following flood extents. This is likely to be caused by the susceptibility of VV to increased backscatter from roughening of the water surface due to wind or heavy rain (Brisco *et al.*, 2008; Manjusree *et al.*, 2012). If a suitable optical reference dataset was available for this date, it is expected that the validation outcome would produce a reduced level of accuracy for VV. The variability in perceived results accuracy on non-validation dates highlights the need for further validation of flood extents produced using the two Sentinel-1 polarisations, particularly in varying environmental conditions.

Caution must be exercised in interpreting the data as an accurate representation of the flooding time series due to the sparse nature of the satellite images, with gaps of two to four days between the Sentinel-1 scenes. This is exacerbated by satellite crossings not covering the full extent of the study area, potentially underestimating the full extent. As well as the maximum flood extent, the speed of onset and recession is important for stakeholders to fully manage the impacts of an event. The linearity of the rising and falling limbs around the 29th Dec peak is questionable. Furthermore, the peak extent seen from the images on the 29th Dec is unlikely to capture the true maximum extent. There is no method to accurately extrapolate the data points to determine the timing and magnitude of the peak flood, as well as the onset and recession speed, without the inclusion of in-situ data. Future events will benefit from the full constellation of two Sentinel-1 satellites, providing a denser time series, allowing better estimation of the flood dynamics.

One of the advantages of using satellite data to map flood extents is the ability to identify wide-scale pluvial flooding away from the floodplains. This data can be costly and time consuming to collect on the ground, with resources often allocated to urban areas during an event due to the more profound risk and impacts. Flooded fields have been identified using the CDAT methodology, although there is variability between the VH and VV polarisations. Comparing the results to the Sentinel-2 image, it appears likely that VH overestimates field flooding, with VV providing a more

plausible representation. Cross-polarised images have been shown to have a wider range of backscatter values from vegetated land covers, potentially creating an overlap with the water backscatter responses, subsequently causing an overestimation of the flood extent (Manjusree *et al.*, 2012; Twele *et al.*, 2016). However, further in-situ data during times of flood is required to fully understand the relative accuracies of the polarisations at this scale, and to help explain the temporal pattern of pluvial flooding.

The EA FMP are used for consultation within the UK planning process (Porter and Demeritt, 2012). The clarification of their accuracy provided by the SAR flood maps supports their continued use for this purpose. Agreement was found between the flood maps and both polarisations of SAR data for the locations of fluvial flooding. Having been created from a hydraulic model, the close correlation between the maps and the satellite data on the floodplains is to be expected. Differences come away from the floodplains, with the EA FMP not designed to predict the location of pluvial or groundwater flooding.

4.5. Identified Areas for Methodology Improvement

The initial study successfully mapped flooding within a small region of Yorkshire over a 5 week period. The calculated total accuracies in this chapter compare well to validation statistics reported elsewhere in the literature produced by other flood mapping techniques. Chapter 5 will attempt to map inundation over a longer time period (November 2015 to February 2016) and over a wider geographical region. Upon reflection, there are several methodological improvements which should improve the robustness and accuracy of the flood mapping workflow. The intention is to implement these within the wider study undertaken in Chapter 5. A brief introduction to these changes is given below, with details of their application provided in the next chapter.

- *Speckle filtering*. A median (5 x 5 window) speckle filter was applied to both SAR and reference images for the initial study. The filter successfully reduced the image speckle, however, on occasion the lack of edge detection within the filter resulted in an over-smoothing of the flood boundary. Further speckle filters are to be investigated for the expanded study. Visual interpretation will

be used to identify suitable results, with the target of smoothing homogenous land covers whilst maintaining edge features.

- *Reference images.* The reference images will be recreated for the expanded study. The addition of images from the relevant post-flood time periods will allow for better representation of dry conditions for the time of year. Furthermore, speckle filtering of the reference image will be removed, with the multi-temporal smoothing of the image deemed to sufficiently represent the spatial variations in backscatter for regions of the same land cover.

- *SAR image thresholding.* One of the simplest techniques for determining flooding extent from a SAR image is histogram thresholding, with the lower water backscatter pixels separated from the stronger land response. For the initial study, a single threshold was determined via Otsu's algorithm, which performed well due to the relatively small geographical area containing a high amount of flooding. The expanded study will cover the north of England, and will utilise the full swath width of Sentinel-1 SAR images, with incidence angles ranging between 29° and 46°. It has been shown that both water and the various land covers have varying backscatter responses with changes in incidence angles (Pham-Duc *et al.*, 2017; Bioresita *et al.*, 2018). To account for this, the aim is to develop a technique for determining the relationship between the ideal land-water threshold value and incidence angle, to allow for reliable, full swath flood detection using the developed methodology.

- *Produce a single thematic flood map*. It is likely that the end-users of satellite-derived flood maps (emergency personnel, the insurance industry, flood modellers etc.) will prefer a single inundation map, instead of polarisation specific flood extents produced in this chapter. The initial study showed that for flood mapping there was no clear preferential polarisation between the VH and VV images produced by Sentinel-1. Both have the potential to produce polarisation specific misclassifications, with VV more susceptible to increased backscatter caused by wind roughening of the water surface, whilst VH has more potential to misclassify land as water due to its susceptibility to volume scattering. The aim for the next chapter is to produce a single flood map for

each date by fusing of data from the two polarisations. This will help to reduce polarisation specific errors, allowing for more accurate flood mapping.

- *Further validation.* Additional sources of validation are to be investigated in an attempt to ensure the workflow provides accurate, robust flood extents. New validation schemes will be developed to account for permanent water bodies in the validation datasets, which are removed by the change detection processing of the SAR imagery.

Chapter 5. Wider Application of SAR Flood Mapping

The following chapter describes the development of a further iteration of the flood detection methodology introduced in Chapter 4. This is subsequently applied across an expanded geographical area and temporal extent, outlined in Sections 5.1 and 5.2. The methodology Section (5.4) will highlight processes that have been updated from the previous chapter.

5.1. Study Area

The initial study mapped flooding in a small section of the Ouse catchment that suffered from significant inundation during the winter of 2015-16. However, numerous additional locations within the north of England were subjected to extensive flooding at this time. One of the main advantages of satellite imagery is its ability to monitor environmental variables across wide geographical regions. Figure 5.1 shows some of the major catchments located within the north of England, that together form the study region for this chapter. The results Section (5.5.3) will analyse results from catchments where spatial and temporal patterns of the derived flood extents are of note, namely the Ouse, Aire, Eden and Lake District regions. Results from other catchments can be found in Appendix B.

5.2. Datasets and SAR Pre-Processing

Similar to the initial study, the main dataset used in this chapter is Sentinel-1 SAR. The expanded study region and time period being analysed has resulted in the number of images downloaded and processed to increase to 105 (a comprehensive list of used images can be found in Appendix A). Images covering the study region are available for 7 different orbit tracks. However, due to the poor geographical coverage provided by some of these, only those from 5 tracks (numbers 30, 52, 81, 132, 154) are selected for processing. Figure 5.2 shows the coverage of each orbit across northern England, and Table 5.1 summarises the amount of coverage each orbit provides over the study catchments. The selected images are available for 37 dates throughout the 93 day period (11th Nov 2015 to 11th Feb 2016).

In the initial study utilised GEE to obtain pre-processed SAR imagery for analysis. However, to allow for improved speckle filtering within the SAR pre-processing, raw

GRD products have been download and processed within the ESA SNAP software and the associated python library. Descriptions of the steps applied to pre-process the data can be found in Chapter 3. GEE is still utilised to create orbit specific reference images, as in Chapter 4.

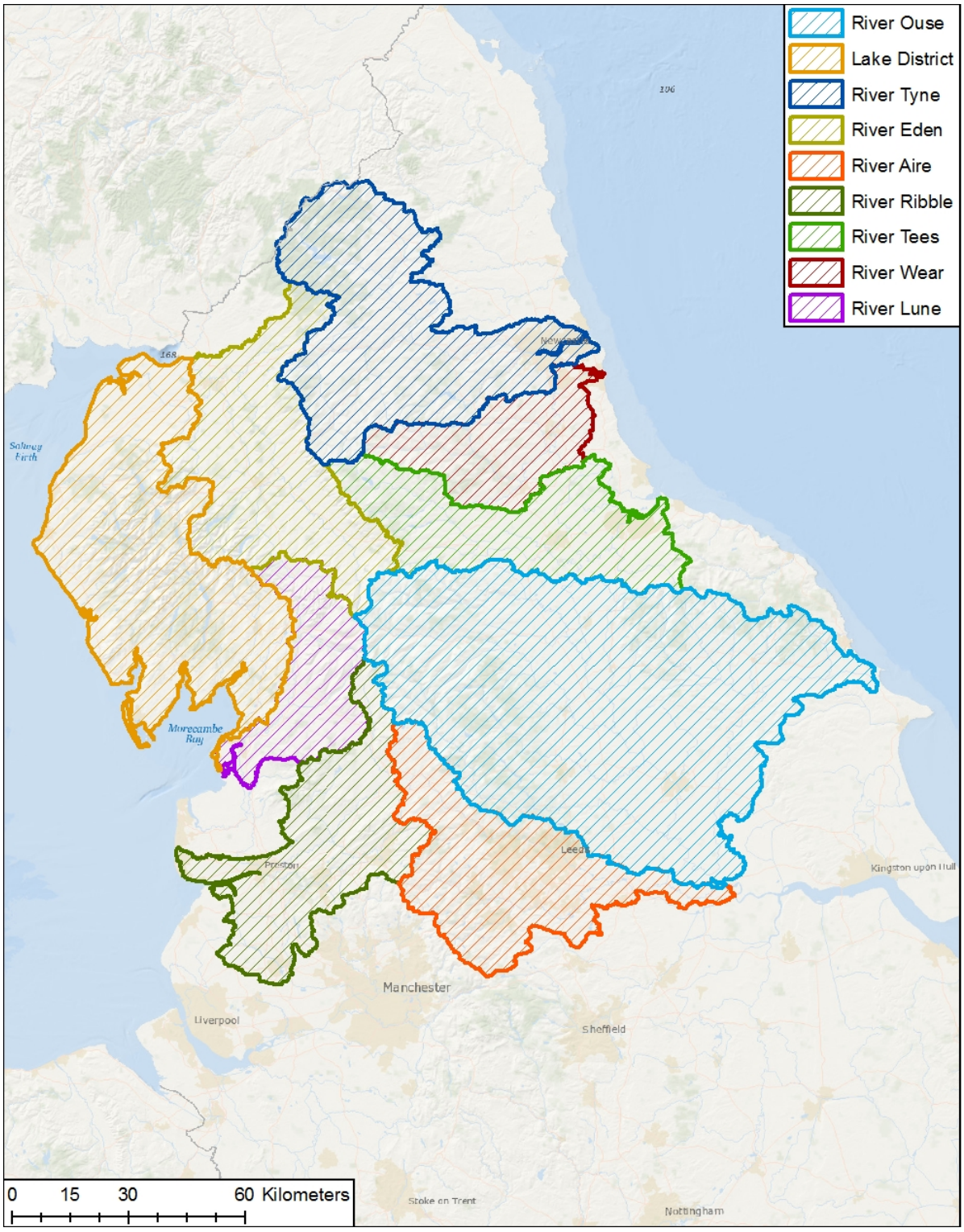

Figure 5.1. Study region across the north of England, with key catchments highlighted.

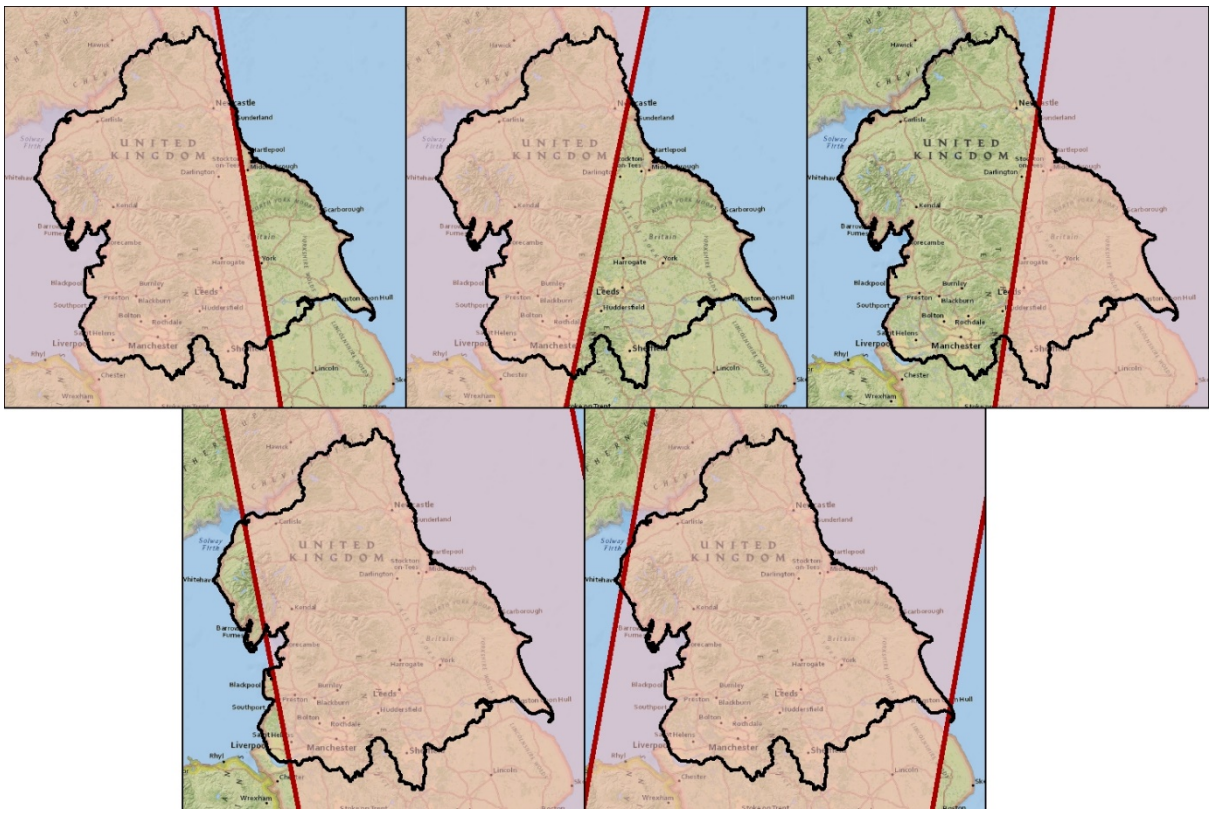

Figure 5.2. Coverage of each Sentinel-1 orbital track (in red) across the north of England. This includes orbit 30 (top left), orbit 52 (top middle), orbit 81 (top right), orbit 132 (bottom left) and orbit 154 (bottom right). Expanded study region shown in black.

	Orbit Track (% Coverage)				
Catchment	**30**	**52**	**81**	**132**	**154**
Aire	**97**	34	35	**100**	**100**
Eden	**100**	**100**	0	**100**	**100**
Lakes	**99**	**99**	0	52	**96**
Lune	**100**	**100**	0	**100**	**100**
Ouse	64	25	63	**100**	**100**
Ribble	**100**	**100**	0	**97**	**100**
Tees	85	51	32	**100**	**100**
Tyne	**100**	**99**	0	**100**	**100**
Wear	**100**	82	0	**100**	**100**

Table 5.1. Sentinel-1 coverage of each study catchment for each orbit track. Good coverage shown in bold, with no coverage shown in red.

The speckle filtering of the flooded SAR images has been updated with the aim of reducing the over-smoothing of high contrast features and edges. Numerous filter types and parameters have been tested and visually compared to one another (see Figure 3.13). It was deemed that the Refined Lee filter sufficiently reduced speckle

whilst maintaining clarity in flood boundary locations, and has subsequently been applied to each image. Furthermore, it was surmised that the creation of the reference image via the selection of the median pixel value from a collection of unflooded Sentinel-1 images produced a sufficiently smooth image, and consequently the speckle filtering of the reference image has been removed.

5.3. Validation Technique and Datasets

With the increase in the study area, an adjustment to the validation strategy is required. In Chapter 4, the contingency matrix was computed across the whole of the analysed region. Total Accuracy (TA) and Critical Success Index (CSI) for the pilot study were calculated as 97.0% and 65.7% for VH polarisation, and 97.4% and 68.4% for VV imagery. A large amount of agreement in non-flooded pixels in both SAR flood maps and the validation dataset can cause positive skewing when reporting TA, and it has been suggested that using CSI will provide a more representative metric of the accuracy of flood maps (Stephens *et al.*, 2014). Alternatively, validating on small subsets of the overall area of interest can minimise any skewing of TA, and allow for a range of values to be established for each accuracy metric. Twenty-six different validation areas of 4 km^2 (Figure 5.3) are used to validate the SAR derived flood extents in this study, producing a range of values for TA, CSI, User's Accuracy (UA_f), Producer's Accuracy (PA_f) and Cohen's Kappa ($C\kappa$).

The updated flood extents will be compared to a number of reference inundation maps. These include the polarisation specific flood extents from Chapter 4 and the MNDWI-Otsu classified Sentinel-2 multispectral image used as validation in the preceding chapter. Additional comparisons are made against the flood extents produced by the Copernicus Emergency Management System (CEMS), extracted from a RADARSAT-2 image. The CEMS flood maps are derived using a semi-automated approach (Dorati *et al.*, 2018). Both the Sentinel-2 and RADARSAT-2 images are acquired approximately 12 hours after the Sentinel-1 image captures on the 29th Dec. Each validation dataset is likely to contain inaccuracies. However, using multiple different datasets for comparison should allow for an improved understanding of where these are occurring, and allow for a robust assessment of the flood maps presented in this chapter.

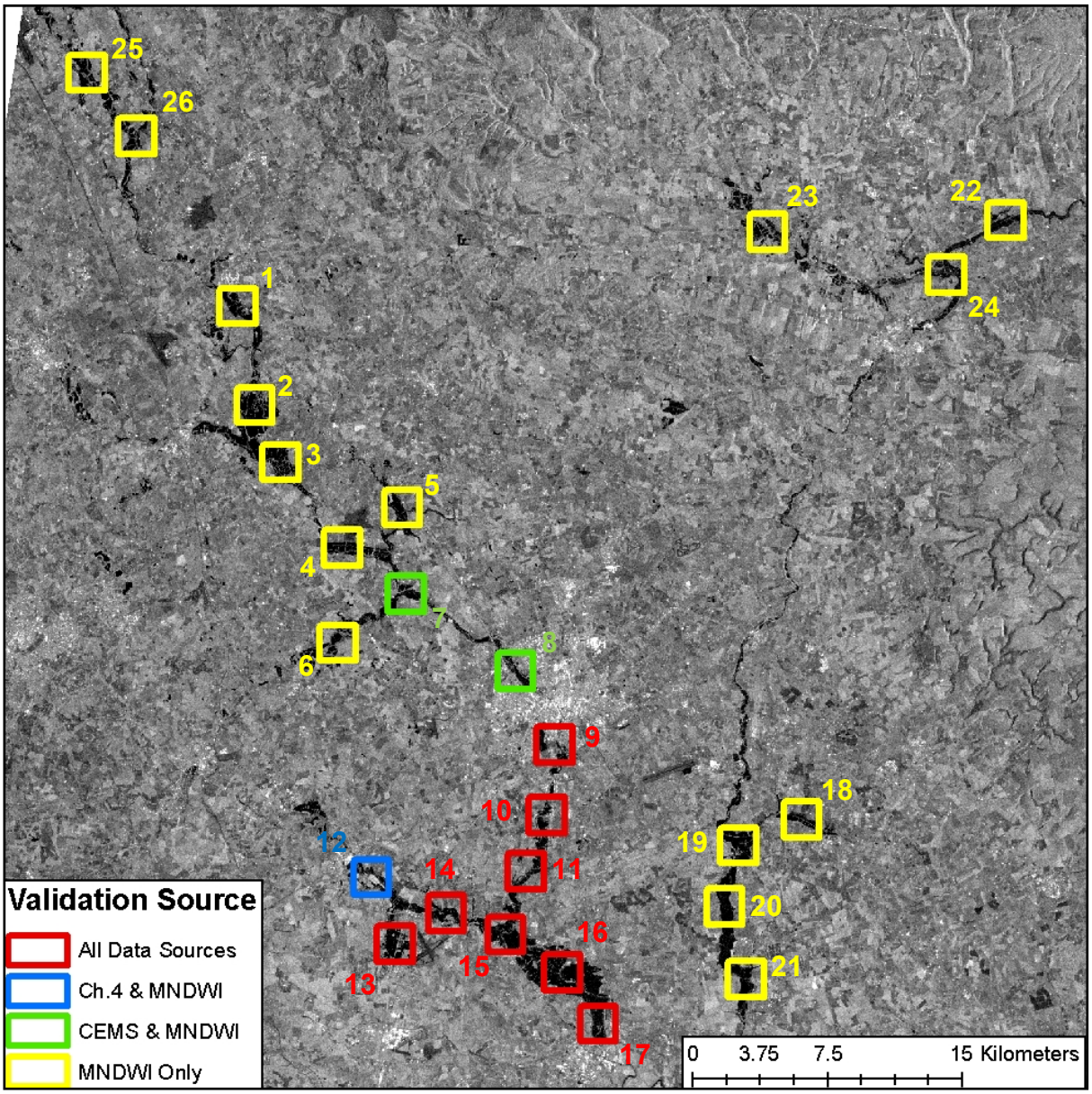

Figure 5.3. Validation locations throughout the River Ouse catchment. The results from the 29th Dec are used to ascertain accuracy of the results against the flood extents produced in Chapter 4, a MNDWI-Otsu classified Sentinel-2 image, and CEMS RADARSAT-2 flood extents. Red squares represent coverage and validation across all datasets; the blue square is within the Chapter 4 study region and covered by the Sentinel-2 imagery; green squares show accuracy assessment against the CEMS flood extents and the Sentinel-2 imagery; yellow squares show validation against the Sentinel-2 imagery only. VV polarised SAR imagery from the 29th Dec shown to give context to validation locations.

5.4. Methodology Adjustments

The methodological concept for deriving flood extents from Sentinel-1 imagery remains the same as that presented in Chapter 4. This involves the use of two pixel-based segmentation techniques as separate processing branches, which are subsequently combined to produce a single flood map. The first branch contains the

CDAT workflow and the second is based around the histogram thresholding of the flooded SAR image. The CDAT branch remains largely unchanged from the original study. An updated terrain mask is produced using the SRTM 30 m DEM to replace the 5 m OS Terrain DTM used in Chapter 4. The use of a globally available DEM ensures applicability of the terrain filtering outside of the UK. There are small differences in the output maps produced from the CDAT branch, which can be attributed to this change in terrain mask and the updated speckle filtering parameters.

The histogram thresholding branch has been heavily modified to improve water detection across whole image swaths and to allow for increased automation of the processing. Whereas in the previous study a fixed Otsu derived threshold was used across all images, a dynamic threshold is now created to account for changes in backscatter responses from different land covers with incidence angle, and the subsequent variation in the optimal land-water threshold. The variability in water backscatter responses with incidence angle have been highlighted by O'Grady *et al.* (2014), Pham-Duc *et al.* (2017) and Schlaffer *et al.* (2017), with Chapman *et al.* (2015) providing an example of how a variable threshold can be applied across the full swath width of an ALOS PALSAR image.

The relationship between the land-water threshold and incidence angle has been derived by analysing numerous image subsets to identify the local threshold value. Target sub-regions are selected based on the likelihood of the location containing a mix of water and land pixels, which will produce a bimodal histogram from which to determine a threshold. These regions are created using the SRTM Water Body Dataset (WBD), a by-product of the SRTM mission. The 150 largest water bodies from across the study area have been identified and buffered to create masks that contain an approximately even number of land and water pixels. Although there is some clustering in specific geographical regions, such as the Lake District, each orbit track views these locations at a different incidence angle. The combined results from the five orbit tracks used within this chapter provide an even spread of locations across the full image of Sentinel-1 incidence angles. Within each lake region, areas that have a slope above 5° are removed to reduce any histogram skewing caused by radar shadow or foreshadowing. The remaining mask is used to extract subsets from each SAR reference image created for the change detection processing. The

histogram from each extracted region first has to pass a bimodality test, which searches for two clear peaks (above 0.07 density) with a deep trough in-between these (below 0.04 density). Once a histogram passes this test, a threshold is determined by identifying the lowest density between the peaks of the histogram. The Minimum-Point (MP) threshold is chosen to curtail the number of misclassifications. It is unlikely to represent the full water extent, however selecting a higher threshold will result in increased land misclassification. A similar threshold selection strategy was utilised by Martinis *et al.* (2009) and Matgen *et al.* (2011).

The addition of an object-based region growing element has been implemented to account for additional pixels at the edge or within an identified water body that may be missed by the MP threshold. To help identify these features, a second set of relationships between incidence angle and local threshold have been identified using Otsu's thresholding. Generally, Otsu's algorithm will tend to select a higher threshold than other thresholding methods, resulting in a greater proportion of water pixels being correctly classified at the cost of increased misclassification of land as water (Landuyt *et al.*, 2018). For each lake sub-region that has an MP threshold determined, an Otsu threshold is also calculated. As this step is targeted at increasing the identified water extents, locations that produce a lower Otsu's threshold value than the MP threshold are removed from both relationships as potentially spurious.

For each polarisation, linear relationships are calculated to describe the variations in both MP and Otsu thresholds with incidence angle, based on the collective local threshold values. The derived linear equations are applied to a raster containing incidence angle data for each orbit track, creating a continuous variable threshold dataset which is used to segment each flooded SAR image. This results in a separate MP and Otsu water extent datasets for each polarisation. The region growing process uses the water pixels identified in the MP flood maps as seeds to identify and extract any overlapping flood polygons produced by the variable Otsu's threshold. By restricting the inundation identified by the Otsu's algorithm to locations previously identified as likely to be water, the procedure maximises the inclusion of correct water pixels whilst minimising the incorrect classification of land away from the flood areas.

Similarly to the initial study, the CDAT and thresholded flood areas are combined to create a polarisation specific flood map. To be included in these maps a pixel has to be identified as flooded by both techniques, meaning it shows the properties of having a low backscatter and has also experienced a large negative shift in backscatter that represents the change in land cover that flooding causes.

One of the potential improvements identified from the initial study is the production of a single flood map, instead of separate extents for each polarisation. The merging of the polarisation specific flood maps is achieved using an object-based approach. Where regions of inundation have been identified in both polarisations, the maximum extent of the overlapping flood locations is used. If flooding is only identified in a single polarisation, then it is disregarded. This helps remove two sources of polarisation specific misclassification. Firstly, VV imagery has a greater susceptibility to wind roughening of the water surface (Manjusree *et al.*, 2012). Selecting the maximum extent allows any gaps within the VV extent to be filled with correctly identified flooding from the VH imagery. Cross-polarised data (VH) often has increased volume scattering from vegetation, producing a wider range of land backscatter values that can overlap with the expected water backscatter values (Twele *et al.*, 2016). This can cause false-positive flood identification within the VH imagery. By combining the data and requiring flooding within a region to have been identified within both polarisations, the majority of misclassifications found in the VH polarisation are removed.

The spatial resolution of Sentinel-1 imagery is such that there is potential for identifying partially flooded fields. The pixel resolution of 10 meters suggests that any surface water larger than 100 m^2 can be extracted. However, there is much uncertainty in doing this due to speckle artefacts that may persist, and consideration is needed when identifying small scale floods as to whether the low value assigned to a pixel is water or remnants of speckle. It is likely that the larger the area of flooding the more confidence the user can have in it being a correctly identified water body. With this in mind, the final flood maps have been created with the assumption that flood regions of or below 3 x 3 pixels (900 m^2) in size are flagged as uncertain, and removed due to their relatively small size.

5.5. Results

5.5.1. Variable Thresholding Relationships

The histogram of each SAR sub-region had to pass a bimodality test before local thresholding is undertaken. Examples of histograms that passed and failed this test are shown in Figures 5.4, 5.5 and 5.6. Table 5.2 summarises the percentage of sub-regions deemed adequately bimodal across both polarisations for each orbit track. On average 45% of histograms passed the bimodality test in both polarisations. The combined VH and VV datasets ended up with 267 and 268 local thresholds to build a relationship on respectively, although the number from each specific orbit track varied. Common reasons for histograms failing the bimodality test include; more than two histogram peaks above the density threshold, often caused by more than a single distinct dry land cover being present, such as urban and agricultural locations (Figure 5.6); less than two clear histogram peaks, caused by reduced land pixels within the sub-region due to the filtering of high topography areas; and the trough between the peaks not being defined enough, such as in Figure 5.5.

The local thresholds have been used to determine linear relationships to describe how the land-water threshold value varies with incidence angle. Figures 5.7 and 5.8 show the derived MP variable thresholds for VH and VV polarisation respectively. When viewed individually, all orbit tracks follow a similar trend apart from orbit 81, which displays an increasing threshold value with incidence angle, instead of the expected decreasing relationship, as observed in other orbits. This is likely caused by the small number of thresholds used to develop this relationship (n = 9), which are located across a relatively narrow portion of the Sentinel-1 image swath. Orbit 52 covers the near range of incidence angles, and displays a slightly steeper trend than the combined relationship. In the VH polarisation for this orbit, there is a cluster of points with lower threshold values located at 36-37°, which may be causing a drawdown effect on the linear relationship presented. Orbit 30 covers the far range half of a swath and shows a similar trend to the combined linear relationship. As shown in Figure 5.2, orbits 132 and 154 cover a large proportion of the study area and subsequently can build a relationship across the majority of the Sentinel-1 swath width. These trends closely follow the overall relationship, with orbit 132 predicting slightly higher threshold values and orbit 154 showcasing slightly lower relationship than the combined trend.

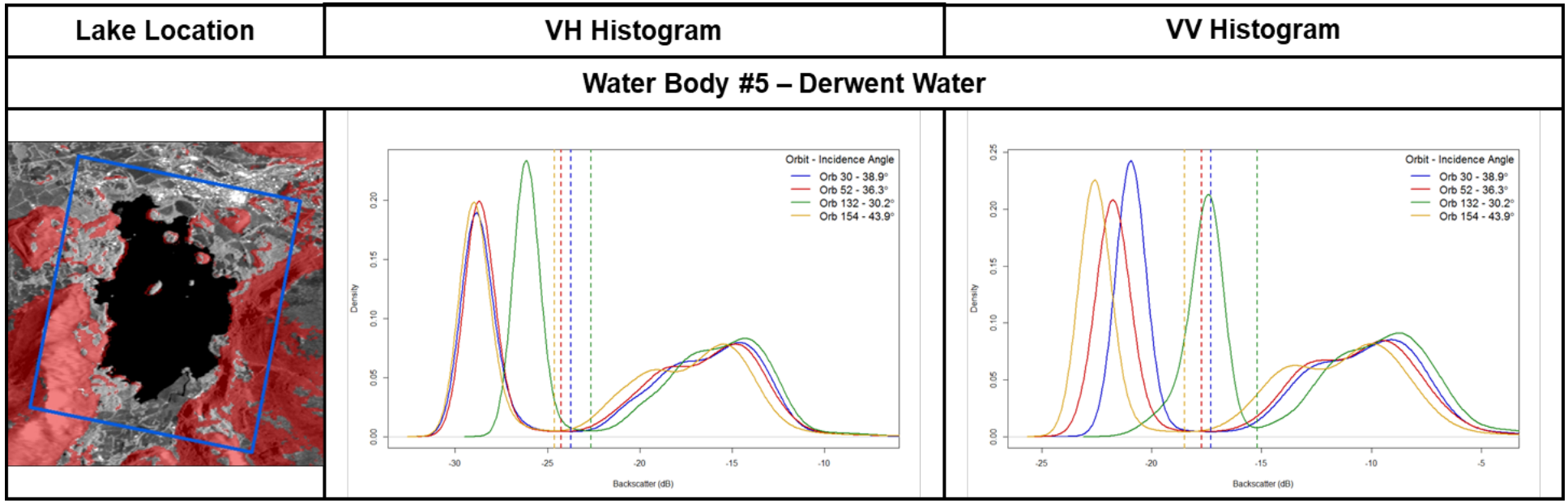

[108]

Figure 5.4. Local histogram thresholds for Derwent Water. From left, area of interest around water body (blue) with masked regions (red), VH polarisation histograms for each orbital track with chosen MP thresholds displayed, and the same plot for VV polarisation.

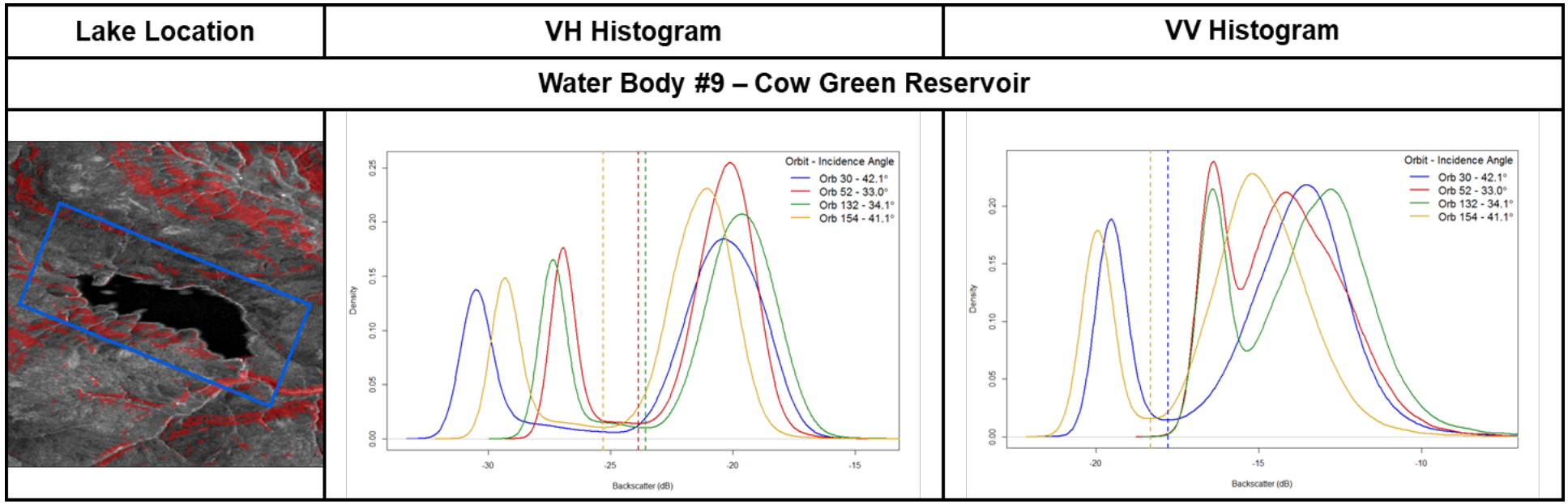

[109]

Figure 5.5. Local histogram thresholds for Cow Green Reservoir. From left, area of interest around water body (blue) with masked regions (red), VH polarisation histograms for each orbital track with chosen MP thresholds displayed, and the same plot for VV polarisation. No threshold is shown for orbit 30 in VH, which produced an Otsu threshold lower than the MP threshold, and orbits 52 and 132 for VV, which failed the histogram bimodality test by not having a low enough trough between the visible peaks.

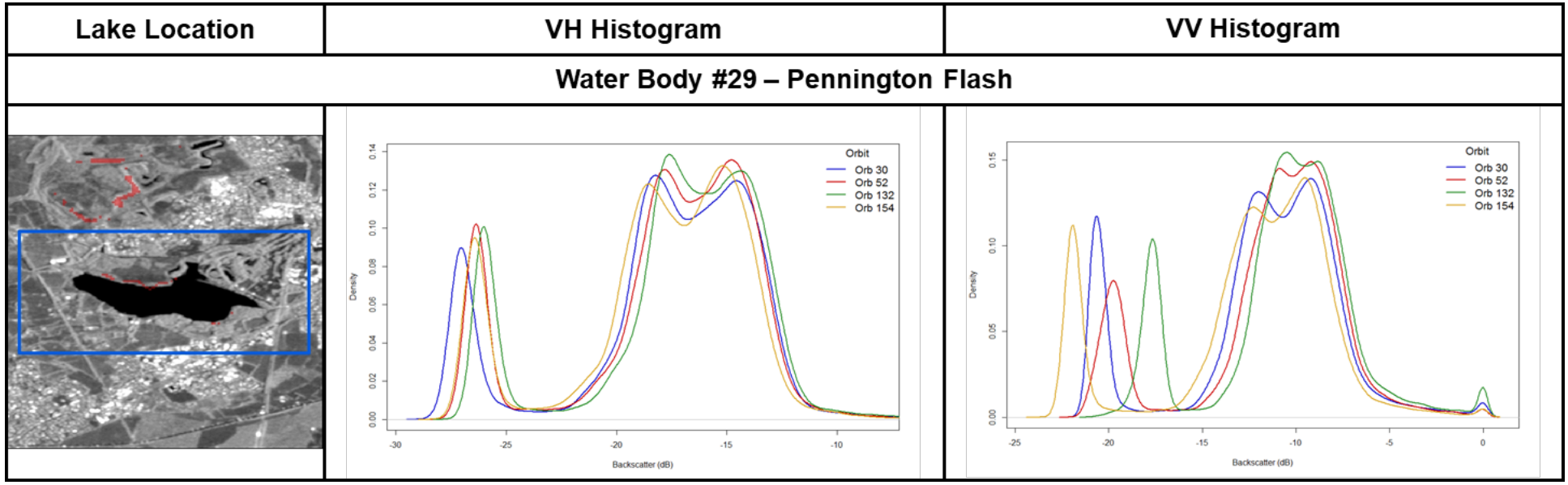

[110]

Figure 5.6. Local histogram thresholds for Pennington Flash. From left, area of interest around water body (blue) with masked regions (red), VH polarisation histograms for each orbital track, and the same plot for VV polarisation. Due to the triple peaked nature of the histograms the bimodality test was not passed, and no thresholds are calculated for this lake for any of the orbit tracks in either polarisation.

Orbit	Pass Bimodality Test		Max. Num. Lakes	VH%	VV%
	VH	VV			
30	66	77	141	46.81	54.61
52	52	42	99	52.53	42.42
81	9	9	32	28.13	28.13
132	73	66	136	53.68	48.53
154	67	74	149	44.97	49.66
Total	**267**	**268**	**557**	**45.22**	**44.67**

Table 5.2. Number of image subsets that's passed the bimodality test.

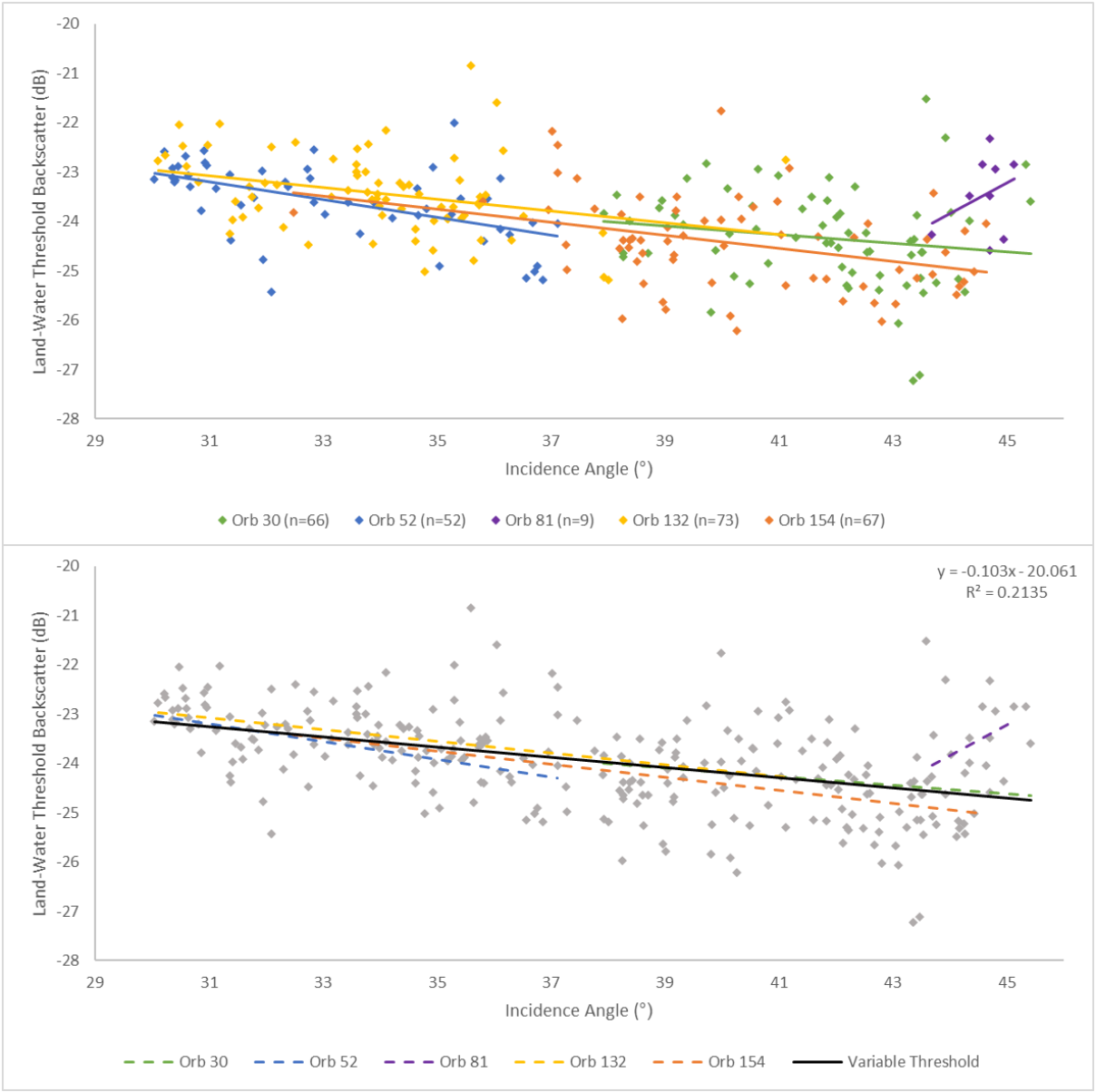

Figure 5.7. Relationships between incidence angle and identified MP thresholds for each orbital track (top) and as a combined dataset (bottom) for VH polarisation. Equation and R^2 values refer to the final variable threshold.

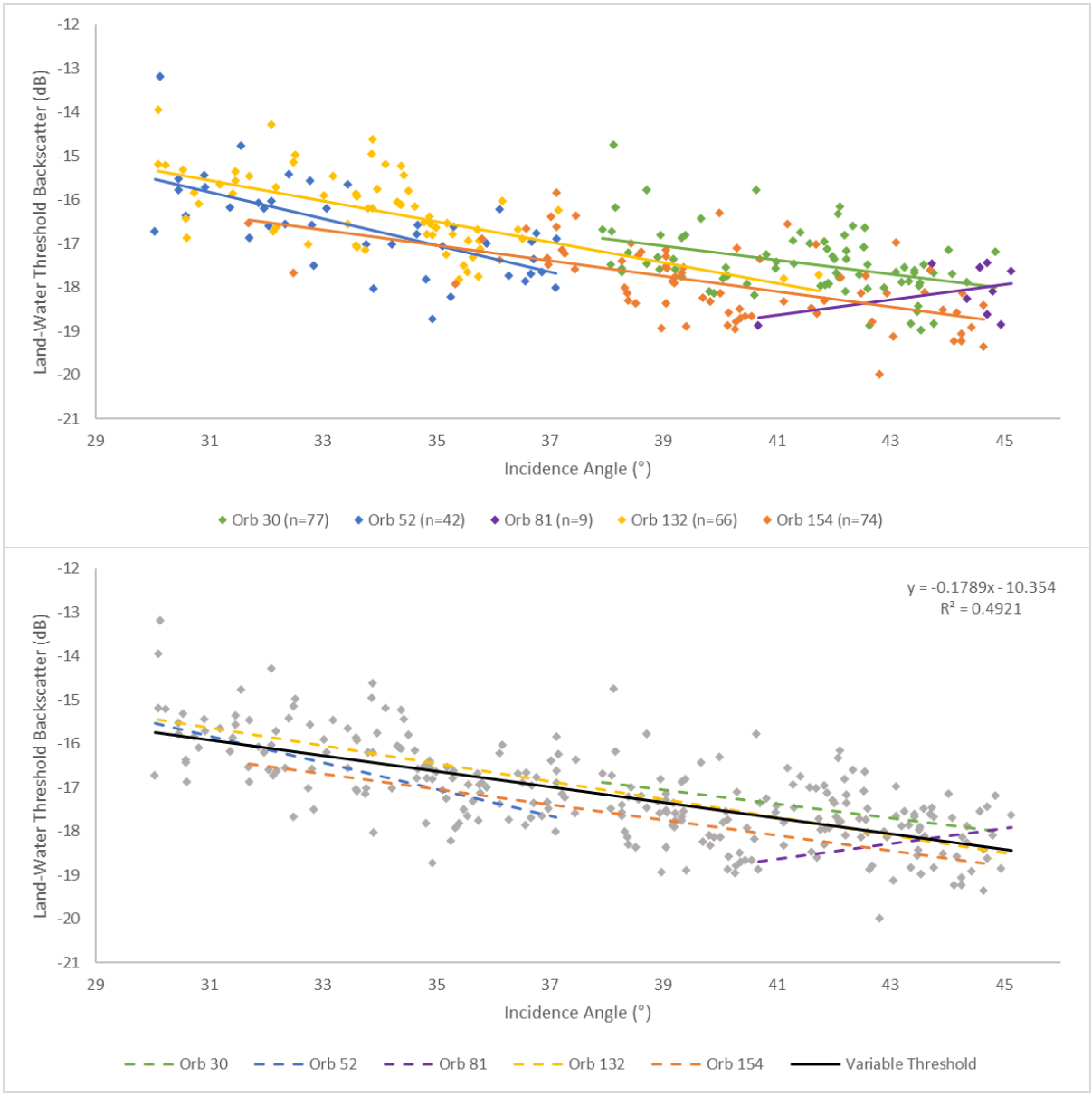

Figure 5.8. Relationships between incidence angle and identified MP thresholds for each orbital track (top) and as a combined dataset (bottom) for VV polarisation. Equation and R^2 values refer to the final variable threshold.

The combined dataset, containing all data points from each of the orbit tracks, provides a good spread of values across the full range of Sentinel-1 incidence angles from which to base the linear relationship upon. R^2 values for the VH and VV combined relationships are 0.214 and 0.492 respectively. The improved R^2 value in VV polarisations represents the reduced variability in threshold values, likely caused by the more stable backscatter response from land surfaces compared to cross-polarised data. For example, a large spread in local thresholds can be seen around 36° and above 43° for VH, whilst for VV the greatest spread is seen at 30°, and a small number of outliers at 38°. Despite the reduced R^2 value, the relationship

between the incidence angle and local threshold backscatter value is considered good for VH polarisation.

Figure 5.9 shows the difference in linear relationships for the MP and Otsu variable thresholds. As expected the trends between the two thresholding techniques are similar, with the only noticeable difference being a slightly steeper slope on the Otsu linear trend in the VV polarisation. R^2 is consistent in VV polarisation between the two threshold types, however, there is a reduced R^2 value for the Otsu relationship in the VH polarisation, down to 0.118. On average, Otsu threshold values are 1.41 dB and 1.55 dB higher for VH and VV polarisation than their MP threshold counterparts.

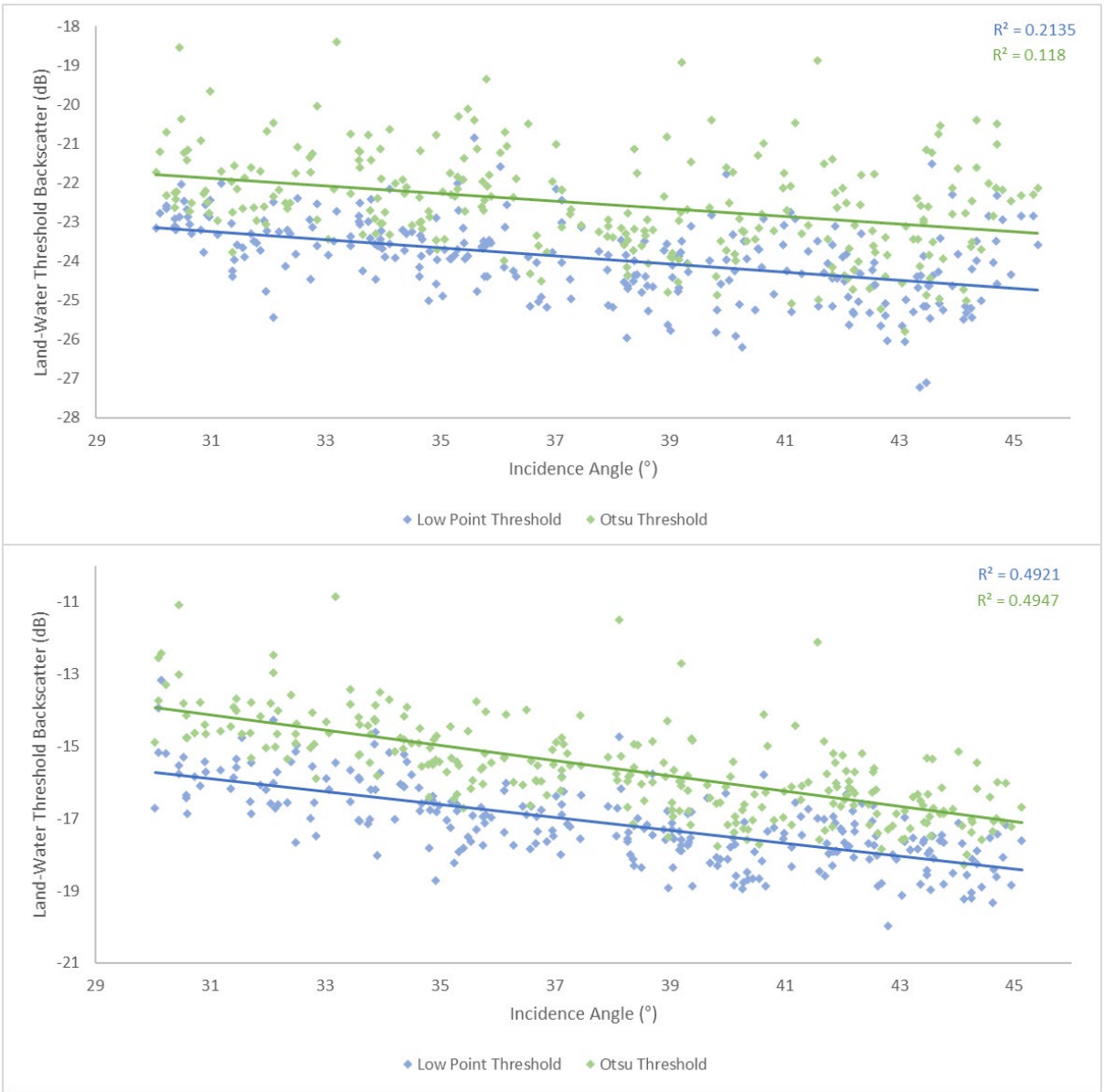

Figure 5.9. Comparison of the relationship between MP and Otsu local threshold values and incidence angle for VH (top) and VV (bottom) polarisations.

5.5.2. Validation

5.5.2.1. Optical Imagery

Contingency matrices and validation statistics have been calculated for 26 sub-regions across the main body of flooding within the Ouse catchment (Figure 5.3), with the average accuracy metric values presented in Table 5.3. The Sentinel-1 flood mapping algorithm performs well, with an average PA_f of 77.69%, UA_f of 95.39%, TA of 89.59%, and a CSI of 74.68%. The mean Cκ is calculated as 0.760.

	Ch. 5 Flood Maps			Ch. 4 Flood Maps (VH)			Ch. 4 Flood Maps (VV)		
	Min.	Mean	Max.	Min.	Mean	Max.	Min.	Mean	Max.
PA_f	52.78	77.69	92.32	52.17	74.64	90.13	47.42	73.73	91.32
UA_f	78.20	95.39	99.63	93.03	96.44	99.42	95.94	97.55	99.55
TA	77.13	89.59	96.73	76.04	88.70	93.83	74.91	88.76	93.65
CSI	51.92	74.68	91.31	50.46	72.76	89.65	46.93	72.35	90.65
Cκ	0.528	0.760	0.929	0.506	0.732	0.862	0.480	0.731	0.852

Table 5.3. Accuracy statistics for validating SAR derived flood extents (from Chapters 4 and 5) against MNDWI Sentinel-2 flood maps. (Ch. 5 Flood Maps, n = 26; Ch. 4 Flood Maps, n = 9).

Nine of the validation sub-regions overlap with the polarisation specific flood maps produced in Chapter 4. Values for the accuracy descriptors have been recalculated for these locations to allow for comparison to the results from this chapter. The updated flood mapping algorithm presented in this chapter provides an improvement for PA_f (an increase of 3.05% for the average values), TA (0.83%), CSI (1.92%) and Cκ (0.03). However, average values for UA_f have decreased by between 1.04% (VH) and 2.15% (VV). If only the 9 sub-regions that cover the polarisation specific maps are used, the average UA_f for the results from this chapter increases to 96.89%, an improvement on the VH value but still below the VV score by 0.66%. One sub-region, located in the upper reaches of the River Derwent (number 22 in Figure 5.3), has a particularly low UA_f value of 78.20%. VV flooding at this location closely matches the optical imagery, however, the VH identifies a larger number of pixels as inundated. Due to the overlap between the polarisations, the larger VH extent is selected for the final flood map, lowering the UA_f score when compared to the optical imagery.

Using optical imagery for identifying flooding is subject to uncertainty, which can result in a reduction in reported accuracy when being used as a reference dataset

against SAR flood extents. The methods used in this chapter produce different map types from the two sources of imagery. A surface water map is produced from the optical imagery and a flood map from the SAR data, due to permanent water bodies being removed via change detection. To account for the difference in map type, additional accuracy metrics are calculated with permanent water locations removed from the reference dataset (Table 5.4). The adjustment to the reference dataset has resulted in improved validation results for PA_f, TA, and CSI, with a slight increase in $C\kappa$, and UA_f remaining consistent. The minimal change to UA_f is expected, as the metric reports the amount of the SAR derived flooding that is similarly classed in the reference dataset. The SAR flood maps contain minimal permanent water bodies, with the slight changes in UA_f coming from the removal of these areas to match the masking applied to the reference dataset.

	With Perm. Water			No Perm. Water			Change		
	Min.	Mean	Max.	Min.	Mean	Max.	Min.	Mean	Max.
PA_f	52.78	77.69	92.32	51.79	80.06	92.84	-0.99	2.37	0.52
UA_f	78.20	95.39	99.63	78.01	95.34	99.61	-0.19	-0.06	-0.02
TA	77.13	89.59	96.73	77.75	91.03	97.06	0.62	1.44	0.33
CSI	51.92	74.68	91.31	50.94	76.88	91.77	-0.98	2.20	0.46
$C\kappa$	0.528	0.760	0.929	0.528	0.791	0.935	0.000	0.030	0.006

Table 5.4. Validation statistics for SAR derived flood extents against MNDWI Sentinel-2 flood maps, with and without locations of permanent water bodies removed, and the subsequent change in values.

The lowest TA (77.75%) and CSI (50.94%) scores occur at region 12, located at Tadcaster. The TA and CSI are caused by the low PA_f of 51.79%. $C\kappa$ is similarly low, scoring 0.528. Visual inspection of the location highlights the high number of buildings in the surrounding area. These are likely to cause an increase in backscatter due to the double bounce effect, resulting in flooding not being identified in the SAR imagery. The improved identification of water in the optical imagery due to the nadir viewing angle of the sensor results in the poor validation statistics observed.

The relationship between each validation metric score and proportional flood area within each sub-region is shown in Figure 5.10. This shows two different relationships. TA and UA_f values remain consistent irrespective of the amount of flooding in the validation area, whilst PA_f and CSI statistics increase with the

proportion of the region that is flooded. Not shown is Cκ, which matches the trend shown by UA$_f$. Within this study, the validation areas have been manually selected to provide a variety of hydrological situations and good geographical coverage across the identified inundations. This is intended to give a good indication of the accuracy of the flood maps by averaging out any skewing of the results due to flood coverage within a single region.

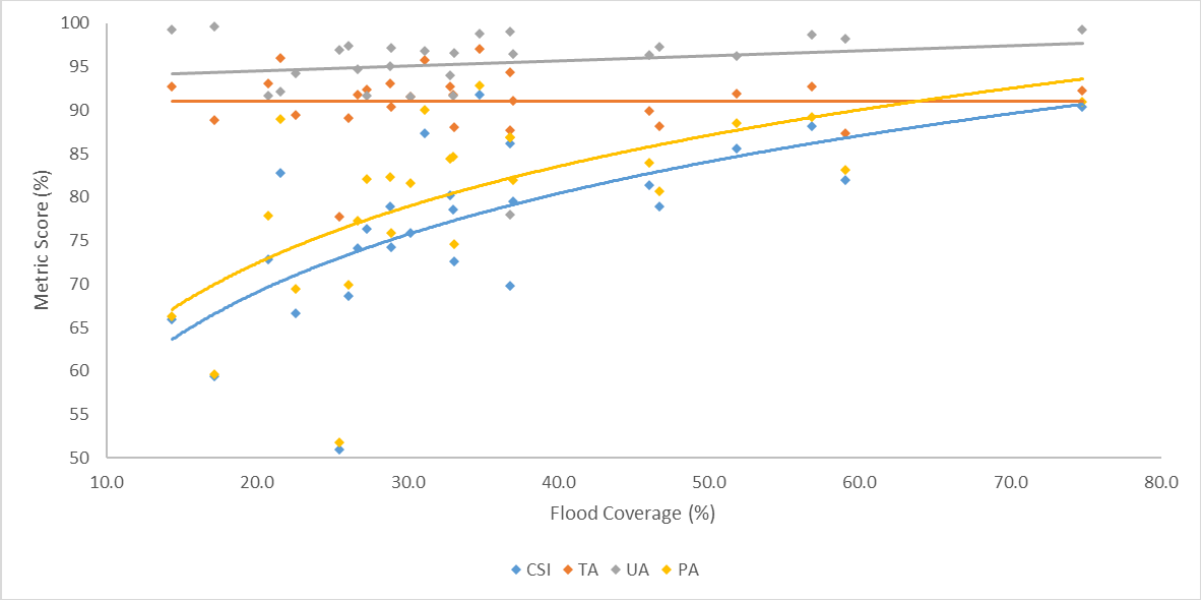

Figure 5.10. Changes in validation metric scores with percentage of region flooded.

5.5.2.2. CEMS Flood Maps

The CEMS flood map has been used to validate the derived results in two separate ways. Firstly, they have been validated against the Sentinel-2 MNDWI reference water extent, with the produced metrics compared to those obtained from the Sentinel-1 flood maps. Secondly, the CEMS flood extents have been used as the reference dataset to ascertain the agreement between the two SAR derived flood maps. The CEMS flood maps are covered by 10 of the validation sub-regions.

The validation statistics for the CEMS flood maps against the MNDWI reference data are similar to those obtained from the Sentinel-1 flood mapping (Table 5.5). The CEMS flood extent has superior scores for UA$_f$ and TA, whilst the Sentinel-1 inundation maps have higher values for PA$_f$, CSI and Cκ. Only PA$_f$ and CSI show a difference greater than 1%. TA is 91% for both datasets, and CSI is 76.88% and 75.64% for the Sentinel-1 and CEMS data respectively. Similar ranges of values are presented across the two datasets. The CEMS dataset does not cover the region of

poorest validation results for the Sentinel-1 flood maps (location 12). However, low statistical accuracy can be found in the region north of York (location 8), with poor CSI values in both the CEMS and the Sentinel-1 results (49.43% and 59.43% respectively) driven by low PA_f (49.62% and 59.56%). However, unlike at location 12, TA is relatively high (86.02% and 88.81%) due to UA_f values above 99%. Cκ values are low, with 0.585 for CEMS and 0.679 for Sentinel-1. Location 8 is in a similar setting to location 12, with a high number of tall features, including buildings and trees, surrounding the identified flood locations, which mask the specular reflection of the radar signal.

	Ch. 5 Flood Maps			CEMS Flood Maps		
	Min.	Mean	Max.	Min.	Mean	Max.
PA_f	51.79	80.06	92.84	49.62	78.08	92.88
UA_f	78.01	95.34	99.61	91.75	96.16	99.27
TA	77.75	91.03	97.06	86.02	91.36	96.94
CSI	50.94	76.88	91.77	49.43	75.64	90.77
Cκ	0.528	0.791	0.935	0.585	0.779	0.929

Table 5.5. Comparison of accuracy metric scores from Sentinel-1 SAR and RADARSAT-2 CEMS flood extents, both validated against Sentinel-2 flood maps. (Ch. 5 Flood Maps, n = 26; CEMS Flood Maps, n = 10).

Table 5.6 shows the results of using the CEMS dataset as a reference for validating the Sentinel-1 inundation maps. The average PA_f of 91.65%, UA_f of 92.21%, TA of 95.46%, CSI of 84.93% and 0.878 Cκ highlight good agreement between the datasets. Differences between the results can be attributed to a higher resolution in the CEMS dataset, differences in SAR viewing geometry, and processing induced variability in derived flood extent.

	CEMS			MNDWI		
	Min.	Mean	Max.	Min.	Mean	Max.
PA_f	84.61	91.65	97.88	51.79	80.06	92.84
UA_f	79.38	92.21	96.02	78.01	95.34	99.61
TA	93.96	95.46	96.89	77.75	91.03	97.06
CSI	76.14	84.93	93.85	50.94	76.88	91.77
Cκ	0.841	0.878	0.926	0.528	0.791	0.935

Table 5.6. Accuracy assessment of the SAR derived flood extents against CEMS flood maps, and how metrics compare to validating the Chapter 5 results against the MNDWI data.

5.5.3. Catchment Scale Flood Dynamics

Results are presented below for a selection of the catchments shown in Figure 5.1. The catchments not displayed show similar trends in flood extent in relation to river stage and the onset of named storms to those detailed below. Further time series plots are provided in Appendix B. It should be noted that spurious flood detection due to snow and frost is discussed in Section 5.5.4., and suspect data points caused by these mechanisms, notably the peak across many catchments on 15th Jan, are not discussed in detail in the following catchment analysis sections.

5.5.3.1. River Ouse

Figure 5.11 shows the amount of flooding in the Ouse catchment compared to river stage data from Myton Bridge, Newton-on-Ouse and Cawood, which are distributed along the Ure-Ouse River from upstream to downstream. The second-largest peak in flood extent (after 15th Jan) is found on the 29th Dec, in the aftermath of Storms Eva and Frank. The large extent of flooding is identified despite the satellite image only covering 63% of the catchment (orbit 81 in Table 5.1). The peak in flood extent does not coincide with the peak stage, with the satellite image captured 35 and 41 hours after peak flows at Myton Bridge and Cawood respectively. The Newton-on-Ouse stage records are missing from this time, likely due to the high flows being outside the operating parameters of the gauging instrument. The previous satellite image on the 27th Dec was acquired closer to peak flows, however, only a quarter of the catchment is imaged from this orbit (number 52), resulting in the small amount of flooding shown in Figure 5.11 at this time. When studying large catchments such as the Ouse, care is needed when interpreting flood extent dynamics due to the different location and extent of coverage from each orbit. Identifying correlations between the stage record and the flood extents in the Ouse is challenging due to the variations in coverage, with only some of the peaks in the gauge data displaying corresponding inundation growth in the flood maps.

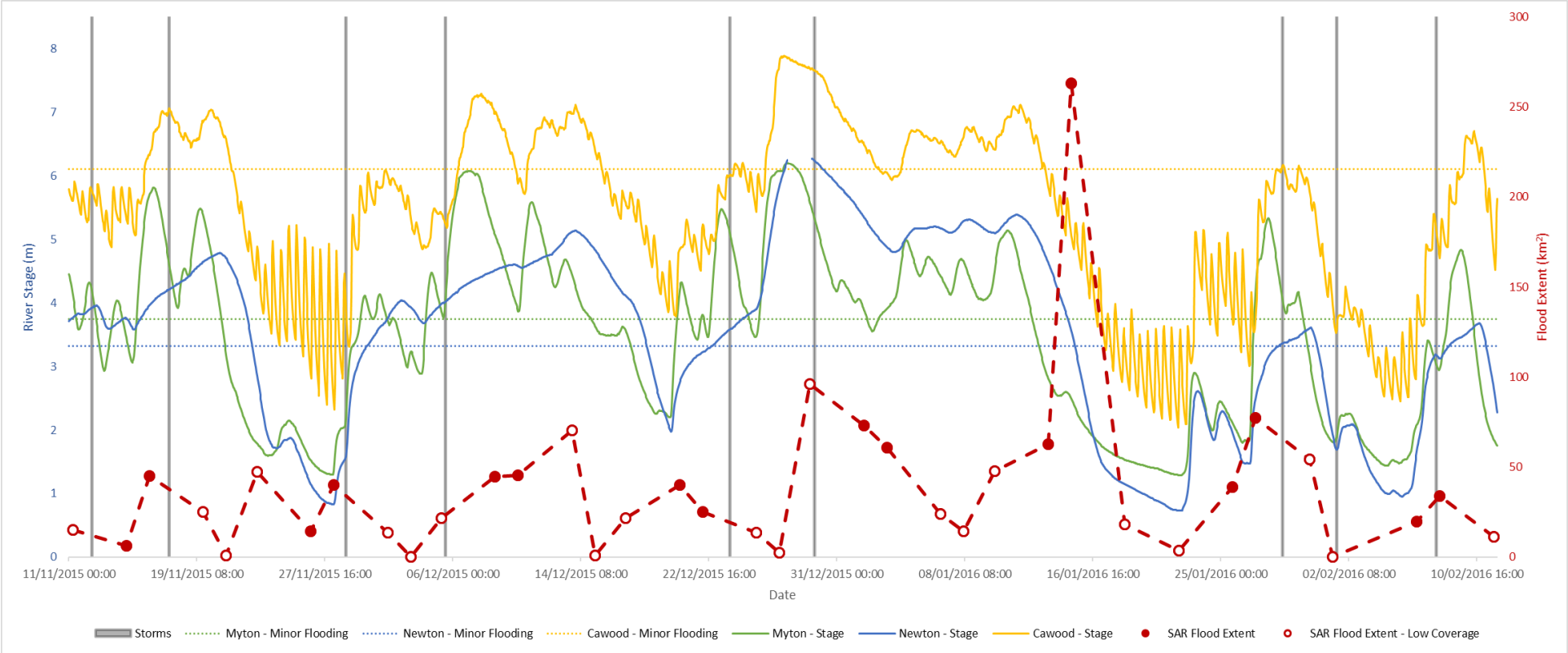

Figure 5.11. The amount of flooding identified in the Ouse catchment compared to river stage at the Myton Bridge, Newton-on-Ouse and Cawood gauges between 11th Nov 2015 and 11th Feb 2016. Low coverage (less than 70% of catchment) SAR images shown as unfilled data points. Approximate start period of named storms (from left, Abigail, Barney, Clodagh, Desmond, Eva, Frank, Gertrude, Henry and Imogen) shown for reference. Threshold for minor flooding occurrence taken from Environment Agency gauge information.

[119]

[120]

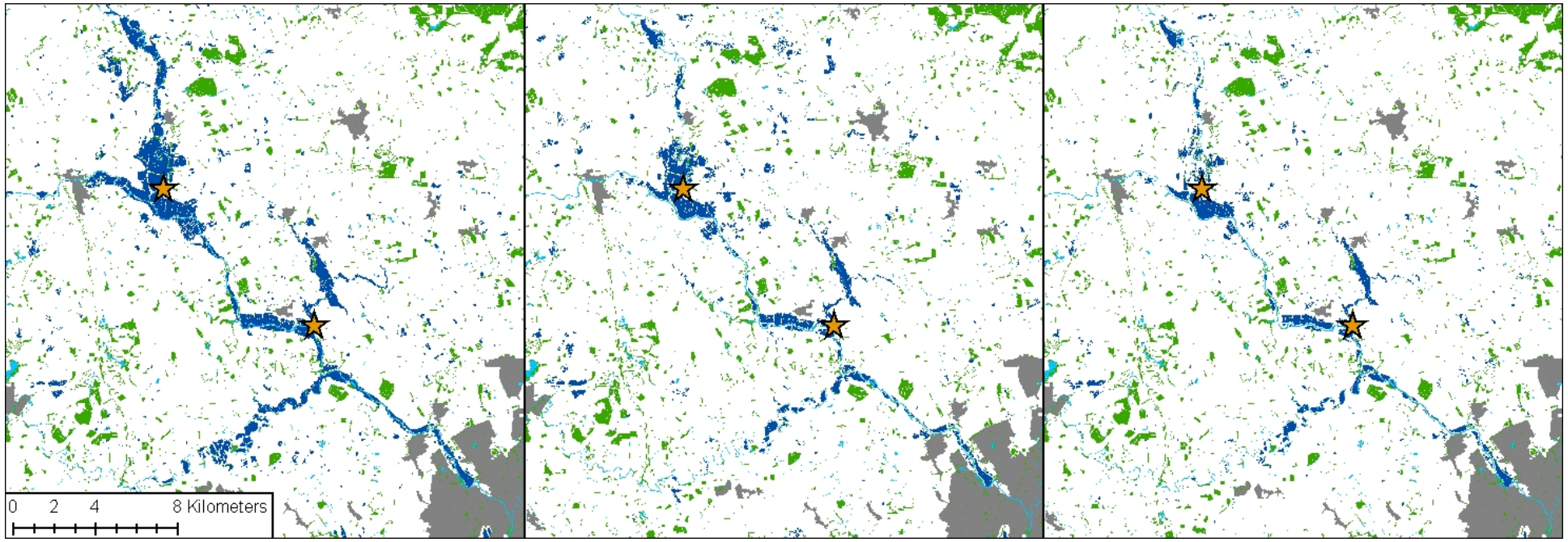

Figure 5.12. Peak flood extent along the River Ure/Ouse and its tributaries located north of York (29th Dec (left)), and the following images (1st Jan (middle) and 3rd Jan (right)) showing the recession of flood waters. Inundated areas identified in dark blue. Urban areas shown in grey, woodland regions in green and permanent water bodies in light blue. Myton Bridge (upper) and Newton-on-Ouse (lower) gauges highlighted by the orange star.

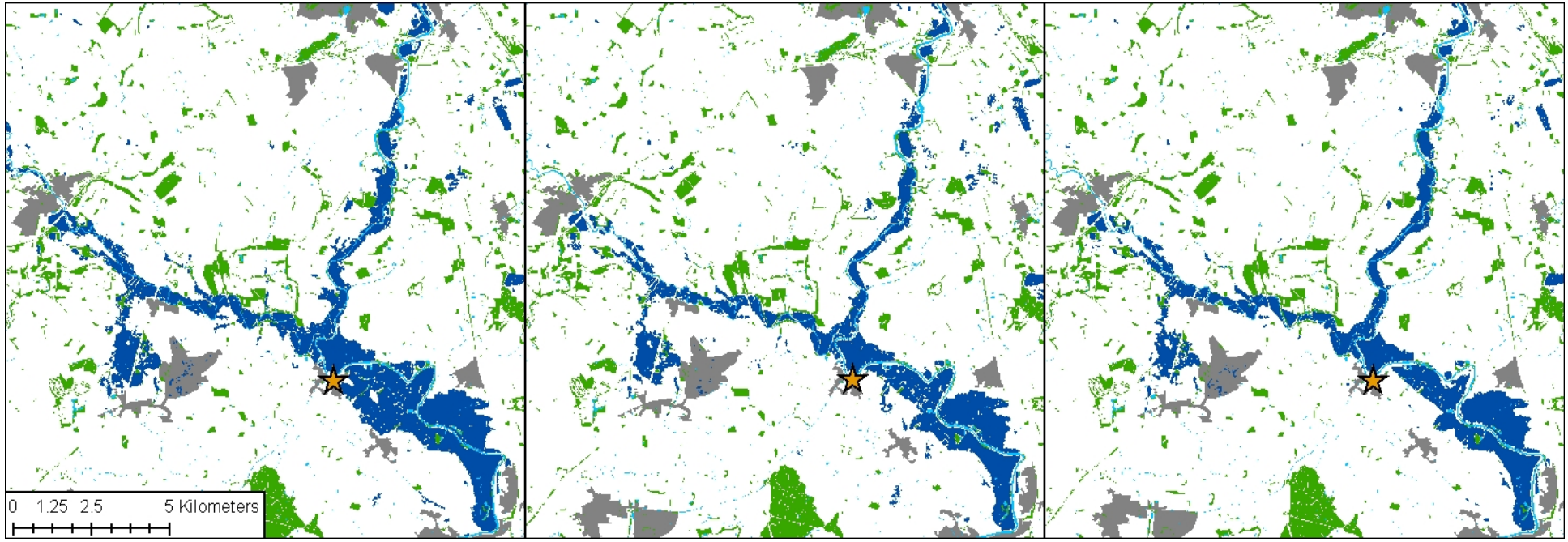

Figure 5.13. Peak flood extent along the River Ouse and its tributaries located south of York (29th Dec (left)), and the following images (1st Jan (middle) and 3rd Jan (right)) showing the recession of flood waters. Note the greater temporal consistency of flooding in these locations compared to north of York (Figure 5.12). Inundated areas identified in dark blue. Urban areas shown in grey, woodland regions in green and permanent water bodies in light blue. Cawood gauge highlighted by the orange star.

The Ouse catchment is the largest within the study and has numerous locations throughout the catchment that suffer from significant flooding. The flood extent during the aftermath of Storms Eva and Frank along the main watercourses, the River Ure and River Ouse, are shown in Figures 5.12 (north of York) and 5.13 (south of York). Extents from three dates are shown, with 29th Dec representing the largest inundation extent, with 1st and 3rd Jan showing the flood retreat. At the maximum extent, extensive inundation is observed along the floodplains of the main river and its tributaries. Significant flooding is observed around river confluences throughout the catchment, with inundation propagating upstream and downstream of where the rivers merge. The spatial and temporal consistency of the extreme rainfall inputs throughout the catchment ensure that all rivers are at capacity, causing these localised inundation maxima at confluences.

The two sections of the river display different rates of water recession. The upstream portion of the river displays a faster decrease in flood extent (Figure 5.12). There is a clear visible retreat of floodwater at locations that have experienced greater localised flooding, such as river confluences. For example, around the Ure-Swale confluence in the north of Figure 5.12, the local flood extent on the 3rd Jan is only 40% of that observed on the 29th Dec.

Further downstream flooding is more temporally consistent, with only 30% of water extent being lost for the region shown in Figure 5.13 across the 6 days (29th Dec to 3rd Jan). Furthermore, the majority of this change has occurred by the 1st Jan, showing a more rapid initial retreat before the catchment hydrology becomes more stable, with the input of floodwaters from further upstream equating to the rate of water output at this time. A large proportion of the flooding in this area is still visible on the 15th Jan, before dissipating by the image captured on the 18th Jan (partial coverage) and the 25th Jan (full coverage). Flooding south of York can be divided into three main locations; the River Wharfe, the River Ouse upstream of the confluence, and the downstream section of the Ouse. The main location of initial water retreat is found in the latter of these, to the south-east of the marked gauge location.

There are some locations within the Ouse catchment that suffer from consistent inundation throughout the study period. Figure 5.14 shows the number of images where flooding has been identified along the River Derwent (with a total of 30

covering the location), with similar flood-prone locations being found throughout the catchment. The temporal consistency of flooding along the River Derwent varied spatially, with more flood-prone sections being inundated for two-thirds of the available images, compared to other sections which are only inundation for a third of the images. Although the maximum extent is often reported in the media as the greatest cause of disruption, prolonged inundation or constant rewetting can extend disruption to homeowners, businesses and agriculture. The winter of 2015-16 brought numerous rainfall events, which individually may not have resulted in flooding. However, the successive nature of the storms resulted in precipitation falling on saturated ground, causing additional water being added to a hydrological system at capacity, increasing overall inundation time.

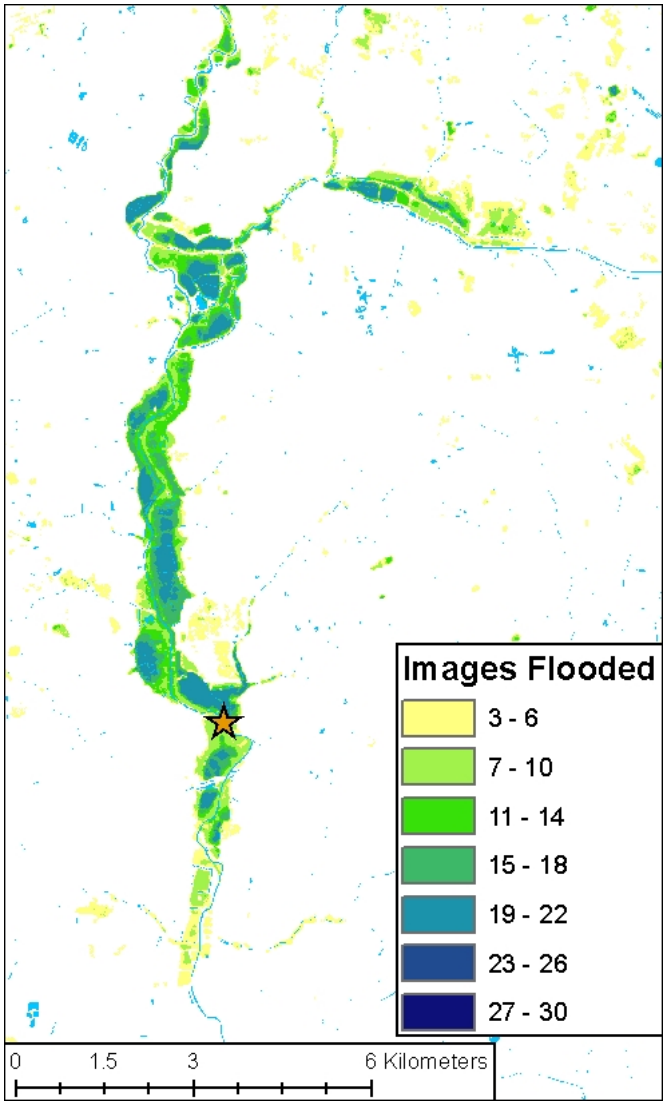

Figure 5.14. Number of satellite images with flood identified between 11th Nov 2015 and 11th Feb 2016 along the River Derwent in the Ouse catchment. Locations flooded in two or less images are not shown. Permanent water bodies are shown in light blue. Bubwith gauge highlighted by the orange star.

5.5.3.2. River Aire

There are two main regions impacted by flooding in the Aire catchment. The first is in the upper portion of the river around the Snaygill gauge, and the second is located downstream near the Beal gauge. Despite being smaller than the Ouse catchment, two of the satellite orbits similarly provide reduced coverage in the Aire catchment. Orbits 52 and 81 each only image 35% of the catchment, with orbit 52 capturing the upstream portion of the Aire (including Snaygill gauge), and orbit 81 the downstream reaches (including Beal gauge). Peaks in the amount of inundation are observed on the 16th Nov, 1st Dec and 13th Dec, all of which correspond well to the observed river stage at the two gauges. The largest flood event occurred in late December from the satellite imagery captured on the 27th (upstream only) to 29th (downstream only), with the greatest extent delineated on the 29th Dec (Figure 5.15). This is the result of Storm Eva, with peak river flows found at 14:00 on the 26th Dec for Snaygill and 20:00 on the 27th Dec at Beal, with the respective satellite images acquired 16 and 34 hours afterwards. Figure 5.16 shows the flood extent for the two locations for the 16th Nov, and the late December flood, and 3rd Jan. At times of peak flood (shown in the top two rows), extensive inundation is visible at both of the locations. For the 16th Nov event, the retreat of floodwaters is similar in both locations, with smaller flood bodies identified in both locations in the 21st Nov results. For the larger event after Storm Eva, floodwaters persist longer at the downstream half of the catchment, being clearly identifiable until the 15th Jan, compared to flooding only being delineated on the 27th Dec for the upstream portion of the catchment.

5.5.3.3. River Eden

Flooding in the Eden catchment is observed in two main locations, upstream in the Vale of Eden and downstream around the city of Carlisle. Figure 5.17 shows gauge data from Temple Sowerby and Sheepmount gauges, located in the respective flood-prone regions, compared to the extent of flooding in the Eden catchment. Both gauges in the Eden catchment display high river flows in the aftermath of Storm Desmond, with peak flows observed on the 5th Dec at 23:00 for Temple Sowerby, and 10 hours later for Sheepmount. No Sentinel-1 imagery is available during this period, and the image on the 8th Dec shows comparatively little flooding (4.01 km^2). Increased flooding is observed on the 10th and 13th Dec (14.63 km^2 and 20.38 km^2 respectively). River flow during this period is lower than observed on the 5th and 6th Dec, with a small peak in stage around on the 10th Dec before a continued decrease

in river height until the 18th Dec. Inspection of the flood extents on these two dates provides very different geographical locations being inundated. On the 10th Dec, flooding is observed along the river reaches around the Temple Sowerby and Sheepmount gauges (Figure 5.18). However, on the 13th Dec, there is minimal flooding in these locations, with possible inundation highlighted in upland locations to the south-west of the catchment. These results are suspect and may be false classifications due to SAR interactions with snow, with further discussion on this topic given in Section 5.5.4.

Given the comparative magnitude of the river flow, the flood extents in the immediate aftermath of Storm Desmond are likely to exceed those observed on the 10th Dec. However, the minimal inundation observed on the 8th Dec potentially means that these waters receded quickly. Alternatively, the antecedent saturated conditions prevalent along the River Eden after the Storm Desmond is likely to have exacerbated the extent of flooding observed on the 10th Dec, resulting in an increased flood extent compared to that expected if the observed precipitation and flow conditions occurred as a standalone event.

Figures 5.17 and 5.18 also show a peak in flood extent after Storm Eva on the 27th Dec, similar to those observed in other catchments. River stage is high at this time, although below the levels observed after Storm Desmond in early December. When comparing the locations of flooding on the 27th Dec to those seen on the 10th Dec, the extents located around Temple Sowerby are very similar. There is a more obvious visual difference in the downstream portion of the catchment, with a more continuous water surface observed for the 27th Dec instead of the more segmented flood locations seen on the 10th Dec. However, the maximum extents of the flood show similarities, highlighting the boundary of the floodplain. Peak flows on the 27th Dec are higher than the 10th Dec, and also align better with the acquisition of the satellite image. The difference in inundation patterns is likely a function of the water depth, with a range of depths possible in this location for the same overall water extent.

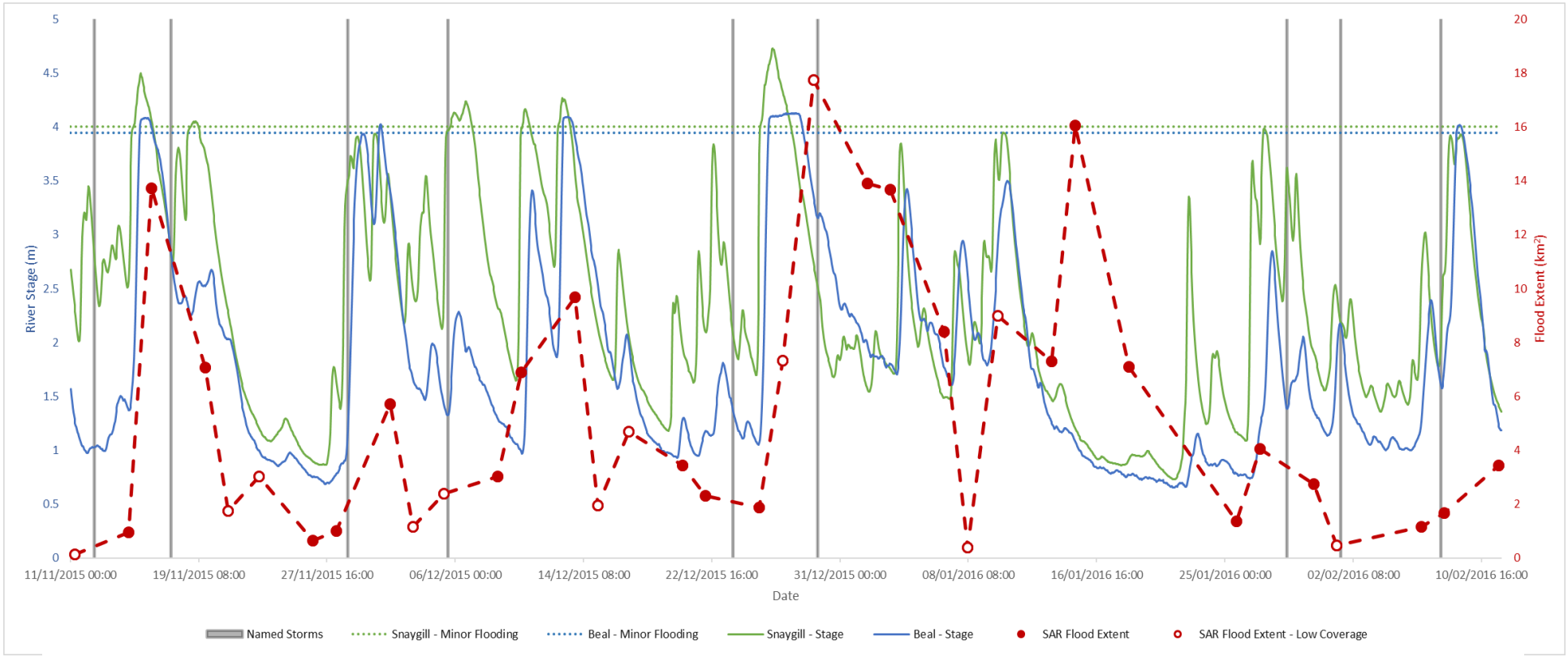

[126]

Figure 5.15. The amount of flooding identified in the Aire catchment compared to river stage at the Snaygill (upstream) and Beal (downstream) gauges between 11th Nov 2015 and 11th Feb 2016. Low coverage (less than 70% of catchment) SAR images shown as unfilled data points. Approximate start period of named storms (from left, Abigail, Barney, Clodagh, Desmond, Eva, Frank, Gertrude, Henry and Imogen) shown for reference. Threshold for minor flooding occurrence taken from Environment Agency gauge information.

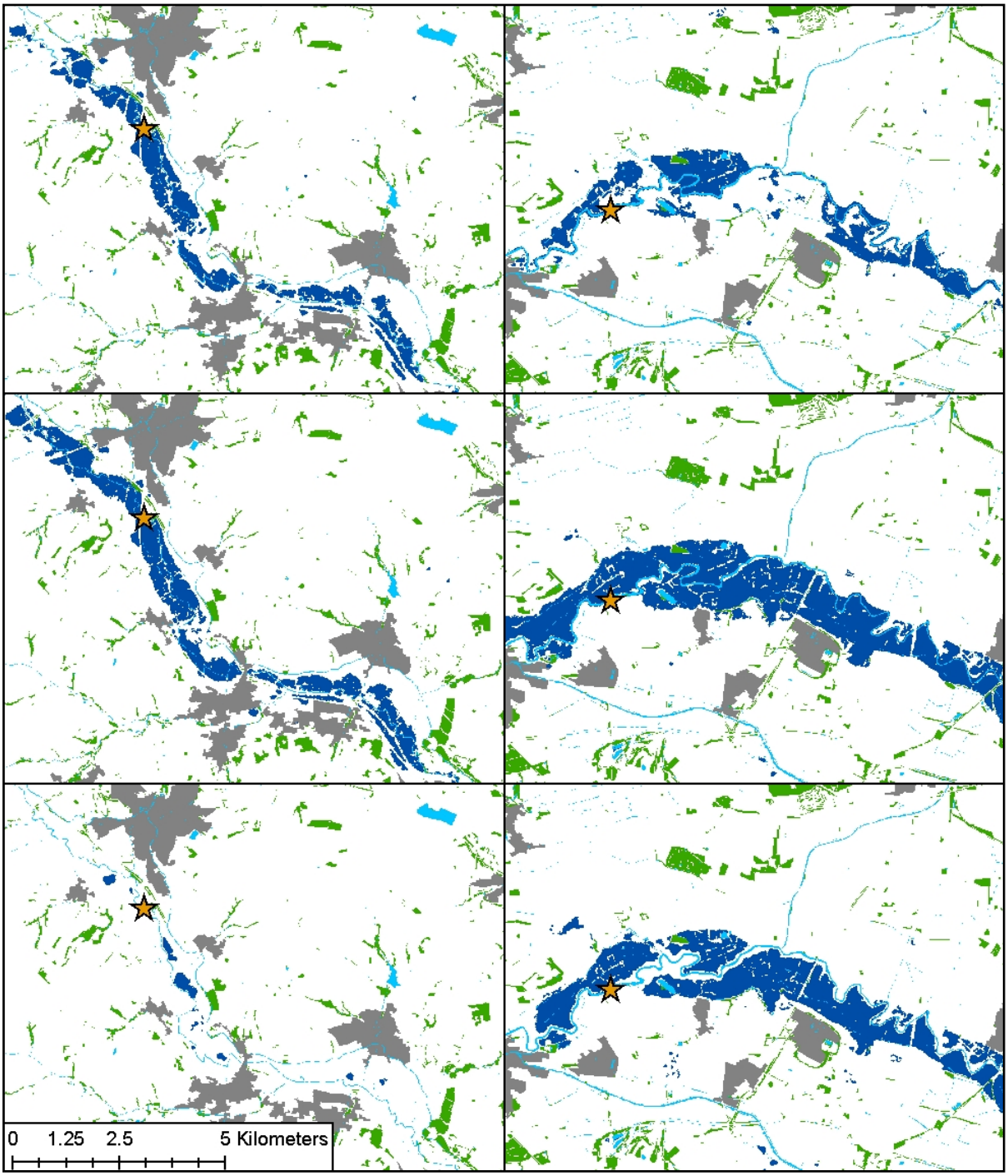

Figure 5.16. Flood extents around the Snaygill (left) and Beal (right) gauges during peak flood in the Aire catchment. Top panel shows the 16th Nov, the middle shows 27th (left) and 29th (right) Dec, and the bottom shows the 3rd Jan. Flood extents shown in dark blue, permanent water bodies in light blue, woodland locations in green and urban regions in grey. Location of gauges are shown by the orange star.

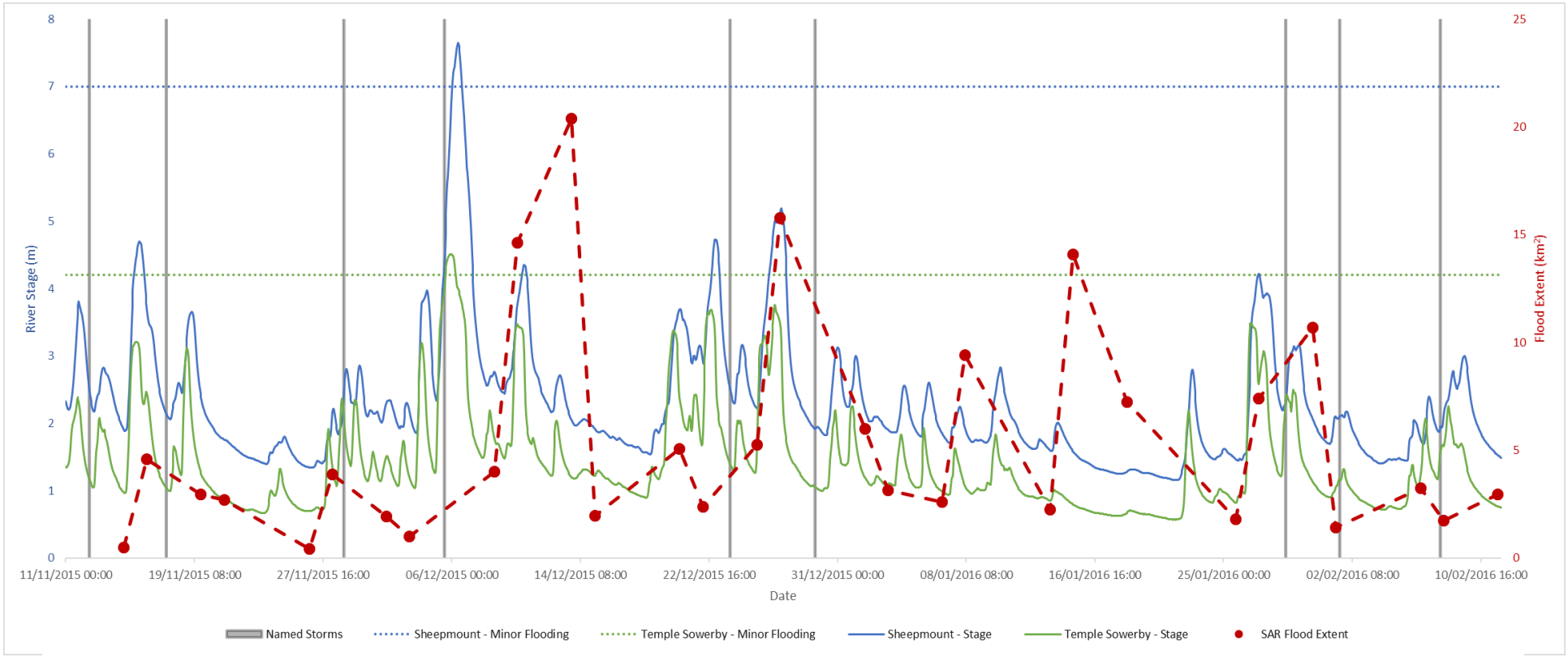

Figure 5.17. The amount of flooding identified in the Eden catchment compared to river stage at Temple Sowerby (upstream) and Sheepmount (downstream) gauges between 11th Nov 2015 and 11th Feb 2016. Approximate start period of named storms (from left, Abigail, Barney, Clodagh, Desmond, Eva, Frank, Gertrude, Henry and Imogen) shown for reference. Threshold for minor flooding occurrence taken from Environment Agency gauge information.

[128]

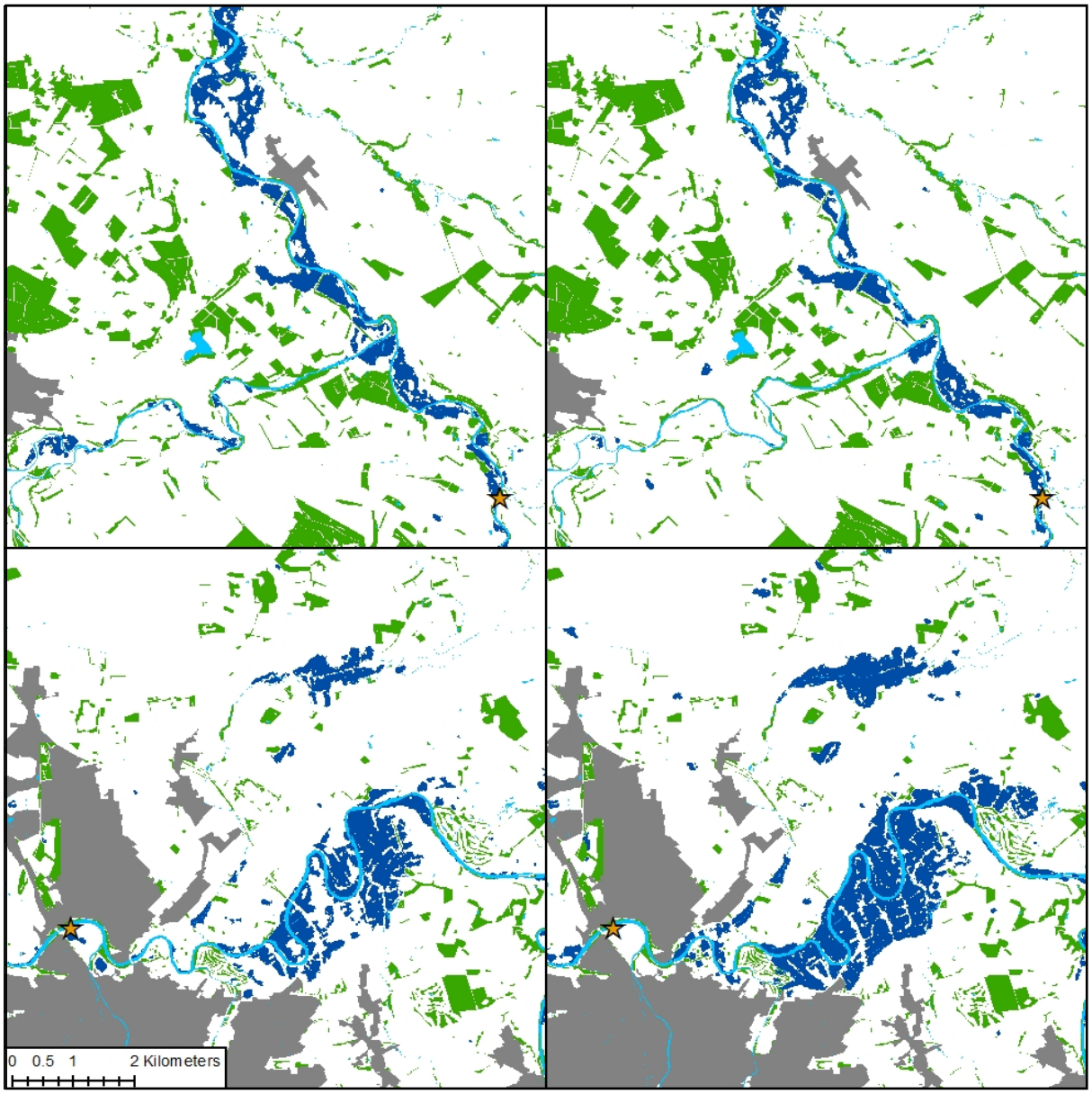

Figure 5.18. Flood extents around the Temple Sowerby (top) and Sheepmount (bottom) gauges during peak flood in the Eden catchment. Left column shows 10th Dec, and right shows 27th Dec. Flood extents shown in dark blue, permanent water bodies in light blue, woodland locations in green and urban regions in grey. Location of gauges are shown by the orange star.

5.5.3.4. Lake District

The Lake District contains a large number of permanent water bodies that can potentially act as a source of flooding when exposed to prolonged or intense rainfall. During the 2015-16 winter storms flooding is primarily located in three locations; in the north of the region along the River Wampool, in the south of the region near the confluence of the Gilpin and Kent Rivers, and around low-lying lakes, such as Bassenthwaite Lake and Derwent Water, situated along the River Derwent. Figure 5.19 shows the number of images with flooding identified at each of these locations.

[130]

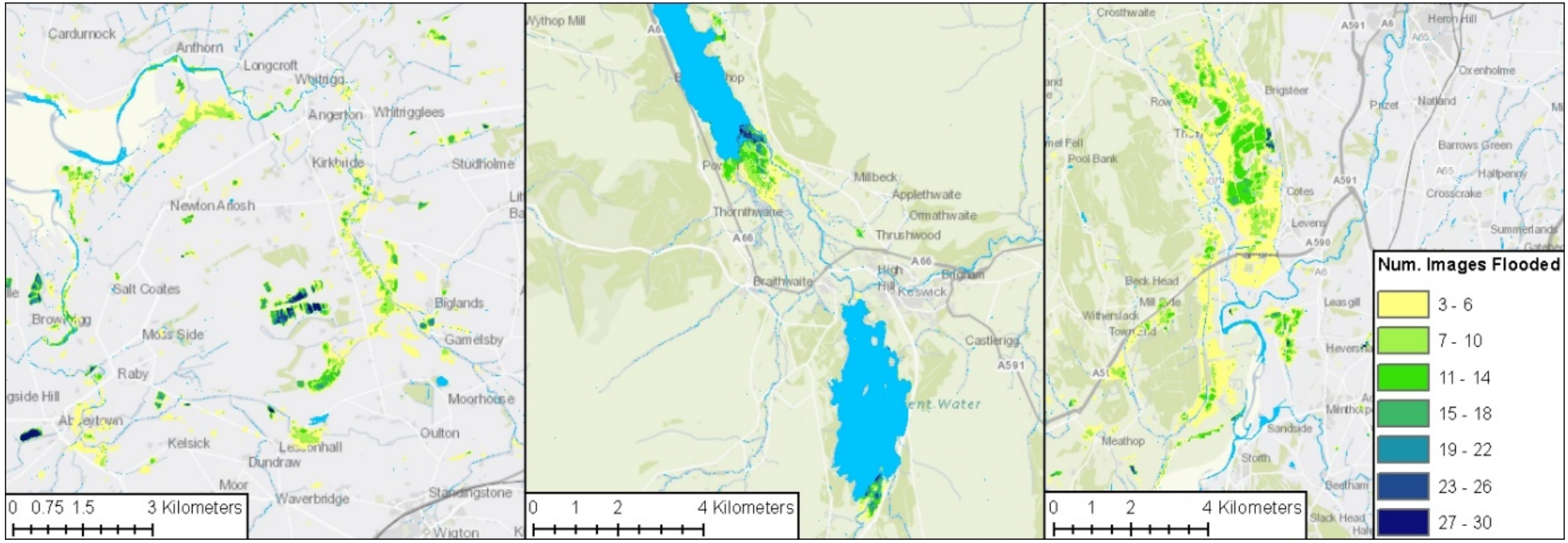

Figure 5.19. Number of satellite images with flood identified throughout the Lake District between 11th Nov 2015 and 11th Feb 2016. Locations based around the three main flood locations; River Wampool (left), River Derwent at Keswick (middle) and the confluence of the River Kent and River Gilpin (right). Locations flooded in two or less images are not shown. Permanent water bodies are shown in light blue.

[131]

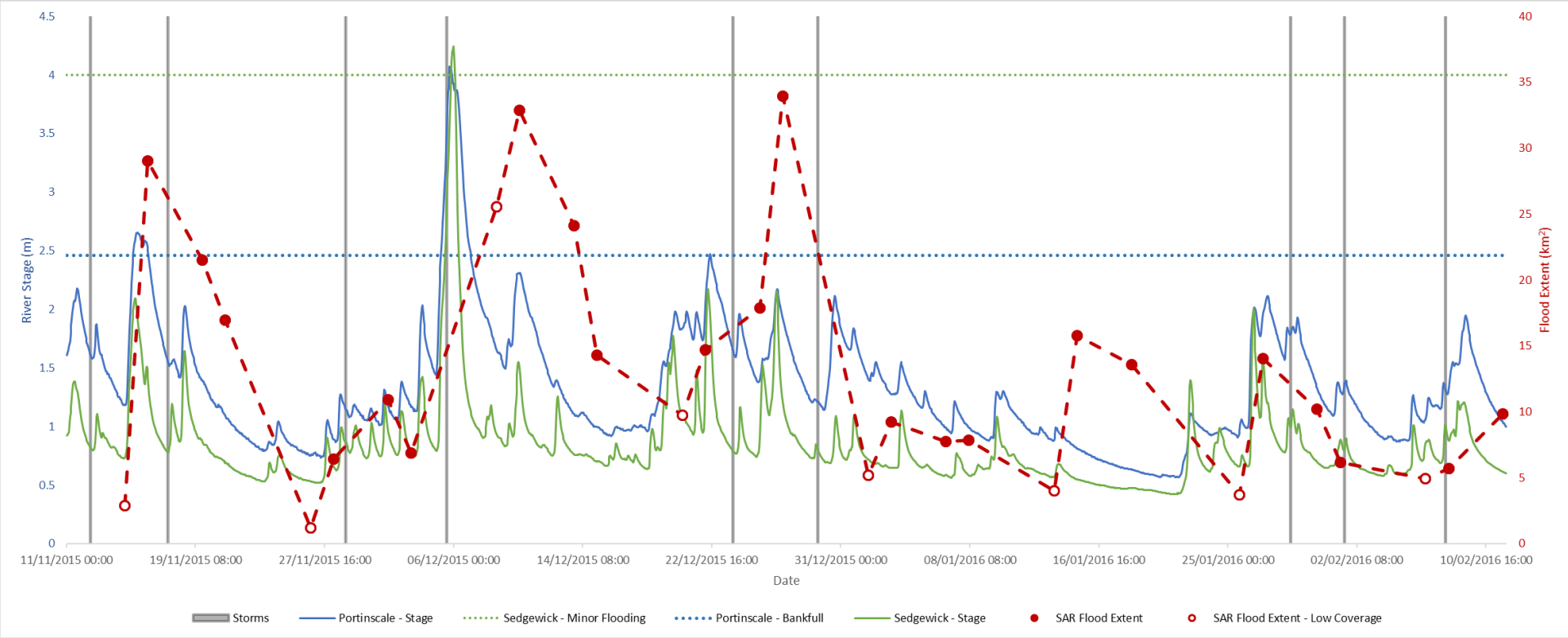

Figure 5.20. The amount of flooding identified across the Lake District compared to river stage at Portinscale and Sedgwick gauges between 11th Nov 2015 and 11th Feb 2016. Low coverage (less than 70% of catchment) SAR images shown as unfilled data points. Approximate start period of named storms (from left, Abigail, Barney, Clodagh, Desmond, Eva, Frank, Gertrude, Henry and Imogen) shown for reference. Threshold for bankfull occurrence taken from National River Flow Archive (NRFA) gauge information (Portinscale) and Environment Agency gauge information (Sedgewick).

The region experienced a number of peaks in flood extent during the time period, including on the 16th Nov (between Storms Abigail and Barney), on the 8th and 10th Dec (after Storm Desmond) and on the 27th Dec (between Storms Eva and Frank, Figure 5.20). As a comparison gauge stage data is shown from Portinscale on the River Derwent, located between Bassenthwaite Lake and Derwent Water, and from Sedgwick on the River Kent, located in the south of the region. Both gauges are located in regions that suffered from flooding during the study period. It is noted that the Lake District provides a spatially variable hydrological setting and that the gauge records presented only provide insight for the regions around them.

River stage during Storm Desmond is extremely high, peaking above 4 m for both gauges, which is 1.6 m above the minor flooding threshold at Portinscale. Flood extents for the images on the 8th, 10th and 13th Dec remain extensive, despite river flows dropping lower. The long lag between stage decrease and flood retreat is expected considering the extreme nature of the flows observed, and the volume of water situated on the floodplains. Our understanding of the peak flood extent across the Lake District is hampered by the Sentinel-1 imagery for the 8th Dec only covering half of the region. Despite this, it still shows a significant amount of flooding, at a similar amount to that observed on the 13th Dec.

A similarly large amount of flooding is observed on the 27th Dec, however, the gauge records showcase smaller peaks in river stage compared to Storm Desmond. Investigation of the spatial patterns of flooding at this time shows inundation located around the three regions shown in Figure 5.19. However, the flooding along the River Derwent and River Kent is more temporally consistent prior to the 27th Dec, with the majority of the increase in flood extent found along the River Wampool. This highlights the differences in hydrological regimes and the subsequent speed of water retreat at different locations within the region. Furthermore, Figure 5.19 shows the increased water extent of the permanent water bodies during the study period, with the surface area of Bassenthwaite Lake and Derwent Water expanded for at least half of the images analysed. This highlights the greater water retention by larger water bodies compared to the faster return to normal flow conditions observed at river gauges. This localised disconnect between the river stage and flood extent, along with the longer water storage seen by lakes, can help explain the occasional

lack of correlation between the in-situ and satellite observations during an extended period of inundation, as seen in early December in Figure 5.20.

5.5.4. Misclassification Due to Snow and Frost

There is a strong peak observed across all catchments on the 15th Jan. In particular, the Ouse catchment shows flood extents approximately 2.5 times what is observed for the next largest peak on the 29th Dec, after Storms Eva and Frank. For a peak of this size, it would be expected that the gauge records would show similar extreme values for river stage. However, on the 15th Jan all the gauges are showing reduced flow. There are similar dates where the river stage and flood extents do not correlate in particular catchments, such as the 13th Dec in the Eden catchment as previously highlighted. Figure 5.21 provides examples of the relationship between stage and flood extent for selected gauges. An increase in the percentage of catchment flooding is observed between the 13th and 15th Jan, whilst the river stage lowers away from the Environment Agency suggested minor flooding thresholds.

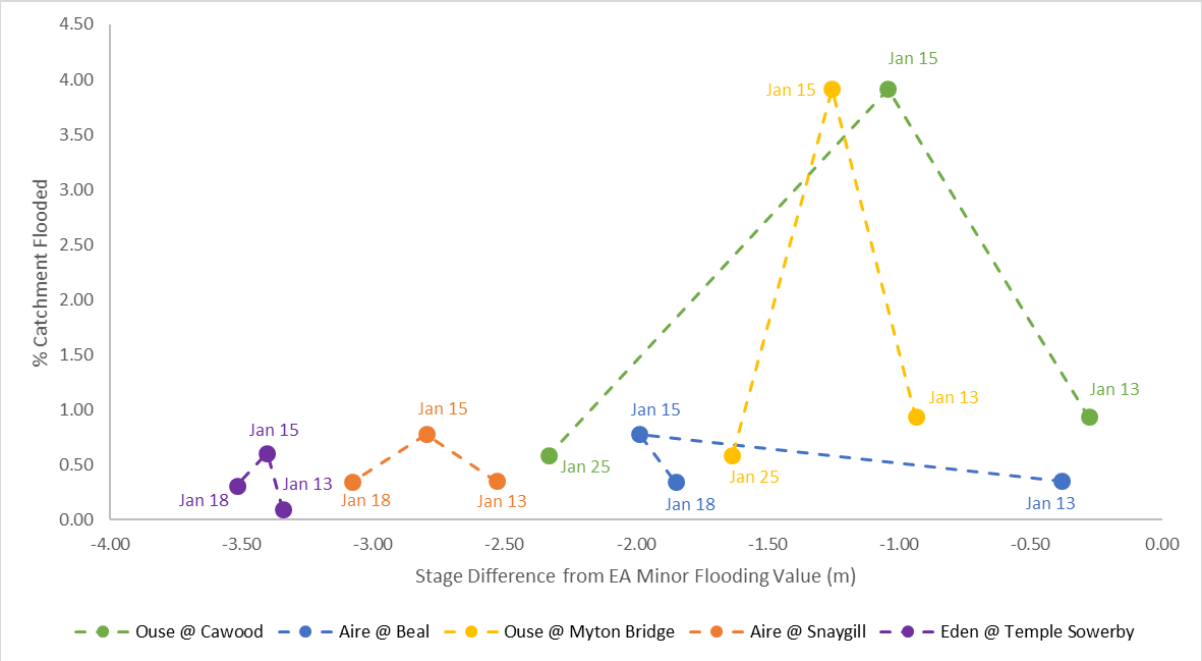

Figure 5.21. Comparison between river stage (in relation to EA minor flooding threshold) and catchment-scale flooding for selected gauges and catchments. Visual inspection of the 15th Jan flood maps suggest erroneous classifications due to the presence of frost and wet snow. This is highlighted by the continuing decrease in river stage before and after 15th Jan, contrary to the sharp increase in identified flooding, particularly in the Ouse catchment (green and yellow).

Comparisons between the flood extents observed on the 13th and 15th Jan are shown in Figure 5.22. The new regions of flooding tend to be not located near any permanent water body. In fact, closer inspection of the extents shows a reduction in the size of the inundation occurring on the river floodplains. The new regions of low backscatter can be generally classed as distinct, medium-sized objects. The homogeneity of the backscatter response in these areas suggests that there is a consistent land cover, either temporary (such as water or snow), or a temporally consistent land cover under new environmental conditions (such as bare soil covered by frost).

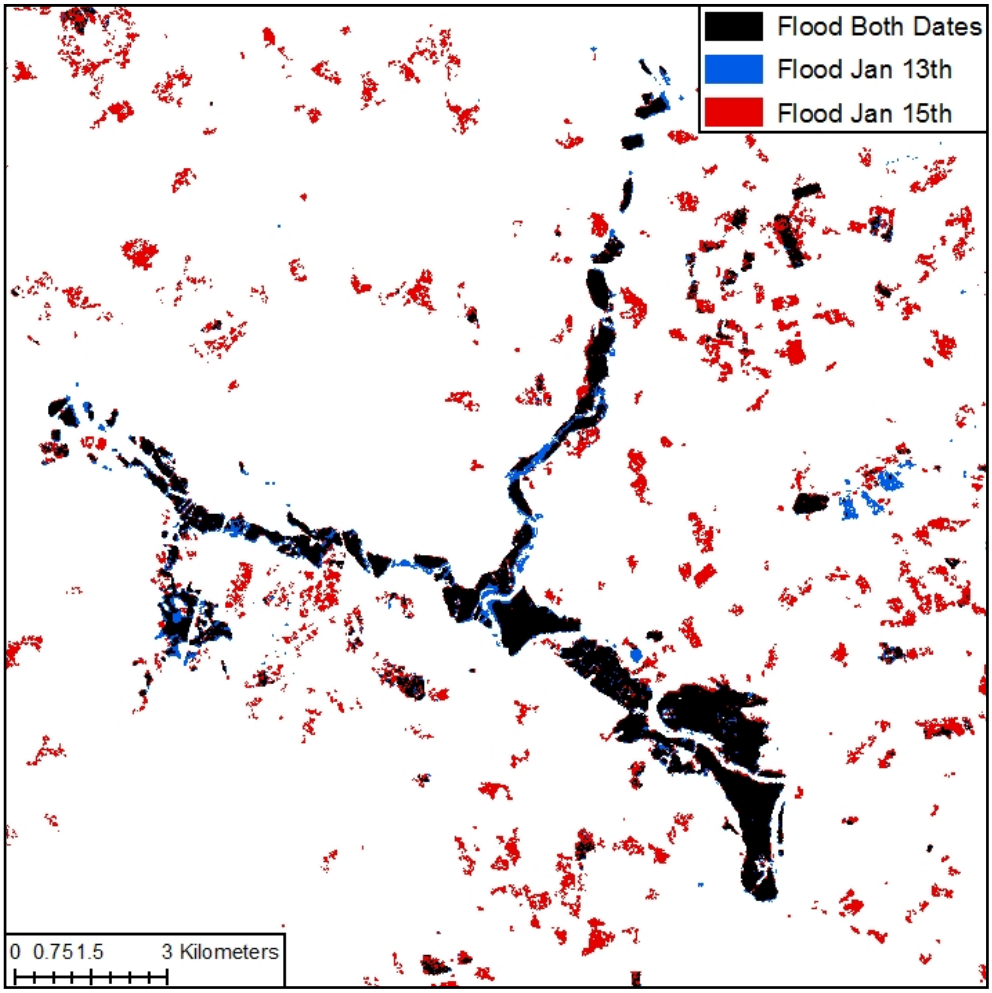

Figure 5.22. Comparison between flood extents on the 13th and 15th Jan.

Figure 5.23 shows the UKCP09 gridded weather observations (Met Office, 2017) across the study region between the 13th and 18th Jan. There was minimal precipitation after the 13th Jan, whilst both minimum and mean temperature show a sharp decrease from the 15th Jan onwards. The precipitation data is questionable,

with other sources suggesting the snowfall during this period. The Met Office summary of the January 2016 weather (Met Office, 2016) states the occurrence of snow on high ground and in the north of England during the middle of the month. This is confirmed by phenocam images from the Moor House soil monitoring station, part of the Cosmos-UK network operated by the Centre for Ecology and Hydrology (CEH). Figure 5.24 shows images from the 13th and 15th Jan, the latter of which shows significant snow coverage. This is further confirmed by the Cosmos-UK precipitation records at the site (Figure 5.25), which show over 140 mm and 170 mm for the 14th and 15th Jan respectively. Based on the evidence from other sources, it can be surmised that the gridded dataset is unable to adequately capture snowfall, and is only a representation of rainfall. Further to the observed snow occurring at this time, the low temperatures also caused widespread frost throughout the middle of the month. Figure 5.26 shows the number of frost days in January 2016. Generally, the study region had between 10 and 18 frost days, although there is no information on which days this occurred on. However, given the low temperatures observed in the middle of the month, it can be assumed that these occurred during this timeframe.

Wet snow has been shown in previous studies to produce low backscatter responses, similar to those observed from water bodies, due to the specular reflection of the radar signal from the snow-air interface (Naeimi *et al.*, 2012; Pivot, 2012). Areas affected by ground frost produce lower backscatter due to the reduction of the dielectric constant of the soil caused by freezing (Rignot and Way, 1994; Khaldoune *et al.*, 2011). Due to the similarities in backscatter response between flood pixels and snow-frost pixels, separating out the false classifications based purely on SAR backscatter intensity is challenging, if not impossible. Ancillary data such as topographic information, optical imagery and land cover maps, the analysis of the temporal consistency of the flooding, or a fuzzy framework combining multiple of the above parameters is often required to refine the flood extents to a more accurate representation of the ground conditions (Pulvirenti *et al.*, 2014).

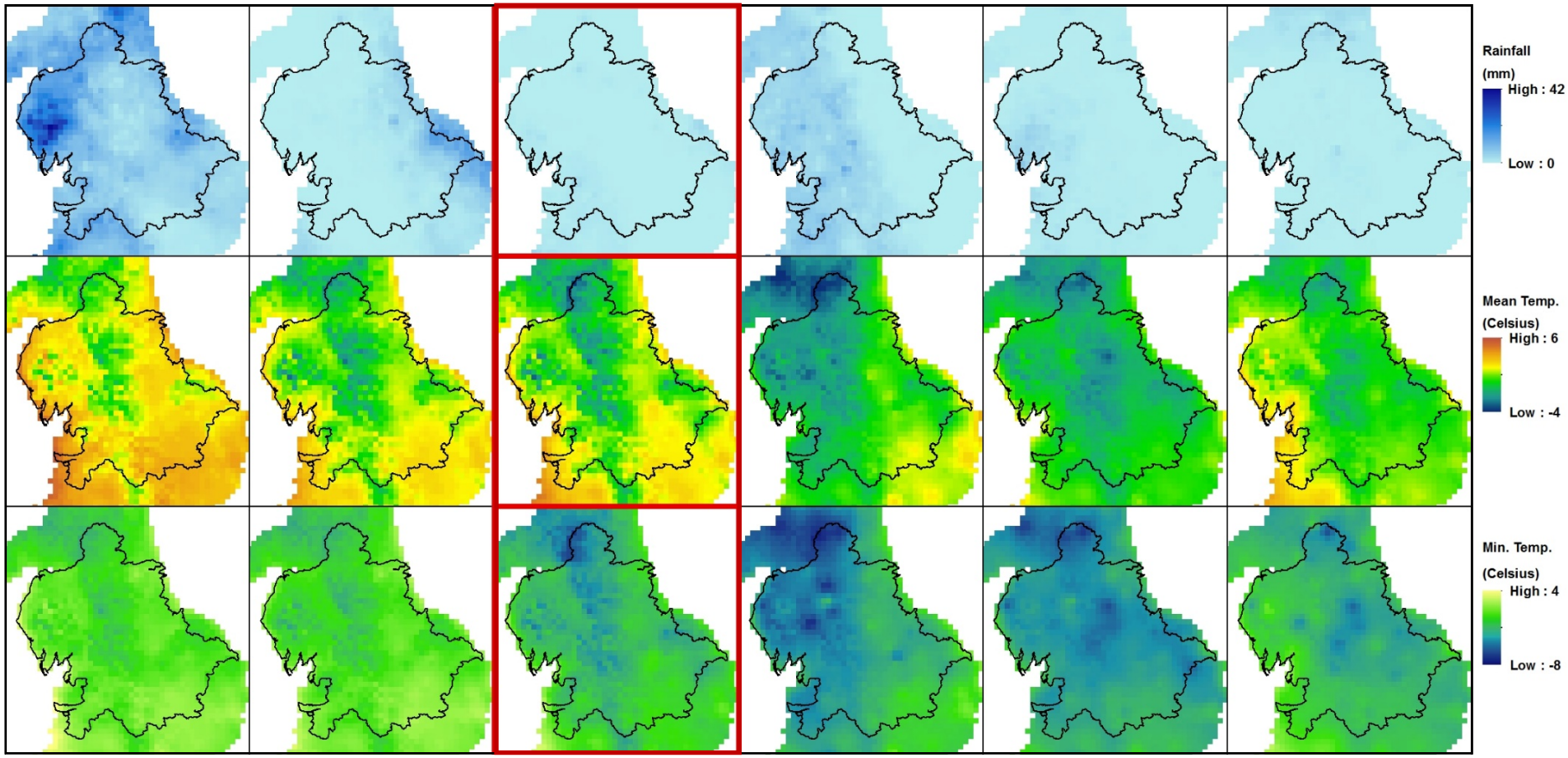

Figure 5.23. UKCP09 gridded (5 km^2) weather observations across the north of England between 13th and 18th Jan. Top row shows daily precipitation (mm), middle row shows mean temperature (°C), and bottom row shows minimum temperature (°C). Columns show each date, with the date of suspect flood extents (15th Jan) highlighted in red (SAR imagery taken at approximately 6 am). Total rainfall is between 9:00 UTC on Day D to 9:00 UTC on Day D+1. Minimum temperature calculated from measurements between 9:00 UTC on Day D-1 to 9:00 UTC on Day D. Mean temperature is taken as an average between minimum temperature and the maximum temperature (calculated over the same time period as rainfall). Note 15th Jan is at the start of a cold weather front, and that snow and frost may be more prevalent on the following days when no SAR imagery is acquired.

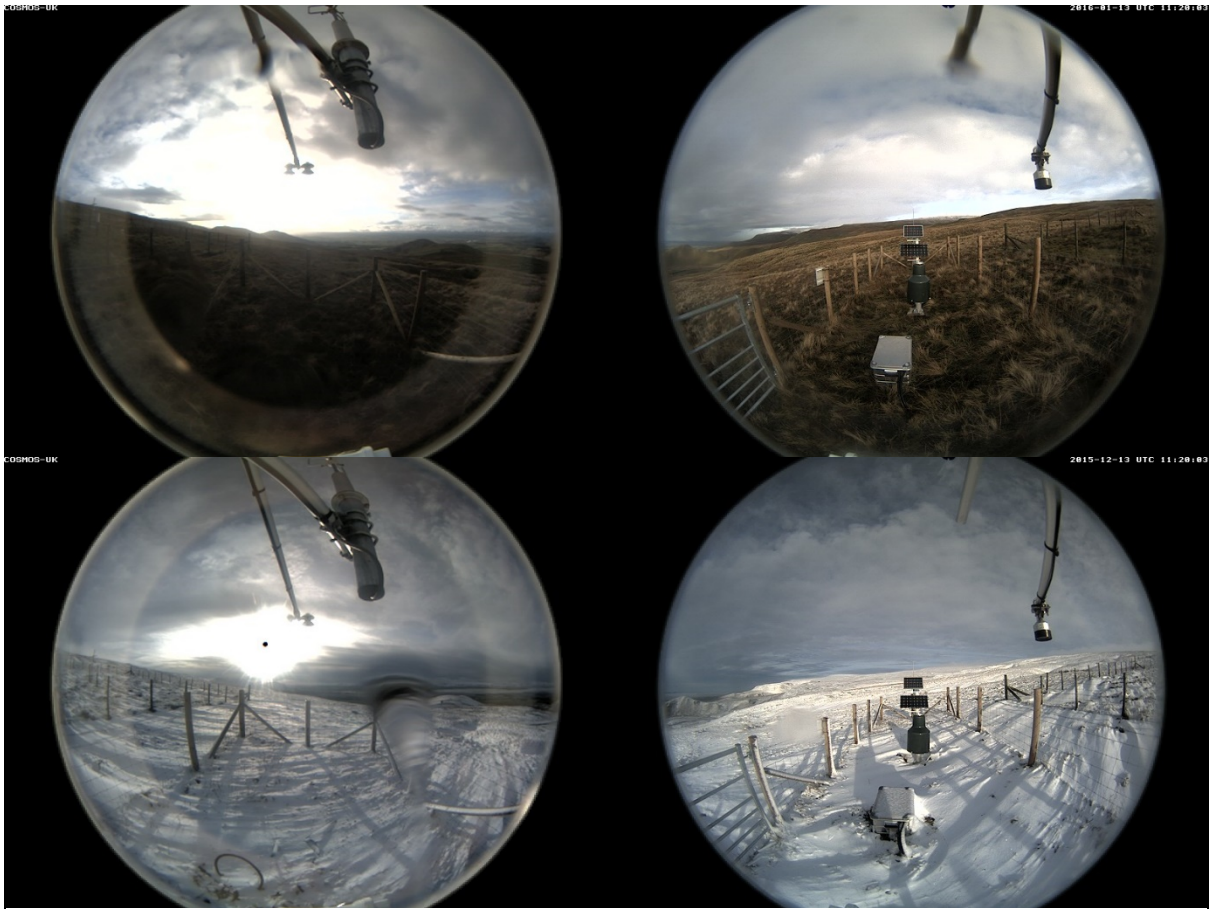

Figure 5.24. Phenocam imagery from CEH Cosmos-UK soil monitoring station at Moor House, located within the Eden catchment. Top images are from the 13th Jan, and bottom images are from the 15th Jan.

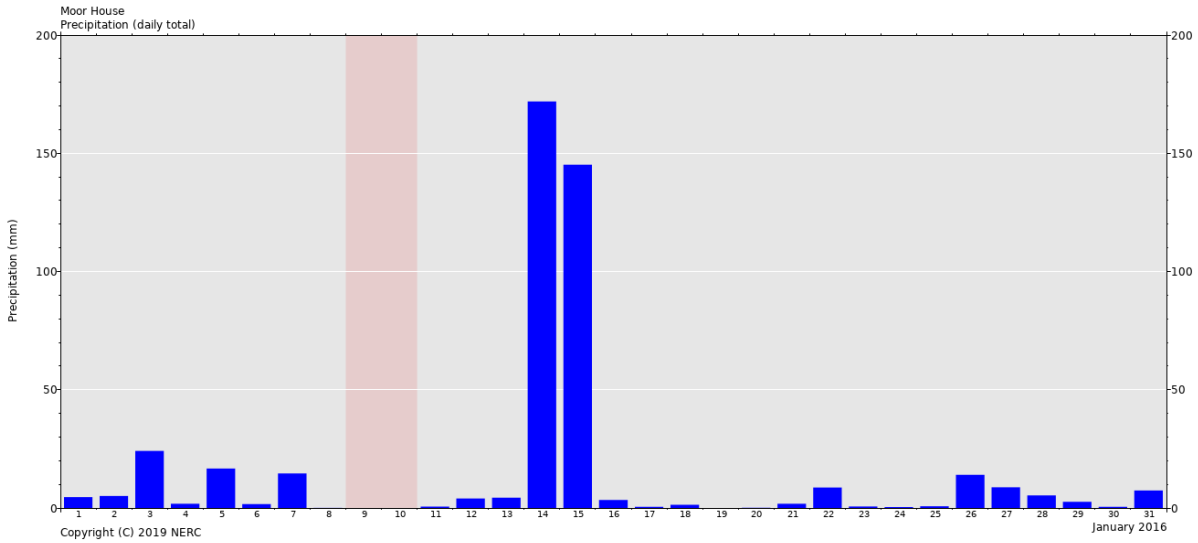

Figure 5.25. Precipitation at the Moor House COSMOS-UK monitoring station. Note large amount on the 14th and 15th Jan. Temperature records from the same site (not shown) observe temperatures mainly below 0°C around this time, suggesting snowfall.

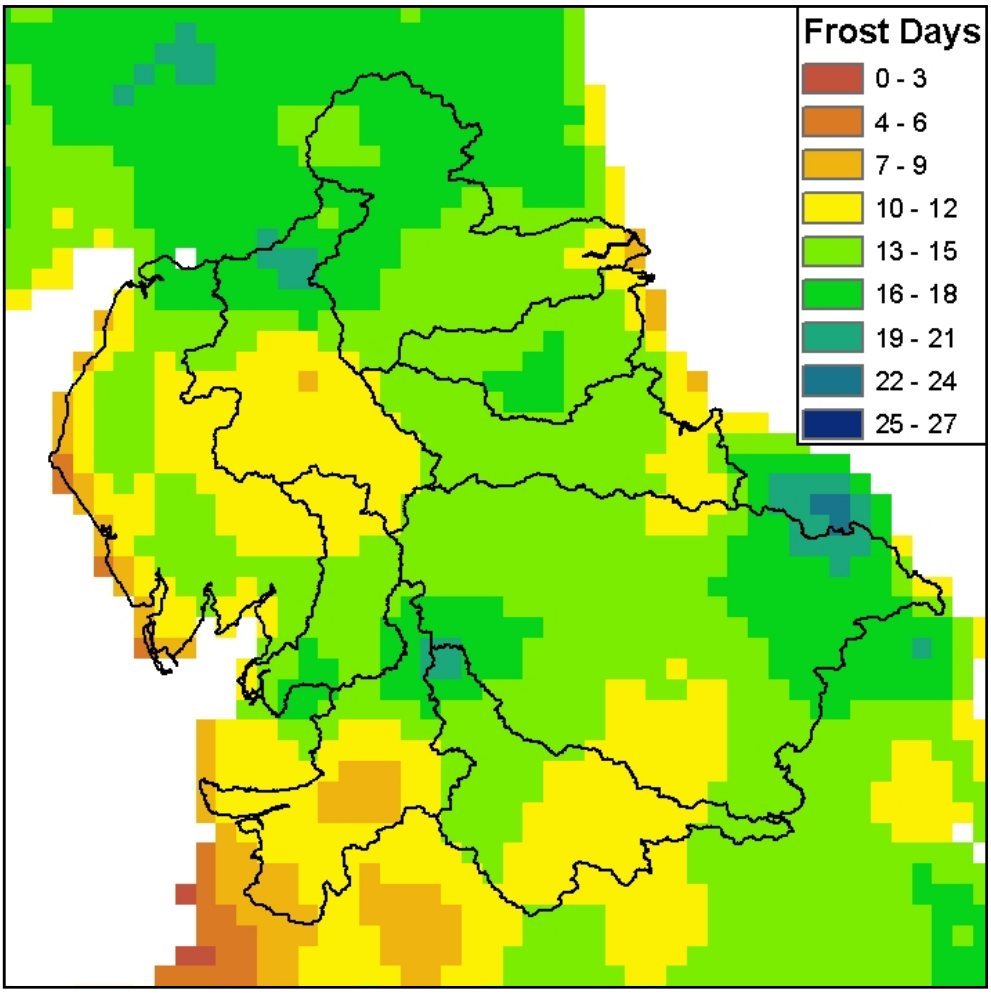

Figure 5.26. UKCP09 number of frost days for January 2016. Data gridded from observations to 5 km^2.

Figure 5.27 shows two potential refinements of the snow-frost misclassifications on the 15th Jan. Firstly, the HAND values for each of the low backscatter regions are shown. The second technique uses the temporal consistency of flooding for each location, via the amount of overlap with the three preceding SAR flood extents (3rd, 10th and 13th Jan). Using HAND to refine the classification proves sub-optimal. The areas of inundation located on the immediate river floodplain have HAND values up to approximately 5 m. These values are similar to some of the snow-frost false classifications further afield, meaning refinement via topographic information may only be applicable in locations with more varied terrain. Using previous flood extents to identify and remove suspect new flood areas results in a more likely representation of the inundation extent on the 15th Jan. For the area shown in the Figure, a reduction in flood extent of around 60% is observed by restricting locations to areas that have at least one overlap in the previous three images. Only 34% and 29% of the 15th Jan flood extent have overlap with two and three of the preceding images

respectively. Despite the positives in using such a temporal based method, there are potential issues with its widespread use due to different coverage between orbits, with the flood maps from the 8th Jan was not selected due to this. Furthermore, there is potential for removing correct classifications of new regions of flooding, particularly when longer temporal time-frames (such as the 12 days in the example in Figure 5.27).

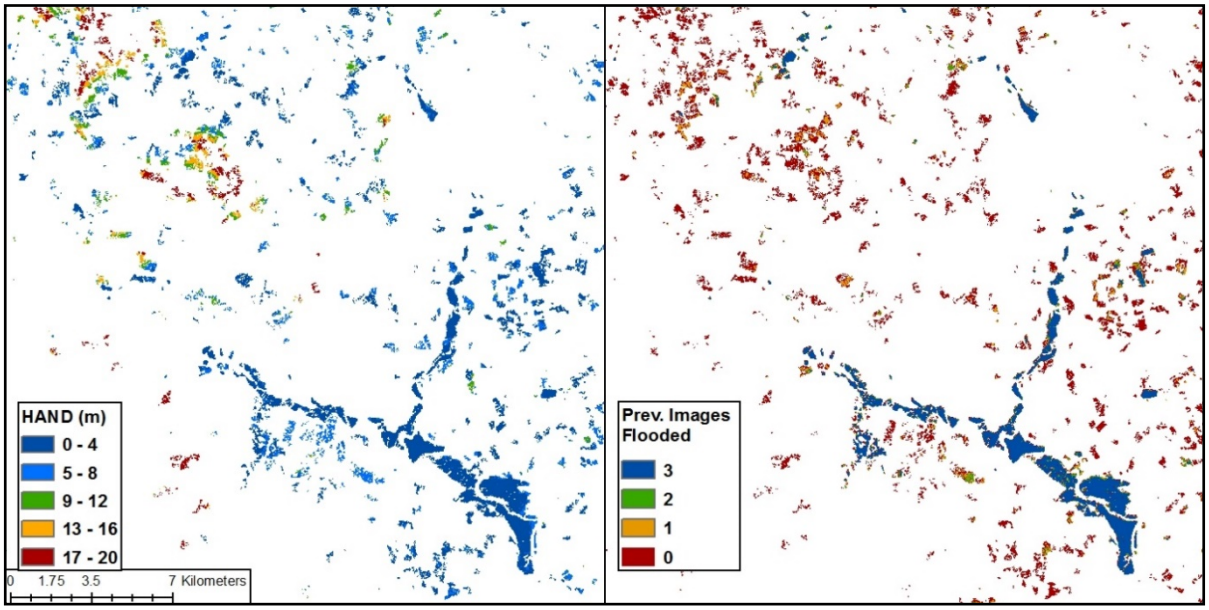

Figure 5.27. Refinement of the snow and frost induced misclassifications on the 15th Jan. The Ouse catchment around York shown, with HAND (left) and temporal flood consistency (right) shown as the basis for refinement.

5.6. Summary

This chapter has presented an update to the existing flood detection methodology from Chapter 4. Changes have been made to the histogram segmentation step, with improved accounting of the changes in land and water backscatter with incidence angle by developing a variable threshold based on local histograms. This allows for reliable flood delineation cross the full Sentinel-1 swaths. The addition of an object-based region growing step helps maximise the inclusion of inundated pixels, particularly along the flood edge and in rougher water conditions. The merging of polarisation specific flood extents, achieved by taking the maximum extent of any overlapping inundated region, reduces the misclassifications highlighted in Chapter 4 for each polarisation. The production of a single final flood map allows for easier interpretation of the results.

A new validation scheme has been implemented in this chapter, utilising numerous smaller subsets of the flood region instead of the whole study area. Validation across larger areas is subject to positive skewing of TA if both flood and reference datasets contain a large proportion of non-flooded pixels (Stephens *et al.*, 2014). This is highlighted with the recalculated of accuracy metrics from Chapter 4, with an average TA of 89% for both polarisations, down from 97% in the initial assessment.

Overall, the changes and expansion of the hybrid flood detection workflow perform well, with improvements in PA_f (average increase of 3.5%), TA (0.9%) and CSI (2.1%) compared to updated accuracy metrics produced by the Chapter 4 flood extents when validated against Sentinel-2 imagery. Additional comparisons are made to CEMS flood maps, delineated from high-resolution RADRSAT-2 imagery, which produce average TA and CSI values of 91.4% and 75.6% when validated against the Sentinel-2 surface water maps, compared to 91.0% and 76.9% for the presented methodology. This shows that the results derived from the two satellites are very similar, further highlighted by values of 95.5% and 0.878 for TA and $C\kappa$ when directly compared.

The flooding observed in the north of England throughout the 2015-16 winter storm season was extensive and prolonged. Peak flood extents are observed at the beginning of December for the Lake District and Eden catchment, and later in the month for the Aire and Ouse catchments. These correspond to precipitation inputs from Storms Desmond and Eva respectively. The trends in flood extent match the gauge data, albeit with none of the satellite acquisitions coinciding with the peaks in river flow. The consistent rainfall inputs throughout December 2015 will have resulted in saturated antecedent ground conditions. Potential impacts of this include increased flashy responses in the hydrographs, the slow retreat of floods waters, and the continual re-flooding of locations throughout the study period. In particular, Figure 5.14 shows regions of the River Derwent floodplain remaining inundated for 25 out of 30 possible images.

Although the presented algorithm has successfully detected flooding in rural, open locations, there are still geographical locations and environmental situations that can result in misclassifications. The inability of SAR to detect surface water in urban and woodland settings is well known. Additionally, this chapter highlighted the potential

for false-positive classifications caused by wet snow and frost, which produce similar low backscatter responses as permanent water bodies. In particular, the amount of identified “flooding” in the Ouse catchment on the 15th Jan far eclipses the maximum extents associated with Storm Eva, the second largest peak. The similarity in backscatter between wet snow, frost and surface water makes removing false classifications based solely on SAR imagery difficult. Highlighted here is the potential for using terrain data or the temporal consistency of flooding to help determine the likelihood of areas of identified flooding being accurate.

The launch of Sentinel-1 has resulted in improved spatial and temporal resolution of global, freely available SAR imagery, ideal for widespread flood monitoring. Due to the global nature of flooding, one of the requirements of any flood delineation algorithm is locational consistency. The developed methodology is based on globally available data, with one of the advantages of satellite imagery being the unrestricted geographical coverage. Chapter 7 will present an application of the workflow for a flood event in Australia, highlighting the potential for flood mapping using the developed algorithm irrespective of location.

Chapter 6. Water Depth and Volume Estimation

The aim of this chapter is to develop a workflow for estimating additional hydrological parameters from the flood extents produced in Chapter 5, allowing for greater insight into the dynamics of the 2015-16 winter floods. The proposed methodology is based around the fusion of the derived inundation extents with terrain data to determine shoreline heights, before interpolating these into a continuous water surface from which depths and volumes can be calculated. Initial workflow development is undertaken using a UK specific, high-resolution Environment Agency (EA) 2 m LiDAR DTM, with the main portion of the results section analysing these outputs. Additional results are generated using the globally available SRTM DEM as the underlying terrain model, with the aim of ascertaining the comparable accuracy using the lower resolution datasets and the applicability of the method on a global scale.

There are two main sources of error that require consideration when determining the shoreline heights of a flood using an overlay approach. Firstly, inaccuracies within the SAR inundation extents may result in under-prediction of the flood boundary location, resulting in the erroneous selection of shoreline heights (Zwenzner and Voigt, 2009). The algorithm presented in Chapter 5 identifies flooding by segmenting locations of low backscatter in the SAR imagery. Subsequently, there is low confidence in the accuracy of the resultant maps in urban and woodland locations due to the masking of the specular reflection via the double bounce effect. An example of SAR derived inundation, with gaps within the flood boundary coinciding with vegetation, is shown in Figure 6.1.

Secondly, the resolution of the SAR imagery and the terrain model are unlikely to match (Cohen *et al.*, 2018). For example, the 10 m pixels in the Sentinel-1 imagery has a lower resolution compared to the 2 m EA LiDAR DTM, but a higher resolution to the 30 m SRTM DEM. The flood boundary delineated from the SAR imagery will provide a different representation of the topographic flood edge compared to those from the various resolution terrain datasets (a comparison to the LiDAR DTM is provided in Figure 6.2). Understanding how accurate the SAR shorelines are in relation to the floodplain boundaries, and adjusting the extracted shoreline heights to represent this, is vital for successfully creating an accurate flood surface.

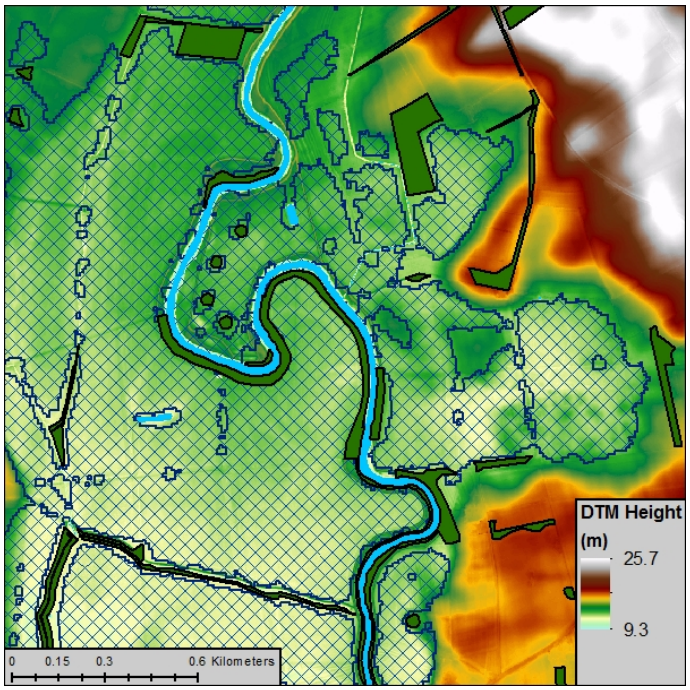

Figure 6.1. Identified flooding (crosshatch blue) overlaid onto the LiDAR DTM, with OS Vector Map Local woodland and river locations shown in dark green and light blue respectively. Note gaps in the water surface that correspond to woodland locations, and unflooded locations (top of image) where DTM values are similar to nearby flooded locations, highlighting potential underestimation of flood extent.

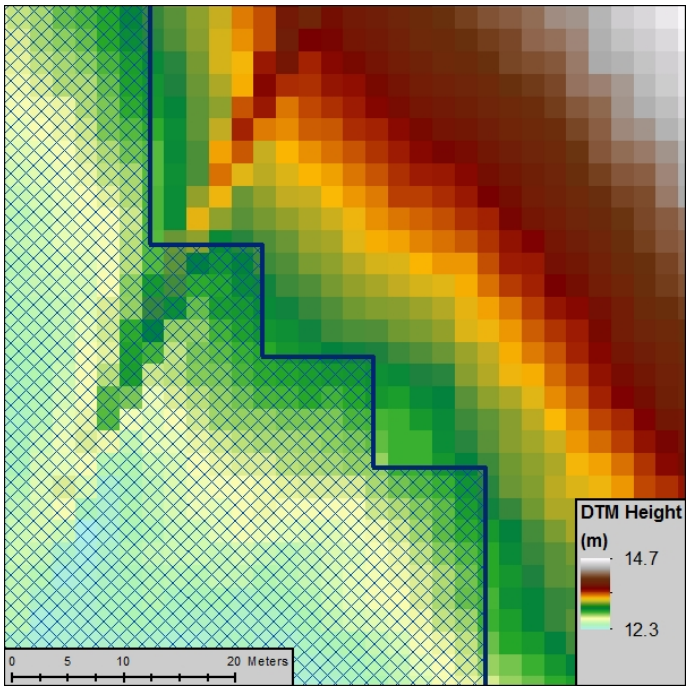

Figure 6.2. Comparison between Sentinel-1 (derived flood boundary shown by blue line, with crosshatch representing flooded) and LiDAR DTM resolution. The satellite observed shoreline provides a poor representation of the topographic floodplain compared to the higher resolution dataset.

6.1. Datasets

6.1.1. Flood Extent Selection

In Chapter 5 flood extents were derived for a number of catchments across the north of England during the winter of 2015-16. Of the studied catchments, the Ouse and Aire contained the greatest extent and longevity of flooding. Although there was significant inundation in other catchments, these coincided with individual Sentinel-1 images instead of multiple successive acquisitions. The ability to determine any changes in water slope, depth and volume throughout the Aire and Ouse catchments across an extended time period will allow for in-depth analysis of the dynamic life-cycle of the flood events. Peak extents for the two catchments are found on the 29th Dec, with inundation found clearly visible in the following seven images (1st, 3rd, 6th, 10th, 13th, 15th and 25th Jan. Note only minimal flooding is visible on the 25th Jan in the Aire catchment and has not been processed). The focus in this chapter will be on deriving a water surface, depths and volumes across these catchments and dates.

The flood extents derived in Chapter 5 can be divided into two broad categories based on their geographical location; flooding close to a river, and likely to be fluvial in nature; and inundation distanced from permanent water bodies, which are likely to be pluvial or groundwater sourced events. The largest water bodies are found in the former category, and the work is the chapter is focused on these fluvial locations. The selection of relevant flood polygons is achieved using a recursive, location-based scheme. Firstly, flood regions that are located within 500 m of a river are selected. Additional water bodies that are found within 500 m of the selected flood locations are then identified and added to the original selection. This iterative process continues until no new flood locations are identified.

Within the flood boundaries, there are gaps caused by pixels of higher backscatter in the SAR imagery. These may be local topographic highs that have remained unflooded and be correctly classified as dry. Alternatively, they could be misclassifications due to features protruding the water surface, such as trees or buildings, which cause the double bounce effect (see Figure 6.1 for examples). For the purpose of calculating flood shoreline height from which to derive a water surface, any holes within the flood boundary have been filled, with only the outer flood edge being considered as a true shoreline. It is expected that once water depths have been calculated that any gaps corresponding to topographic highs will

be highlighted as being above the derived water surface, and those caused by protruding features will be correctly identified as flooded. The final step involves the removal of smaller flood bodies below 10,000 m^2 (10 pixels squared) from the selection to ensure processing efficiency, with the selected larger water bodies providing sufficient shoreline heights to calculate a water surface. It is considered that the larger the flood polygon the greater confidence there is in the observed extent being accurate in location, with smaller water bodies potentially subject to false detections due to speckle, volume scattering, specular reflection from flat, man-made surfaces and snow-frost misclassifications. It is likely that some of the removed smaller inundated regions are correctly classified flood areas. These will be re-identified later in the processing chain as a location with positive water depth, indicating flooding.

Flood extents observed on one of the dates required additional processing. There is significant uncertainty with the results on the 15th Jan due to false classifications from wet snow and frost, which display a similar low backscatter intensity to open water in the SAR imagery. As discussed in Chapter 5, one of the potential methods for refining these uncertain flood locations is a comparison to the previously derived extents. For this chapter, a flood region from the 15th Jan is considered accurate if it overlaps with two out of the previous three inundation extents, acquired on the 3rd, 10th and 13th Jan, as well as passing the previously discussed location and size requirements.

For this chapter, the Ouse catchment has been subdivided into 5 distinct regions, based on where the identified flooding is most prevalent. This allows processing to be achieved in an efficient manner, whilst presenting the opportunity to investigate the inter-catchment water movement throughout the study period. Figure 6.3 provides an overview of the sub-regions within the two catchments. The Sentinel-1 imagery does not provide full coverage of the Ouse catchment on all dates. In particular, extents on the 6th and 10th Jan are missing complete coverage for two of the sub-regions (Ouse 4 and 5 on the 6th, Ouse 1 and 4 on the 10th). The 6th Jan extents additionally have partial coverage for two other regions (Ouse 2 and 3), providing the challenge of having the edge of the image occurring within an area of inundation, resulting in the boundary of the flood polygon representing the image edge instead of the inundation shoreline. These locations have still been processed

to ascertain the robustness of the developed methodology. Only the downstream portion of the Aire catchment has been studied. Although there is flooding further upstream, these tend to be on a single flood image instead of a longer time-series, which do not coincide with the flood dates identified for analysis for the downstream portion of the Aire.

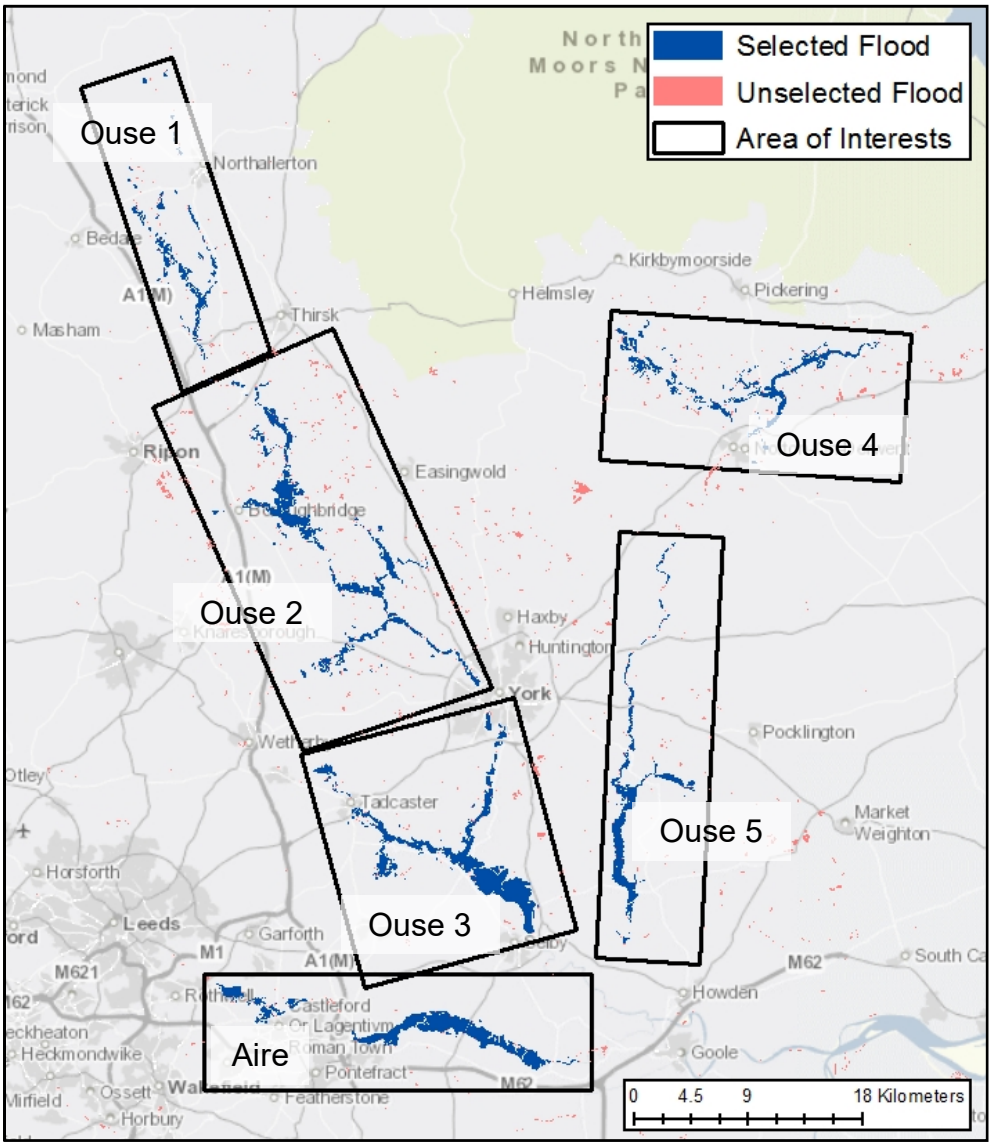

Figure 6.3. Sub-regions within the Aire and the Ouse catchments covering the most flood prone locations. Flood extents from the 29th Dec are shown, with those used to calculate the water surface shown in blue, and those discarded from the processing (due to their small size or distance from a permanent water body) shown in light red. Results on the 6th Jan have no coverage for Ouse 4 and 5, and partial coverage for Ouse 2 and 3. Results on the 10th Jan have no coverage for Ouse 1 and 4.

6.1.2. Terrain Models

Two terrain datasets are used in this chapter. The EA LiDAR 2 m Composite DTM is used to develop the methodology and provide initial results. The dataset is updated

annually via aerial survey, with coverage over a large proportion of England and Wales. The developed techniques are subsequently applied using the 1 arc-second SRTM DEM, collected via radar satellite in 2000. Further information on both datasets, including reported height accuracies, can be found in Chapter 3.

6.1.3. Vector Datasets

Shoreline heights located near woodland and urban areas are likely to skew the calculation of a water surface towards an erroneously low value, caused by the SAR observations misrepresenting the shoreline locations resulting in the often under-predicted inundation edge being found on the lower-lying floodplain (Horritt, 2003). Additionally, the change detection processing used in Chapter 5 removes permanent water bodies, resulting in the production of a flood map instead of a surface water map. Subsequently, sections of the shoreline correspond to locations where the river is located instead of the outer flood boundary, misrepresenting the continuous water surface that is likely present in these locations. Furthermore, due to the mismatch in resolution between SAR and the DTM, the SAR flood boundary can fall within the river channel, causing an exacerbation of the under-estimation of the surface height by including water surface LiDAR returns.

Vector datasets for urban areas, woodland locations and permanent water bodies have been combined to create a mask to identify where the SAR flood extents may be inaccurate. Two different groups of vector datasets have been used to correspond to the LiDAR and SRTM terrain datasets. For the higher resolution DTM study, vector feature classes that form part of the Ordnance Survey (OS) Vector Map Local dataset are used. These are available at scales between 1:3,000 and 1:20,000 (Ordnance Survey, 2018). For the analysis using the SRTM DEM, the CORINE land cover map (2012 edition) produced by Copernicus is utilised. Derived using optical imagery, CORINE provides data across Europe at a scale of 1:250,000 at a thematic accuracy above 85% (EEA, 2017). Once the woodland, urban and water polygons are combined from both source datasets, each feature is buffered by 10 m to account for inaccuracies in the feature locations and the mismatch in resolution between the SAR and the source material used to derive the vector data. A description of how the final feature mask is used within the study is given below.

The location of flood defences, available from the EA, is utilised in Section 6.2.4. Over 32,000 assets have been digitised from survey information and are available at a resolution of at least 1:3,000 (Environment Agency, 2018). These assets are designed to provide protection against a 1-in-100 river and 1-in-200 coastal flood events. As this dataset is not globally available it has not been used in the study assessing the applicability of the methodology with SRTM (Section 6.2.6).

6.2. Methodology

Sections 6.2.1 through 6.2.5 outline the development of the methodology used to determine a water surface by combining the SAR derived flood extents with the LiDAR DTM, which is subsequently used to calculate water depth and volume. Any reference to the terrain data in these sections is referring to the EA LiDAR DTM dataset unless stated. Section 6.2.6 reviews any changes to the methodology that is required when applied using lower resolution terrain and vector datasets.

6.2.1. Determining Shoreline Heights

The methodology for determining the height of the flood shoreline is based around the assumption that although there may be local inaccuracies in the location of the delineated flood edge, at a regional scale the error is on average less than 1 pixel (10 m) of the true boundary location. Based on this assumption, an estimate of the water surface height can be made for each SAR pixel that is adjacent to the flood shoreline by analysing the DTM height values that fall within the pixel (Figure 6.4). Different percentiles of the DTM values have been extracted based on whether the SAR pixel has been classified as flooded or non-flooded.

For the pixels on the flooded side of the shoreline, a secondary assumption has been made, in that the identified regions of inundation are inherently accurate and that any uncertainty on the waterside of the flood boundary is due to the mismatch in resolution between the SAR and DTM datasets. The mapping algorithm in Chapter 5 identifies flooding based on the specular reflection of the radar signal. Previous work by Santoro and Wegmüller (2014) analysed backscatter responses from 300 m pixel ASAR data in relation to land cover. Their work showed that even a small proportion of land (greater than 5%) within a pixel space will increase backscatter intensity, resulting in the pixel not being classified as water. Depending on how the Sentinel-1 and LiDAR DTM pixels align, there will be between 25 and 36 height values within

each SAR pixel. If the derived flood boundary is completely accurate, then the water surface height will be equal to the maximum height value within the wet pixel or the minimum value from the dry pixel. However, even if the flood boundary has been correctly identified in location, the shape of the shoreline is likely to be inaccurate due to the lower resolution of the Sentinel-1 imagery (Figure 6.2). The higher resolution DTM will provide a more realistic depiction of the curvature of the flood edge, and it is plausible that a small number of DTM pixels within a SAR pixel may be above the water surface when the shoreline is derived at a higher accuracy. However, for the SAR pixel to still produce a specular reflection of the radar signal, this will likely be less than 5% of the height values. The 95th percentile height value for each flooded shoreline adjacent SAR pixel is extracted as a potential estimate of the water surface height.

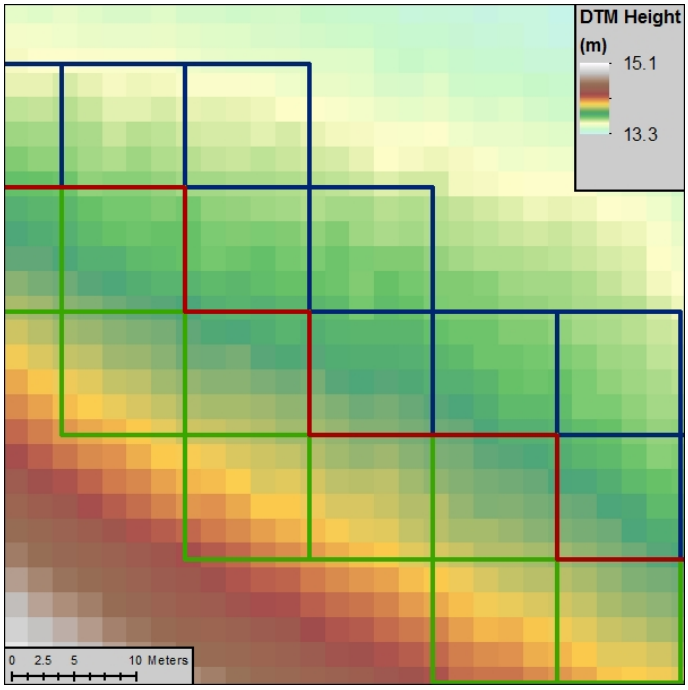

Figure 6.4. SAR derived flood shoreline (red) with adjacent SAR pixels (flooded in blue, unflooded in green). Note the number of DTM pixels in each SAR cell, and the range of heights found within.

The assumed 1-pixel locational accuracy is of greater importance for the non-flooded side of the derived shoreline. The double bounce mechanism can often cause under-prediction of the flood extent when being extracted from SAR imagery. The mapping algorithm presented in Chapter 5 is unable to reliably delineate flooding when features protrude the water surface, including emergent vegetation at the flood edge. In areas of under-detection, there is no accurate method based purely on SAR

backscatter intensity to determine how much further inundation occurs outside the derived extent. It is possible that the true flood boundary extends a number of pixels beyond the observed shoreline. To negate the likely underestimation of the flood boundary, shoreline locations near woodland and urban areas are removed later in the processing chain.

Determining shoreline heights from the remaining unflooded pixels is still challenging, and liable to inaccuracies. The work by Santoro and Wegmüller (2014) showed that only a small percentage of a pixel needs to be land for it to produce significant backscatter. For the dry pixels adjacent to the flood boundary, there is no way of determining the land to water ratio. The true flood boundary could be close to the delineated shoreline location, or closer to the far edge of the SAR pixel. To account for this inaccuracy, alongside the overall assumption that open shoreline locations derived from the SAR imagery are within a single pixel of the true extent, the median height value has been selected from each shoreline adjacent dry SAR pixel as a potential water surface height. Although there is likely to be local differences to this, over a region this value should provide a good representation of shoreline height.

6.2.2. Grid Creation

A continuous water surface is produced by mosaicking a series of smaller, local water surfaces. This is to allow for the reduction in water surface height as the flood wave travels downstream, conforming to the hydraulic and energy loss principles outlined by Raclot (2006). The flood extent extracted from each satellite image has been subdivided into distinct regions (Figure 6.3), and a 1 km grid is created over the derived inundation extent within each sub-region on each date. An example flood grid is shown in Figure 6.5. Each cell from this derived grid will be referred to as a flood cell henceforth.

6.2.3. Water Surface Height Estimation

A planar water surface is fitted for each flood cell based on the estimated shoreline heights found within its bounds, combining estimates from both flooded and unflooded shoreline adjacent SAR pixels. A planar surface is chosen under the assumption that water surfaces are likely to be flat over small areas (Cian *et al.*, 2018a). Although the initial grid contains 1 km cells, each flood cell is buffered by 500 m in all directions to allow for a smoother transition between neighbouring cells.

Furthermore, the flood extent can on occasion exceed widths of 1 km, and the buffering of flood cells allows for a water surface to be fitted in locations where no shoreline is found within the initial flood cell.

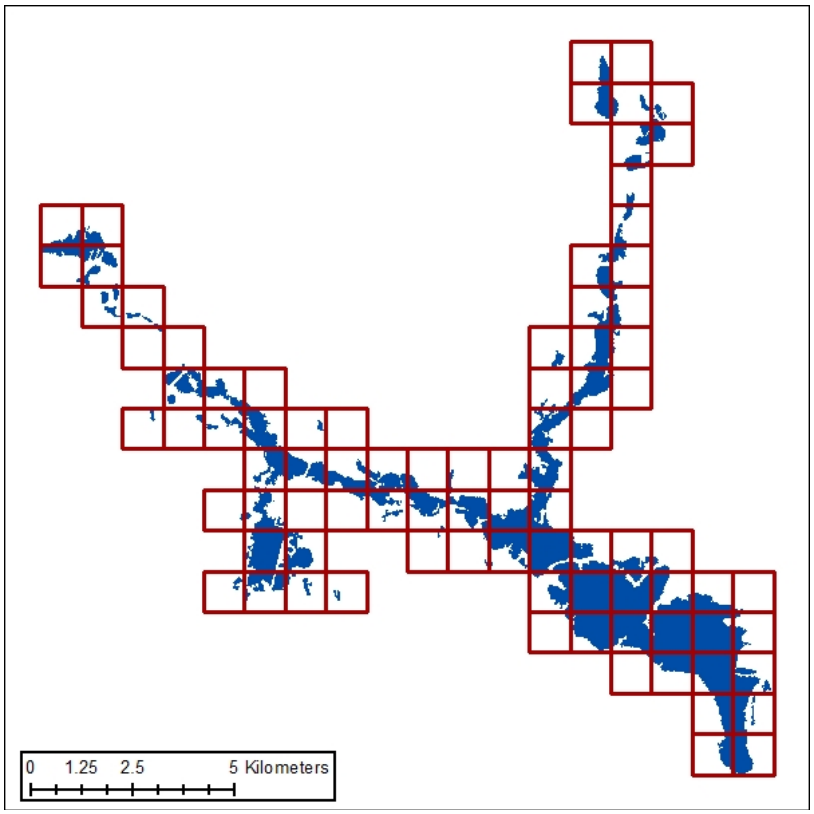

Figure 6.5. Example of 1 km flood grid covering the SAR observed flood extent. A local water surface is estimated for each flood cell, before combining into a continuous water surface.

At this stage, heights derived from SAR pixels that fall within 10 m of a permanent water body, urban areas or woodland regions are removed to account for inaccuracies in the flood boundary, and the subsequent under-estimation of height within the analysed SAR pixels. The histogram of the remaining shoreline heights within each flood cell are analysed to determine the most likely local water surface height (Figure 6.6). The ideal histogram will show a singular peak, giving a clear indication of the shoreline height. However, this is often not the case, and a series of rules have been developed to help guide the delineation of the water surface estimate. Firstly, a target range is determined to discount peaks at heights that are deemed unlikely. The lower boundary is defined as the median value of just the water SAR pixel height estimates, whilst the upper boundary is set as the 90th percentile value of the combined heights dataset. Analysis is subsequently undertaken to identify local histogram peaks within the target range. If a single peak is found then

this is taken as the water surface height. If two or more peaks are found, then the peak with the maximum density is used. If no peaks are found within the bounds then histograms of the wet and dry pixel heights are analysed separately, with the same aim and process of identifying peaks within the original target bounds, and determining the water surface height based on the number of peaks. If two or more peaks are found from the water and land datasets then the median value is taken as the water surface estimate (an example is shown in Figure 6.7). Any flood cells that do not produce a water surface height based on the histogram analysis detailed above are left blank, with a height estimate assigned during the focal filtering stage described below.

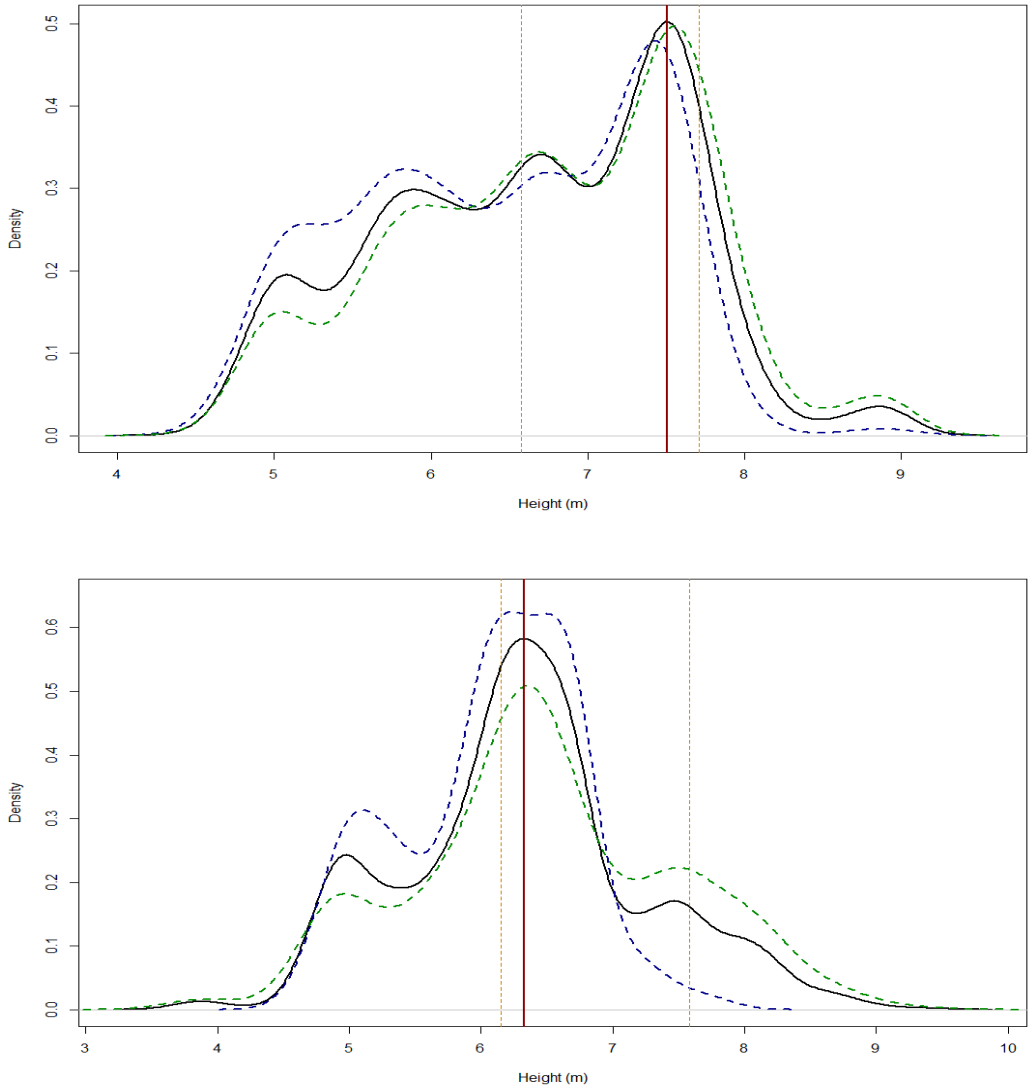

Figure 6.6. Example density histograms of SAR pixel height values found within buffered flood cell. Water surface value, shown in red, chosen as peak density of combined histogram (black) within search window (orange). Individual water-pixel height and land-pixel height histograms are shown in blue and green respectively.

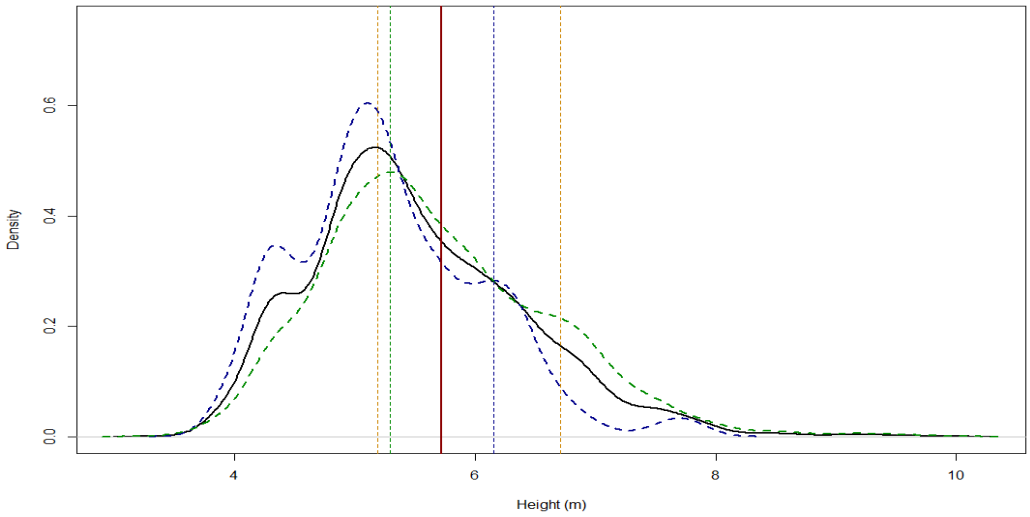

Figure 6.7. Density histograms for a flood cell where the combined SAR pixel heights (black) fail to produce a peak within the search window (orange). However, both individual land (green) and water (blue) have peak values, with the final water surface height taken as the median of these.

Although it is expected that the estimated water surface height for each flood cell will correspond closely to the neighbouring cells, this is not always the case. This is likely caused by local scale inaccuracies in the delineated flood boundary, and a subsequent under- or over-estimation of the water surface height. A two-pass focal smoothing has been applied across the flood cells. Firstly, each flood cell is compared to its adjacent cells, and if the height value of the target cell is either the maximum or minimum then the value is replaced with the median of the neighbours. This is to remove any large outliers that have occurred. The second pass of the filter replaces the target cell value with the median of the cell and its neighbours. This is to smooth the transition of flood cell values, resulting in a more realistic portrayal of water surface height across the flood by reducing any large gradients between cells, and minimising locations where water surface height increases downstream.

Once the final cell heights are calculated, the buffered flood cells (2 km^2) are rasterised at 10 m pixels, with the z value set to the final cell water surface height. The cells are then mosaicked into a continuous flood surface, with the median value taken in areas of overlap. Finally, the raster surface is focally smoothed to remove any remaining artefacts at the cell boundaries, with the median value taken from a search radius of 500 m in x and y directions.

6.2.4. Deriving Water Depth and Post-Processing

The derived water surface allows for water depths to be determined across the region via subtraction of the LiDAR DTM. This in turn can identify new regions of flooding that remained undetected from the SAR imagery, both within and outside of the flood extents presented in Chapter 5. Although some of these new regions represent correctly identified inundation, such as that under emergent vegetation at the flood boundary or in woodland and urban locations, others are likely to be false classifications. For example, the calculated water surface can suggest flooding across wide stretches of the floodplain that are in reality protected by an embankment, and was not inundated during the flood event being studied.

To refine the updated flood areas and remove any false classifications, the depth-derived water extents have been subdivided using the locations of flood defences and embankments. For each subdivision, the amount of overlap between the flood extents derived via the two methods (SAR observations and indirect estimate from derived water surface) is calculated. If the SAR-derived extent covers more than 50% of the depth-derived flood regions, than the expanded water extent is considered accurate. This process is completed a number of times, firstly selecting out all pixels with depth above 0 m, and subsequently reselecting those above 0.25 m, 0.50 m and 1 m. It was found that selecting all pixels with positive depth, combined with the required 50% overlap with the SAR flood extent, resulted in locations with observed inundation in the SAR imagery being flagged as false. This is due to low-level flooding causing a significant increase in extent compared to the satellite inundation maps. The error margins of the DTM (+/- 15 cm RMSE) along with the applied technique for estimating the water surface means that any low-level flooding is questionable. The additional assessment of flood extent at depths above 0.25 m, 0.5 m and 1 m is designed to maximise the identification of likely inundated sub-divisions by accounting for the uncertainty within the datasets and methods.

In addition to the identified flood sub-divisions, locations that are expected to have a water depth, namely permanent water bodies and the SAR identified flood extents, are considered correct if they have a flood depth greater than 0 m. Rivers are commonly surrounded by embankments, resulting in them being classed as their own sub-division in the process described above. Due to the SAR derived maps not containing rivers and lakes due to the change detection process, they remain

unidentified due to lack of overlap with the input extents. Regions identified in Chapter 5 as flooded are occasionally not selected if there is significant growth in the depth-derived flood extent, likely caused by an overestimation of the water surface height. The addition of areas of positive water depth from the input SAR flood extents results in a more accurate representation of the spatial occurrence of flooding. However, this produces the same limitations in the location of the flood boundary and the potential underestimation of flood extent as is found in the original SAR observations.

Finally, locations identified as having a positive water depth from the selected flood sub-divisions, permanent water bodies and input extents are merged to create an updated water extent, which in turn is used to mask the surface and depth datasets to allow for volume estimation solely using the locations where confidence in flood likelihood is high.

6.2.5. Calculating Flood Volume

After the depth maps have been edited to remove erroneously flooded locations, water volume is calculated for each pixel by multiplying the cell resolution by the calculated depth. These are summed to provide volume estimates for each sub-region. The subdividing of the flood locations for the Ouse catchment earlier in the processing chain allows for regional changes in water volume to be analysed, or full catchment analysis of the flood dynamics by combining the water volume values from all sub-regions.

6.2.6. Methodology Adjustments for SRTM

To determine methodological robustness in the absence of high-resolution ancillary datasets, regions 2 and 3 for the Ouse catchment on the 29th Dec, 1st Jan and 3rd Jan have additionally been processed using the SRTM DEM instead of the LiDAR DTM. Most of the processing steps are immediately transferrable when using the lower resolution terrain model. In particular, Sections 6.2.1, 6.2.2, 6.2.3 and 6.2.5 have not been adjusted apart from the change in terrain and vector datasets. It should be noted that the number of DEM height values found within each shoreline adjacent SAR pixel is greatly reduced, possibly to a single value. However, the percentile selection of estimated heights is not adjusted to allow for methodological consistency regardless of the underlying terrain data. The calculation of water depths in Section

6.2.4 is similarly applicable. However, the flood embankment based post-processing analysis of the newly derived depth locations has been changed, due to the primary dataset being UK specific. It should be noted that the embankment segmentation process outlined in Section 6.2.4 could be applied successfully to the SRTM derived depth locations within the UK, or in other locations with the relevant datasets.

An object-based probabilistic framework has been developed to ascertain the likelihood and accuracy of new flood locations, identified as having positive water depths from the SRTM water surface. Two parameters of equal weighting are created and combined, representing HAND and distance from the SAR observed flood locations. Figure 6.8 shows the Z-membership function (Pal and Rosenfeld, 1988) used to reclassify both variables, with values used for the *χ1* and *χ2* thresholds found in Table 6.1. HAND has been selected as a variable as it represents the height distance between the river and the pixel of interest, with lower HAND values representing the reduced water heights required to cause the inundation. HAND values of 1 m are given a score of 1 (high probability), with a score of 0 assigned to 20 m HAND. The closer to the SAR identified flood extents an area of positive water depth is, the greater the probability of the locations being connected during peak flood. Distances below 10 m are given a score of 1, with 500 m representing a score of 0. The individual variables are then combined to provide an overall probability map. Finally, the average value for each new depth-derived flood polygon is calculated to provide a probability of the area being accurately classified and belonging to the flood class.

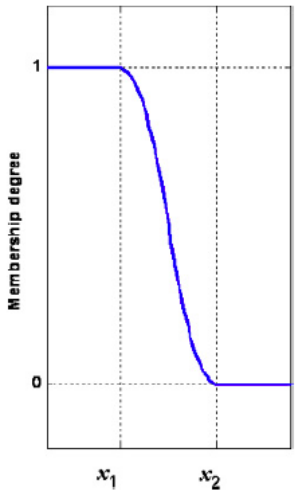

Figure 6.8. Z-membership function used in the probability classification. Image originally published in Pulvirenti *et al.* (2011).

	χ_1	χ_2
HAND (m)	1	20
Distance from SAR Flood (m)	10	500

Table 6.1. Probability thresholds selected for each variable dataset.

6.3. Results

6.3.1. Water Surface

The derived water surfaces have been compared to in-situ stage records at the time of each satellite pass. Twenty-one gauges have been used, spread throughout the Ouse and Aire catchments (Figure 6.9). Heights have been extracted for the gauge locations from the calculated water surfaces on six of the study dates. The 15th Jan has been excluded due to the large uncertainty caused by wet snow and frost SAR misclassifications, and the 25th Jan is not used due to the limited gauges covered by the water surface due to the reduced extent of flooding. In total 120 comparisons between river stage and water surface height are made. To allow for easier comparison, water surface heights have been adjusted at each gauge location using the local datum provided in the metadata by the EA (further information for each gauge supplied in Appendix C). Figure 6.10 shows the relationship between the two variables. There is a clear correlation between the datasets, albeit with some variability in accuracy, with an R^2 value of 0.798. However, the trend does not follow an $x=y$ relationship, with the derived water surface tending to overestimate height when the river stage is lower and underestimate at times of peak flows. The difference in relationship equates to 30 cm error from the $x=y$ at 1 m (observed trend equals 1.3 m) and 9 m (8.7 m).

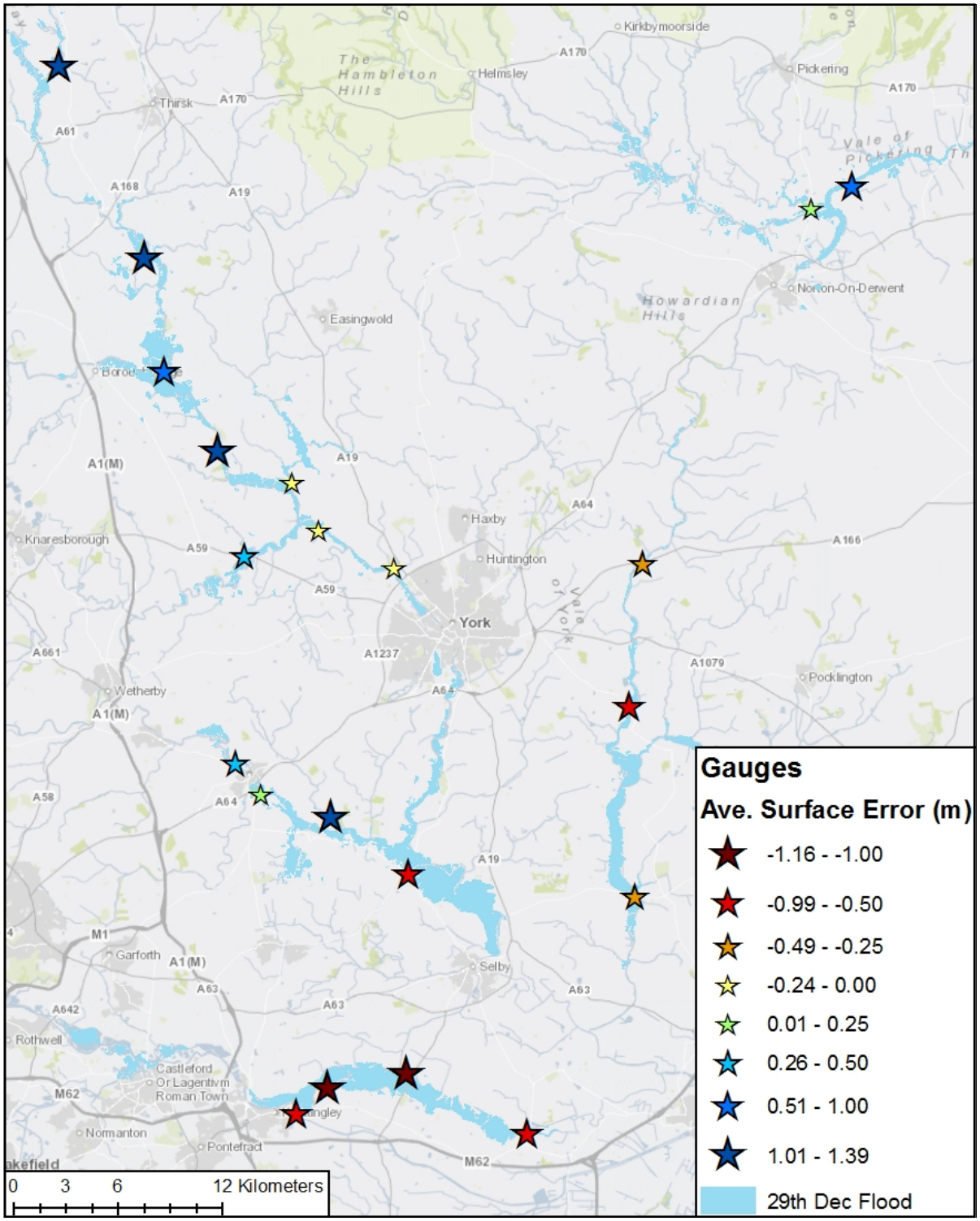

Figure 6.9. Gauge locations throughout the Ouse and Aire catchment, and average error between derived water surfaces and river stage across six dates. Minus numbers represent prevalent underestimation for the derived water surfaces, with positive number suggesting over-prediction.

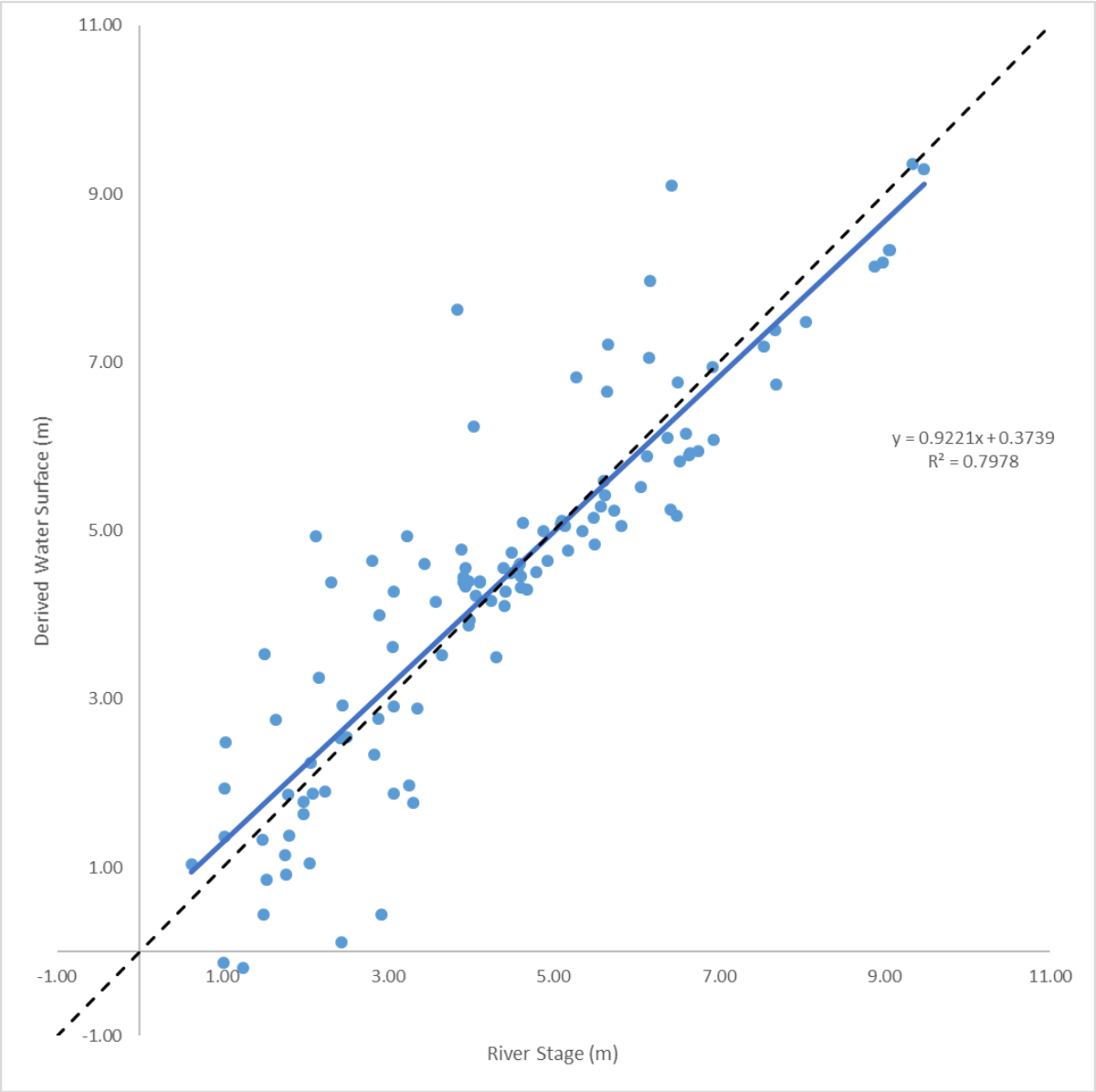

Figure 6.10. Relationship between the derived water surface heights (datum corrected) and river stage across 21 gauges for six imagery dates (n = 120). *x* = *y* shown as reference.

The accuracy between the in-situ and derived datasets varies with each gauge. Overall, the derived water surfaces have an average overestimation of 0.03 m, with a maximum overestimation of 3.79 m and underestimation of 2.47 m (Table 6.2). RMSE across all gauges is calculated as 0.98 m, ranging from 0.22 m to 1.68 m. Assessing the average error at each gauge individually shows the largest differences between the datasets occur in locations where inundation is more extensive (Figure 6.9). Furthermore, there is a tendency to over-estimate water surface heights in more upstream regions of the catchment, and under-predict in low-lying locations downstream.

Gauge	River	Difference (m): +ive = Water Surface Higher; -ive = River Stage Higher						Average Error (m)	RMSE
		Dec 29th	Jan 1st	Jan 3rd	Jan 6th	Jan 10th	Jan 13th		
Aldwark Bridge	Ure	3.79	0.05	0.11	-0.11	1.11	1.11	1.01	1.68
Beal	Aire	-0.46	-0.35	-0.42	-0.85	-2.47	-1.44	-1.00	1.25
Bolton Percy	Bolton Percy Drain	1.80	0.90	0.26	1.55	1.01	1.56	1.18	1.29
Bubwith	Derwent	-0.66	-0.01	-0.34	*No Data*	-0.49	-0.19	-0.34	0.41
Carlton Bridge	Aire	-0.81	-0.16	-0.49	*No Data*	-1.28	0.17	-0.51	0.72
Cawood	Ouse	-0.95	-1.31	-0.53	-0.70	-1.16	-0.77	-0.90	0.94
Chapel Haddlesey	Aire	-1.19	-0.61	-0.67	-1.05	-2.33	-1.14	-1.16	1.29
Crakehill Topcliffe	Swale	-0.02	1.70	1.16	0.28	*No Data*	2.07	1.04	1.31
Elvington Sluices	Derwent	-0.86	-0.73	-0.44	*No Data*	-0.81	-0.72	-0.71	0.73
Howe Bridge	Rye	-0.02	0.40	-0.09	*No Data*	*No Data*	0.17	0.12	0.22
Kirby Wiske	Wiske	0.56	2.80	1.08	0.48	*No Data*	2.03	1.39	1.66
Knottingley Bank	Aire	-0.13	-0.34	-0.20	-1.00	-1.54	-0.16	-0.56	0.77
Low Marishes	Derwent	0.01	2.20	-0.04	*No Data*	*No Data*	0.29	0.61	1.11
Moor Monkton	Ouse	-0.27	-0.28	-0.14	-0.09	-0.29	0.43	-0.11	0.28
Myton Bridge	Swale	-0.29	0.89	0.54	-0.14	0.24	1.83	0.51	0.88
Newton-on-Ouse	Kyle	*No Data*	-0.36	0.11	-0.40	0.02	0.46	-0.03	0.32
Skelton	Ouse	-0.24	-0.27	-0.30	*No Data*	-0.38	0.62	-0.11	0.39
Skip Bridge	Nidd	0.02	0.57	0.48	-0.08	0.16	1.21	0.39	0.59
Stamford Bridge	Derwent	-0.18	-0.71	-0.79	*No Data*	0.01	-0.74	-0.48	0.58
Tadcaster	Wharfe	0.08	1.44	0.34	0.91	-0.20	0.42	0.50	0.74
Tadcaster Sluices	Wharfe	-0.74	2.67	-0.35	-0.29	-0.57	0.02	0.12	1.17
						Total Average		**0.03**	**0.98**

Table 6.2. Difference between derived water surface height and river stage across 21 gauges.

The water surface can be used to assess how the slope of the flood changes both spatially and temporally. Locations of three transects along the Rivers Aire, Ouse and Derwent, are shown in Figure 6.11. The transects highlight the differing flood regimes occurring along each of the rivers. Flooding on the River Aire (Transect A) shows a gradual lowering of the water surface from the peak on the 29th Dec through to the 13th Jan (Figure 6.12). The middle third of the transects appear largely flat across all dates, with some steeper, potentially erroneous, gradients at the edges. Along the River Ouse (Transect B), water surface heights on 29th Dec are far above those seen on the following dates (Figure 6.13). All dates show a relatively steep decrease in water surface after the confluence of the Ouse and Wharfe Rivers (left of Figure), before presenting a flatter surface for the remainder of the transect. The four water surfaces calculated in January correspond closely to one another near the confluence, before becoming more distinct further downstream, with the 1st and 3rd Jan maintaining a higher water surface whilst the 10th and 13th showcase a steeper gradient as the water travels downstream. The River Derwent (Transect C) shows greater temporally consistency between image dates, which is expected considering the similarity between the input flood extents (Figure 6.14). However, the relative similarity between dates helps highlight some of the uncertainty and inaccuracies found within the methodology and results, as described below.

It should be noted that the calculated water surface is an estimate that has been derived using a methodology designed to be broadly applicable across varying geographical locations and flood events, based on input inundation data that is likely to contain inaccuracies. Accordingly, there are situations where the estimated water surface height for a flood cell is inaccurate, and the propagation of these errors can be observed in the cross-sections in Figures 6.12, 6.13 and 6.14. The observed steep surface gradients and the downstream increase in water surface height, as seen in some transects, are unlikely to be accurate. Closer inspection of the SAR derived flood extents and the DTM highlights some of the sources of error. An example is shown in Figure 6.15, which is located around the localised bump for the water surface on the 1st Jan along the River Derwent (Figure 6.14). Comparing the inundation extents from the 29th Dec and 1st Jan, there are additional areas of potential inundation located on relative topographic highs for the latter date. An example of a histogram of height values within an impacted flood cell is shown in Figure 6.16. Due to the width of the flooding in this location, three flood cells are

positively skewed by the additional flood locations, negating the use of focal filtering in attenuating the higher water surface estimates. Refinement of the input flood polygons shows an improved, lower histogram for selecting a water surface, with around half of the height values in the original histogram coming from the suspect locations (Figure 6.16). However, manual adjustment of input flood extents in suspect locations will be time-consuming, and alteration of the current automated flood selection technique to be stricter may result in accurate flood polygons being flagged as questionable elsewhere in the catchment, reducing the input into the presented workflow.

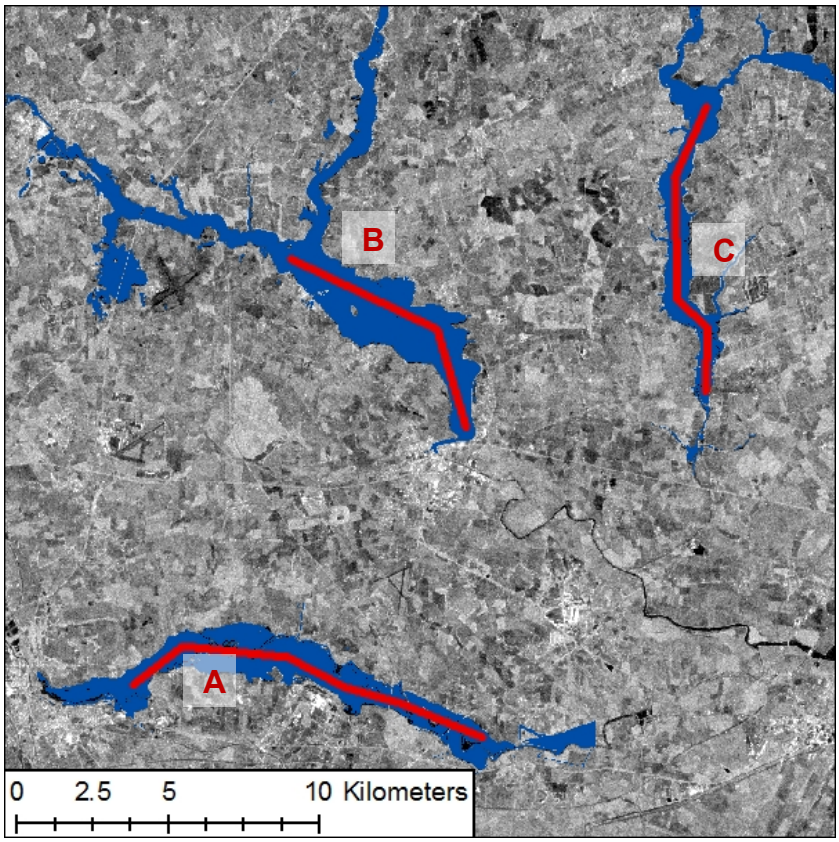

Figure 6.11. Location of transects in relation to the main body of flooding from 29th Dec along the Rivers Aire (A), Ouse (B) and Derwent (C).

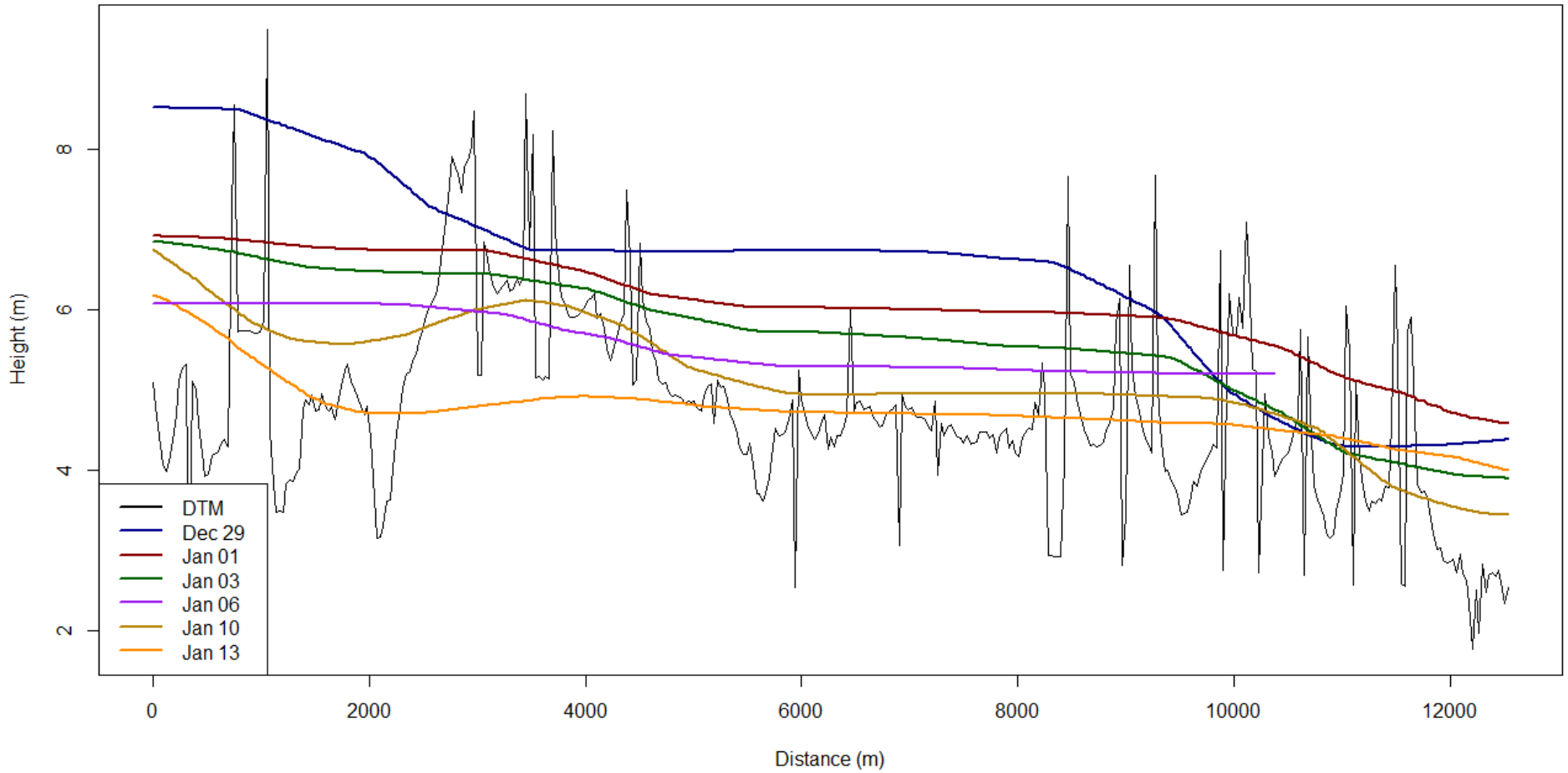

[163]

Figure 6.12. Transects for six of the image dates along the River Aire. Note the slow decline in water surface through time. Steep gradients in water surface and locations of increase are likely erroneous.

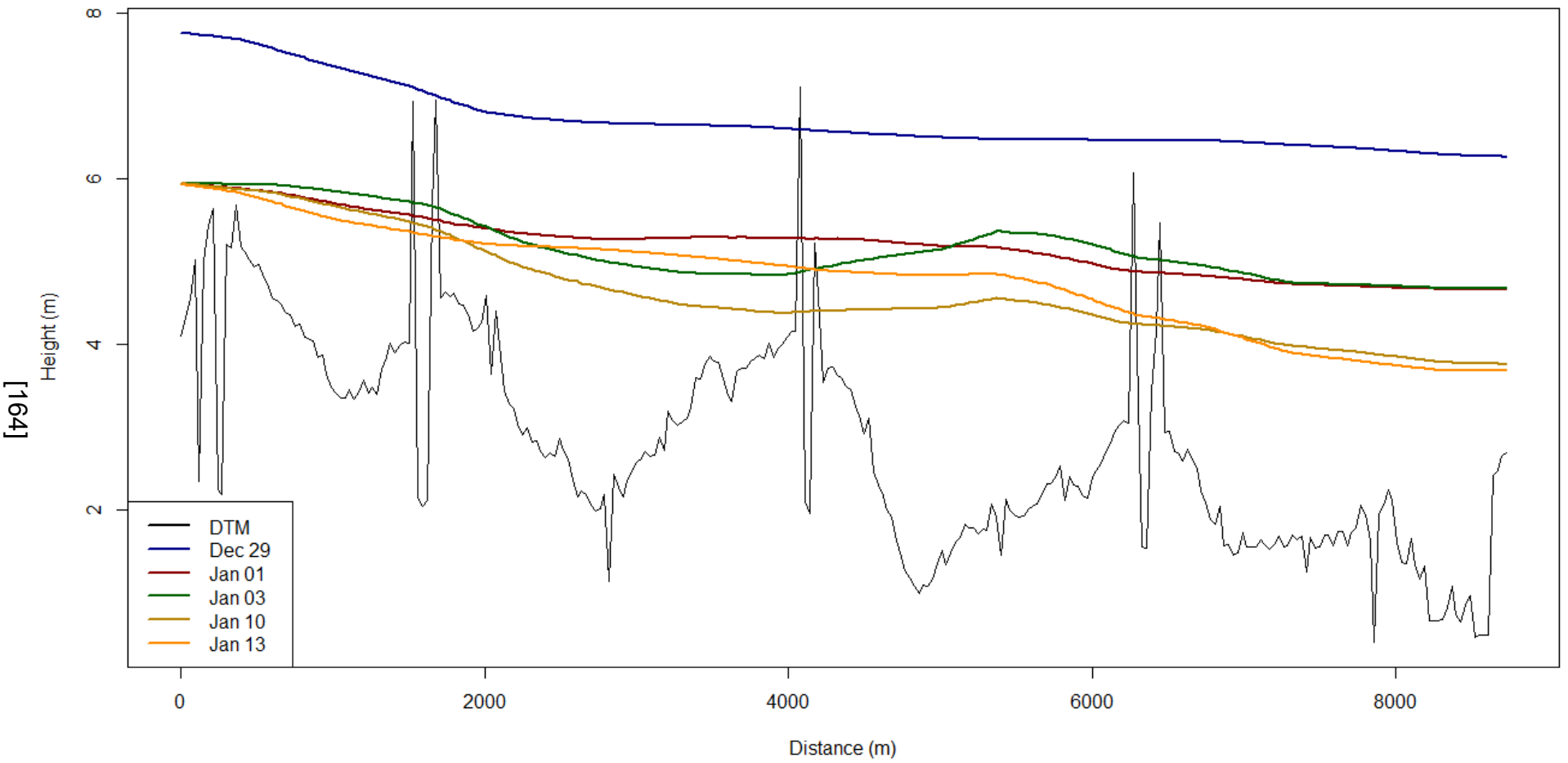

[164]

Figure 6.13. Transects for five of the image dates along the River Ouse. Note the extreme water levels observed on the 29th Dec compared to the more stable water levels on the following dates. Water levels drop more significantly with distance downstream between early and mid-January (right of image).

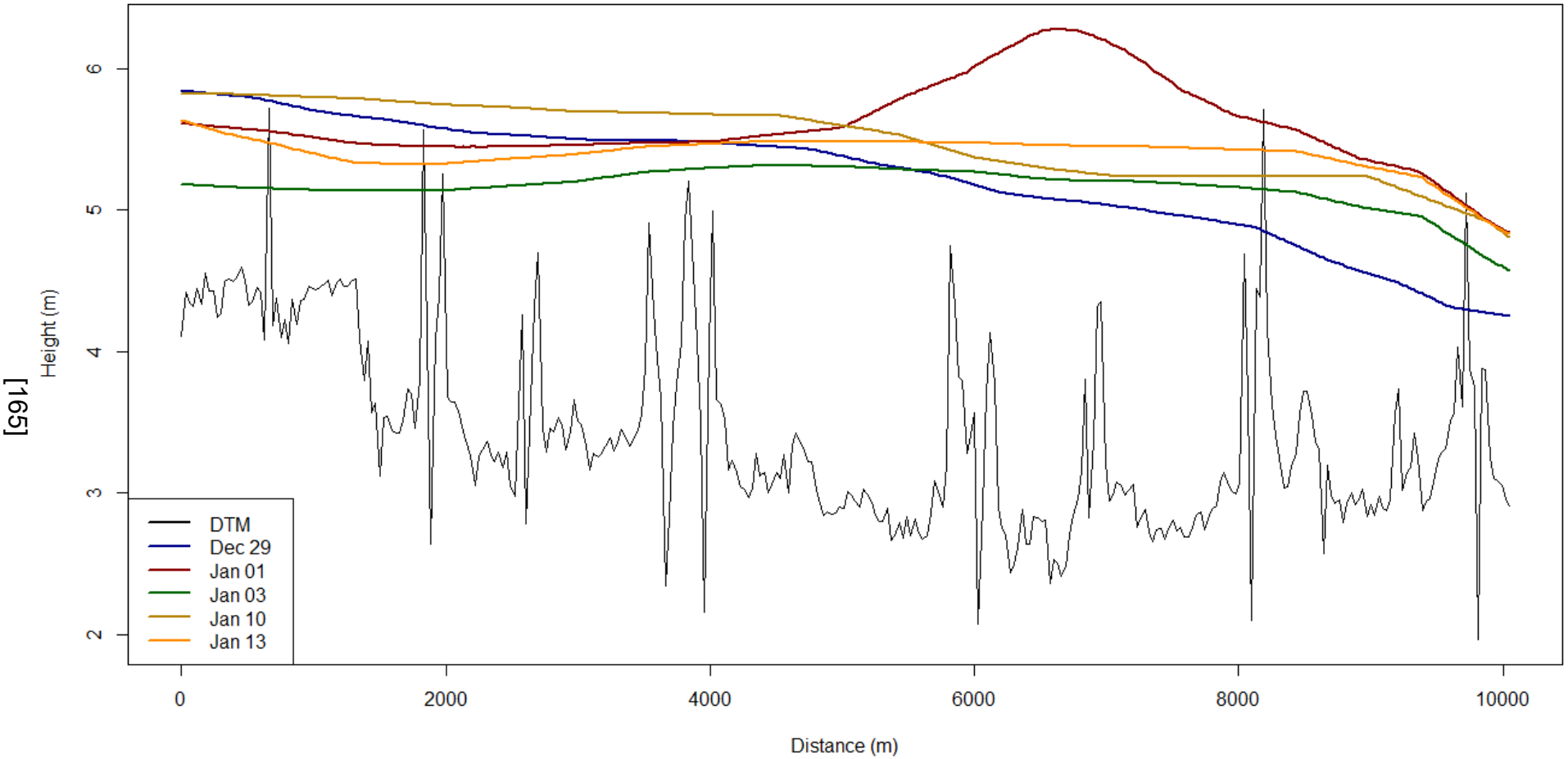

[165]

Figure 6.14. Transects for five of the image dates along the River Derwent. Overall water levels are largely consistent. Steep gradients in water surface and locations of increase, such as in the 1st Jan transect, are likely erroneous.

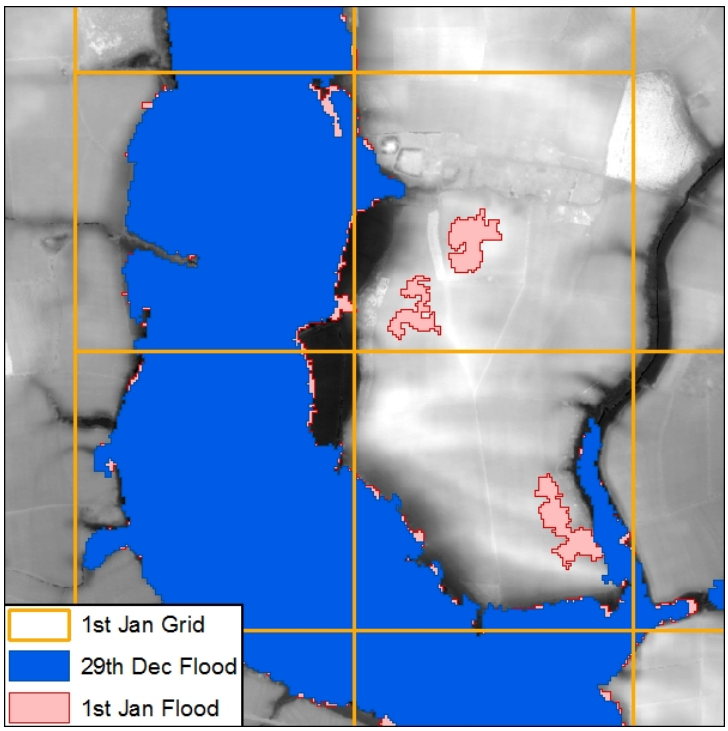

Figure 6.15. Comparison between the derived flood extents on the 29th Dec and 1st Jan for the section of the River Derwent, located where the water surface increases in Figure 6.14. Note the additional three distinct areas of flooding located on higher ground on the second date. These are either joined to the main body of flooding, or pass the selection technique due to their relatively large size and proximity to the river. The additional heights from the SAR cells in these locations impact the final water surface height for three of the buffered flood cells, limiting the ability of the focal filters to smooth the flood surface values.

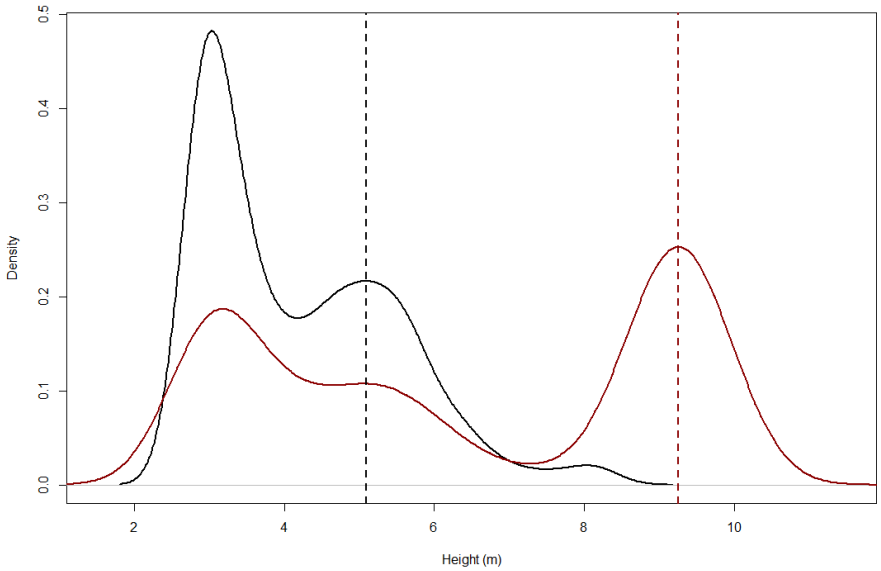

Figure 6.16. Histograms and derived water surface heights for a downstream flood cell from the River Derwent (located in the region shown in Figure 6.15) on 1st Jan, comparing all flood extents (red) with a manually edited dataset (black) with false classifications on higher terrain removed. Difference between estimated flood surfaces is 4.17 m.

6.3.2. Water Depth and Updated Water Extent

Water depth maps are produced by subtracting the DTM from the derived flood surface. Numerous locations that are not identified as flooded in the SAR imagery showcase a positive water depth. Post-processing of these locations, based around identifying and removing those areas protected by flood defences, is demonstrated in Figure 6.17. Overall, the technique sufficiently removes water depth regions that show no indication of being flooded in the satellite imagery. The requirement for numerous iterations, where inundation above increasing depths are compared to the SAR flood extents, is due to the inherent uncertainty in the SAR flood detection, water surface creation and DTM dataset. Solely using pixels with positive water depths results in numerous areas of SAR observed flooding being flagged as suspect. The iterative process strikes the balance between ensuring the inclusion of the SAR derived flooding, whilst restricting the false classification of protected locations. There is still an expansion of the flood extent, such as at the edge of the flood in the north-west of Figure 6.17, an area potentially impacted by emergent vegetation. Table 6.3 shows the amount of the Sentinel-1 derived flood extent that is similarly classified after post-processing of the water depth locations. On average, the updated water extents identify 90.1% and 88.6% of the SAR derived flood extent for the Ouse and Aire respectively. Differences are likely to be caused by false classifications within the SAR flood extents, or the under-prediction of the estimated water surface height.

Figure 6.18 shows how water depth changes over time, from peak flood through the initial recession, for the upper Ouse (region 2), lower Ouse (region 3) and Aire. Maximum water depths of up to 12 m are observed, although these tend to be rare, small groups of pixels, with more common localised maximum depths often not exceeding 8 m. As well as showing changes in depth, these images show the spatial retreat of floodwaters over time. For example, water surface area decreases significantly for the upper Ouse between the 1st and 3rd Jan, with a large portion of the flooding upstream of the confluence along the River Swale retreating. The lower Ouse shows more consistency in flood location and depth after the initial retreat after the 29th Dec, matching the temporal relationship observed in Figure 6.13. The Aire shows constant retreat through every date in the time series. On the 10th and 13th Jan, river locations are often not highlighted as having water depth due to the reduced extent of flooding inputted into the algorithm. This subsequently reduces the

coverage of the flood grid, resulting in less permanent water body locations being analysed.

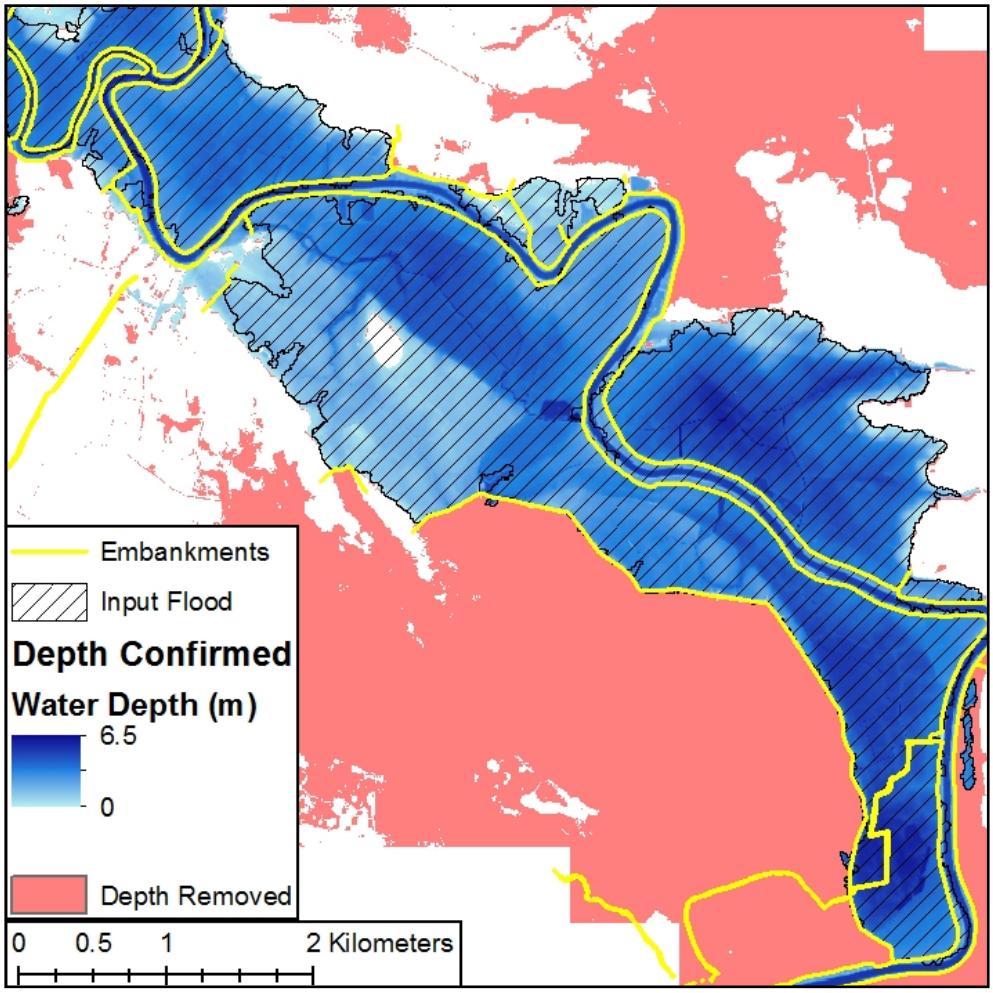

Figure 6.17. Editing of locations with water depth based on the locations of embankments. These are used to divide the potential flood region, with sub-area that have limited overlap with the input SAR observed flood extents flagged as unlikely and removed. Note the increase in water extent compared to the SAR flood maps towards the north-west of the image.

	Dec 29th	Jan 1st	Jan 3rd	Jan 6th	Jan 10th	Jan 13th
Ouse	90.31	88.78	89.53	92.15	92.17	87.70
Aire	92.19	93.53	92.72	83.12	87.28	82.74

Table 6.3. Percentage of SAR observed flood extents that overlap with the updated water extents, derived via water surface and depth estimation, and subsequently refined based on embankment locations.

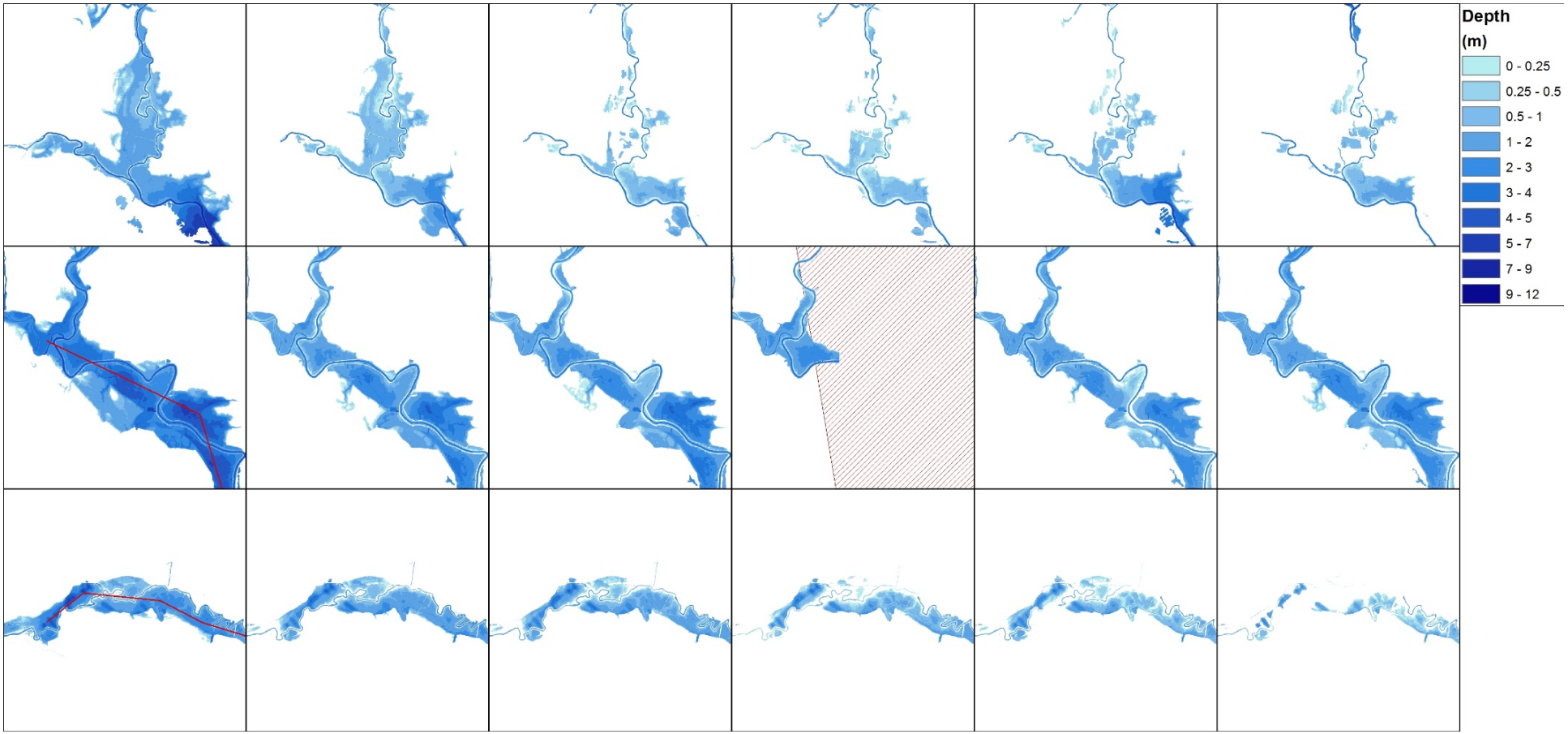

Figure 6.18. Changes in water depth over time for the upper Ouse (region 2, top), lower Ouse (region 3, middle) and Aire (bottom). Dates shown (from left) are 29th Dec, 1st Jan, 3rd Jan, 6th Jan, 10th Jan and 13th Jan. Area with no satellite coverage shown for the lower Ouse on 6th Jan, resulting in a reduced water extent. Transect locations shown for the lower Ouse and Aire on the 29th Dec panels, referencing Figures 6.13 and 6.12 respectively.

Despite the overarching pattern of flood retreat over time, there are situations where inundation has visibly increased. For the upper Ouse, water depths are greater on the 10th Jan than the 6th Jan. Similarly, there is a slight increase in depth and extent on the 13th Jan for the lower Ouse, compared to the 10th Jan. There are approximately 84 hours between the images on the 10th and 13th Jan. Rainfall data suggests that there were minimal inputs across the Ouse catchment after the intense event observed on the 9th Jan. It is likely that the increase in depth and extent at the two locations is caused by the same flood wave travelling downstream.

6.3.3. Water Volume

Figures 6.19 and 6.20 show how the water volume changes throughout the study period for the cumulative Ouse and Aire catchments respectively. Also shown is the derived water extent, river stage and cumulative catchment daily rainfall calculated from gridded UKCP09 data.

It should be noted that the reported volumes and the changes between image dates may be unrepresentative of the actual water dynamics in the catchment. There are three primary reasons for this. Firstly, the satellite imagery does not provide full catchment coverage with every orbit track, and volumes have only be calculated for flood-prone sub-regions instead of the whole catchment. This means that either the image acquisition parameters or the defined study region may remove areas of inundation, resulting in under-prediction of catchment water volume.

Furthermore, the flood grid used to calculate water surfaces, depths and volumes is recreated around the main locations of fluvial flooding on each image date, meaning the spatial extent of the flood grid and analysed area changes depending on the satellite-derived inundation extent. This results in a different proportion of permanent water locations being covered by the flood grid on each date, which can result in inconsistencies when assessing the trend in volume. Table 6.4 shows the total permanent water bodies in each catchment sub-region, and the percentage of these that fall within the flood grid on each image date. As expected, the maximum flood extent on the 29th Dec results in the greatest amount of permanent water bodies being included by the flood grid. On average, 55% of water bodies are covered by the flood grids, with Ouse regions 4 and 5 showing the lowest (45.5%) and highest (67.9%) averages respectively.

The final source of uncertainty with the reported volumes is the poor representation of bathymetry within the DTM. Commonly, water pixels within terrain models display the water surface height at the time of data acquisition. The depths calculated for these pixels will not be representative of the full water depth to the river bed, and will subsequently cause an under-estimation of volume in these locations.

To help understand the flood dynamics considering the lack of river and lake bathymetry, and the variable coverage of permanent water bodies in the developed methodology, Figures 6.19 and 6.20 show the trends for extent and volume with the permanent water bodies both included and removed. These trends match closely, and the discussion below and in Chapter 8 will primarily consider the changes in flood dynamics as being reliable, albeit with caveats due to poor satellite coverage and temporal resolution.

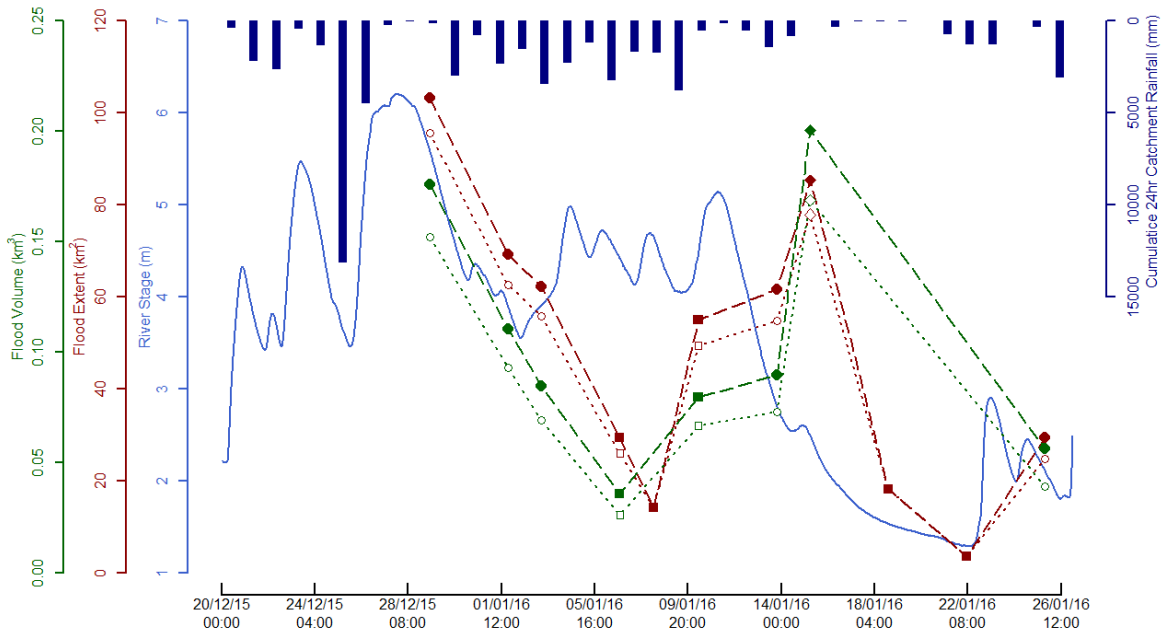

Figure 6.19. Water volume for the Ouse catchment compared to flood extent (depth derived where available, SAR derived if no water surface was created), river stage (from Myton Bridge gauge) and cumulative gridded 24 hour rainfall across the whole catchment (UKCP09). For water extent (red) and volume (green), circle points represent full coverage of the five study regions, square points show partial coverage, and the diamond points highlights Jan 15th, where the SAR data suffers from significant misclassification due to wet snow and frost. For this date, flood extent locations used to derive the volume are selected based on their temporal consistency with previous flood dates, instead of the full classification delineated in Chapter 5. The dotted lines and unfilled points represent the flood extent and volume with permanent water locations removed. Note that not every date with flooding has had a volume calculated due to the geographical coverage in relation to the flooding. Rainfall on each date is for 9 am (date – 1) to 9am (date of interest).

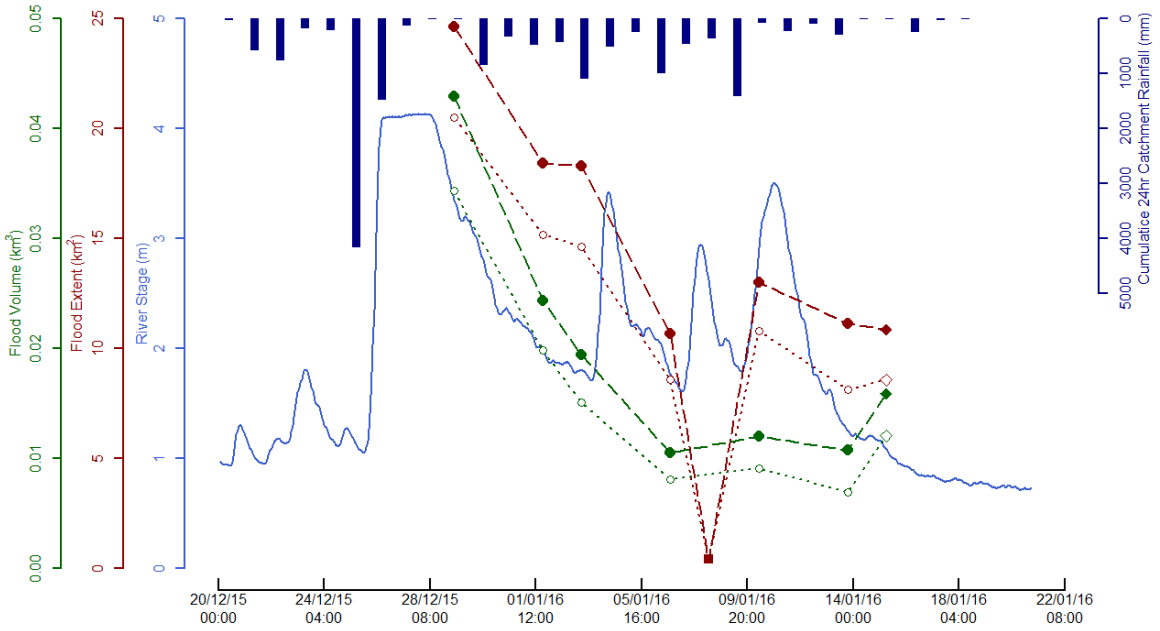

Figure 6.20. Water volume for the Aire catchment in comparison to flood extent (depth derived where available, SAR derived if no water surface was created), river stage (from Beal gauge) and cumulative gridded 24 hour rainfall across the whole catchment (UKCP09). For water extent (red) and volume (green), circle points represent full coverage, square points show partial coverage, and the diamond points highlight the Jan 15th, where the SAR data suffers from significant misclassification due to wet snow and frost. For this date, flood extent locations used to derive the volume are selected based on their temporal consistency with previous flood dates, instead of the full classification delineated in Chapter 5. The dotted lines and unfilled points represent the flood extent and volume with permanent water locations removed. Note that not every date with flooding has had a volume calculated due to the geographical coverage in relation to the flooding. Rainfall on each date is for 9 am (date – 1) to 9am (date of interest).

	Water Bodies (km^2)	% Within Flood Grid used to Calculate Water Surface								Average %
		29th Dec	1st Jan	3rd Jan	6th Jan	10th Jan	13th Jan	15th Jan	25th Jan	
Aire	7.78	65.4	58.1	62.9	49.5	49.1	57.5	42.4	---	55.0
Ouse 1	1.61	72.0	50.9	53.4	48.4	---	46.6	75.8	43.5	55.8
Ouse 2	4.49	69.5	55.0	55.7	*51.4*	54.3	57.0	67.5	29.8	55.0
Ouse 3	3.40	76.2	66.2	69.1	*30.6*	67.9	69.1	72.1	45.0	62.0
Ouse 4	1.76	54.5	46.0	47.7	---	---	47.7	53.4	23.9	45.5
Ouse 5	2.54	71.3	65.0	66.5	---	72.0	70.1	71.7	59.1	67.9
	Average %	68.2	56.9	59.1	*45.0*	60.9	58.0	63.8	40.2	

Table 6.4. Permanent water bodies (OS Vector Map Local) found within each catchment sub-region, and the percentage of these covered by the flood grid on each image date. Percentages in italics represent regions without full satellite coverage on the date shown.

As expected the trends for both extent and volume are similar. Peak flooding is observed on the 29th Dec, caused by a large amount of rainfall across both catchments on the 25th and 26th Dec, the impact of which is clearly seen in the gauge

data. Peak extents for the Ouse and Aire catchments are approximately 100 km^2 and 25 km^2 respectively, producing volumes of 0.17 km^3 and 0.04 km^3.

In the Ouse catchment, there is a decreasing trend in flood magnitude for the two dates following the peak flood. Water extents reduce to 70 km^2 and 60 km^2 on the 1st and 3rd Jan respectively, correlating to volumes of 0.11 km^3 and 0.08 km^3. This is despite there being a prolonged period of rainfall from the 30th Dec onwards, up until the 9th Jan. The rainfall stabilises the river stage between 4 m and 5 m, although there are small fluctuations in river flow corresponding to more intense rainfall events. Unfortunately, the majority of the SAR images captured during this time have limited coverage across the catchment. Water extent and volume on 10th Jan is similar to the 3rd Jan despite the reduced coverage available for this date, with a water extent of 55 km^2 and a volume just below 0.08 km^3. Values for the 13th Jan, which has full coverage, approximately match those from the 3rd Jan. Overall this suggests the catchment system and the floodwaters reached an approximate equilibrium during this time, with rainfall inputs equating to flow outputs.

The Aire catchment shows a similar overall trend, although there are occasional differences observed between the rate of recession in the water extent and volume with the data including permanent water bodies. An example of this is found on the 3rd Jan. The water volume shows a decreasing trend from the 29th Dec through the 1st and 3rd Jan, including a decrease of around 0.005 km^3 (20% of the volume calculated for the 1st Jan) between the 1st and 3rd. However, water extents remain more consistent during this time, with only a decrease of 0.15 km^2 (less than 1% of the extent on 1st Jan). Closer inspection of the water surfaces on these dates shows that the 1st Jan has a higher water surface for the majority of the Aire study region, which corresponds with the change in volume. The consistency in extent between the dates is due to an increased number of flood cells within the grid covering the SAR inundation on the 3rd Jan, resulting in a water surface being calculated over a wider geographical extent. As a consequence, there is increased inclusion of the permanent water bodies found in the Aire catchment on the 3rd Jan compared to the 1st Jan (Table 6.4). This counteracts the reduced flood extent elsewhere in the region which results in the lower water surface height. The trend for the flood extent with permanent water bodies removed shows a steeper decrease earlier in the time series, although still not matching the gradient of the volume reduction. Similar to the

Ouse catchment, water extents and volumes approximately stabilise between the 6th and 13th Jan. Gauge records show a more sensitive response to the rainfall inputs at the time than in the Ouse catchment, however, this has minimal impact on the flood dynamics observed.

As mentioned in Chapter 5, the imagery from the 15th Jan is subject to misclassification due to wet snow and frost. Visual inspection has suggested that the inundation in the immediate floodplain shows a slight decrease in extent, with the majority of new classifications occurring away from these regions. For the analysis is this chapter, flood extents that do not have temporal consistency with the inundation from previous image dates are flagged as spurious and removed from the dataset used to derive the water surface. These attempts to restrict the inclusion of false classifications appear to have produced inconsistent results. Updated water extents in the Aire catchment are comparable to the preceding dates, although the volume shows an increase of almost 50% from the 13th Jan image, suggesting an overestimation of the water surface height. In the Ouse catchment, there is still a strong peak in both water extent and volume on the 15th Jan. Based on these results, it appears that the selection of flood extents based on the temporal consistency of inundation still results in erroneous classifications persisting.

By calculating water volumes and extents for separate regions throughout the Ouse catchment it is possible to identify patterns in water movement between image dates. Figure 6.21 shows the percentage change in water extent and volume from the values calculated on the previous image date using the results with the permanent water bodies removed. The top graph shows Ouse regions 1-3, covering the main watercourse in the catchment. Similar trends are observed for all three regions between the 1st and 6th Jan, with a fast initial decline on the 1st Jan, and a more steady retreat afterwards. The maximum initial decline for water extent was found in region 1 (-58%) and for volume is observed in region 2 (-66%). A difference in pattern is observed on the 10th Jan, with region 2 showing an increase in both water extent and volume, whereas region 3 shows a continuing decrease. Region 1 has no coverage on the 10th Jan. Both region 1 and 3 show increases on the 13th Jan, with region 2 decreasing. It can be hypothesised that if region 1 had coverage on the 10th Jan, that a similar increase in extent and volume would be seen as is shown for region 2, before a subsequent decrease on the 13th Jan. This potentially highlights

inter-catchment water movement, with an increase in flooding in the upstream portion of the river on the 10th Jan, before the water travels downstream for the 13th Jan causing the increases in extent and volume observed in region 3.

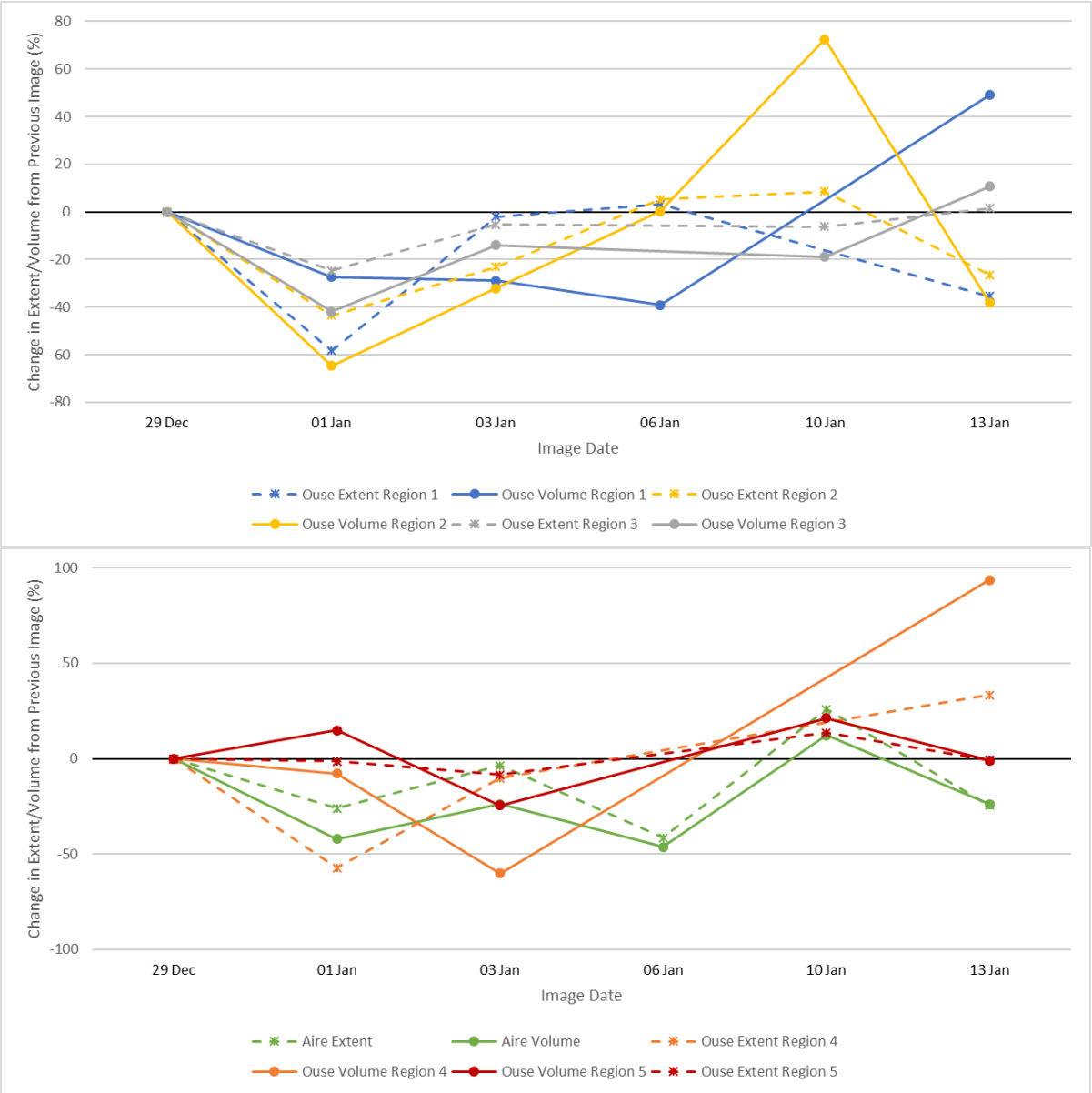

Figure 6.21. Changes in water extent (dashed lines) and volume (solid lines) as a percentage compared to the previous image date between Dec 29th and Jan 13th. Values shown are with permanent water bodies removed. Top graph shows the main River Ure/Ouse branch in the Ouse catchment. Bottom graph shows the River Derwent branch of the Ouse catchment and the River Aire. Dec 29th values shown as 0 for extents due to the extreme increase in flood extent from the previous imagery date (Dec 25th or 27th) across many regions. Volumes first calculated from Dec 29th onwards, resulting in no prior values to calculate change from. Flood regions shown in Figure 6.3.

The water extents and volumes for region 5 of the Ouse catchment, shown in the bottom half of Figure 6.21, are a lot more consistent, with the minimum observed water extent and volume equating to 88% and 76% of the maximums observed. Region 4 shows some highly variable changes, in particular on the 13th Jan where water volume increases by 94%. However, it should be noted that there is no coverage on the previous two imagery dates (6th and 10th Jan) and the amount of increase is likely to be more gradual than is observed. As there is only a single region in the Aire catchment, changes in extent and volume match those observed in Figure 6.20, with decreases throughout the studied period apart from an increase of 26% (extent) and 12% (volume) on the 10th Jan.

6.3.4. Comparison between LiDAR and SRTM Results

The differences between the water surfaces calculated using the LiDAR DTM and SRTM DEM throughout Ouse regions 2 and 3 on the 29th Dec are shown in Figure 6.22. The SRTM water surface has a maximum increase of 3.42 m and a deficit of 4.61 m when compared to the LiDAR-derived surface. It should be noted that the areas of largest variations are located at the edge of the flood grid away from the SAR flood extents, with the largest difference inside the observed inundated area being 1.53 m. On average, the SRTM water surface is 0.03 m lower than the LiDAR surface, increasing to 0.27 m when restricted to the SAR flood extents.

The spatial patterns broadly show the LiDAR surface producing a higher water surface in the downstream portion of the study area, and the SRTM producing increased heights further upstream. These patterns can be directly linked to the spatial resolution of the terrain models. For example, the LiDAR water surface shows an increased height, approximately ranging between 0.7 m and 1.3 m, downstream of the confluence of the Ouse and Wharfe Rivers in the south of Figure 6.22. The SAR derived flood extents closely follow the embankments in this region (see Figure 6.17), with these surface features visible in the LiDAR data, whilst being unrepresented in the lower resolution SRTM. When analysing the height values found within shoreline and embankment adjacent SAR pixels, the LiDAR height estimates include the presence of the embankment. This will subsequently produce a higher SAR pixel height estimate than the SRTM, which provides a value based purely on the floodplain height, subsequently resulting in a higher overall water surface from the LiDAR in the region.

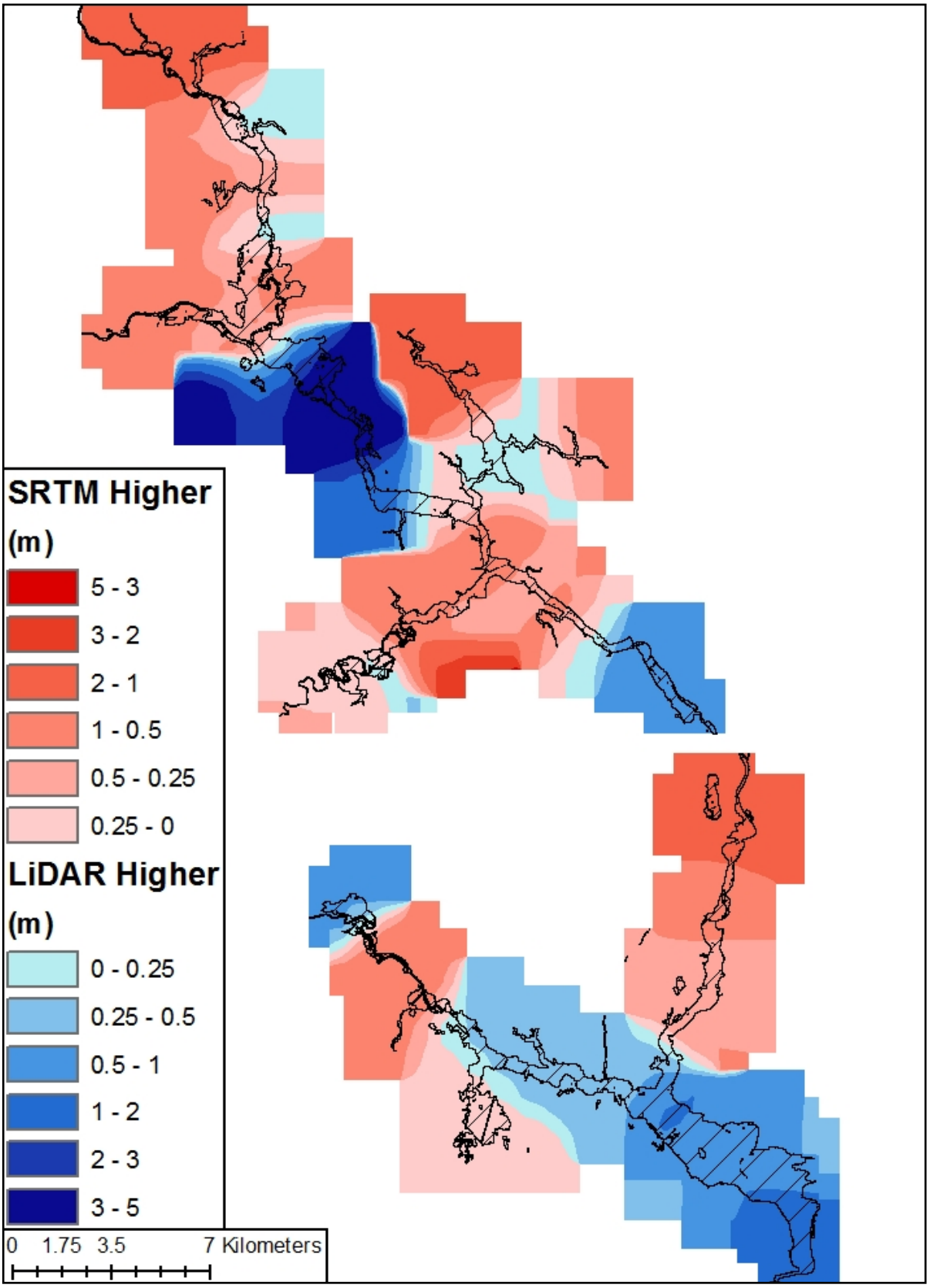

Figure 6.22. Comparison between the heights of derived flood surfaces for Ouse regions 2 and 3 from EA LiDAR DTM (with high resolution vector mask) and SRTM 1 arc-second DEM (and low resolution vector mask) for the 29th Dec. Input, gap-filled flood extents show in black as reference.

Further upstream there are areas where the SRTM produces a higher water surface. The edge of the floodplains in these areas tend to be defined by steeper gradients. When analysing heights within a shoreline adjacent SAR pixel, the overlapping LiDAR pixels are generally restricted to the approximate boundary of the SAR pixel due to their higher resolution. However, the lower resolution of the SRTM compared to Sentinel-1 results in an increase in the effective geographical area analysed when estimating the water surface height. The pixel alignment between the datasets can result in SRTM cells that have minimal overlap with the SAR pixel being included in the analysis. In regions of steeper gradients, this can result in an increased range of potential heights, which may include values that are 10's meters away from the SAR shoreline when viewed in the LiDAR data. The larger height range results in increased individual SAR pixel water height estimates, subsequently creating a higher SRTM water surface in upstream locations.

Table 6.5 provides a comparison between the SAR observed flood extents and the updated depth-derived water extents calculated from both the LiDAR and SRTM datasets. On average, the SRTM results successfully identifies 86.3% of the SAR flood extent, a reduction of 6.9% compared to the LiDAR. The largest difference in percentage is found for Ouse region 3 on the 29th Dec, where the LiDAR results identify 97.5% of the SAR extent compared to 84.8% from the SRTM. The SRTM primarily fails to identify flooding in two locations, the first of which is located in the embankment constrained floodplains after the confluence of the Ouse and Wharfe Rivers. As discussed previously, the SRTM often produces a lower water surface in locations with embankments, and in this case results in reduced depth-derived flooding. This can be seen in Figure 6.23, with the general patterns of depth being similar when using the two terrain models. However, there are edge location in the SRTM that are above the water surface, which are identified as flooding in the SAR and LiDAR. The second region of SRTM depth under-prediction is located on the River Wharfe close to Tadcaster (south-west of Figure 6.22). This SRTM water surface is approximately 0.2 m higher in this location. However, the increased variability in the SRTM DEM caused by the presence of buildings and trees, which have been removed in the LiDAR DTM, results in some pixels not having sufficient depth to be classed as flooded.

Date	Region	SAR Derived Flood Extent km²	LiDAR Depth-Derived Extent			SRTM Depth-Derived Extent					LiDAR (Depth Derived) - SRTM Extent Difference		
			km²	SAR Extent Match %	New Flood km²	SAR - SRTM Extent Match		Additional Area km²			Extent Match	Incl. Prob. > 0.9	Incl. Prob. > 0.8
						km²	%	Prob > 0.9	Prob > 0.8	Prob > 0.7	%	%	%
29th Dec	Ouse 2	23.6	32.0	91.2	10.5	20.6	87.4	8.7	10.0	12.1	64.4	91.6	95.6
	Ouse 3	24.5	27.1	97.5	3.2	20.8	84.8	2.6	3.6	12.5	76.7	86.3	90
1st Jan	Ouse 2	12.4	18.7	88.9	7.7	10.5	84.8	2.6	10.3	15.6	56.1	70.1	111.2
	Ouse 3	17.3	23.3	95.8	6.7	15.0	86.6	2.6	3.6	11.3	64.4	75.5	79.8
3rd Jan	Ouse 2	10.1	14.9	90.1	5.8	8.6	85.1	4.2	10.9	12.9	57.7	89.9	130.9
	Ouse 3	17.2	22.2	95.6	5.8	15.3	89.2	2.5	3.1	12.9	68.9	80.2	82.9
			Average %	93.2		Average %	86.3			Average %	64.7	81.6	98.4

Table 6.5. Similarity between SAR observed flood extents and LiDAR and SRTM derived locations of water depth.

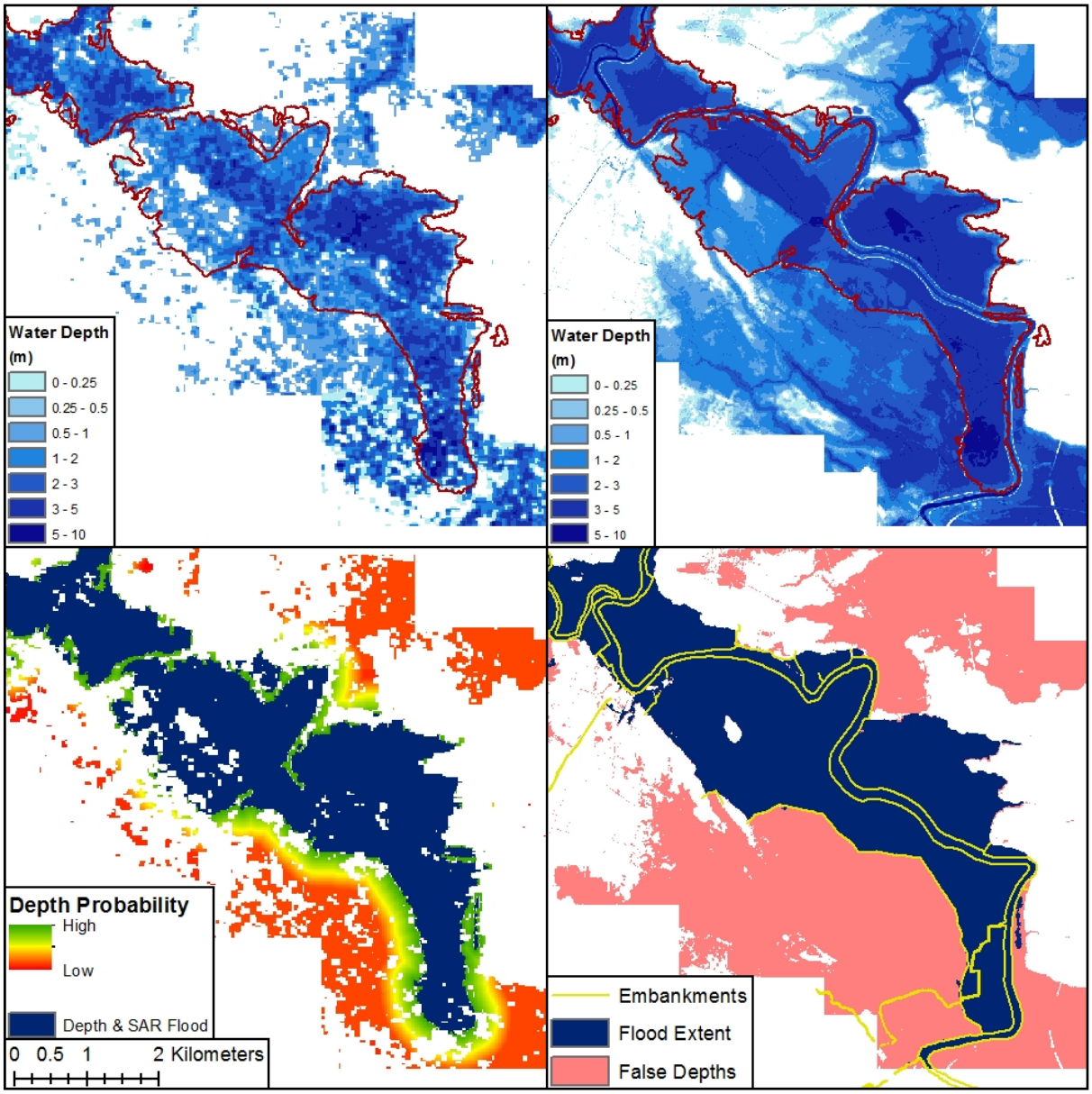

Figure 6.23. Locations of positive water depth derived from low resolution (top left) and high resolution (top right) terrain and vector datasets, with SAR flood extents shown in red for reference. Bottom row shows methods for refining newly identified areas of water depth to determine their likelihood. Bottom left shows pixel-based probability of inundation for the lower resolution datasets (see Figure 6.24), and bottom right shows the embankment segmentation method for higher resolution data (see Figure 6.17).

A probability framework has been developed to determine the likelihood of new areas of water depth belonging to the flood class. This acts as a replacement to the embankment segmentation method applied to the LiDAR depth results. A comparison between the two methods is provided in Figure 6.23, with a breakdown of the probability variables shown in Figure 6.24. The HAND variable map shows a large proportion of the shown area (Ouse region 3) having a high probability due to the low-lying nature of the terrain. This results in widespread areas of the final

probability map scoring in the region of 0.4 to 0.5. Scores are higher closer to the SAR flood extents due to the distance variable membership being above 0. An object-based assessment of the average flood probability has been used to determine the overall likelihood of new depth areas being inundated. Higher scores (0.8 and above) are only found close to the satellite-derived flood extents, with moderate scores (0.6 to 0.8) found for polygons that extend from the edge of the identified flood to further than 500 m distance. A pixel-based approach would produce variable probabilities across single flood areas, including high probability pixels close to the SAR observed inundation. However, given the flat terrain it is likely that the flooding would be consistent across the areas, justifying the use of an object-based classification.

The extent match between the LiDAR-derived flood extents (including the locations identified by the embankment based post-processing) and the SRTM-derived flood areas, with the inclusion of flood polygons of varying degrees of probabilities, are shown in Table 6.5. The locations of SRTM water depth within the SAR observed flood boundaries equates to an average of 64.7% of the LiDAR-derived inundation. The addition of probabilities above 0.9 and 0.8 to the baseline SRTM flood areas produces respective average agreements of 81.6% and 98.4% with the LiDAR extents. However, there is a lot of variability in the degree of correlation across the different dates for the two regions. For example, with probabilities over 0.8, the level of agreement ranges between 79.8% and 130.9%. It is unlikely that the lower resolution SRTM will produce a more reliable flood map than those calculated from the higher-resolution DTM, and additional flood locations outside the LiDAR extents are of questionable quality.

The comparison between SRTM and LiDAR water volumes show similar patterns to the water extent (Table 6.6). There are regions that show a greater improvement in the percentage agreement for flood extent with the inclusion of additional SRTM probabilities compared to the corresponding water volume. For example, with the inclusion of new flood areas at probabilities greater than 0.9, Ouse region 2 on the 29th Dec has an increase in flood extent match of 27.2%, compared to 15.1% for volume. The underlying cause of these differences is likely due to the SRTM DEM being a measurement of the surface, including features such as buildings and trees, as opposed to the LiDAR DTM which has been processed to provide a

representation of the ground terrain. The SRTM will have regions of pixels with an increased height compared to the LiDAR, resulting in reduced water depth. Similarly, the LiDAR will better represent any localised terrain features which are too small to be captured in the SRTM dataset. These small scale variations can result in a large difference in volume, even when calculated from similar flood extents. This can also work in reverse, shown by Ouse region 2 on the 1st Jan, where the SRTM volume provides a closer agreement to the LiDAR compared to the water extent at 0.9 probability. Individual adjustment of the probability threshold for each region on each date is likely to produce a closer match between the datasets for both water extent and volume.

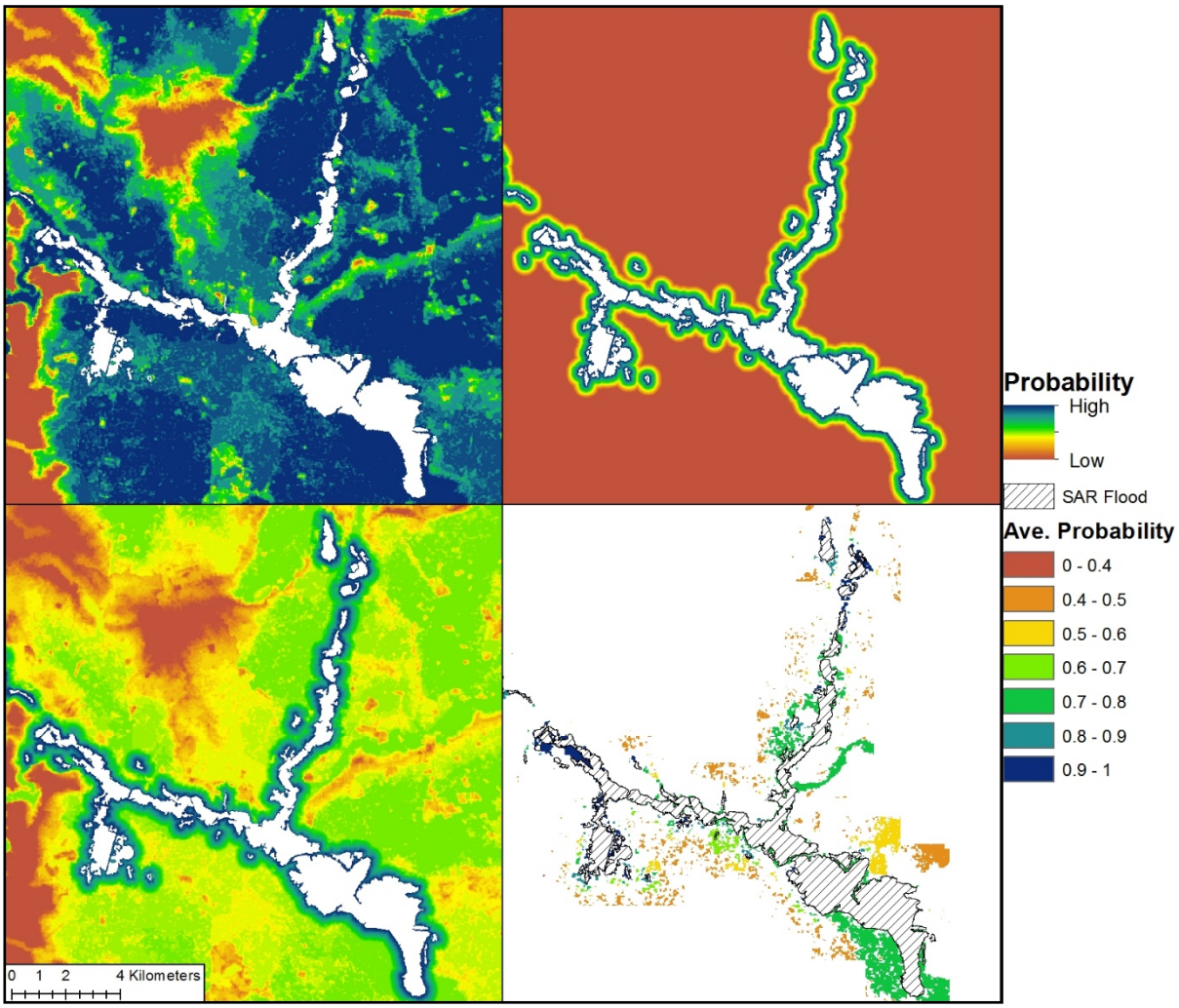

Figure 6.24. Probability classification for ascertaining the likelihood of pixels with positive water depth in the SRTM results, previously unidentified in the SAR flood extents, belonging to the flood class. Top left shows the variable membership derived from HAND, with "1" equalling values of 1 m and "0" scaled at 20 m. Top right shows the variable membership for distance from SAR derived flood extent, with "1" set at 10 m and "0" at 500 m. Bottom left shows the final probability map, created with equal weighting for the two memberships on the top row. Bottom right shows the average value for each polygon of new positive water depth.

		SRTM in SAR Extent		SRTM & Porb, > 90%		SRTM & Prob. > 80%	
		Extent %	Volumes %	Extent %	Volumes %	Extent %	Volumes %
29th Dec	Ouse 2	64.4	61.6	91.6	76.7	95.6	79.5
	Ouse 3	76.7	64.3	86.3	69.2	90.0	70.1
1st Jan	Ouse 2	56.1	81.8	70.1	97.5	111.2	136.6
	Ouse 3	64.4	68.9	75.5	77.4	79.8	79.8
3rd Jan	Ouse 2	57.7	80.9	85.9	107.9	130.9	146.5
	Ouse 3	68.9	86.4	80.2	94.6	82.9	96.8

Table 6.6. Flood extent and volume changes with inclusion of new SRTM-derived flood areas with increasing probability values. Expressed as a percentage of the LiDAR flood extent and volume for each sub-region and date.

6.4. Summary

This chapter has presented a methodology for deriving water surfaces, depths and volumes using the SAR observed flood extents from Chapter 5 and a high-resolution LiDAR DTM. The techniques have been developed and applied on the flooding observed in the Aire and Ouse catchments, covering the peak flood observed on the 29th Dec and subsequent water retreat.

When combining satellite flood extents with terrain data, both the mismatch in spatial resolution and the accuracy of the flood delineation are often cited as the main sources of error. Based on the accuracy of the results in Chapter 5, the assumption that the flood shorelines have a 1-pixel accuracy is used to develop a novel workflow for estimating shoreline heights. The algorithm uses the terrain found within each shoreline adjacent SAR pixel to select a percentile, determined by the SAR classification of flood and non-flood, as the pixel height estimate.

A grid-based framework is used to estimate local water surfaces based on SAR pixel height estimates that fall within each cell. Neighbourhood filtering and merging of the local surfaces produce a continuous water surface. The workflow has successfully derived largely plausible water surfaces from which to calculate water depth and volume. A comparison is made to in-situ river stage data, with the results producing an average overestimation of 3 cm and an RMSE of 98 cm. The comparison shows a prevailing under-prediction of water surface height during higher flows and in the downstream regions of the catchments, with greater over-estimation further upstream

and during low flow. The further parametrisation of the workflow is likely to reduce these errors, with potential avenues of investigation discussed in Chapter 8.

Depths are calculated by subtracting the LiDAR DTM from the water surfaces. There are locations of positive water depth identified outside of the observed SAR flood extents. The likelihood of these new inundated areas being correct is determined via analysing the results against the location of flood defences and the satellite-derived inundation. The ability to identify flooding unobserved by the SAR highlights the potential for deriving inundation in woodland and urban areas using the methodology, providing value by reducing the well-known limitations when using SAR imagery to map flooding.

Water volumes are calculated from the confirmed water depths, allowing for catchment-wide analysis of the changing flood dynamics. The ability to derive changes in water volumes based solely on satellite imagery, with previous studies often utilising satellite altimetry or in-situ gauge data to help derive the water surface, allows for the global analysis of flood dynamics with reduced data requirements. Also highlighted in the results is the ability to monitor inter-catchment water movement, with the improved temporal resolution of Sentinel-1 imagery allowing for the approximation of the flood wave transition throughout an event.

Good correlation is observed between rainfall, river flow, flood extent and water volume trends. As expected, peak water volume coincides with maximum observed flood extent, occurring on the 29th Dec after Storm Eva. All variables show a rapid decline after the peak, before an approximate hydrological equilibrium is reached in early January. Rainfall reduces after the 10th Jan, resulting in a reduction in river flow and flooding. Inter-catchment water movement has been identified in the Ouse catchment, with the upstream reaches showing increases in water extent and volume on the 10th Jan, before the flood wave moves downstream for the image acquired on the 13th.

The absolute volume values produced are not accurate due to how the underlying terrain data represents water bodies. LiDAR sensors are unable to measure bathymetry, and the DTM shows water surface height at the time of data acquisition. Furthermore, the developed algorithm produces varying sizes of flood grid for each

date based on the observed SAR inundation extent. Subsequently, the volume values do not include water found within the wider catchment river network. However, given the scale of observed flooding and the close trend with flood extent, particularly when locations of permanent water are removed from the datasets, the reported changes in flood volume between image dates provide a good representation of the changes in hydrology occurring.

An initial assessment of the global applicability of the methodology is undertaken using the lower resolution SRTM DEM. Locations of positive water depth from the SRTM capture 86.3% of the area of the SAR derived flood extents, compared to 93.2% from the fully processed LiDAR depths. SRTM calculated water volumes show a reduction in the region of around 25% compared to those from the LiDAR. There are many uncertainties raised when using the lower resolution terrain dataset when compared to the LiDAR. For example, surface features such as flood embankments are contained in the LiDAR data but are unrepresented in the SRTM. The reduced height values in embankment constrained floodplains has resulted in a lower water surface estimate in these areas. There are further challenges in determining the accuracy of new locations of depth-derived inundation in the absence of flood embankment datasets.

It should be noted that SRTM has been surpassed in terms of resolution and accuracy by other global DEMs, both those commercially and freely available (Proietti *et al*., 2017). Furthermore, having been acquired in 2000, there are likely to be differences in the representation of ground terrain between SRTM and the current real-world topography. It is possible that the use of a more recent DEM, either at the same resolution as SRTM or finer, would produce results more closely correlated to those obtained using the LiDAR DTM. However, the results produced by SRTM are still of value. There is a large back-catalogue of research using SRTM, with its limitations well understood, and it provides a good benchmark for comparison with other global DEMs when undertaking geospatial analysis. Further investigation into the global robustness of the presented methodology is provided in Chapter 7, including an assessment of different globally available DEMs (in comparison to SRTM) to ascertain their suitability for estimating flood dynamics using the techniques developed in this chapter.

Chapter 7. Global Terrain Models and Deriving Flood Dynamics

The aim of this chapter is to further ascertain the global applicability of the methodology developed in Chapters 4, 5 and 6 by applying them to a different flood event. The new case study, based in Queensland, Australia, provides an additional opportunity for comparing the performance of different globally available terrain datasets within the flood dynamics workflow.

7.1. Study Location and Data

Widespread flooding occurred along the Mackenzie River, in Queensland, Australia, as a result of heavy rainfall from Tropical Cyclone Debbie in late March and early April 2017. The study region is shown in Figure 7.1. The confluence of the Mackenzie and Isaac Rivers, around which a large proportion of the flooding occurred, is approximately 200 km south of Mackay, 700 km north-west of Brisbane, and around 20 km east of the edge of Junee State Forest. The shown study region is approximately 210 by 40 km. Flood extents have been derived from a Sentinel-1 image acquired on the 31st March 2017, with validation provided from a Sentinel-2 image captured on the 1st April. The temporal gap between the acquisitions by the two satellites is 5 hours. The Sentinel-2 image only provides coverage over the top portion (62%) of the study region. Also shown in Figure 7.1 is the location of three river gauges, with the Isaac River at Yatton furthest north, the Mackenzie River at Bingegang to the west and Dawson River at Boolburra in the south of the study region. These are used to help provide hydrological context to the derived flood dynamics.

7.1.1. Global Terrain Models

Table 7.1 provides information on a range of commercial and freely available global terrain datasets. Four DEMs have been selected for application within the methodology developed in Chapter 6 to determine their comparable accuracy when deriving flood dynamics. These include SRTM (providing continuation from Chapter 6); an SRTM derivative with smoothing and vegetation removal applied; and the freely available ASTER GDEM v2 and ALOS World 3D DSM, chosen due to their consistent spatial resolution with SRTM (1 arc-second, or approximately 30 m). The following sections give a brief overview of each terrain dataset, including data sources and reported accuracies. A comparison between the four datasets is

provided in Figure 7.2. Each has been used to estimate the flood shoreline heights and in the calculation of water depths and volumes. The terrain mask used to assist the derivation of flooding from the SAR imagery has only been calculated using SRTM, as in Chapter 5.

7.1.1.1. SRTM

Information regarding the acquisition and accuracy of the 1-arc second SRTM DEM is provided in Chapter 3.

7.1.1.2. Smoothed SRTM

Geoscience Australia (GA) has produced a smoothed, vegetation removed version of the original SRTM dataset (Geoscience Australia, 2010). This dataset has been downloaded through Google Earth Engine (GEE, 2019a). Landsat imagery has been used to identify locations of significant vegetation, with border terrain heights interpolated into these areas to provide an estimate of terrain height under vegetation. The documentation for the dataset states that this process has worked best on small woodland areas in flat locations, with reduced reliability if the vegetation is found on more variable terrain. After the vegetation effects are removed the dataset is smoothed. An adaptive filter is applied, with different window sizes used depending on the underlying terrain and the degree of noise in the original SRTM.

The smoothed SRTM has been validated against a variety of datasets, including permanent survey marks (n = 1198), contour datasets (2 m interval) and LiDAR terrain models (5 m resolution). Mean errors vary between 1.29 m and 3.74 m, with RMSE errors between 3.87 m and 6.59 m (Geoscience Australia, 2010). Known sources of error have been identified as the lack of removal of urban structures (which is not attempted in the processing), incomplete or poor removal of vegetation features, and occasional noise artefacts, both from the original SRTM and introduced in the processing. Although not a global dataset, the Australian smoothed SRTM has been included to highlight the potential added value that can be achieved if the pre-processing techniques are applied globally.

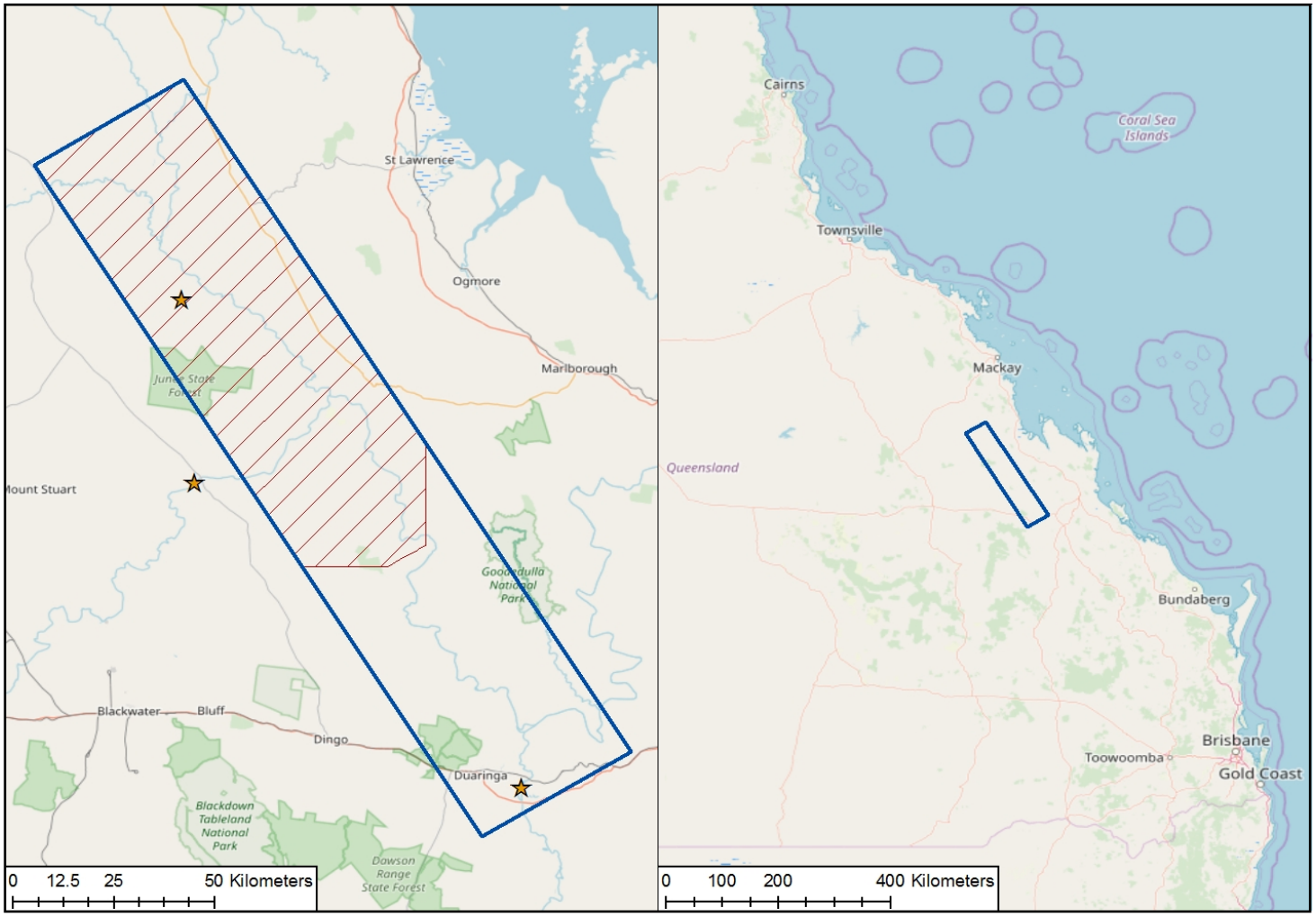

Figure 7.1. Study region (in blue) along the Mackenzie River in Queensland, Australia. Sentinel-2 coverage shown in red cross-hatch. Confluence between Isaac and Mackenzie Rivers visible on left, with gauges at Yatton, Bingegang and Boolburra shown from top to bottom. Panel on right shows study location within Queensland, with the flooding occurring 700 km north-west of Brisbane.

	Source	Satellite	Years Acquired	Update Frequency	Horizontal Resolution (m)	Accuracy (m) Vertical	Accuracy (m) Horizontal	Coverage	
Freely Available Datasets									
ALOS World 3D 30m	JAXA	ALOS-1	2006-2011	Potential with ALOS-2/3	30	7	7	82°N to 82°S	
ASTER GDEM v2	NASA	Terra	2000-2009	v3 released late 2019	30	15-20	15-20	83°N to 83°S	
MERIT	Yamazaki et al., 2017	Various	Other DEM Products	None	90	~2	Not Specified	Global	
SRTM	NASA	Space Shuttle Endeavour	2000.00	None	30-90	7-12	6-9	60°N to 56°S	
TanDEM-X DEM	Airbus & DLR	TanDEM-X & TerraSAR-X	2010-2014	Update planned post-2020	12-90	<10	<10	Global	
Commercial Datasets									
	Source	**Satellite**	**Years Acquired**	**Update Frequency**	**Horizontal Resolution (m)**	**Accuracy (m) Vertical**	**Accuracy (m) Horizontal**	**Coverage**	**Price**
ALOS World 3D 5m	JAXA	ALOS-1	2006-2011	Potential with ALOS-2/3	5	5	5	Global	€4 per sq.km DSM; €12.8 per sq.km DTM
Euro-Maps 3D	GAF	Cartosat-1	2005 onwards	Planned update missions	5	<10 - Slope Dependent	<10	2.5 million sq.km	€4 per sq.km
NextMap World	Intermap	Various	Other DEM Products	None	10 or 30	10	Not Specified	Global	€0.006 per sq.km
PlanetDEM 30	PlanetObserver	Various	Other DEM Products	None	30	<10	<10	Global	€25,000 - €50,000
Reference3D	Airbus	SPOT-5	2002-2015	None	20 - 30	10 - Slope Dependent	10	80 million sq.km	€7 per sq.km
SPOT DEM	Airbus	SPOT-5	2002-2015	None	20 - 30	10-30 - Slope Dependent	10-20	80 million sq.km	€2.3 per sq.km
Vricon DSM	Vricon	DigitalGlobe Imagery	None specified	When new stereo-pairs are acquired	0.5 - 10	3	3	Global	$2 to $25 per sq.km DSM; $35 per sq.km DTM
WorldDEM	Airbus & DLR	TanDEM-X & TerraSAR-X	2010-2014	Update planned post-2020	12	<4	<10	Global	€10 per sq.km DSM; €16 per sq.km DTM

Table 7.1. Global freely available and commercial DEMs, along with main acquisition, resolution, accuracy and cost information. Datasets with spatial resolution coarser than 100 m are not listed. Adapted from Proietti *et al*. (2017), with additional information from Wessel (2016) and Yamazaki *et al*. (2017).

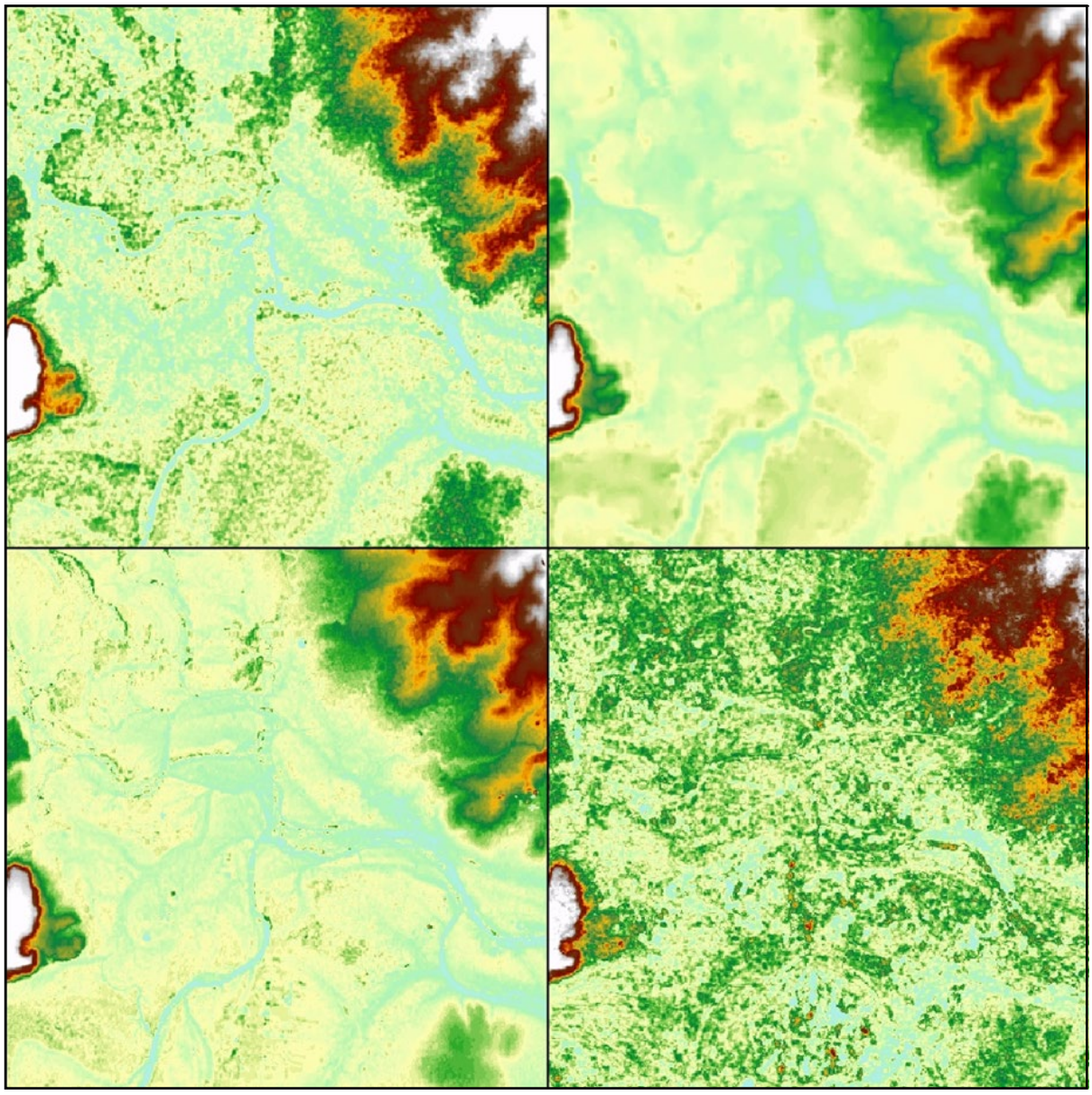

Figure 7.2. Comparison between the four terrain datasets used in this study: SRTM (top left), Geoscience Australia produced smoothed SRTM with vegetation removed (top right), ALOS World 3D30 (bottom left), and ASTER GDEMv2 (bottom right).

7.1.1.3. ASTER GDEMv2

Acquired using NASA's Terra satellite, the second version of the Advanced Spaceborne Thermal Emission and Reflection Radiometer (ASTER) global DEM (GDEM) was released in 2011. Elevation data is derived from stereo pairs of infrared imagery, with over 1.4 million scenes used to create the DEM. ASTER GDEMv2 has been compared to a number of validation datasets, including absolute geodetic references and national elevation grids in the US and Japan, and laser altimetry measurements from ICESat. Reported accuracies when compared to the national grids and geodetic references produce a mean error ranging between -0.2 m and -0.7 m, with an accuracy of 17 m at the 95% confidence level (Tachikawa *et al.*,

2011). Average differences over forested areas are larger, with reported values of 7.4 m in Japan and 8.0 m in the US. Over Australia, the comparison with ICESat produced a mean error of -2.83 m, a standard deviation of 7.08 m and an RMSE of 7.62 m (Tachikawa *et al.*, 2011). The dataset is released with known artefacts, including high-frequency noise in higher topographic regions, poor delineation of water bodies, and occasional voids due to lack of coverage or cloud cover.

7.1.1.4. ALOS World 3D (AW3D30)

The ALOS World 3D DSM has been produced by the Japan Aerospace Exploration Agency (JAXA) using panchromatic stereo-mapping of data acquired between 2006 and 2011 onboard the Advanced Land Observing Satellite (ALOS). The dataset is freely available from Google Earth Engine (GEE, 2019b). High spatial resolution (5 m) DEMs and DSMs, created from ALOS imagery, have been resampled to 1-arc second to create the freely available AW3D30. To ascertain the vertical accuracy of the resampled dataset, 5,121 independent and global validation locations have been used. These produce an average error of -0.44 m, a standard deviation of 4.38 m and an RMSE of 4.40 m (Tadono *et al.*, 2016). As a comparison, SRTM produces values of -1.00 m (average error), 7.43 m (standard deviation) and 7.50 m (RMSE) using the same validation locations (Tadono *et al.*, 2016).

7.1.2. Global Land Cover Data

Two separate sources of globally available land cover information are used in this chapter. The Global Land Cover Map (GlobCover) is derived by ESA from data acquired in 2009 by ENVISAT's Medium Resolution Imaging Spectrometer (MERIS) instrument, and is available globally at a spatial resolution of approximately 300 m (ESA, 2010). Water bodies, urban locations and woodland areas have been extracted to form the land cover mask. There are a wide variety of vegetation classes within GlobCover, and which of these form the vegetation mask is open to interpretation. Any land cover that is predominately woodland has been used in this case; however, land covers that suggest mixed vegetation (which may include woodland) have been disregarded. A list of GlobCover land cover classes and whether they have been used or not can be found in Appendix D.

In addition to the general land cover classification, a medium-high resolution water body specific dataset has been used to improve the delineation of water within the

feature mask. Pekel *et al.* (2016) analysed the full time-series of Landsat imagery to produce a dataset of water occurrence and seasonality, known as the Global Surface Water Explorer. Locations with water occurrence greater than 10% have been identified and joined with the GlobCover feature mask. As in Chapter 6, each feature is buffered to help account for uncertainty in the location of the feature datasets. This has been increased to 20 m given the lower resolution of some of the vector datasets, and the subsequent increased mismatch in resolution with Sentinel-1.

7.2. Flood Extent Delineation

The Sentinel-1 image from the 31st March 2017 has been processed using the workflow presented in Chapter 5. This includes the use of GEE to produce a median reference image from 30 Sentinel-1 images acquired between 1st Jan and 30th June 2018. The terrain mask, comprising of locations with high HAND and slope, has been created using SRTM. The relationships between the incidence angle and the two local thresholds (MP and Otsu) are the same as those derived in Chapter 5.

Similarly, the processing steps used to extract water extent from the optical validation image in previous chapters are applied here. Locations of water are identified using the Modified Normalised Difference Water Index (MNDWI, Xu (2006)) before being segmented using Otsu's threshold. The validation metrics described in Chapter 4 have been calculated using a 5 km grid covering the optical flood extent, providing insight into the spatial patterns of accuracy between the datasets.

7.2.1. Results

Flooding has been successfully identified from the SAR imagery throughout the study area. Examples of the identified flood extent in comparison to the Sentinel-1 imagery is provided in Figure 7.3. In total, 977.4 km^2 of flooding has been identified, equating to 10.6% of the study region highlighted in Figure 7.1.

7.2.2. Validation

There are locations with significant differences in the flood extents derived from the Sentinel-1 and Sentinel-2 imagery. Despite covering a smaller proportion of the study region (62%), the optical image identifies 1197.5 km^2 of inundation, more than the SAR derived flood extent. Sentinel-1 identifies 58.1% of the inundated areas derived from Sentinel-2. An example of the difference in derived flooding is provided in Figure

7.4, showing the region around the confluence of the Isaac and Mackenzie Rivers. The top row shows that the SAR flood detection algorithm works well in identifying the locations where specular reflection has occurred. However, there are regions of higher backscatter within the flood boundary not extracted from the Sentinel-1 that have been identified as flooded in the Sentinel-2. These coincide with locations of significant vegetation. Within the Sentinel-2 image (bottom left panel) sediment-rich water is visible around the vegetation in the centre of the region shown.

There are two possible reasons for the difference in flood classification. The first is that the presence of trees has resulted in an increase in backscatter, either from volume scattering of the radar pulse from the tree canopy, or by the double bounce effect when the signal penetrates through to ground level, subsequently masking the expected low backscatter flood signal. The inability to reliably map inundation in woodland locations is a well-known disadvantage of flood mapping using SAR imagery. The nadir viewing angle of the optical imagery allows for improved identification of the ground conditions, in this case allowing for flooding to be identified between the trees. There is clear variation in between the MNDWI values for open water and the flooding in woodland areas. Although both have been extracted by the Otsu algorithm, manual adjustment of the threshold may result in only the selection of open water, providing a closer match to the Sentinel-1 extents. However, visual inspection of the Sentinel-2 image shows clear inundation under the vegetation, suggesting the Otsu segmentation has provided accurate results.

The other potential explanation is that there was a significant change in water height during the five hours between the two image acquisitions. Table 7.2 shows river heights at three gauges (locations are shown in Figure 7.1) at the time of the image acquisition. During the 5 hours between the satellite orbits, the two gauges upstream of the confluence show a decrease in river stage, whilst the gauge downstream displays an increase in water height, showing the transition of the flood wave. Both the upstream gauges are around 40 km before the confluence, with the downstream gauge approximately 110 km after. It is possible that the water inputs from both rivers have resulted in a bottleneck around the confluence, causing a prolonged increase in water height in the central part of the study area resulting in the additional flooding identified in the Sentinel-2. Unfortunately there is no gauge at the confluence to provide a clear indication of the river signal during this time.

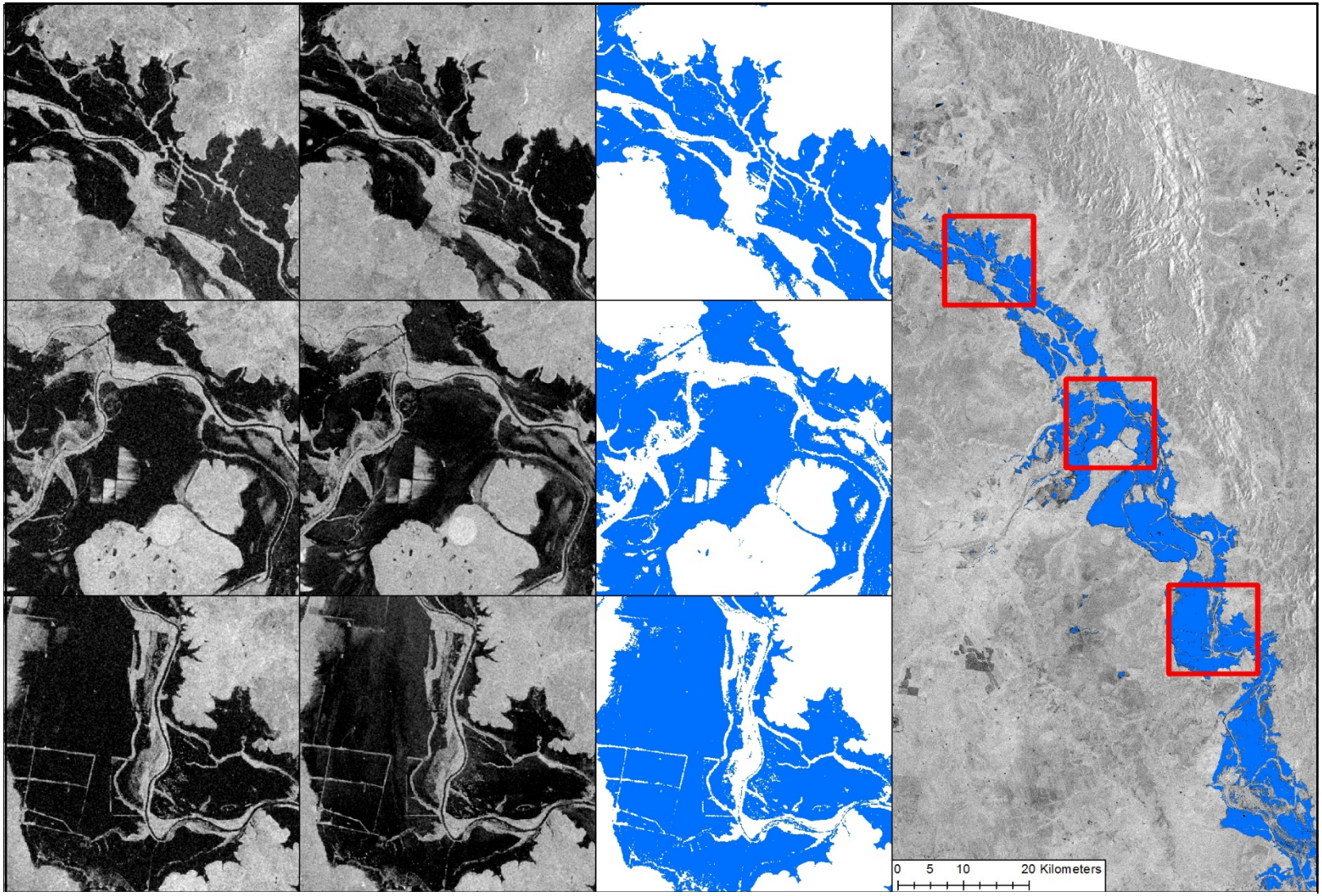

Figure 7.3. Flood extents derived from the Sentinel-1 imagery. Columns show (from left) VH SAR imagery, VV SAR imagery, derived flood extent, and a study region overview showing the location of each example panel.

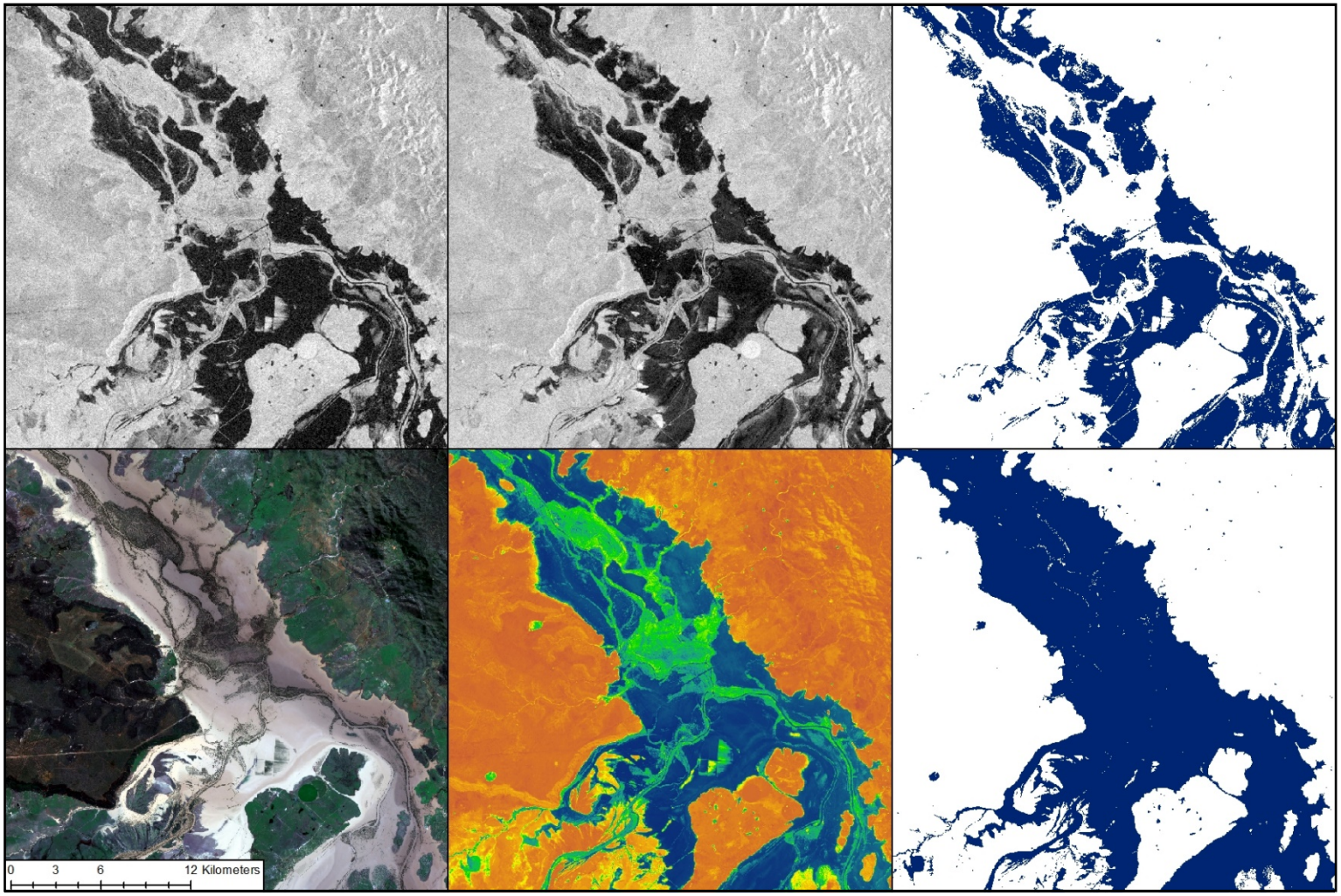

Figure 7.4. Differences in the flood extents derived from Sentinel-1 and Sentinel-2 imagery. Top row (from left) shows VH SAR imagery, VV SAR imagery and derived flood extent. Bottom row (from left) shows True Colour Composite (TCC) Sentinel-2 image, MNDWI classification, and flood extent derived from Otsu's thresholding the MNDWI map.

	River Stage (m)		
	Sentinel-1 01/04/2017 05:00	Sentinel-2 01/04/2017 10:00	Change
Isaac River @ Yatton	17.21	16.90	-0.32
Mackenzie River @ Bingegang	9.61	8.90	-0.71
Dawson River @ Boolburra	10.20	11.62	1.42

Table 7.2. River stage at the three gauges at the time of Sentinel-1 and Sentinel-2 imagery acquisition.

As expected with such large differences between the SAR and optical derived flood extents, accuracy scores are lower than those reported in Chapter 5. Figure 7.5 shows the validation scores for each metric (PA_f, UA_f, TA and CSI) throughout a 5 km grid covering the reference flood extent (which does not cover the full Sentinel-1 derived extent). Summary statistics are provided in Table 7.3. PA_f shows highly variable results, with an inter-quartile range of 45.9%. The median of 59.7% highlights the increased flood extent in the validation dataset, with the grid visualisation showing distinct areas where there is minimal classification from the SAR imagery compared to the optical. UA_f produces a median value of 99.4%, with the majority of the study area showing scores above 97%. The maximum flood boundaries derived from each dataset are similar, as can be seen by the extent comparison in Figure 7.5. This means the majority of the SAR identified flooding falls within the optical inundated areas, resulting in the high UA_f. This strongly translates into the TA scores, with the cells located at the flood edge producing high values due to the correlation between the maximum flood extent. Average TA is 86.9%, which is likely positively skewed due to the high amount of non-flood locations across both datasets in some grid cells. The lack of variability in UA_f results in the CSI closely matching the patterns and statistics of PA_f.

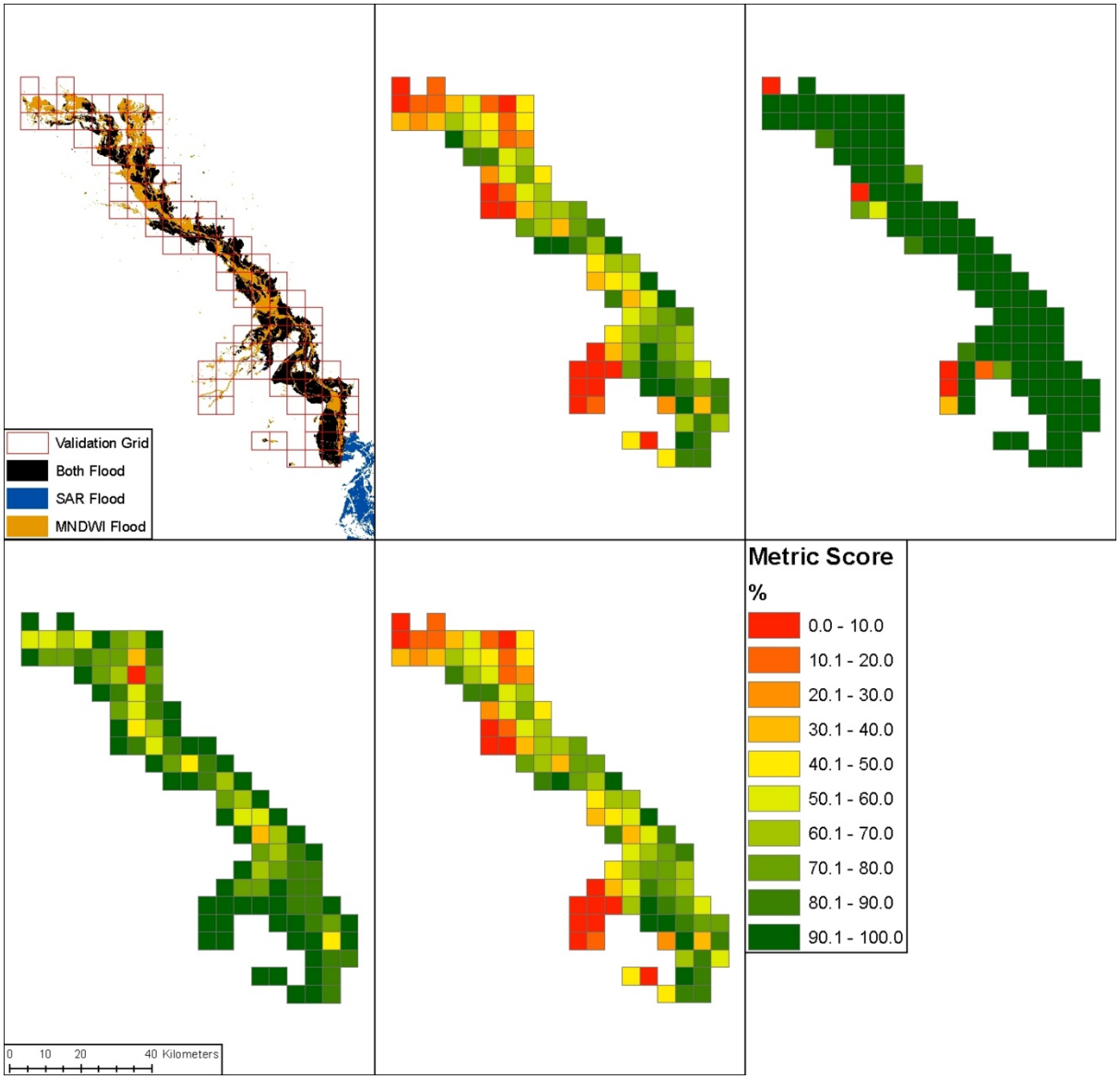

Figure 7.5. Accuracy scores for the Sentinel-1 flood extents when validated against the Sentinel-2 inundation locations. Validation undertaken using a 5 km grid. Top left shows a visual comparison between the extents, including location of overlap. Top middle and right show PA_f and UA_f respectively, with TA and CSI shown in bottom left and middle.

	Q_{MIN}	Q_{25}	Q_{MED}	Q_{75}	Q_{MAX}
PA_f	0.00	31.19	59.65	77.13	97.90
UA_f	0.00	97.71	99.43	99.83	100.00
TA	28.94	72.97	86.89	95.68	99.99
CSI	0.00	31.17	58.92	76.76	97.66

Table 7.3. Summary statistics for each of the validation metrics shown in Figure 7.5. Shown is the minimum, 25th quartile, median, 75th quartile and maximum of the combined grid cells.

7.3. Water Surface, Depth and Volume Estimation

Due to the large differences between the SAR and optical flood extents, both datasets will be used as the basis for estimating water surfaces using each DEM. The locations of positive water depth calculated from each terrain model will be compared to the respective satellite-observed flood extent used as input to ascertain the level of agreement, providing an approximation of success for each respective DEM within the methodology.

7.3.1. Methodological Adjustments

Apart from the changes in terrain and vector datasets described previously, the methodology presented in Chapter 6 is applied with only minor adjustments. The same refinement techniques are utilised for deselecting smaller water bodies and those distanced from the river network, as well as filling gaps within the flood boundaries that may correspond to the locations of surface features. The amount of flooding observed, removed and added in each of these steps is summarised in Table 7.4. Due to the width of the inundated area, the size of the cells within the flood grid has been increased from 1 km to 3 km, minimising the number of cells that do not contain SAR pixel height estimates within them. Additionally, the rural nature of the study area suggests there is a lack of flood defences along the river. Even if there are embankments, information on their location is difficult to obtain. Due to the lack of data, both at this location and on a global scale, the refinement of the areas with positive water depth via segmentation using the locations of flood defences is not performed.

	Full Derived Flood (km^2)	Derived Flood used as Input (km^2)	Gaps Filled (km^2)	Total Flood Input (km^2)
SAR Flood Extent	977.4	944.6	47.9	992.5
Optical Flood Extent	1197.5	1177.1	65.7	1242.8

Table 7.4. Amount of satellite derived flooding (both SAR and optical), and the subsequent amount used to calculate water surface, depth and volume after locational deselection and gap filling.

7.3.2. Results

7.3.2.1. Water Surfaces

Figure 7.6 shows the range in water surface height produced by the four DEMs when using each input flood extent. The optical input produces an average height range of 5.00 m with a maximum variation of 8.23 m, compared to 5.14 m and 10.40 m for the SAR input. There is good correlation for the locations of greatest variability in the SAR and optical derived water surfaces. The large variations are primarily caused by the ASTER water surface being significantly lower than those derived from the other DEMs. By removing the ASTER water surfaces, the average range is reduced to under 1.5 m for both input flood extents, with maximum differences of around 3 m. The ASTER GDEM shows the smallest average difference between the SAR and optical water surfaces at 1.27 m, with the unsmoothed SRTM having the largest at 2.03 m. The water surfaces derived from each DEM have similar height variations between the different input extents, with the SAR water surfaces having a typical maximum increase of 2.1 m, compared to 7.8 m in the optical counterparts.

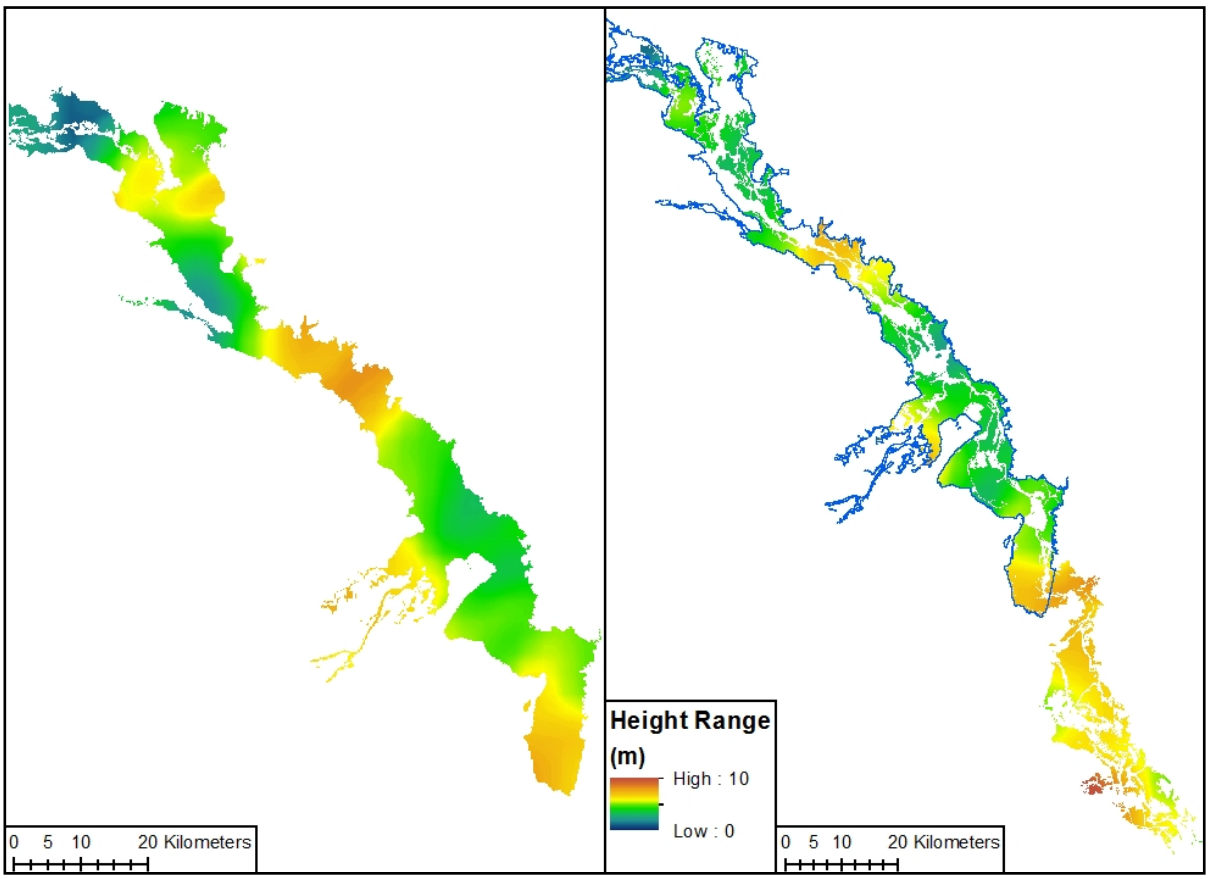

Figure 7.6. Variability in water surfaces produced from the four DEMs using optical (left) and SAR (right, with the optical extent shown in blue as reference) flood extents as inputs. Each surface raster is clipped to their respective input flood extent.

Direct comparison between the water surfaces derived using the unsmoothed and smoothed SRTM datasets show average height differences of 0.88 m and 0.73 m when using the optical and SAR inputs respectively, with the unsmoothed terrain model producing higher surfaces in both cases.

7.3.2.2. Locations of Water Depth

Figures 7.7 and 7.8 show the locations of water depth calculated for each DEM when combined with the SAR (7.7) and optical (7.8) input flood extents. There are a few patterns of note. Firstly, the ASTER produces a very noisy result irrespective of input, with minimal correlation to the corresponding observed flood extents. The smoothed SRTM provides a more continuous depth map compared to the raw SRTM, with the prevalent noise in the unsmoothed dataset often resulting in smaller, separated groups of pixels with water depth. Overall, the ALOS, SRTM and smoothed SRTM depth maps all match the respective satellite extents reasonably well, with Table 7.5 summarising the number of pixels with water depth as a percentage of the flood extent observed by each satellite.

Based on the visual and statistical assessment of the results, it becomes clear that the ASTER GDEM is unsuitable for terrain-based flood assessment using the developed methodology. The agreement between derived water depths and observed flood extents are 15% to 25% below those from the other DEMs. This result is largely expected. Out of the DEMs tested, the ASTER dataset is the only one where the river system is not easily identifiable in Figure 7.2 due to the inherent noise on the floodplain. The large amount of noise within the dataset results in numerous groups of pixels remaining above the derived water surface within the main body of observed flooding.

Water depths from the ALOS and two SRTM DEMs all produce similar percentage agreements when compared to the SAR input flood extents. When using the optical extents as input, ALOS and the smoothed SRTM identify approximately 89% of the input, 5% more than the raw SRTM. When using the SAR observations, the unsmoothed SRTM produces around 81% correlation, ahead of ALOS at 79% and the smoothed SRTM at 77%.

Across all of the depth maps there are distinct regions within the input (gap-filled) flood boundary that remain above the derived water surfaces. However, when compared to the satellite observed flood extents these locations tend to correspond with unflooded regions. In these locations, the lack of flooding across both the satellite observations and depth-derived results helps confirm the presence of local topographic highs which have remained above the water surface.

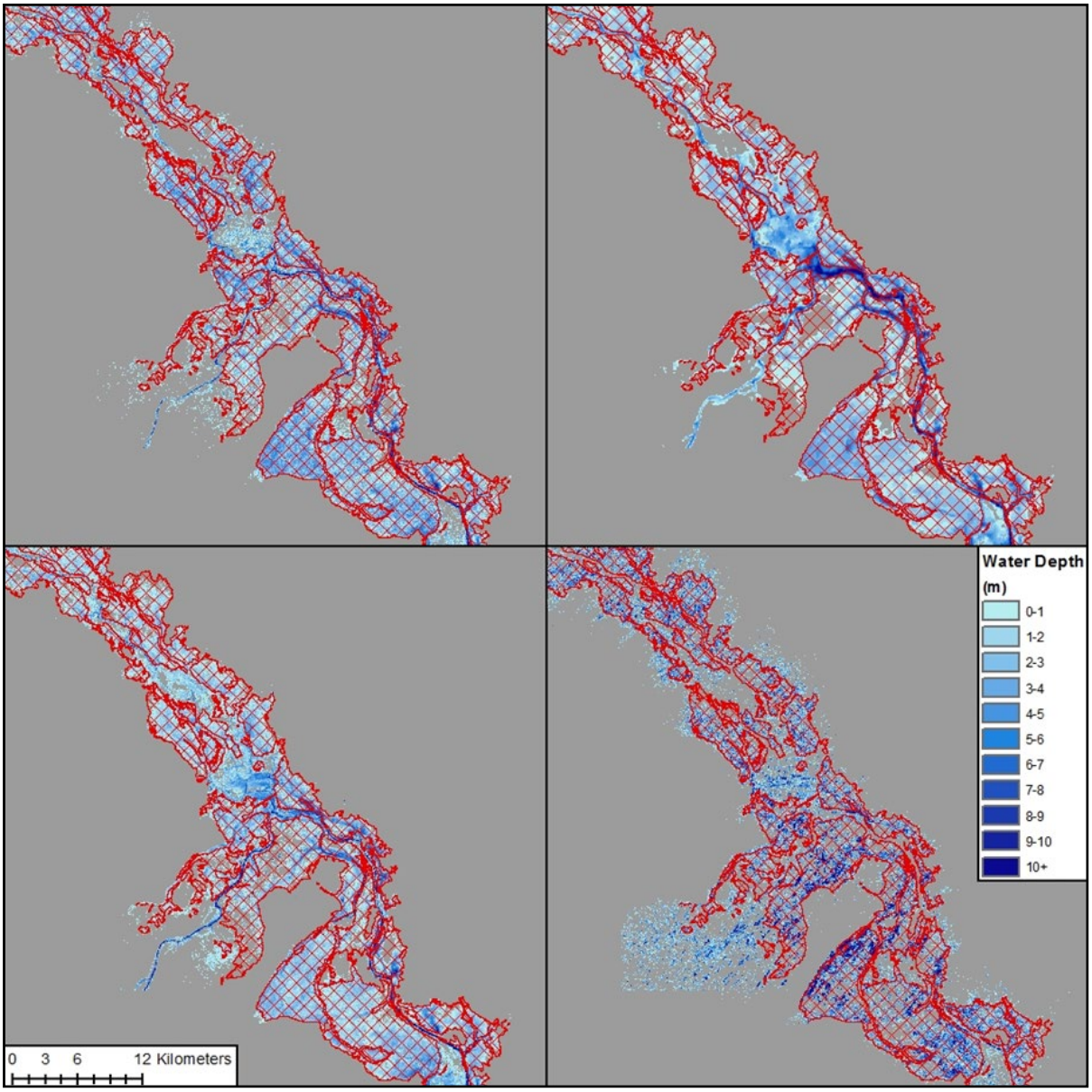

Figure 7.7. Water depths calculated from each DEM using the SAR flood extents (with the gap-filled extents shown by red crosshatch) as input. Top left is SRTM, top right is the smoothed SRTM, bottom left is the ALOS and bottom right is the ASTER GDEM.

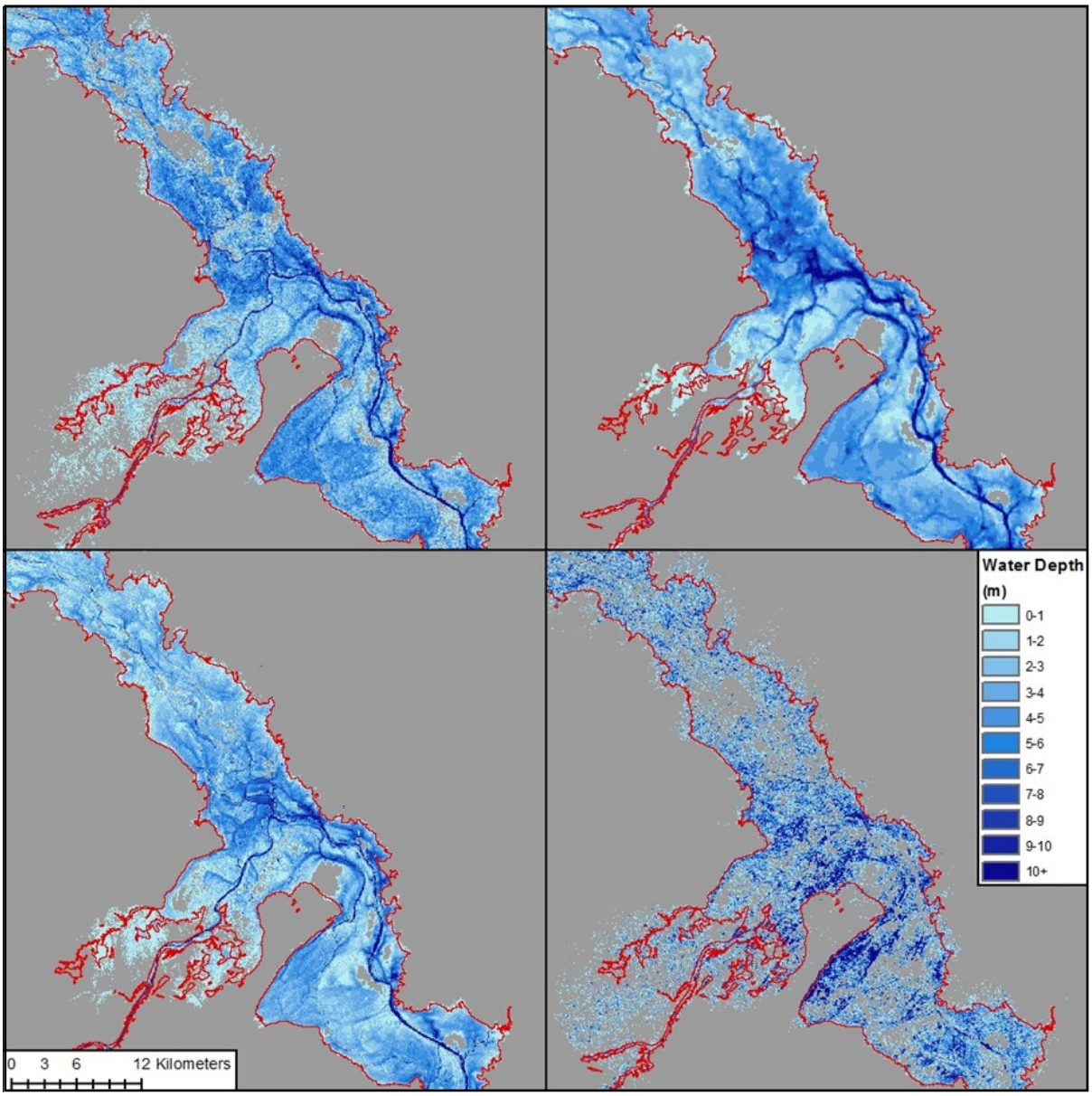

Figure 7.8. Water depths calculated from each DEM using the optical flood extents (with the gap-filled extents shown by red outline) as input. Top left is SRTM, top right is the smoothed SRTM, bottom left is the ALOS and bottom right is the ASTER GDEM.

	Full Optical	Input Optical	Full SAR	Input SAR
ALOS World 3D30	89.3	88.6	78.0	78.8
ASTER GDEMv2	59.6	59.4	59.7	60.2
SRTM	84.2	83.7	80.3	81.1
Smoothed SRTM	89.2	89.2	75.7	76.6

Table 7.5. Percentage of satellite observed flooding (both the full extent and the adjusted input) that have derived positive water depths for each of the DEMs. Full satellites derivations include classifications not used as an input into the flood surface algorithm. Input extents include filled gaps, locations which may have been undetected in the satellite imagery due to the presence of local topographic high.

7.3.2.3. Additional Flood Locations

All of the DEMs produce new areas of water depth outside of the respective satellite observed extents. When using the SAR input, the smoothed SRTM produces the greatest amount of new water depth locations, with just under 500 km^2. Much of this corresponds to gaps within the outer extremities of the observed inundation, such as the central location for each panel in Figure 7.7. These locations tend to be classed as flooded within the optical data. As discussed earlier, there is uncertainty in the accuracy of the SAR flood observations as they only identify 58% of the flood extent derived from the optical imagery. It is plausible that the SAR underestimates the extent of flooding due to the presence of vegetation, with the optical derived flood areas provide a better representation of the ground conditions at the time the SAR image is acquired. If this assumption is taken as correct, then there is added value to be found in the new flood locations identified from the SAR depth maps. The greatest improvement in this regard comes from the smoothed SRTM, which identifies an additional 12% to match 70% of the optical observed inundation. Similar numbers are produced by the ALOS dataset. It should be noted that ASTER GDEM actually identifies less than 50% of the optical observed flood area, showing a loss of accuracy compared to the original SAR flood delineation. However, caution is needed when using the new areas of water depth to expand on the observed flood extents given the uncertainties in the datasets and methodologies.

When using the Sentinel-2 input extent, the ASTER and raw SRTM highlight the most potential new flood locations, identifying approximately 280 km^2 and 250 km^2 respectively. This includes locations in the south-west of Figure 7.8, where the optical water extent is restricted to the river locations. It can be surmised that the ALOS and smoothed SRTM provide a better representation of the hydrological terrain in these locations, with their respective water depth maps either providing agreement with the Sentinel-2 observations, or showing consistent areas of water depths if found outside the optical flood extent. The inherent noise in the ASTER and raw SRTM results in dispersed small groups of pixels with water depth, both within and outside of the observed flood extent (Figure 7.8). It should be noted that all of the optical depth maps show a significant increase in flooding outside of the Sentinel-2 observed inundation, caused by the grid-based methodology expanding the analysed region beyond the Sentinel-2 image bounds.

7.3.2.4. Water Volumes

Calculated volumes vary drastically between the input datasets (Table 7.6). The SAR input extents produce the highest water volume when using the ASTER dataset. This appears contrary to the other results, which shows the water surfaces derived using ASTER are typically the lowest, and subsequently have the smallest agreement with the SAR observed flooding. Water depths calculated using the ASTER produce average and maximum values of 2.4 m and 59.3 m respectively. Results from ALOS produce similar maximum water depths of 59.1 m, compared to the two SRTM depth maps which show a substantially lower maximum of around 20 m. All three datasets produce average water depths ranging between 1.4 m and 1.9 m. The higher depth and volume values produced by the ASTER are likely caused by the noise prevalent throughout the dataset. Interestingly, the water volumes calculated from ASTER using the optical input match more closely to those from the other datasets. Mean water depths across all datasets with the Sentinel-2 input are between 2.7 m and 3.1 m. The ASTER still produces extreme depth values (as does ALOS), however, when combined with the reduced number of pixels with water depth, the resulting volume is comparable to those calculated from the other DEMs.

	Volume (km^3) Input Extents	
	SAR	Optical
ALOS	1.47	3.16
ASTER	2.33	3.22
SRTM	1.87	3.68
Smoothed SRTM	1.40	3.57

Table 7.6. Water volumes calculated from each terrain model and input extent combination. Note volumes only calculated for the extent of the satellite observed inundation, with any new locations displaying a positive water depth discarded due to the underlying uncertainty.

When using the SAR input, the ALOS, SRTM and smoothed SRTM produce water volumes that correlate well with the respective agreements between the derived water depth and the SAR observed flood extents. The raw SRTM produces the greatest match to the SAR observations (80.3%), which translates into the highest volume (1.87 km^3). Between the three datasets there is a range in volume of 0.47 km^3 and a 4.6% difference in agreement with the SAR flood extent. With the

optical input extents, the two SRTM datasets produce higher water volumes, driven by higher mean water depths above 3 m, compared to the ALOS, which produces average depths of 2.7 m. For the raw SRTM, this counteracts the decreased spatial extent of water depths, ultimately resulting in the highest water volume of the three. The range between water volumes for the three DEMs is 0.52 km^3, with a difference of 5.1% for agreement between the depth locations and optical flood extent.

The ALOS and smoothed SRTM provide an interesting comparison when using the optical input, showing a large variation in water volume (3.16 km^3 and 3.57 km^3 respectively) despite locations of water depths from both having a similar agreement with the observed flood extents (89%, Table 7.5). Furthermore, the datasets produce comparable water volumes (0.07 km^3 difference) when using the SAR input extents. Figure 7.9 shows the differences between the two DEMs, the derived water surfaces using the optical flood input, and the subsequent water depths. Generally, the ALOS DEM and water surface are higher than the smoothed SRTM counterparts, with average differences across the study area of 91.6 cm and 15.5 cm respectively. However, there are consistent areas of higher water depths from the smoothed SRTM, such as towards the north of the region shown. These correspond to areas of significant vegetation in the Sentinel-2 image. The creation of the smoothed SRTM includes filtering to remove vegetation, whilst the ALOS data shows high variability, with an underlying greater average height, in these locations due to the prevalent surface features. There is less vegetation in the southern part of Figure 7.9, resulting in reduced differences between the two water depth datasets, although still remaining highly variable. Although the ALOS DEM has less noise compared to the ASTER and raw SRTM, the increased surface heights in areas of vegetation have a significant impact on the calculated water depths and volumes. The similarity in volumes when using the SAR inputs can be explained by these vegetated locations not being within the Sentinel-1 observed extent, and consequently are not used within the volume calculation.

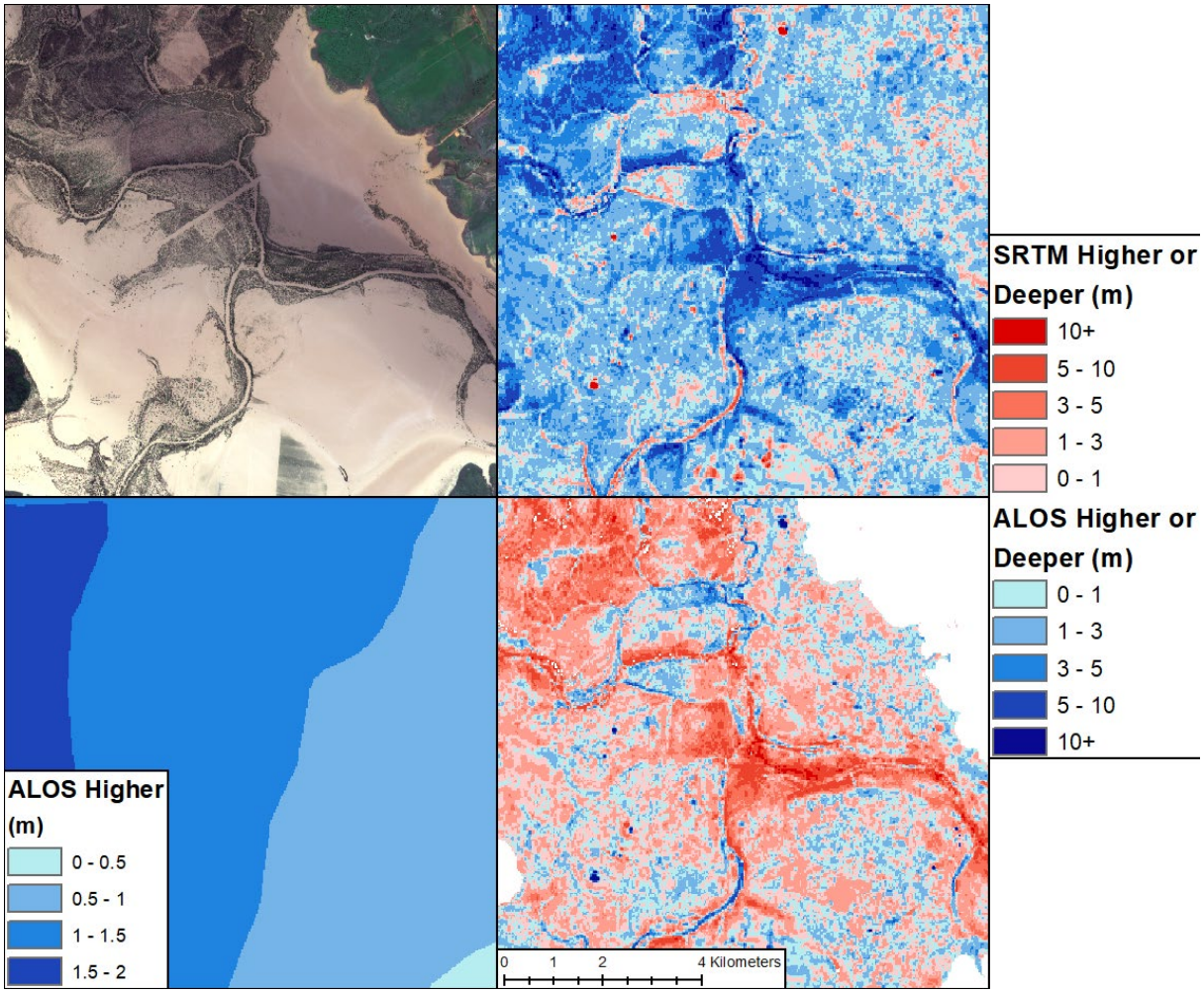

Figure 7.9. Comparison between results generated from the ALOS and smoothed SRTM DEMs. Top left shows the Sentinel-2 image; top right is the height difference between input DEMs; bottom left shows the prevalently higher water surface from the ALOS; bottom right shows the variations in calculated water depths. Legend on right describes the two right-hand panels.

7.4. Summary

The aim of this chapter was to investigate the strengths and potential limitations of the developed methodologies when applied at a global scale. Three lower-resolution, globally available DEMs, along with one Australia specific terrain dataset, have been compared to ascertain which produces the optimal results when estimating flood depth and volume.

Sentinel-1 imagery has been used to derive flood extent using the hybrid workflow developed in Chapter 5, resulting in the successful identification of areas of specular reflection, synonymous with flooding. However, there are large differences when compared to the Sentinel-2 optical image used as validation, acquired 5 hours after

the SAR image. One of the known limitations of SAR flood mapping is the inability to reliably derive inundation under vegetation. The optical image has identified flooding in a number of woodland locations, with these areas remaining unidentified in the SAR due to higher backscatter values. These locations may have been inundated at the time the SAR image is acquired, highlighting the possibility that the Sentinel-2 image provides a more accurate delineation of inundation at the time of the Sentinel-1 pass. Overall, the difference in the two satellite-derived flood extents results in poor accuracy metrics, including an average CSI of 58.9%.

However, the conclusion that the Sentinel-1 has failed to identify flooded vegetation is potentially false, and it is equally plausible that both SAR and optical flood maps accurately represent the ground conditions at the time of their respective image acquisition. Analysis of gauge data suggests that the satellite imagery has been acquired around peak flood, with river flow decreasing upstream and increasing downstream between the satellite orbits. This potentially signifies a change in flood dynamics that can explain the variations in flood extent, with the flood wave moving downstream through the confluence of the Isaac and Mackenzie Rivers, creating a bottleneck of floodwater that remains during the Sentinel-2 image. Caution is needed when using a different source of satellite data as validation for SAR flood maps. It is rare for two sources of data to be collected simultaneously. This thesis has found gaps of 5 hours (Australia) and 12 hours (UK) between SAR and optical image acquisitions. As shown for the Mackenzie River, it is possible that the two satellite images represent different ground conditions, particularly in flashier river regimes. Without further data it is impossible to ascertain which of the two explanations for the difference in satellite-observed extents presented in this chapter is correct.

As expected, the quality of the underlying terrain model has a major impact on the accuracy of the derived water depths and volumes. Higher accuracy, less noisy datasets are shown to produce more plausible results when comparing locations of water depth to the satellite observed flood extent. Of the global datasets tested, the water depth results derived from the ALOS produce the greatest reliability, correlating with 89.3% of the optical and 78.0% of the SAR observed flood. The former is comparable to the LiDAR-based study completed in Chapter 6, which had an average agreement of 93%. The ASTER performs poorly compared to the other terrain models due to the large amount of noise within the dataset. The respective

good and poor performances of the ALOS and ASTER DEMs have been previously highlighted in catchment delineation studies (Keys and Baade, 2019), coastal flooding assessment (Zhang *et al.*, 2019b) and general accuracy assessments (Alganci *et al.*, 2018).

The smoothed, vegetation-removed version of the SRTM produced by Geoscience Australia achieves similar results to the ALOS data. When using the optical flood input, locations of water depth calculated using the smoothed SRTM provide a closer match to the observed inundation (89.2%) compared to the raw SRTM (84.2%). Conversely, when using the SAR input extents there is a better agreement using the unsmoothed SRTM (80.3% compared to 75.7% for the smoothed). The original SRTM produces a higher average water surface irrespective of input flood extent, an artefact of vegetation noise within the unsmoothed terrain model. There is minimal vegetation within the observed SAR flood extent, and the smoothing of the SRTM dataset results in an average height reduction of 0.26 m. This is compared to 1.01 m within the optical flood extents, which contains areas of substantial vegetation. The combination of a higher water surface from the unsmoothed SRTM (by an average of 0.73 m), along with the reduced vegetation noise in the analysed region of the terrain dataset, results in the greater correlation between water depth locations from the raw SRTM and the SAR flood extents.

The depth maps produced from the unsmoothed SRTM often show small, dispersed groups of pixels with water depth. In comparison, using the smoothed SRTM results in a larger, more spatially consistent areas of water depth. Although the smoothed SRTM may miss some of the observed flooding when using the SAR input, it could be argued that the more continuous depiction of water depth is more reliable than the spatially inconsistent representation derived from the raw SRTM. The further parameterisation of the developed algorithm will likely yield improvements in the statistical appraisal of the results when using the smoothed dataset. Overall, the results from the smoothed SRTM are good, and the wider application of the algorithm used to create this Australia specific DEM is encouraged.

The results include the identification of new locations of water depth outside of the Sentinel-1 flood extents. Given the inherent uncertainty in the SAR flood mapping, the global DEMs and the processing algorithms, caution is required when assessing

the accuracy of flooding that is derived, and not observed. However, the presented methodology has the potential to add value to the SAR flood maps, namely in helping highlight inundation in urban and woodland settings. This is likely to be very situational, and further investigation is required to ascertain the best techniques for determining the accuracy of secondary flood extent information.

Overall, the algorithms developed in this thesis have been shown to be globally applicable, allowing for the mapping flood extent, depth and volume using SAR imagery and ancillary geospatial datasets. This is with a caveat, given the difference in the SAR and validation flood maps, and the uncertainty in the flood hydrology occurring during the time of image acquisition. Further case studies are required to ensure the algorithms are applicable in all geographical situations, alongside confirming the accuracy of the techniques applied. The assessment of globally available terrain datasets is valuable, and the expansion of the study in terms of flood location and DEMs analysed will help inform future hydrological, remote sensing and geospatial research. In particular, a number of the datasets listed in Table 7.1 provide either finer resolution or higher level of vertical accuracy than those used within this chapter, albeit at a monetary cost in some examples. Completing similar comparisons with these DEMs as has been presented here will provide further insight into the relative strengths and limitations of each terrain dataset, whilst providing a measure of how accuracy is improved with increased user costs.

Chapter 8. Discussion and Conclusion

The following discussion will critically asses the developed algorithms and analysis presented in the preceding chapters in relation to the Aims and Objectives outlined in Section 1.2. As stated earlier, the aim of the project was to develop innovative algorithms for estimating flood dynamics using SAR imagery and ancillary geospatial datasets. The project objectives specified the development of workflows to estimate flood extent, depth and volume from satellite imagery and terrain data, the results of which are used to assess the utility of recent satellite datasets in providing further understanding of the dynamics of a flood event. Furthermore, all algorithms were to be globally applicable to maximise the potential application using Sentinel-1 imagery.

8.1. Dynamics of the 2015-16 UK Winter Floods

The results presented in this thesis highlight the extreme nature of the flooding caused by the 2015-16 winter storms. Numerous precipitation events brought prolonged and intensive rainfall, resulting in widespread inundation across many catchments in the north of England. Numerous flood characteristics have been derived using satellite imagery, which in conjunction with in-situ gauge records and gridded catchment-wide rainfall, help describe the onset, peak, equilibrium and recession of the flooding throughout the study period.

The results from Chapter 5 show the changes in SAR derived flood extent for a three month period for the Aire, Eden and Ouse catchments, along with the Lake District. In each catchment, the timing and magnitude of the peak flood correspond well to those observed within the gauge records. Storm Desmond caused the greatest flood extent in the Eden catchment and Lake District during early December, whilst Storm Eva triggered widespread inundation throughout the Aire and Ouse catchments later in the month. The algorithms in Chapter 6 have been used to calculate water surface slope, depth and volumes for the Aire and Ouse catchments based on the observed flood extents and terrain data. In-situ data from these catchments show that precipitation and river flow correlate strongly, with peak flows occurring up to a couple of days after maximum precipitation inputs. As expected, flood extent and water volume broadly match these trends, with peak inundation occurring on the 29th Dec, with significant flooding visible until mid and late January in the Aire and Ouse catchments respectively.

The consecutive nature of the rainfall events is likely to have caused consistently saturated ground conditions and high river flows, subsequently exacerbating the impacts of each individual precipitation event. In Chapter 5, the slow retreat of inundation and the continual re-flooding of low-lying areas is identified in the Ouse catchment and Lake District (Figures 5.14 and 5.19). In Chapter 6, rainfall data shows more consistent inputs across the Aire and Ouse catchments between the 30th Dec and 8th Jan, resulting in an approximate stabilisation of river flow. There are still peaks in river stage during this time, a result of periods of more intense rainfall. It is likely that there is minimal water infiltrating into the ground at this time due to the soil water storage being at capacity, subsequently reducing the lag time between precipitation inputs and river flow increase. The Aire catchment in particular shows a very flashy response to rainfall inputs on the 3rd, 6th and 9th Jan, with river stage increasing by more than 1 m in each case (Figure 6.20).

Ideally, it would be possible to clearly derive the above intricacies in flood dynamics from the satellite imagery. However, there are limitations when using satellite data, namely the lack of temporal resolution and geographical coverage when studying large catchments. The linear representation of the temporal changes in flood extent and volume presented in this thesis is unlikely to be accurate. In Chapter 6, peak floods in both the Ouse and Aire catchments occur on the 29th Dec (discounting the 15th Jan in the Ouse catchment due to classification errors), before a rapid retreat on the 1st and 3rd Jan, a trend that broadly matches the in-situ measurements. Flood extent and volume values on the 3rd and 10th Jan are similar in the Ouse catchment (the 6th Jan shows much lower values but has limited coverage), supporting the idea of a catchment in temporary hydrological equilibrium. In the Aire catchment, flood extent and volume trends on the 6th and 10th Jan match those observed for river flow, including a slight increase in inundation of the 10th Jan, which coincides with the rising limb in the hydrograph as a result of intense rainfall on the 9th Jan. This highlights the potential for monitoring broad trends of flood dynamics from space, albeit without the finer temporal detail.

There are a number of distinct flood-prone regions in the Ouse catchment. Flood extents and water volumes have been calculated for each sub-region individually, with the aim of identifying the transition of the flood wave through the catchment. An example is found on the 10th Jan, with the upper regions of the Ouse showing a

relative increase in flood extent and volume (Figure 6.21). This is followed by the downstream regions showing increased inundation on the 13th Jan, coinciding with flood recession in the upstream locations. This inter-catchment analysis has great potential for improving our understanding of the temporal and spatial characteristics of a flood within a catchment.

Alongside the analysis of flood extent and water volume, the estimation of the water surface allows for changes in slope to be determined. Results from three separate transects are presented in Section 6.3.1, with the River Ouse transect in particular showing interesting results (Figure 6.13). As expected with the extent of flooding observed across the catchment, the derived water surface on the 29th Dec is significantly higher than those from the following dates. The left of the transect is located at the confluence of the Ouse and Wharfe Rivers, and there are minimal variations in water surface height at this location for the other shown dates. It is likely that the large inputs of water from both rivers has resulted in a bottleneck effect, maintaining the consistently high water levels. The increase in pooling of water around confluences can be observed in the SAR flood extents throughout the study area. At the other end of the transect, 8 km downstream from the confluence, water surfaces on the 1st and 3rd Jan are approximately half a meter higher than the 10th and 13th. This evolution of the flood surface suggests the hydrology has shifted from a more equilibrated system, with a gentler gradient downstream, to a more recession orientated situation with a steeper water slope. Figure 6.21 shows a reduction in extent and volume of 6% and 19% respectively between the 3rd and 10th Jan.

The goal of Objective 3 was to ascertain the potential for improved understanding of flood dynamics based on satellite-derived products. The algorithms presented in this thesis have successfully produced data on flood extent, water surface slope, water depth and volume. The combined analysis of these observations has provided new insights into the dynamics of the 2015-16 UK winter floods, both in a temporal and spatial context. Future flood events will benefit from the full constellation of Sentinel-1, with the second satellite improving the temporal resolution compared to the presented analysis. The results have potential for validating hydrodynamic models using multiple parameters.

8.2. Comments on Methodology

Objectives 1 and 2 outline the development of algorithms for delineating flood extent from SAR imagery, and combining these with terrain data to estimate water depth and volume. The results presented throughout this project have shown that these Objectives have been successfully achieved. The final results have high accuracy when compared to other sources of data. The following paragraphs will highlight some of the specific strengths and limitations of the workflow. Specifics of potential future adjustments to the developed techniques are detailed in Section 8.5.1.

A hybrid methodology for extracting flood extent from SAR imagery has been conceptualised in Chapter 4 and refined in Chapter 5. Included in the workflow are change detection, variable radiometric thresholding and object-based region growing processes. All methods are applied to both available polarisations before an object-based merging scheme is applied to produce a single flood map. Each technique has been designed to detect inundation, either by identifying the change in surface conditions from pre-flood conditions, or by analysing the co-flood imagery as a singular dataset. Although each process can be used to map flooding individually, the combination of these methods, as well as the polarisations, helps eliminate some of the sources of misclassification common with SAR flood mapping.

Within the change detection step, references images have been created using the median pixel value from a stack of images acquired along the corresponding orbit track. This is easily achieved using Google Earth Engine, and can provide an advantage over using a single image as a reference by removing any short-term environmental or speckle effects propagating into the difference image. Previous work in the literature has highlighted the changes in backscatter with incidence angle for various land covers (O'Grady *et al.*, 2014; Chapman *et al.*, 2015). This can result in under- or over-estimating the land-water threshold if a static boundary is applied. In Chapter 5 a relationship between incidence angle and land-water threshold is derived based on segmenting local histograms of the backscatter of permanent water bodies and their surrounding land. The relationship allows for improved delineation of surface water using histogram thresholding across full image swaths. Initial polarisation specific flood maps are produced, which are subsequently combined via selecting the maximum of the overlapping inundated locations. Previous research has highlighted the improved accuracy possible by combining polarisation specific

flood maps (Manjusree *et al.*, 2012). The techniques used in this thesis helps remove polarisation specific classification errors, such as wind-roughening of the water surface in VV imagery, and false classifications from volume scattering in VH.

In Chapter 5, the SAR flood extents are validated against Sentinel-2 optical imagery, producing a CSI score of 76.9% and a TA of 91.0%. These values appear comparable to accuracies reported elsewhere the literature (Martinis *et al.*, 2015b; Landuyt *et al.*, 2018), albeit with the caveat of direct statistical comparisons being difficult due to the differences in how validation of SAR flood maps is undertaken and reported. Comparisons are also made to CEMS flood maps, produced using higher-resolution SAR imagery. There is a high degree of similarity between the two SAR flood maps, both when directly compared (TA of 95.4%, an improvement on the results of Amitrano *et al.* (2018)) or the comparative metrics against the Sentinel-2 optical results (less than 1.2% and 0.3% difference for CSI and TA respectively). The similarity in flood extents highlights the role that medium-resolution SAR imagery, such as that acquired by Sentinel-1, has in flood management alongside more costly, higher resolution imagery sources.

Chapter 6 presents a grid-based methodology for estimating water surfaces, depths and volumes based on the SAR derived flood extents and a high-resolution LiDAR DTM. One of the main challenges outlined at the beginning of Chapter 6 was accounting for uncertainty, both from the shoreline position of the SAR flood extents and those introduced by the mismatch in dataset resolution. A novel approach is used to determine boundary height estimates based on the analysis of the terrain found within the shoreline adjacent SAR pixels. The methodology is based on two key assumptions, namely that locations classified as flooded in the SAR imagery are inherently correct, and that the shoreline location has a one-pixel accuracy at the regional scale. Each shoreline adjacent SAR pixel has a height estimated based on these assumptions, with the 95th percentile and median height values selected for flood and non-flood pixels respectively.

The SAR pixel heights are subsequently used to derive local water surfaces within a grid framework. A rule-based system is used to estimate the most likely local water surface height based on the histogram of the SAR heights within each grid cell. Neighbourhood filtering of the derived cell water surfaces helps removes any outliers,

whilst ensuring a smooth water surface transition downstream. Water surfaces for each grid cell are merged to create a continuous water surface, which is used to calculate water depths and volumes. The likelihood of new areas of flooding is confirmed using a novel segmentation technique based on the location of flood embankments.

The derived water surfaces are compared to in-situ river gauges, with a mean error of 3 cm and an RMSE of 98 cm. Compared to other results reported in the literature, these values show a slightly lower accuracy (Di Baldassarre *et al.*, 2011), although there is uncertainty when comparing results between different studies due to the variety of validation sources (including model results, field data and in-situ gauges), each with their own potential inaccuracies. Locations of derived water depth largely correspond to the satellite-observed flood extents, identifying approximately 90% of the inundated area. The lack of full correlation highlights an underestimation of the water surface height in some locations, potentially caused by emergent vegetation limiting the delineation of the full flood extent from the SAR imagery, an issue identified in Mason *et al.* (2012b) and Zwenzner and Voigt (2009). The calculated volumes closely match the trends of the flood extents, as well as in-situ precipitation and river flow datasets.

Despite the successes outlined above, there are geographical situations where the algorithms produce a less accurate representation of the likely flood dynamics. These are largely found with the estimation of the water surface, with the methodology for extracting flood extent from SAR imagery performing well, albeit with the drawbacks commonly found when using SAR data, which are described in detail in Section 8.4.

There is a visible bias in the derived water surfaces when compared to in-situ stage data. At this stage it should be noted that the in-situ gauge data used to validate the water surfaces may be inaccurate. Depending on the operating parameters of the gauging instrument, measurement quality can be questionable during periods of high flow. Additionally, there is contradictory metadata regarding site datum are provided by the Environment Agency and the National River Flow Archive which may have resulted in the imprecise adjustment of the water surface measurements for Figure 6.10. However, the clear trend of overestimation at low flows and in the upstream part of the catchment, and the under-prediction during higher flows and the

downstream portion of the flood merits investigation (Figure 6.9). Additionally, results are less accurate when flooding is more extensive. There are a number of steps within the methodology that may be contributing to the observed inaccuracies.

There are potential errors introduced when estimating the water surface heights for each SAR pixel. The assumption that the SAR flood maps successfully classify inundation to within 1 pixel may be false in some localised settings. Any under-estimation of flood extent will cause an under-prediction of water height, due to the analysed terrain heights being located within the main body of flooding, instead of representing the flood boundary (Horritt, 2003). When estimating the dry SAR pixel heights, the use of the median value can result in questionable results depending on the underlying terrain. For example, in flatter terrain there is a greater probability of the flood boundary extending beyond the shoreline adjacent pixel due to the increased backscatter from emergent vegetation. The median height is also unlikely to sufficiently capture water surface variability when the flood boundary is located next to embankments (Hostache *et al.*, 2009). This highlights the inherent complexity and challenges when trying to estimate flood shoreline heights.

The current rule-based process for determining water surface height within each flood grid cell operates by first setting search based on the statistics of the input SAR pixel heights, before identifying the peak density as the local water surface. The boundaries are designed to reduce the impact of SAR flood under-estimation, which can result in histogram peaks at lower topographic heights. However, there are situations where plausible peaks in the histogram fall just outside the set boundaries (such as in Figure 6.7), resulting in a more rudimentary, percentile-based estimate being made for the water surface height for the grid cell.

Although theoretically each grid cell will have similar height values to its neighbours, in practice the inaccuracies in derived flood extent alongside the uncertainties from the methodology can result in large differences between cells. The transects in Chapter 6 highlight some areas for improvement. There are steeper gradients in the water surfaces which are unlikely, likely caused the poor estimation of both SAR pixel and flood cell water heights. Alongside sections of steeper gradients, the Derwent transect also shows water surface increasing with flow downstream on the 1st Jan (Figure 6.14). This is due to erroneous flood extents forming the input to the surface

estimation workflow (Figure 6.15), highlighting the need for accurate delineation from the SAR imagery. However, it's the view of the author that a "perfect" flood delineation from is unlikely, and so a robust scheme for selecting which observed flooding is used as the input for later processing is required. A balance is needed to ensure enough accurate flood shorelines are selected whilst removing the majority of the false positives, which is largely achieved throughout the study area and period presented in this thesis.

The volume totals presented in Chapter 6 are not a true reflection of water volume across the Aire and Ouse catchments. River bathymetry is rarely available in terrain datasets, with the heights in locations of permanent water is often representative of the water surface at the time of data acquisition. Furthermore, the flood grid is recalculated for each image date based on the extent of observed flooding, subsequently resulting in a different proportion of permanent water bodies included for each time-stamp of the analysis. To account for this (Figure 6.19 and 6.20), comparisons are made between flood extent and water volume values with and without the locations of permanent water, with a similar trend observed between the two. Although there is some uncertainty with the absolute values, the changes in volume through time can still be used to help provide valuable insight into the flood dynamics.

8.3. Global Applications of SAR Flood Mapping

Flooding is a global hazard, and one of the advantages of satellite data is the ability to acquire imagery of flood events irrespective of location. The goal of Objective 4 was to ensure the algorithms developed in Chapters 5 and 6 are globally applicable. Chapter 7 presents a study of the flooding in Queensland, Australia caused by Tropical Cyclone Debbie in 2017. Flood extents have been extracted with no changes to the hybrid methodology, which combines change detection, variable thresholding and object-based region growing. Despite the success in identifying locations of specular reflection in the SAR imagery, there are large differences in the overall flood extent when compared to optical data (acquired 5 hours afterwards), with two possible reasons being proposed for the lack of correlation. The areas of uncertainty are found in predominately vegetated locations, which has potentially limited the ability of the SAR to identify the inundation (Figure 7.4). Alternatively, river stage data highlights the transition of the flood wave through the catchment between

satellite orbits, potentially resulting in an increase in inundation extent at the time of the Sentinel-2 image (Table 7.1). The uncertainty from the Australia case study highlights the need for further investigations to confirm the accuracy of the flood delineation algorithm achieved for the UK in Chapter 5, and to provide full confidence that Objective 4 has been met.

An initial comparison is made in Chapter 6 between the LiDAR DTM, used to produce the volume results for the UK described above, and SRTM, which is available globally. Using the lower resolution dataset produces a reduction in derived extent and volume of 35% and 26% respectively. Variations between the results are largely caused by the different representation of surface features in the underlying terrain models, which propagate into the derived water surfaces. For example, the lack of representation of features such as embankments in the SRTM has resulted in lower water surfaces in some downstream locations. Elsewhere, the SRTM produces higher water surfaces when the shoreline is found amongst steeper gradients. The larger DEM cell size covers a wider area, with the single pixel height value providing a large RMSE compared to the actual range of heights within the cell space (Satgé *et al.*, 2015). When the DEM cells overlapping the SAR pixel are analysed, this results in a wider range of height values on which to base a surface water estimate, often causing over-prediction.

As with the LiDAR results, there are locations of positive water depth derived from the SRTM that are outside the SAR observed extents. However, these locations have not been refined using the same embankment-based technique as before due to the ancillary dataset being UK specific. Instead a probabilistic framework has been devised combining the HAND index and distance from the observed Sentinel-1 flood extents (Figure 6.24). Using the average probability value for new flood areas, it is found that the inclusion of probabilities above either 0.8 or 0.9 resulted in the closest match to the LiDAR-derived extent and volume. However, the results are very situational. For example, at probabilities over 0.8, agreement for flood volume ranges between 70.1% and 146.5%. Only two variables are used in the framework, likely rendering it overly sensitive to extreme values, and with the variability of the initial results, caution is required when using the probability-based refinement without user interaction.

Chapter 7 contains a comparison between the performance of three global DEMs (ALOS World 3D30, SRTM (1 arc-second) and ASTER GDEM v2) within the methodology developed in Chapter 6. Also used is an Australia specific version of SRTM, which has had vegetation noise removed and a smoothing filter applied. Initial results show that ALOS produces good reliability in deriving locations of water depth, matching 78% and 89% of the SAR and optical derived flood extents respectively. The SRTM similarly performs well (80% and 84% match with SAR and optical). However, visual inspection shows locations of water depth are often found in smaller dispersed pixel groups, instead of the more continuous locations found in ALOS (Figures 7.7 and 7.8). The smoothing of the SRTM remedies this, producing results similar to the ALOS, suggesting that the pre-processing undertaken has the potential to improve results from hydrological applications using SRTM. The ASTER data shows itself unsuitable for future use due to the high degree of noise found within the dataset. Further research is needed to confirm the most suitable choice of terrain model for global estimation of flood depth and volume. Based on the results in Chapter 7, this should include ALOS, SRTM (1-arc second), and, if possible, a smoothed SRTM, alongside other lower-resolution datasets, such as the MERIT and TanDEM-X 3-arc second products. Ideally, future studies will include a variety of validation sources, allowing for a more reliable assessment of the accuracies produced by each terrain model.

The recent launch of the Sentinel-1 constellation enhances the temporal resolution of freely-available medium-to-high resolution imagery. The improvements in satellite technology coincide with increased access to high-performance computing (HPC - such as Google Earth Engine and ESA Grid Processing on Demand (G-POD (ESA, 2015)). These technological advances provide the capability to analyse a large number of images as they are acquired, allowing for near real-time flood monitoring. The availability of flood extents during an event provides a vital resource for emergency management and response, as well as allowing for data assimilation and validation of hydrodynamic models. A key requirement for near real-time flood monitoring is timely access to data after acquisition. Sentinel-1 data is typically available within a few hours of acquisition, utilising the European Data Relay Service (EDRS) to deliver data without the requirement for Sentinel-1 to have a line of sight to the ground station (Torres *et al.*, 2012). Currently, platforms such as the Copernicus Emergency Management System (CEMS), the Dartmouth Flood

Observatory (DFO, 2019), and the Luxembourg Institute of Science and Technology (LIST) HASARD tool (Chini *et al.*, 2019), which is hosted on G-POD, all provide examples of operational near real-time flood delineation. Further examples of near real-time algorithms in the literature include those proposed by Boni *et al.* (2016), Martinis *et al.* (2009, 2015b) and Mason *et al*. (2012a). The algorithms developed in the preceding chapters would require adjusting for near-real-time applications, namely to allow for faster and distributed processing within an HPC environment. To the best of this author's knowledge, the currently available real-time services do not supply an estimate of water depth and volume. The addition of this information, whether via the presented algorithms or other techniques in the literature, will allow for improved, evidence-based emergency management during an event.

Often these tools utilise more costly, higher resolution imagery from satellites such as TerraSAR-X, RADARSAT-2 and COSMO-SkyMED when activated during a large flood event. The ability to guarantee imagery for a particular location at a specific time can be vital during an event, and highlights why the more costly imagery is procured during an emergency. However, this study has shown that analysis of the freely available imagery from Sentinel-1 can provide equally valuable information. The accuracy of the flood maps produced in Chapter 5 are comparable to those produced by CEMS using higher resolution RADARSAT-2 imagery (Table 5.5). The regular Sentinel-1 imagery throughout a flood life cycle can help improve our understanding of the flood dynamics through the onset, peak and retreat of an event. However, as shown for the UK case study, Sentinel-1 is likely to miss the flood peak due to the fixed orbit. A likely solution is the use of multi-satellite constellations, as demonstrated by Boni *et al.* (2016) and Martinis and Rieke (2015), resulting in a further increase to the temporal resolution of flood extents.

8.4. Limitations of SAR Flood Mapping

Despite the advantages of using SAR imagery to map flooding, there are still well-known limitations that require addressing. The biggest drawback is SAR's inability to map flooding when features protrude the water surface, which results in the double bounce effect. This limits the classification of inundation in urban and woodland locations, whilst also causing extent under-prediction when emergent vegetation is present at the flood edge.

Potential examples of these interactions are found within the preceding chapters, although without further validation data it is unclear as to whether significant inundation has been missed in the presented flood maps. In Chapter 5, extensive flooding has been identified immediately upstream and downstream of York in the Ouse catchment (Figures 5.12 and 5.13), and around Carlisle in the Eden catchment (Figure 5.18). However, minimal inundation was detected within the city limits. This is contrary to media reports, which suggest that there was significant flooding in both cities during Storms Desmond (Carlisle) and Eva (York) (BBC, 2015a, 2015b). It should be noted that the floodwaters may have receded during the time between the peak flow in the hydrographs and satellite images being acquired, although it would be expected that given the scale of the inundation that some would persist. The lack of urban flooding in York in both Sentinel-1 and CEMS flood maps shows that the challenge is a wider SAR data challenge, instead of a spatial resolution issue. Current work within the discipline is focusing on the use of SAR coherence for identifying flooding in urban settings (Chini *et al.*, 2019; Li *et al.*, 2019). Although these methods show potential, the work in this field is currently in its infancy. Questions remain about the ability of medium resolution sensors to sufficiently derive flooding via coherence, the impacts of radar shadow from buildings, and the level of refinement required to remove naturally incoherent land covers (vegetation) from any classification.

Flooding under vegetation often provides a different challenge due to the variability in backscatter response with vegetation type. The prevalence of volume scattering from the tree canopies in C-Band imagery, such as that from Sentinel-1, limits signal penetration through to ground level. L-Band sensors, such as that onboard ALOS-2, have greater potential for monitoring flooded vegetation due to the increased canopy penetration (Plank *et al.*, 2017). Depending on the canopy thickness and composition, Sentinel-1 imagery will show a minimal difference in backscatter intensity between wet and dry conditions, making assessing changes in the ground conditions impossible. However, there is potential for delineating flooding under emergent vegetation or flooded grassland and shrubs, due to the more noticeable change in backscatter. Recent examples include time series analysis of polarisation ratio (VV/VH) (Tsyganskaya *et al.*, 2018) and indices such as the Normalised Difference Flood in Vegetation Index (NDFVI) (Cian *et al.*, 2018b).

Highlighted in this research is the potential for false classifications due to the low backscatter responses produced by ground frost and wet snow. In Chapter 5, there are extensive low backscatter responses across the north of England on the 15th Jan. However, this contradicts weather records at the time, which show limited rainfall and a lowering of river stage, alongside gridded temperature observations which display a drop to around freezing point. Determining which classifications are false is difficult due to the similarity in backscatter intensity between water, wet snow and frozen ground. Suggested ancillary information to help refine the results include terrain data and the spatial overlap of previously identified flooding, both of which have their drawbacks depending on geographical location and satellite coverage (Figure 5.27). The latter is used to refine the flood extents for volume estimation in Chapter 6. Despite the removal of suspect inundation, calculated volumes are still larger than expected. In particular, volumes in the Ouse catchment on the 15th Jan are greater than on the 29th Dec, the flood peak caused by Storm Eva (Figure 6.19). Further investigation into automated methods for refining the flood classifications in the presence of wet snow and frost is required.

Sentinel-1 operates on a fixed, conflict-free orbit, and is rarely specifically tasked to image a flood event based on predictions of maximum inundation. As such, the majority of the satellite passes presented here fail to coincide with the peak river flow of the hydrographs shown in Chapter 5, and there is no method for accurately temporally interpolate the extent of flooding. The linearity of the time series for flood extent and volume displayed in Chapters 5 and 6 is not a representation of the true flood dynamics between image dates. It should be noted that only one of the Sentinel-1 satellites being operational at the time, resulting in approximately 3-6 day coverage over the UK. With both satellites operation coverage is improved, with images every 2-3 days for all of the UK. However, even at full constellation it is likely that Sentinel-1 acquisitions will not capture the peak of the flood. Further to the temporal gaps in data, large catchments such as the Ouse are often only partially covered by the satellite imagery. The under-estimation of the reported inundation statistics when an image does not provide full coverage needs to be acknowledged when assessing the flood dynamics across wide geographical areas.

8.5. Future Work

Despite the successful development and application of algorithms for determining flood extent, depth and volume, there is inevitably improvements to be found. The following sections highlight potential future work, including further expansion of the presented deterministic algorithms, and the potential for the development of a probabilistic flood mapping or machine learning frameworks. Underlying all of these is the requirement for more case studies to further understand the strengths and weaknesses of the presented algorithms, and to provide additional validation of results.

8.5.1. Further Development of Current Algorithms

There are a number of steps within the presented work that could be further tested and parametrised.

The relationship between the ideal local land-water threshold and incidence angle has been defined using SAR backscatter histograms of permanent water bodies and their surrounding locations. All orbit tracks are combined, resulting in around 260 individual thresholds for each polarisation, which cover the full Sentinel-1 swath width, upon which the variable threshold is defined. There is scope for either confirming or updating the variable threshold by analysing additional local histograms. This can be achieved by adding new permanent water locations using the current methodology, or by updating the bimodality test to increase the number of the existing histograms successfully analysed. The current rule-based system is susceptible to rejecting histograms that have uneven water and land peaks (caused by the removal of high slope locations), multiple dry peaks (when urban and rural areas are present), or those without a deep trough between the peaks. The addition of further rules will allow for the inclusion of other suitable histograms that have been previously rejected. Alternatively, a more statistical assessment of each histogram, such as the Ashman's D value, which assesses the difference between two Gaussian distributions (Chini *et al.*, 2017), is likely to result in an increased number of local histograms passing the bimodality test.

The technique for estimating waterline heights based on the assumption that over a region, the location of the satellite-derived flood boundary is inherently correct. Heights are estimated each shoreline-adjacent SAR pixel, with the 95th percentile

and median height values from the underlying terrain selected for flood and dry pixels respectively. However, these values may misrepresent the shoreline height due to the potential underestimation of the SAR flood extents and the difference in dataset resolution. Examples of potential future parameterisation tests include the addition of height estimates from additional dry SAR pixels further away from the shoreline, or the selection of multiple heights from within each dry SAR pixel (25^{th}, 50^{th}, 75^{th} percentiles). It is likely that the locational accuracy of the satellite flood boundary will vary with the underlying terrain. Locations with gentle gradients at the flood edge will have a greater chance of the inundation extending beyond the shoreline adjacent SAR pixel, with the specular reflection masked by emergent vegetation. In steeper terrain, the flood boundary is likely to be clearer in the SAR imagery, albeit with greater uncertainty when combining with terrain data due to the broader range of possible heights. Additionally, Mason *et al.* (2012b) demonstrated that although emergent vegetation masks the specular reflection of the radar signal, there is potential for identifying flooding using the increased backscatter caused by the double bounce effect, albeit with large uncertainty bounds. The development of a rule-based system for selecting the SAR pixel height, which accounts for underlying terrain gradients, SAR backscatter (both within the flood image and variations from dry reference backscatter) and land-cover, is likely to produce more geographically robust results.

The addition of improved accounting for erroneous shoreline heights in locations where the edge of the SAR image intersects the body of flooding will further increase the reliability of the workflow. An example of this can be seen for the 6^{th} Jan in Figure 6.18. Currently no additional processing is applied in these locations when calculating water surfaces within the shoreline adjacent SAR pixels, resulting in lower height values from the floodplain being used to calculate local water surfaces. The removal of observed flood edges that correspond to the image edge instead of the targeted flood boundary will allow for more realistic surfaces to be produced in these locations.

There are adjustments that could be made in the selection of local water surface heights. The current system uses a search window based on the histogram statistics, within which peak values are identified. However, there are occasions where there is no peak within the search boundaries, in which case a rule-based system is used to

determine the water surface height. Often in these situations, a clear, plausible histogram peak is found just outside the search window. An iterative system is proposed, where the selection boundaries become more open if no initial peak is found. This will allow for a local water surface height to always be determined based on the histogram of the SAR pixel heights, theoretically making the process more robust.

In Chapter 6 the refinement of the water depth maps is completed based on the location of flood embankments. This allows for updated flood extents to be produced, which includes new locations of inundation unobserved by SAR, whilst accounting for the successful protection of low-lying land by the flood defences. However, the dataset of flood defences is UK specific, and spatial information of this kind is unlikely to be easily obtainable on a global scale. It may be possible to derive the locations of flood embankments, either from high-resolution terrain dataset (again, if available) or from Sentinel-1 imagery, as demonstrated by Wood *et al.* (2018). In the absence of embankment data, a probabilistic refinement framework is suggested based on terrain and distance from SAR identified flooding. The results show potential for producing similar refinement of new potential inundated areas as the embankment-based technique. Further investigation is needed to test, and likely improve, the reliability of probabilistic framework, including the inclusion of additional global datasets, and the undertaking of thorough sensitivity analysis.

8.5.2. Probabilistic Flood Mapping

The field of remote sensing for flood management is highly active, with new methods and applications being regularly developed in academia and industry. Due to this, the limitations of SAR flood mapping are well understood, namely the inability to reliably map inundation in urban and woodland locations, and the potential for emergent vegetation to cause underestimation of the full flood extent.

Given the inherent uncertainty with SAR flood mapping, the development and application of probabilistic frameworks have their merits. Probabilistic and fuzzy flood mapping has previously been demonstrated by Pierdicca *et al.* (2008) and Pulvirenti *et al.* (2011). The topics and processing techniques applied in these studies are worth revisiting after the launch of Sentinel-1, and with recent advancements in processing algorithms and analysis. There are a number of variables that can help

inform a probabilistic flood classification, including various SAR data products and ancillary datasets. The methodologies used in this thesis, and the majority of algorithms in the literature, are based on the use of SAR backscatter intensity to identify the specular reflection of the radar signal off the water surface. However, recent studies have shown that SAR polarimetry and interferometric coherence can both indicate flooding, including in vegetated and urban locations where SAR backscatter alone is unreliable (Tsyganskaya *et al.*, 2018; Li *et al.*, 2019). Flooding impacts the SAR backscatter response by altering the smoothness and height of the imaged ground surface, subsequently changing the radar pathways. Change detection is an effective technique for identifying inundation due to these alterations in ground conditions, as demonstrated with backscatter intensity in Chapters 4 and 5. Similar analysis based on the changes in SAR return signal with inundation can be undertaken when using polarisation ratios (VV/VH), or when comparing dry-dry image coherence to dry-flooded.

The number of available SAR segmentation processes, either based on the co-flood image or changes from dry conditions, means a robust probabilistic framework can be developed. There are two potential techniques for achieving this. Firstly, each method can be used to deterministically identify flooding, with locations highlighted as inundated using multiple processes having a higher probability when combined (Schumann *et al.*, 2009b). Alternatively, probability functions (such as the Z-function shown in Figure 6.8) can be used to classify each technique with regards to the likelihood of flooding (Pulvirenti *et al.*, 2011). These can then be combined to provide overall probabilities. Additional information based on terrain, such as the HAND index used within this thesis, and land cover maps, notably urban and woodland regions, can help further understand the probabilities and uncertainty produced by the SAR flood maps.

8.5.3. Machine Learning Frameworks for SAR Flood Mapping

Another approach to satellite flood mapping is the utilisation of machine learning algorithms. Sections 2.2.3 and 2.3.4 outline the current applications within the literature for multispectral and SAR imagery respectively. The research and development of machine learning algorithms for extracting surface water from SAR imagery is relatively unexplored, with numerous challenges requiring solutions before more widespread use occurs. A priority amongst these is the utilisation of emerging

HPC technologies (as discussed in Section 2.5) to allow for the efficient transfer, processing, storage and analysis of large volumes of data using machine learning algorithms, which tend to have a heavy computing cost (Sun and Scanlon, 2019).

Similar to the probabilistic frameworks outlined above, machine learning algorithms have the potential to utilise SAR coherence and polarisation ratios within the learning and classification processes to improve the reliability of the results. Li *et al*. (2019) provide an example of a deep-learning neural network to map urban inundation based on SAR intensity and coherence. The increasing amount of SAR imagery (and derivatives) has great potential for improving the consistency and quality of training samples used in learning algorithms (McCabe *et al*., 2017). Furthermore, past machine learning implementations have combined sources of imagery (optical and SAR) to increase both the quantity and quality of training data, whilst allowing analysis to be undertaken at a finer temporal resolution (Bangira *et al*., 2019; Benoudjit and Guida, 2019). The further development of the current machine learning frameworks, including the addition of SAR image derivatives to the training datasets, improved automated labelling of training samples, and the deployment of algorithms onto HPC clusters or cloud computing services, has potential to provide another source of reliable flood extent mapping.

8.5.4. Validation Framework

Further validation is required to confirm the accuracy of the presented algorithms. For the UK case study, a TA of 91% and a CSI of 77% are achieved when compared to optical imagery. The Australia study produced greater spatial variability in reported accuracy, albeit with large uncertainty over the similarity of the hydrological conditions between SAR and validation image acquisition. More case studies with suitable validation data will allow for increased confidence in the algorithm.

Validation of spaceborne derived flood maps is often a challenge. In-situ datasets normally lack the geographical coverage to adequately determine the quality of the classification. Results from hydrodynamic models commonly have large uncertainties. Often the default is to compare the extents to those derived from a different satellite or aerial image, nominally using optical sensors, which are frequently rendered unusable by cloud cover. Furthermore, any remote sensing

classification is likely to have inaccuracies, which need acknowledging when being used as the source of validation.

There is a lack of consistency in the literature with validating satellite observed flood extents, making it difficult to ascertain which algorithms provide the most accurate results. There are a number of variables that can impact an accuracy assessment, including which SAR imagery is used, the processing methodology, source of the validation dataset, and the geographical setting. Furthermore, different accuracy metrics are commonly applied, and on varying scales. As shown in Chapters 5 and 7, TA and CSI can vary significantly across the same flood, and the land-to-flood ratio in a validation area can change the produced accuracy values. Accounting for all of these variables often masks the information that is of interest, namely how SAR acquisition parameters and the applied processing techniques have changed the quality of the classification.

A useful endeavour would be the development of a validation standard. This would include a number of case studies, encompassing SAR data from a variety of satellites, alongside a variety of reliable validation sources, with fixed validation areas and metrics. Recently, Landuyt *et al.* (2018) published a study directly comparing a number of techniques across a variety of flood events. The scaling up of this work, both in terms of the algorithms compared and flood events analysed, would allow for easier direct comparison between different flood delineation algorithms. Furthermore, multiple case studies will ensure algorithms are robust in terms of geographical location, as well as sensor-specific acquisition parameters. Overall, the direct comparison between algorithms will help inform future research opportunities, whilst providing confidence to non-expert stakeholders with regards to the accuracy of the flood maps. Making the various SAR and validation datasets openly available will allow for fast, informative comparisons for future research projects, whilst helping to encourage further collaboration in the hydrological remote sensing community.

The derived water surfaces have been compared to in-situ gauge measurements. Although providing an indication of accuracy, stage measurements can be unreliable when flows exceed instrument design parameters, a possibility during the extreme events analysed in Chapter 6. Therefore, additional research would include finding other validation sources for the reported water surfaces, depths and volumes. The

derived water surfaces could potentially be validated against spaceborne altimetry, although there are drawbacks caused by the limited coverage provided by altimetry satellites. The upcoming Surface Water and Ocean Topography (SWOT) mission, due for launch in September 2021, will provide improved spaceborne water height measurements, alongside simultaneous extent data. This is going to revolutionise hydrological monitoring from space. SWOT data has utility for validating the algorithms presented in this thesis, alongside providing its own estimates of flood dynamics. There is also the possibility of using aerial or Unmanned Aerial Vehicles (UAVs) as validation platforms, both of which have the ability to carry LiDAR sensors. Although there are still challenges due to weather dependence, cost and survey planning, there is potential to arrange data acquisition to coincide with the satellite orbit, allowing for greater confidence in the validation.

Hydrodynamic models and flood observations from remote sensing have been previously used to validate one another (Matgen *et al*., 2016; Scarpino *et al*., 2018). As well as a comparison of flood extent, other hydrodynamic model outputs such as water depths and volumes, can be compared to results produced by the algorithms presented in this thesis. Care is required when undertaken such comparisons to ensure that a suitable model, with accurate parameterisation, is used. The development and application of a suitable hydrodynamic model is outside the remit of the current project. However, there is future scope in cross-validating hydrodynamic model outputs with remote sensing observations across multiple flood parameters.

8.6. Conclusions

This thesis has presented a series of innovative, globally-applicable algorithms for accurately mapping flood dynamics (extent, depth and volume) based on SAR imagery and terrain data, achieving the aims of the project that were specified in Chapter 1. Chapters 5 presents a hybrid workflow for delineating flood extents from Sentinel-1 SAR, applied to the flooding observed in the UK during the winter of 2015-16. The results are shown to be accurate when validated against flood maps from other data sources. Challenges remain in delineating inundation in urban and woodland locations when using SAR data. Chapter 6 combined the SAR flood extents with high-resolution LiDAR terrain data to provide estimates of water depth and volume. A novel framework is presented for deriving shoreline height, with a grid-based technique used for creating water surfaces. Inter-catchment water movements

are identified from the results, which show good correlation to river flow and rainfall. Chapter 7 applied the derived methodologies to an international case study. The processes generally perform well, although further validation is required. The results show that lower-resolution global DEMs can still be used to estimate flood dynamics. Of the global terrain models tested, the less noisy ALOS DEM produced the most reliable results.

Overall, the project objectives have largely been successfully met, albeit with the requirement for further global case studies to confirm the applicability of the algorithms developed and the results accuracy. The work highlights the vital role satellite remote sensing plays in flood risk management. In particular, the ability to monitor wide geographical regions provides an advantage over in-situ measurements. Commonly, spaceborne flood mapping research in the literature does not fully analyse the temporal nature of flooding, whilst often only reporting flood extent and depth. The high temporal resolution of Sentinel-1 allows for improved mapping of the changing characteristics of a flood during an event. Reporting flood volume alongside other descriptors provides additional insight into the onset, peak and retreat of a flood, with the inter-catchment analysis having the potential for increasing our understanding of catchment-scale inundation dynamics. These improved insights have value throughout the flood management cycle, including helping to assess future flood risk, assisting emergency management during an event, and for validating hydrodynamic models.

Bibliography

ABI (2016) *New figures reveal scale of insurance response after recent floods ABI*. [Online]. Available from: https://www.abi.org.uk/news/news-articles/2016/01/new-figures-reveal-scale-of-insurance-response-after-recent-floods/. Last Accessed 05/03/2019.

Acharya, T.D., Subedi, A. and Lee, D.H. (2019) Evaluation of Machine Learning Algorithms for Surface Water Extraction in a Landsat 8 Scene of Nepal. *Sensors*. **19**, 2769. doi:10.3390/s19122769.

Alganci, U., Besol, B. and Sertel, E. (2018) Accuracy Assessment of Different Digital Surface Models. *ISPRS International Journal of Geo-Information*. **7**:(3), 114. doi:10.3390/ijgi7030114.

Alsdorf, D., Birkett, C., Dunne, T., Melack, J. and Hess, L. (2001) Water level changes in a large Amazon lake measured with spaceborne radar interferometry and altimetry. *Geophysical Research Letters*. **28**:(14), 2671–2674. doi:10.1029/2001GL012962.

Alsdorf, D., Rodríguez, E. and Lettenmaier, D.P. (2007) Measuring surface water from space. *Reviews of Geophysics*. **45**:(2), RG2002. doi:10.1029/2006RG000197.

Amitrano, D., Di Martino, G., Iodice, A., Riccio, D. and Ruello, G. (2018) Unsupervised Rapid Flood Mapping Using Sentinel-1 GRD SAR Images. *IEEE Transactions on Geoscience and Remote Sensing*. **56**:(6), 3290–3299. doi:10.1109/TGRS.2018.2797536.

Arnell, N.W. and Gosling, S.N. (2016) The impacts of climate change on river flood risk at the global scale. *Climatic Change*. **134**:(3), 387–401. doi:10.1007/s10584-014-1084-5.

Augustin, H., Sudmanns, M., Tiede, D., Lang, S. and Baraldi, A. (2019) Semantic Earth Observation Data Cubes. *Data.* **4**, 102. doi:10.3390/data4030102.

Baghdadi, N., Zribi, M., Loumagne, C., Ansart, P. and Anguela, T.P. (2008) Analysis of TerraSAR-X data and their sensitivity to soil surface parameters over bare agricultural fields. *Remote Sensing of Environment*. **112**:(12), 4370–4379. doi:10.1016/j.rse.2008.08.004.

Bangira, T., Alfieri, S.M., Menenti, M. and van Niekerk, A. (2019) Comparing Thresholding with Machine Learning Classifiers for Mapping Complex Water. *Remote Sensing.* **11**, 1351. doi:10.3390/rs11111351.

Barker, L., Muchan, K. and Turner, S. (2016) The winter 2015 / 2016 floods in the UK : a hydrological appraisal. *Weather*. **71**:(12), 324–333. doi:10.1002/wea.2822.

Barra, A., Monserrat, O., Mazzanti, P., Esposito, C., Crosetto, M. and Scarascia Mugnozza, G. (2016) First insights on the potential of Sentinel-1 for landslides detection. *Geomatics, Natural Hazards and Risk*. **7**:(6), 1874–1883. doi:10.1080/19475705.2016.1171258.

Bates, P.D., Pappenberger, F. and Romanowicz, R.J. (2014) Uncertainty in Flood Inundation Modelling. In: *Applied Uncertainty Analysis for Flood Risk Management*. Imperial College Press. 232–269. doi:10.1142/9781848162716_0010.

Bazi, Y., Bruzzone, L. and Melgani, F. (2005) An unsupervised approach based on the generalized Gaussian model to automatic change detection in multitemporal SAR images. *IEEE Transactions on Geoscience and Remote Sensing*. **43**:(4), 874–887. doi:10.1109/TGRS.2004.842441.

BBC (2015a) *Storm Desmond: Thousands of people flooded out of homes - BBC News.* [Online]. Available from: https://www.bbc.co.uk/news/uk-35023558. Last Accessed 22/05/2019.

BBC (2015b) *UK floods: Cost of Storms Eva and Desmond could top £1.5bn - BBC News.*

[Online]. Available from: https://www.bbc.co.uk/news/business-35189179. Last Accessed 10/09/2019.

Below, R. and Wallemacq, P. (2018) Annual Disaster Statistical Review 2017 *Centre for Research on Epidemiology of Disasters*. [Online]. Available from: https://www.cred.be/publications. Last Accessed 22/09/2019.

Benoudjit, A. and Guida, R. (2019) A Novel Fully Automated Mapping of the Flood Extent om SAR Images Using a Supervised Classifier. *Remote Sensing.* **11**, 779. doi:10.3390/rs11070779.

Berry, P.A.M., Garlick, J.D., Freeman, J.A. and Mathers, E.L. (2005) Global inland water monitoring from multi-mission altimetry. *Geophysical Research Letters*. **32**:(16), L16401. doi:10.1029/2005GL022814.

Betbeder, J., Rapinel, S., Corpetti, T., Pottier, E., Corgne, S. and Hubert-Moy, L. (2014) Multitemporal classification of TerraSAR-X data for wetland vegetation mapping. *Journal of Applied Remote Sensing*. **8**:(1), 083648. doi:10.1117/1.JRS.8.083648.

Bhatt, C.M., Rao, G.S., Diwakar, P.G. and Dadhwal, V.K. (2017) Development of flood inundation extent libraries over a range of potential flood levels: a practical framework for quick flood response. *Geomatics, Natural Hazards and Risk*. **8**:(2), 384–401. doi:10.1080/19475705.2016.1220025.

Bioresita, F., Puissant, A., Stumpf, A. and Malet, J.P. (2018) A method for automatic and rapid mapping of water surfaces from Sentinel-1 imagery. *Remote Sensing*. **10**, 217. doi:10.3390/rs10020217.

Birkinshaw, S.J., Moore, P., Kilsby, C.G., O'Donnell, G.M., Hardy, A.J. and Berry, P.A.M. (2014) Daily discharge estimation at ungauged river sites using remote sensing. *Hydrological Processes*. **28**:(3), 1043–1054. doi:10.1002/hyp.9647.

Boni, G., Ferraris, L., Pulvirenti, L., Squicciarino, G., Pierdicca, N., Candela, L., Pisani, A.R., Zoffoli, S., Onori, R., Proietti, C. and Pagliara, P. (2016) A Prototype System for Flood Monitoring Based on Flood Forecast Combined with COSMO-SkyMed and Sentinel-1 Data. *IEEE Journal of Selected Topics in Applied Earth Observations and Remote Sensing*. **9**:(6), 2794–2805. doi:10.1109/JSTARS.2016.2514402.

Bonn, F. and Dixon, R. (2005) Monitoring flood extent and forecasting excess runoff risk with RADARSAT-1 data. *Natural Hazards*. **35**:(3), 377–393. doi:10.1007/s11069-004-1798-1.

Bovolo, F. and Bruzzone, L. (2007) A Split-Based Approach to Unsupervised Change Detection in Large-Size Multitemporal Images: Application to Tsunami-Damage Assessment. *IEEE Transactions on Geoscience and Remote Sensing*. **45**:(6), 1658–1670. doi:10.1109/TGRS.2007.895835.

Braud, I., Breil, P., Thollet, F., Lagouy, M., Branger, F., Jacqueminet, C., Kermadi, S. and Michel, K. (2013) Evidence of the impact of urbanization on the hydrological regime of a medium-sized periurban catchment in France. *Journal of Hydrology*. **485**, 5–23. doi:10.1016/j.jhydrol.2012.04.049.

Brisco, B., Touzi, R., van der Sanden, J.J., Charbonneau, F., Pultz, T.J. and D'Iorio, M. (2008) Water resource applications with RADARSAT-2 – a preview. *International Journal of Digital Earth*. **1**:(1), 130–147. doi:10.1080/17538940701782577.

Brivio, P.A., Colombo, R., Maggi, M. and Tomasoni, R. (2002) Integration of remote sensing data and GIS for accurate mapping of flooded areas. *International Journal of Remote Sensing*. **23**:(3), 429–441. doi:10.1080/01431160010014729.

Brown, K.M., Hambidge, C.H. and Brownett, J.M. (2016) Progress in operational flood mapping using satellite synthetic aperture radar (SAR) and airborne light detection and ranging (LiDAR) data. *Progress in Physical Geography*. **40**:(2), 196–214.

doi:10.1177/0309133316633570.

Burt, S. (2016) New extreme monthly rainfall totals for the United Kingdom and Ireland: December 2015. *Weather*. **71**:(12), 333–338. doi:10.1002/wea.2801.

Cao, H., Zhang, H., Wang, C. and Zhang, B. (2018) Operational Built-Up Areas Extraction for Cities in China Using Sentinel-1 SAR Data. *Remote Sensing*. **10**:(6), 874. doi:10.3390/rs10060874.

Chan, T.F. and Vese, L.A. (2001) Active Contours Without Edges. *IEEE Transactions on Image Processing*. **10**:(2), 266–277. doi:10.1109/83.902291.

Chapman, B., McDonald, K., Shimada, M., Rosenqvist, A., Schroeder, R. and Hess, L. (2015) Mapping regional inundation with spaceborne L-Band SAR. *Remote Sensing*. **7**:(5), 5440–5470. doi:10.3390/rs70505440.

Chen, M., Tomás, R., Li, Z., Motagh, M., Li, T., Hu, L., Gong, H., Li, X., Yu, J. and Gong, X. (2016) Imaging Land Subsidence Induced by Groundwater Extraction in Beijing (China) Using Satellite Radar Interferometry. *Remote Sensing*. **8**:(6), 468. doi:10.3390/rs8060468.

Chini, M., Hostache, R., Giustarini, L. and Matgen, P. (2017) A Hierarchical Split-Based Approach for Parametric Thresholding of SAR Images: Flood Inundation as a Test Case. *IEEE Transactions on Geoscience and Remote Sensing*. **55**:(12), 6975–6988. doi:10.1109/TGRS.2017.2737664.

Chini, M., Pelich, R., Pulvirenti, L., Pierdicca, N., Hostache, R. and Matgen, P. (2019) Sentinel-1 InSAR Coherence to Detect Floodwater in Urban Areas: Houston and Hurricane Harvey as A Test Case. *Remote Sensing*. **11**:(2), 107. doi:10.3390/rs11020107.

Chung, H.W., Liu, C.C., Cheng, I.F., Lee, Y.R. and Shieh, M.C. (2015) Rapid response to a typhoon-induced flood with an SAR-derived map of inundated areas: Case study and validation. *Remote Sensing*. **7**:(9), 11954–11973. doi:10.3390/rs70911954.

Cian, F., Marconcini, M., Ceccato, P. and Giupponi, C. (2018a) Flood depth estimation by means of high-resolution SAR images and LiDAR data. *Natural Hazards and Earth System Sciences Discussions*. **18**, 3063–3084. doi:10.5194/nhess-2018-158.

Cian, F., Marconcini, M. and Ceccato, P. (2018b) Normalized Difference Flood Index for rapid flood mapping: Taking advantage of EO big data. *Remote Sensing of Environment*. **209**, 712–730. doi:10.1016/j.rse.2018.03.006.

Coe, M.T. and Birkett, C.M. (2004) Calculation of river discharge and prediction of lake height from satellite radar altimetry: Example for the Lake Chad basin. *Water Resources Research*. **40**, W10205. doi:10.1029/2003WR002543.

Cohen, S., Brakenridge, G.R., Kettner, A., Bates, B., Nelson, J., McDonald, R., Huang, Y.F., Munasinghe, D. and Zhang, J. (2018) Estimating Floodwater Depths from Flood Inundation Maps and Topography. *Journal of the American Water Resources Association*. **54**:(4), 847–858. doi:10.1111/1752-1688.12609.

Copernicus (2018) *Copernicus Sentinel Data Access Annual Report 2018.* [Online]. Available from: https://scihub.copernicus.eu/twiki/do/view/SciHubWebPortal/AnnualReport2018. Last Accessed 05/01/2020

Copernicus (2019) *Copernicus Market Report - February 2019.* [Online]. Available from: https://www.copernicus.eu/sites/default/files/2019-02/PwC_Copernicus_Market_Report_2019_PDF_version.pdf. Last Accessed 05/01/2020

Corbane, C., Lemoine, G., Pesaresi, M., Kemper, T., Sabo, F., Ferri, S. and Syrris, V. (2018)

Enhanced automatic detection of human settlements using Sentinel-1 interferometric coherence. *International Journal of Remote Sensing*. **39**:(3), 842–853. doi:10.1080/01431161.2017.1392642.

Crétaux, J.-F. and Birkett, C. (2006) Lake studies from satellite radar altimetry. *Comptes Rendus Geoscience*. **338**:(14–15), 1098–1112. doi:10.1016/j.crte.2006.08.002.

Cunha, L.K., Krajewski, W.F., Mantilla, R. and Cunha, L. (2011) A framework for flood risk assessment under nonstationary conditions or in the absence of historical data. *Journal of Flood Risk Management*. **4**:(1), 3–22. doi:10.1111/j.1753-318X.2010.01085.x.

D'aria, D., Zan, F. De, Giudici, D., Guarnieri, A.M. and Rocca, F. (2007) Burst-mode SARs for wide-swath surveys. *Canadian Journal of Remote Sensing*. **33**:(1), 27–38. doi:10.5589/m07-008.

Dai, A., Qian, T., Trenberth, K.E. and Milliman, J.D. (2009) Changes in Continental Freshwater Discharge from 1948 to 2004. *Journal of Climate*. **22**:(10), 2773–2792. doi:10.1175/2008JCLI2592.1.

Dai, K., Li, Z., Tomás, R., Liu, G., Yu, B., Wang, X., Cheng, H., Chen, J. and Stockamp, J. (2016) Monitoring activity at the Daguangbao mega-landslide (China) using Sentinel-1 TOPS time series interferometry. *Remote Sensing of Environment*. **186**, 501–513. doi:10.1016/j.rse.2016.09.009.

Data.Gov.UK (2017) *LIDAR Composite DTM - 2m - Metadata*. [Online]. Available from: https://data.gov.uk/harvest/gemini-object/bb9cb765-e69e-4271-ba29-e94e8291f195. Last Accessed 27/09/2018.

De Roo, A., van der Knijff, J., Horritt, M., Schmuck, G. and De Jong, S. (1999) Assessing flood damages of the 1997 Oder flood and the 1995 Meuse flood. In: *Proceedings - 2nd International Symposium on Operationalization of Remote Sensing. Enschede, The Netherlands*. 1999. doi:10.1016/S1464-1909(01)00054-5.

De Zan, F. and Guarnieri, A.M. (2006) TOPSAR: Terrain observation by progressive scans. *IEEE Transactions on Geoscience and Remote Sensing*. **44**:(9), 2352–2360. doi:10.1109/TGRS.2006.873853.

DFO (2019) Dartmouth Flood Observatory, Founded 1993. [Online]. Available from: http://floodobservatory.colorado.edu/index.html. Last Accessed 22/05/2019.

Di Baldassarre, G., Schumann, G.J.P., Brandimarte, L. and Bates, P. (2011) Timely Low Resolution SAR Imagery To Support Floodplain Modelling: a Case Study Review. *Surveys in Geophysics*. **32**:(3), 255–269. doi:10.1007/s10712-011-9111-9.

Dorati, C., Kucera, J., Marí Rivero, I. and Wania, A. (2018) *Product User Manual for Copernicus EMS Rapid Mapping*. [Online]. Available from: https://ec.europa.eu/jrc. Last Accessed 21/05/2019.

EEA (2017) *CORINE Land Cover*. European Commision, Copenhagen, Denmark.

Environment Agency (2018) *Spatial Flood Defences*. [Online]. Available from: https://data.gov.uk/dataset/6884fcc7-4204-4028-b2fb-5059ea159f1c/spatial-flood-defences-including-standardised-attributes. Last Accessed 22/09/2019.

Environment Agency (2019) *Environment Agency Geomatics Survey Data*. [Online]. Available from: https://www.arcgis.com/apps/MapJournal/index.html?appid=c6cef6cc642a48838d38e722ea8ccfee&fbclid=IwAR0DMG2wcB_9nIIAiklRRk4BCEr7wrp7ZfvtcC8hUlrln63uUxD9urltXA. Last Accessed 05/01/2020.

ESA-ARTES (2017) *European Data Relay Satellite System (EDRS) Overview*. [Online]. Available from: https://artes.esa.int/edrs/overview. Last Accessed 03/02/2019.

ESA (2010) *GlobCover Portal*. [Online]. Available from: http://due.esrin.esa.int/page_globcover.php. Last Accessed 01/07/2019.

ESA (2015) *Grid Processing on Demand*. [Online]. Available from: https://gpod.eo.esa.int/. Last Accessed 22/05/2019.

ESA (2018a) *SAR Instrument - Sentinel-1 SAR Technical Guide - Sentinel Online*. [Online]. Available from: https://sentinel.esa.int/web/sentinel/technical-guides/sentinel-1-sar/sar-instrument. Last Accessed 27/09/2019.

ESA (2018b) *User Guides - Sentinel-1 SAR - Revisit and Coverage - Sentinel Online*. [Online]. Available from: https://sentinel.esa.int/web/sentinel/user-guides/sentinel-1-sar/revisit-and-coverage. Last Accessed 27/09/2019.

ESA (2018c) *User Guides - Sentinel-1 SAR - Extra Wide Swath - Sentinel Online*. [Online]. Available from: https://sentinel.esa.int/web/sentinel/user-guides/sentinel-1-sar/acquisition-modes/extra-wide-swath. Last Accessed 27/09/2019.

ESA (2018d) *User Guides - Sentinel-1 SAR - Stripmap - Sentinel Online*. [Online]. Available from: https://sentinel.esa.int/web/sentinel/user-guides/sentinel-1-sar/acquisition-modes/stripmap. Last Accessed 27/09/2019.

ESA (2018e) *User Guides - Sentinel-1 SAR - Wave - Sentinel Online*. [Online]. Available from: https://sentinel.esa.int/web/sentinel/user-guides/sentinel-1-sar/acquisition-modes/wave. Last Accessed 27/09/2019.

ESA (2018f) *User Guides - Sentinel-1 SAR - Interferometric Wide Swath - Sentinel Online*. [Online]. Available from: https://sentinel.esa.int/web/sentinel/user-guides/sentinel-1-sar/acquisition-modes/interferometric-wide-swath. Last Accessed 27/09/2019.

ESA (2018g) *User Guides - Sentinel-1 SAR - Product Types and Processing Levels - Sentinel Online*. [Online]. Available from: https://earth.esa.int/web/sentinel/user-guides/sentinel-1-sar/product-types-processing-levels. Last Accessed 27/09/2019.

ESA (2018h) *User Guides - Sentinel-1 SAR - Level-1 - Sentinel Online*. [Online]. Available from: https://earth.esa.int/web/sentinel/user-guides/sentinel-1-sar/product-types-processing-levels/level-1. Last Accessed 27/09/2019.

Esch, T., Schenk, A., Ullmann, T., Thiel, M., Roth, A. and Dech, S. (2011) Characterization of Land Cover Types in TerraSAR-X Images by Combined Analysis of Speckle Statistics and Intensity Information. *IEEE Transactions on Geoscience and Remote Sensing*. **49**:(6), 1911–1925. doi:10.1109/TGRS.2010.2091644.

European Commission (2019) *Copernicus Emergency Management Service*. [Online]. Available from: https://emergency.copernicus.eu/mapping/#zoom=4&lat=40.7626&lon=0.78575&layers=0BT00. Last Accessed 08/08/2019.

Farr, T., Rosen, P., Caro, E., Crippen, R., Duren, R., Hensley, S., Kobrick, M., Paller, M., Rodriguez, E., Roth, L., Seal, D., Shaffer, S., Shimada, J., Umland, J., et al. (2007) The shuttle radar topography mission. *Reviews of Geophysics*. **45**:(2005), 1–33. doi:10.1029/2005RG000183.

Feng, Q., Gong, J., Liu, J. and Li, Y. (2015) Flood Mapping Based on Multiple Endmember Spectral Mixture Analysis and Random Forest Classifier - The Case of Yuyao, China. *Remote Sensing.* **7**, 12539-12562. doi:10.3390/rs70912539.

Feyisa, G.L., Meilby, H., Fensholt, R. and Proud, S.R. (2014) Automated Water Extraction Index: A new technique for surface water mapping using Landsat imagery. *Remote Sensing of Environment*. **140**, 23–35. doi:10.1016/j.rse.2013.08.029.

Fischer, E.M. and Knutti, R. (2015) Anthropogenic contribution to global occurrence of heavy-precipitation and high-temperature extremes. *Nature Climate Change*. **5**:(6), 560–564. doi:10.1038/nclimate2617.

Foody, G.M. (2006) What is the difference between two maps? A remote senser's view. *Journal of Geographical Systems*. **8**:(2), 119–130. doi:10.1007/s10109-006-0023-z.

Fu, L.L. (2001) *Ocean Circulation and Variability from Satellite Altimetry*. J.C. Gerold Siedler and G. John (eds.). Cambridge, Massachusetts (USA): Academic Press. doi:10.1016/S0074-6142(01)80116-9

Gan, T.Y., Zunic, F., Kuo, C.-C. and Strobl, T. (2012) Flood mapping of Danube River at Romania using single and multi-date ERS2-SAR images. *International Journal of Applied Earth Observation and Geoinformation*. **18**:(1), 69–81. doi:10.1016/j.jag.2012.01.012.

Gao, Q., Zribi, M., Escorihuela, M.J. and Baghdadi, N. (2017) Synergetic use of sentinel-1 and sentinel-2 data for soil moisture mapping at 100 m resolution. *Sensors*. **17**:(9), 1966. doi:10.3390/s17091966.

García, A.J., Bakon, M., Martínez, R. and Marchamalo, M. (2018) Evolution of urban monitoring with radar interferometry in Madrid City: performance of ERS-1/ERS-2, ENVISAT, COSMO-SkyMed, and Sentinel-1 products. *International Journal of Remote Sensing*. **39**:(9), 2969–2990. doi:10.1080/01431161.2018.1437299.

Garschagen, M. and Romero-Lankao, P. (2015) Exploring the relationships between urbanization trends and climate change vulnerability. *Climatic Change*. **133**:(1), 37–52. doi:10.1007/s10584-013-0812-6.

GEE (2015) *Google Earth Engine: Sentinel-1 SAR GRD*. [Online]. Available from: https://explorer.earthengine.google.com/#detail/COPERNICUS%2FS1_GRD. Last Accessed 06/03/2019.

GEE (2019a) *ALOS DSM: Global 30m*. [Online]. Available from: https://developers.google.com/earth-engine/datasets/catalog/JAXA_ALOS_AW3D30_V1_1?fbclid=IwAR09OQ. Last Accessed 30/06/2019.

GEE (2019b) *DEM-S: Australian Smoothed Digital Elevation Model*. [Online]. Available from: https://developers.google.com/earth-engine/datasets/catalog/AU_GA_DEM_1SEC_v10_DEM-S?fbclid=IwAR0npHXaD6M8Z2Os4ymFnSRr8CP3P75hQPuKCqFXOt_FrGG1pEJv4dXyYlg. Last Accessed 30/06/2019.

Geng, J., Wang, H., Fan, J. and Ma, X. (2017) Deep Supervised and Contractive Neural Network for SAR Image Classification. *IEEE Transactions on Geoscience and Remote Sensing.* **55**:(4), 2442-2459. doi:10.1109/TGRS.2016.2645226.

Geoscience Australia (2010) *1 second SRTM Derived Digital Elevation Models User Guide – Version 1.0.3.* [Online]. Available from: https://d28rz98at9flks.cloudfront.net/72759/1secSRTM_Derived_DEMs_UserGuide_v1.0.4.pdf. Last Accessed 22/08/2019.

Geudtner, D., Torres, R., Snoeij, P., Davidson, M. and Rommen, B. (2014) Sentinel-1 System capabilities and applications. In: *Proceedings - IEEE Geoscience and Remote Sensing Symposium. Quebec City, Canada*. 2014. doi:10.1109/IGARSS.2014.6946711.

Gharari, S., Hrachowitz, M., Fenicia, F. and Savenije, H.H.G. (2011) Hydrological landscape classification: investigating the performance of HAND based landscape classifications in a central European meso-scale catchment. *Hydrology and Earth System Sciences.* **15**, 3275-3291. doi:10.5194/hess-15-3275-2011.

Giordan, D., Notti, D., Villa, A., Zucca, F., Calò, F., Pepe, A., Dutto, F., Pari, P., Baldo, M. and Allasia, P. (2018) Low cost , multiscale and multi-sensor application for flooded area mapping. *Natural Hazards and Earth System Science*. **18**, 1493–1516. doi:doi.org/10.5194/nhess-18-1483-2018.

Giustarini, L., Matgen, P., Hostache, R., Montanari, M., Plaza, D., Pauwels, V.R.N., De Lannoy, G.J.M., De Keyser, R., Pfister, L., Hoffmann, L. and Savenije, H.H.G. (2011) Assimilating SAR-derived water level data into a hydraulic model: a case study. *Hydrology and Earth System Sciences*. **15**:(7), 2349–2365. doi:10.5194/hess-15-2349-2011.

Giustarini, L., Hostache, R., Matgen, P., Schumann, G.J.P., Bates, P.D. and Mason, D.C. (2013) A Change Detection Approach to Flood Mapping in Urban Areas Using TerraSAR-X. *IEEE Transactions on Geoscience and Remote Sensing*. **51**:(4), 2417–2430. doi:10.1109/TGRS.2012.2210901.

Giustarini, L., Chini, M., Hostache, R., Pappenberger, F. and Matgen, P. (2015) Flood hazard mapping combining hydrodynamic modeling and multi annual remote sensing data. *Remote Sensing*. **7**:(10), 14200–14226. doi:10.3390/rs71014200.

González, P.J., Bagnardi, M., Hooper, A.J., Larsen, Y., Marinkovic, P., Samsonov, S. V. and Wright, T.J. (2015) The 2014-2015 eruption of Fogo volcano: Geodetic modeling of Sentinel-1 TOPS interferometry. *Geophysical Research Letters*. **42**:(21), 9239–9246. doi:10.1002/2015GL066003.

Gorelick, N., Hancher, M., Dixon, M., Ilyushchenko, S., Thau, D. and Moore, R. (2017) Google Earth Engine: Planetary-scale geospatial analysis for everyone. *Remote Sensing of Environment.* **202**, 18-27. doi:10.1016/j.rse.2017.06.031.

Gorokhovich, Y. and Voustianiouk, A. (2006) Accuracy assessment of the processed SRTM-based elevation data by CGIAR using field data from USA and Thailand and its relation to the terrain characteristics. *Remote Sensing of Environment*. **104**:(4), 409–415. doi:10.1016/j.rse.2006.05.012.

Grimaldi, S., Li, Y., Pauwels, V.R.N. and Walker, J.P. (2016) Remote Sensing-Derived Water Extent and Level to Constrain Hydraulic Flood Forecasting Models: Opportunities and Challenges. *Surveys in Geophysics*. **37**:(5), 977–1034. doi:10.1007/s10712-016-9378-y.

Güneralp, B., Güneralp, İ. and Liu, Y. (2015) Changing global patterns of urban exposure to flood and drought hazards. *Global Environmental Change*. **31**, 217–225. doi:10.1016/j.gloenvcha.2015.01.002.

Hansard, H.C. (2016) *Flooding Debate, Volume 604, Column 69*. [Online]. Available from: https://publications.parliament.uk/pa/cm201516/cmhansrd/cm160105/debtext/160105-0002.htm#16010519000001. Last Accessed 05/03/2019.

Henderson, F.M. and Lewis, A.J. (2008) Radar detection of wetland ecosystems: a review. *International Journal of Remote Sensing*. **29**:(20), 5809–5835. doi:10.1080/01431160801958405.

Henry, J.B., Chastanet, P., Fellah, K. and Desnos, Y.L. (2006) Envisat multi-polarized ASAR data for flood mapping. *International Journal of Remote Sensing*. **27**:(9–10), 1921–1929. doi:10.1080/01431160500486724.

Hess, L.L., Melack, J.M., Filoso, S. and Wang, Y. (1995) Delineation of Inundated Area and Vegetation Along the Amazon Floodplain with the SIR-C Synthetic Aperture Radar. *IEEE Transactions on Geoscience and Remote Sensing*. **33**:(4), 896–904. doi:10.1109/36.406675.

Hirt, C. (2014) Digital Terrain Models. *Encyclopedia of Geodesy.* Springer International Publishing, Switzerland. doi:10.1007/978-3-319-02370-0_31-1.

Holloway, J. and Mengersen K. (2018) Statistical Machine Learning Methods and Remote Sensing for Sustainable Development Goals: A Review. *Remote Sensing.* **10**, 1365. doi:10.3390/rs10091365.

Horritt, M. (1999) A statistical active contour model for SAR image segmentation. *Image and Vision Computing*. **17**:(3–4), 213–224. doi:10.1016/S0262-8856(98)00101-2.

Horritt, M., Mason, D.C. and Luckman, A.J. (2001) Flood boundary delineation from Synthetic Aperture Radar imagery using a statistical active contour model. *International Journal of Remote Sensing*. **22**:(13), 2489–2507. doi:10.1080/01431160152497691.

Horritt, M. (2003) Waterline mapping in flooded vegetation from airborne SAR imagery. *Remote Sensing of Environment*. **85**:(3), 271–281. doi:10.1016/S0034-4257(03)00006-3.

Hostache, R., Matgen, P., Schumann, G.J.P., Puech, C., Hoffmann, L. and Pfister, L. (2009) Water Level Estimation and Reduction of Hydraulic Model Calibration Uncertainties Using Satellite SAR Images of Floods. *IEEE Transactions on Geoscience and Remote Sensing*. **47**:(2), 431–441. doi:10.1109/TGRS.2008.2008718.

Hostache, R., Matgen, P. and Wagner, W. (2012) Change detection approaches for flood extent mapping: How to select the most adequate reference image from online archives? *International Journal of Applied Earth Observation and Geoinformation*. **19**:(1), 205–213. doi:10.1016/j.jag.2012.05.003.

Huang, C., Chen, Y., Wu, J., Chen, Z., Li, L., Liu, R. and Yu, J. (2014) Integration of remotely sensed inundation extent and high-precision topographic data for mapping inundation depth. In: *Proceedings - 3rd International Conference on Agro-Geoinformatics. Beijing, China.* 2014. doi:10.1109/Agro-Geoinformatics.2014.6910580.

Huang, C., Nguyen, B.D., Zhang, S., Cao, S. and Wagner, W. (2017) A Comparison of Terrain Indices toward Their Ability in Assisting Surface Water Mapping from Sentinel-1 Data. *International Journal of Geo-Information*. **6**:(140), 1–16. doi:10.3390/ijgi6050140.

Huang, H., Cheng, S., Wen, J. and Lee, J. (2008) Effect of growing watershed imperviousness on hydrograph parameters and peak discharge. *Hydrological Processes*. **22**:(13), 2075–2085. doi:10.1002/hyp.6807.

Huang, W., DeVries, B., Huang, C., Lang, M., Jones, J., Creed, I. and Carroll, M. (2018) Automated Extraction of Surface Water Extent from Sentinel-1 Data. *Remote Sensing*. **10**:(5), 797. doi:10.3390/rs10050797.

Huete, A., Didan, K., Miura, T., Rodriguez, E.P., Gao, X. and Ferreira, L.. (2002) Overview of the radiometric and biophysical performance of the MODIS vegetation indices. *Remote Sensing of Environment*. **83**:(1–2), 195–213. doi:10.1016/S0034-4257(02)00096-2.

Hunt, E.R., Gillham, J.H. and Daughtry, C.S.T. (2010) Improving potential geographic distribution models for invasive plants by remote sensing. *Rangeland Ecology and Management*. **63**:(5), 505–513. doi:10.2111/REM-D-09-00137.1.

Insom, P., Cao, C., Boonsrimuang, P., Liu, D., Saokarn, A., Yomwan, P. and Xu, Y. (2015) A Suppoert Vector Machine-Based Particle Filter Method for Improved Flooding Classification. *IEEE Geoscience and Remote Sensing Letters.* **12**:(9), 1943-1947. doi:10.1109/LGRS.2015.2439575.

IPCC (2012) *Managing the Risks of Extreme Events and Disasters to Advance Climate Change Adaptation.* Christopher B. Field, Vicente Barros, Thomas F. Stocker, and Qin Dahe (eds.). Cambridge: Cambridge University Press. [Online]. Available from: https://www.ipcc.ch/report/managing-the-risks-of-extreme-events-and-disasters-to-advance-climate-change-adaptation/.

Isikdogan, F., Bovik, A.C. and Passalacqua, P. (2017) Surface Water Mapping by Deep

Learning. *IEEE Journal of Selected Topics in Applied Earth Observations and Remote Sensing.* **10**:(11), 4909-4918. doi:0.1109/JSTARS.2017.2735443.

Jackson, T.J. (2002) Remote sensing of soil moisture: Implications for groundwater recharge. *Hydrogeology Journal*. **10**:(1), 40–51. doi:10.1007/s10040-001-0168-2.

Jarihani, A.A., Callow, J.N., Johansen, K. and Gouweleeuw, B. (2013) Evaluation of multiple satellite altimetry data for studying inland water bodies and river floods. *Journal of Hydrology*. **505**, 78–90. doi:10.1016/j.jhydrol.2013.09.010.

Jin, Y.Q. and Xu, F. (2013) *Polarimetric scattering and SAR information retrieval*. Hoboken, N.J.: John Wiley & Sons Inc.

Jongman, B., Ward, P.J. and Aerts, J.C.J.H. (2012) Global exposure to river and coastal flooding: Long term trends and changes. *Global Environmental Change*. **22**:(4), 823–835. doi:10.1016/j.gloenvcha.2012.07.004.

Jung, H.C., Hamski, J., Durand, M., Alsdorf, D., Hossain, F., Lee, H., Hossain, A.K.M.A., Hasan, K., Khan, A.S. and Hoque, A.K.M.Z. (2010) Characterization of complex fluvial systems using remote sensing of spatial and temporal water level variations in the Amazon, Congo, and Brahmaputra Rivers. *Earth Surface Processes and Landforms*. **35**:(3), 294–304. doi:10.1002/esp.1914.

Karvonen, J. (2018) Estimation of Arctic land-fast ice cover based on dual-polarized Sentinel-1 SAR imagery. *The Cryosphere*. **12**, 2595–2607. doi:10.5194/tc-12-2595-2018.

Kay, A.L., Davies, H.N., Bell, V.A. and Jones, R.G. (2009) Comparison of uncertainty sources for climate chnage impacts: flood frequency in England. *Climate Change*. **92**, 41–63. doi:10.1007/s10584-008-9471-4.

Keys, L. and Baade, J. (2019) Uncertainty in Catchment Delineations as a Result of Digital Elevation Model Choice. *Hydrology*. **6**:(1), 13. doi:10.3390/hydrology6010013.

Khaldoune, J., Van Bochove, E., Bernier, M. and Nolin, M.C. (2011) Mapping Agricultural Frozen Soil on the Watershed Scale Using Remote Sensing Data. *Applied and Environmental Soil Science*. **2011**, 1–16. doi:10.1155/2011/193237.

Kittler, J. and Illingworth, J. (1986) Minimum Error Thresholding. *Pattern Recognition*. **19**:(1), 41–47. doi:10.1016/0031-3203(86)90030-0.

Kolecka, N. and Kozak, J. (2014) Assessment of the Accuracy of SRTM C- and X-Band High Mountain Elevation Data: A Case Study of the Polish Tatra Mountains. *Pure and Applied Geophysics*. **171**:(6), 897–912. doi:10.1007/s00024-013-0695-5.

Kouraev, A. V, Zakharova, E.A., Samain, O., Mognard, N.M. and Cazenave, A. (2004) Ob' river discharge from TOPEX/Poseidon satellite altimetry (1992-2002). *Remote Sensing of Environment*. **93**:(1–2), 238–245. doi:10.1016/j.rse.2004.07.007.

Kundzewicz, Z.W., Kanae, S., Seneviratne, S.I., Handmer, J., Nicholls, N., Peduzzi, P., Mechler, R., Bouwer, L.M., Arnell, N., Mach, K., Muir-Wood, R., Brakenridge, G.R., Kron, W., Benito, G., et al. (2014) Flood risk and climate change: global and regional perspectives. *Hydrological Sciences Journal*. **59**:(1), 1–28. doi:10.1080/02626667.2013.857411.

Landuyt, L., Van Wesemael, A., Schumann, G.J.P., Hostache, R., Verhoest, N.E.C. and Van Coillie, F.M.B. (2018) Flood Mapping Based on Synthetic Aperture Radar: An Assessment of Established Approaches. *IEEE Transactions on Geoscience and Remote Sensing*. **57**:(2), 722–739. doi:10.1109/TGRS.2018.2860054.

Lau, N., Tymofyeyeva, E. and Fialko, Y. (2018) Variations in the long-term uplift rate due to the Altiplano–Puna magma body observed with Sentinel-1 interferometry. *Earth and Planetary Science Letters*. **491**, 43–47. doi:10.1016/j.epsl.2018.03.026.

Lee, J. Sen (1983) Digital image smoothing and the sigma filter. *Computer Vision, Graphics and Image Processing*. **24**:(2), 255–269. doi:10.1016/0734-189X(83)90047-6.

Lee, J. Sen, Wen, J.H., Ainsworth, T.L., Chen, K.S. and Chen, A.J. (2009) Improved sigma filter for speckle filtering of SAR imagery. *IEEE Transactions on Geoscience and Remote Sensing*. **47**:(1), 202–213. doi:10.1109/TGRS.2008.2002881.

Lemos, A., Shepherd, A., McMillan, M., Hogg, A.E., Hatton, E. and Joughin, I. (2018) Ice velocity of Jakobshavn Isbræ, Petermann Glacier, Nioghalvfjerdsfjorden, and Zachariæ Isstrøm, 2015–2017, from Sentinel 1-a/b SAR imagery. *The Cryosphere*. **12**:(6), 2087–2097. doi:10.5194/tc-12-2087-2018.

Lewis, A., Oliver, S., Lymburner, L., Evans, B., Wyborn, L., Mueller, N., Raevksi, G., Hooke, J., Woodcock, R., Sixsmith, J., Wu, W., Tan, P., Li, F., Killough, B., Minchin, S., Roberts, D., Ayers, D., Bala, B., Dwyer, J., Dekker, A., Dhu, T., Hicks, A., Ip, A., Purss, M., Richards, C., Sagar, S., Trenham, C., Wang, P. and Wang, L.-W. (2017) The Australian Geoscience Data Cube - Foundations and lessons learned. *Remote Sensing of Environment.* **202**, 276-292. doi:10.1016/j.rse.2017.03.015.

Li, L., Chen, Y., Xu, T., Liu, R., Shi, K. and Huang, C. (2015) Super-resolution mapping of wetland inundation from remote sensing imagery based on integration of back-propagation neural network and genertic algorithm. *Remote Sensing of Environment.* **164**, 142-154. doi:10.1016/j.rse.2015.04.009.

Li, S., Dragicevic, S., Castro, F.A., Sester, M., Winter, S., Coltekin, A., Pettit, C., Jiang, B., Haworth, J., Stein, A. and Cheng, T. (2016) Geospatial big data handling theory and methods: A review and research challenges. *ISPRS Journal of Photogrammetry and Remote Sensing.* **115**, 119-133. doi:10.1016/j.isprsjprs.2015.10.012.

Li, Y., Martinis, S. and Wieland, M. (2019) Urban flood mapping with an active self-learning convolutional neural network based on TerraSAR-X intensity and interferometric coherence. *ISPRS Journal of Photogrammetry and Remote Sensing*. **152**, 178–191. doi:10.1016/j.isprsjprs.2019.04.014.

Li, Z., Zhu, Q. and Gold, C. (2004) *Digital Terrain Modelling: Principles and Methodology*. Boca Raton, Fla., London: CRC.

Liang, S., Li, X. and Wang, J. (2012) *Advanced remote sensing : terrestrial information extraction and applications*. Amsterdam ; London: Elsevier Academic Press.

Lillesand, T.M., Kiefer, R.W. and Chipman, J.W. (2008) *Remote sensing and image interpretation*. 6th ed.. Hoboken, N.J.: John Wiley & Sons.

Long, S., Fatoyinbo, T.E. and Policelli, F. (2014) Flood extent mapping for Namibia using change detection and thresholding with SAR. *Environmental Research Letters*. **9**:(3), 035002. doi:10.1088/1748-9326/9/3/035002.

Loritz, R., Kleidon, A., Jackisch, C., Westhoff, M., Ehret, U., Gupta, H. and Zehe, E. (2019) A topographic index explaining hydrological similarity by accounting for the joint controls of runoff formation. *Hydrology and Earth System Sciences.* **23**, 3807-3821. doi:10.5194/hess-23-3807-2019.

Lu, J., Giustarini, L., Xiong, B., Zhao, L., Jiang, Y. and Kuang, G. (2014) Automated flood detection with improved robustness and efficiency using multi-temporal SAR data. *Remote Sensing Letters*. **5**:(3), 240–248. doi:10.1080/2150704X.2014.898190.

Lu, J., Li, J., Chen, G., Zhao, L., Xiong, B. and Kuang, G. (2015) Improving pixel-based change detection accuracy using an object-based approach in multitemporal SAR flood images. *IEEE Journal of Selected Topics in Applied Earth Observations and Remote Sensing*. **8**:(7), 3486–3496. doi:10.1109/JSTARS.2015.2416635.

Ludwig, R. and Schneider, P. (2006) Validation of digital elevation models from SRTM X-

SAR for applications in hydrologic modeling. *ISPRS Journal of Photogrammetry and Remote Sensing*. **60**:(5), 339–358. doi:10.1016/j.isprsjprs.2006.05.003.

Lunetta, R.S., Johnson, D.M., Lyon, J.G. and Crotwell, J. (2004) Impacts of imagery temporal frequency on land-cover change detection monitoring. *Remote Sensing of Environment*. **89**:(4), 444–454. doi:10.1016/j.rse.2003.10.022.

Ma, Y., Wu, H., Wang, L., Huang, B., Ranjan, R., Zomaya, A. and Jie, W. (2015) Remote sensing big data computing: Challenges and opportunities. *Future Generation Computer Systems.* **51**, 47-60. doi:10.1016/j.future.2014.10.029.

Madsen, H., Lawrence, D., Lang, M., Martinkova, M. and Kjeldsen, T.R. (2014) Review of trend analysis and climate change projections of extreme precipitation and floods in Europe. *Journal of Hydrology*. **519**, 3634–3650. doi:10.1016/j.jhydrol.2014.11.003.

Maheu, C., Cazenave, A. and Mechoso, C.R. (2003) Water level fluctuations in the Plata Basin (South America) from Topex/Poseidon Satellite Altimetry. *Geophysical Research Letters*. **30**:(3), 2019. doi:10.1029/2002GL016033.

Manavalan, R. (2018) Review of synthetic aperture radar frequency, polarization, and incidence angle data for mapping the inundated regions. *Journal of Applied Remote Sensing.* **12**:(2), 021501. doi:10.1117/1.JRS.12.021501.

Manjusree, P., Prasanna Kumar, L., Bhatt, C.M., Rao, G.S. and Bhanumurthy, V. (2012) Optimization of threshold ranges for rapid flood inundation mapping by evaluating backscatter profiles of high incidence angle SAR images. *International Journal of Disaster Risk Science*. **3**:(2), 113–122. doi:10.1007/s13753-012-0011-5.

Mansourpour, M., Rajabi, M.A. and Blais, J.A.R. (2006) Effects and performance of speckle noise reduction filters on active radar and SAR images. In: *Proceedings - Workshop on Topographic Mapping from Space, Ankara, Turkey*. 2006

Martinez, J. and Le Toan, T. (2007) Mapping of flood dynamics and spatial distribution of vegetation in the Amazon floodplain using multitemporal SAR data. *Remote Sensing of Environment*. **108**:(3), 209–223. doi:10.1016/j.rse.2006.11.012.

Martinis, S., Twele, A. and Voigt, S. (2009) Towards operational near real-time flood detection using a split-based automatic thresholding procedure on high resolution TerraSAR-X data. *Natural Hazards and Earth System Sciences*. **9**:(2), 303–314. doi:10.5194/nhess-9-303-2009.

Martinis, S. and Rieke, C. (2015) Backscatter analysis using multi-temporal and multi-frequency SAR data in the context of flood mapping at River Saale, Germany. *Remote Sensing*. **7**:(6), 7732–7752. doi:10.3390/rs70607732.

Martinis, S., Kuenzer, C., Wendleder, A., Huth, J., Twele, A., Roth, A. and Dech, S. (2015a) Comparing four operational SAR-based water and flood detection approaches. *International Journal of Remote Sensing*. **36**:(13), 3519–3543. doi:10.1080/01431161.2015.1060647.

Martinis, S., Kersten, J. and Twele, A. (2015b) A fully automated TerraSAR-X based flood service. *ISPRS Journal of Photogrammetry and Remote Sensing*. **104**, 203–212. doi:10.1016/j.isprsjprs.2014.07.014.

Martinis, S., Plank, S. and Ćwik, K. (2018) The use of Sentinel-1 time-series data to improve flood monitoring in arid areas. *Remote Sensing*. **10**, 583. doi:10.3390/rs10040583.

Mason, D.C., Horritt, M.S., Amico, J.T.D., Scott, T.R. and Bates, P.D. (2007) Improving River Flood Extent Delineation From Synthetic Aperture Radar Using Airborne Laser Altimetry. *IEEE Geoscience and Remote Sensing*. **45**:(12), 3932–3943. doi:10.1109/TGRS.2007.901032.

Mason, D.C., Davenport, I.J., Neal, J.C., Schumann, G.J.P. and Bates, P.D. (2012a) Near real-time flood detection in urban and rural areas using high-resolution synthetic aperture radar images. *IEEE Transactions on Geoscience and Remote Sensing*. **50**:(8), 3041–3052. doi:10.1109/TGRS.2011.2178030.

Mason, D.C., Schumann, G.J.P., Neal, J.C., Garcia-Pintado, J. and Bates, P.D. (2012b) Automatic near real-time selection of flood water levels from high resolution Synthetic Aperture Radar images for assimilation into hydraulic models: A case study. *Remote Sensing of Environment*. **124**, 705–716. doi:10.1016/j.rse.2012.06.017.

Mason, D.C., Giustarini, L., Garcia-Pintado, J. and Cloke, H.L. (2014) Detection of flooded urban areas in high resolution Synthetic Aperture Radar images using double scattering. *International Journal of Applied Earth Observation and Geoinformation*. **28**:(1), 150–159. doi:10.1016/j.jag.2013.12.002.

Matgen, P., Idrissi, A. El, Henry, J., Tholey, N., Hoffmann, L., Fraipont, P. De and Pfister, L. (2006) Patterns of remotely sensed floodplain saturation and its use in runoff predictions. *Hydrological Processes.* **20**, 1805–1825. doi:10.1002/hyp.5963.

Matgen, P., Schumann, G.J.P., Henry, J.-B., Hoffmann, L. and Pfister, L. (2007) Integration of SAR-derived river inundation areas, high-precision topographic data and a river flow model toward near real-time flood management. *International Journal of Applied Earth Observation and Geoinformation*. **9**:(3), 247–263. doi:10.1016/j.jag.2006.03.003.

Matgen, P., Montanari, M., Hostache, R., Pfister, L., Hoffmann, L., Plaza, D., Pauwels, V.R.N., De Lannoy, G.J.M., De Keyser, R. and Savenije, H.H.G. (2010) Towards the sequential assimilation of SAR-derived water stages into hydraulic models using the Particle Filter: Proof of concept. *Hydrology and Earth System Sciences*. **14**:(9), 1773–1785. doi:10.5194/hess-14-1773-2010.

Matgen, P., Hostache, R., Schumann, G.J.P., Pfister, L., Hoffmann, L. and Savenije, H.H.G. (2011) Towards an automated SAR-based flood monitoring system: Lessons learned from two case studies. *Physics and Chemistry of the Earth, Parts A/B/C*. **36**:(7–8), 241–252. doi:10.1016/j.pce.2010.12.009.

Matgen, P., Giustarini, L., Chini, M., Hostache, R., Wood, M. and Schlaffer, S. (2016) Creating a water depth map from SAR flood extent and topography data. *International Geoscience and Remote Sensing Symposium (IGARSS)*. 7635–7638. doi:10.1109/IGARSS.2016.7730991.

Mather, P.M. and Koch, M. (2011) *Computer processing of remotely-sensed images : an introduction*. 4th ed.. Chichester, West Sussex, UK ; Hoboken, NJ: Wiley-Blackwell.

Maune, D.F. (2007) *Digital Elevation Model Technologies and Applications: The DEM Users Manual*. 2nd ed.. Bethesda, MD: American Society for Photogrammetry and Remote Sensing.

McCabe, M.F., Rodell, M., Alsdorf, D.E., Miralles, D.G., Uijlenhoet, R., Wagner, W., Lucieer, A., Houborg, R., Verhoest, N.E.C., Franz, T.E., Shi, J., Gao, H. and Wood, E.F. (2017) The future of Earth observation in hydrology. *Hydrology and Earth System Sciences.* **21**, 3879-3914. doi:10.5194/hess-21-3879-2017.

McCarthy, M., Walsh, S. and Kendon, M. (2016) The meteorology of the exceptional winter of 2015 / 2016 across the UK and Ireland. *Weather*. **71**, 305–313. doi:10.1002/wea.2823.

McFeeters, S.K. (1996) The use of the Normalized Difference Water Index (NDWI) in the delineation of open water features. *International Journal of Remote Sensing*. **17**:(7), 1425–1432. doi:10.1080/01431169608948714.

McGrath, H., Proulx-Bourque, J.-S., Bourgon, J.-F., Nastev, M. and Abo El Ezz, A. (2018) A

Comparison of Rapid DTM Based Approaches for on-demand Flood Inundation Mapping. In: *Proceedings - IEEE International Geoscience and Remote Sensing Symposium. Valencia, Spain.* 2018. doi:10.1109/IGARSS.2018.8517772.

Merz, B. and Thieken, A.H. (2005) Separating natural and epistemic uncertainty in flood frequency analysis. *Journal of Hydrology*. **309**:(1–4), 114–132. doi:10.1016/j.jhydrol.2004.11.015.

Met Office (2015) *UK Storm Centre - Met Office Barometer*. [Online]. Available from: https://www.metoffice.gov.uk/barometer/uk-storm-centre. Last Accessed 05/03/2019.

Met Office (2016) *Summary - January 2016*. [Online]. Available from: https://www.metoffice.gov.uk/climate/uk/summaries/2016/january. Last Accessed 06/05/2019.

Met Office (2017) *UKCP09 Datasets*. [Online]. Available from: https://www.metoffice.gov.uk/climate/uk/data/ukcp09/datasets. Last Accessed 21/05/2019.

Meta, A., Prats, P., Steinbrecher, U., Mittermayer, J. and Scheiber, R. (2008) TerraSAR-X TOPSAR and ScanSAR comparison. In: *Proceedings - 7th European Conference on Synthetic Aperture Radar. Friedrichshafen, Germany.* 2008

Miller, J.D., Kim, H., Kjeldsen, T.R., Packman, J., Grebby, S. and Dearden, R. (2014) Assessing the impact of urbanization on storm runoff in a peri-urban catchment using historical change in impervious cover. *Journal of Hydrology*. **515**, 59–70. doi:10.1016/j.jhydrol.2014.04.011.

Milly, P.C.D., Wetherald, R.T., Dunne, K.A. and Delworth, T.L. (2002) Increasing risk of great floods in a changing climate. *Nature*. **415**, 514. doi:10.1038/415514a.

Minh, D.H.T., Ienco, D., Gaetano, R., Lalande, N., Ndikumana, E., Osman, F. and Maurel, P. (2017) Deep Recurrent Neural Networks for mapping winter vegetation quality coverage via multi-temporal SAR Sentinel-1. *IEEE Geoscience and Remote Sensing Letters*. **15**:(3), 464–468. doi:10.1109/LGRS.2018.2794581.

Mitchell, A.L., Milne, A.K. and Tapley, I. (2014) Towards an operational SAR monitoring system for monitoring environmental flows in the Macquarie Marshes. *Wetlands Ecology and Management*. **23**:(1), 61–77. doi:10.1007/s11273-014-9358-2.

Molleri, G.S.F., Kampel, M. and Leao de Moraes Novo, E.M. (2010) Spectral classification of water masses under the influence of the Amazon River plume. *Acta Oceanol. Sin.* **29:**(3), 1-8. doi:10.1007/s13131-010-0031-1.

Moser, G. and Serpico, S.B. (2005) Generalized minimum-error thresholding for unsupervised change detection from SAR amplitude imagery. In: *Proceedings - IEEE International Geoscience and Remote Sensing Symposium. Seoul, South Korea.* 2005. doi:10.1109/IGARSS.2005.1526436.

Mouginot, J., Rignot, E., Scheuchl, B. and Millan, R. (2017) Comprehensive Annual Ice Sheet Velocity Mapping Using Landsat-8, Sentinel-1, and RADARSAT-2 Data. *Remote Sensing*. **9**:(4), 364. doi:10.3390/rs9040364.

Muckenhuber, S., Korosov, A.A. and Sandven, S. (2016) Open-source feature-tracking algorithm for sea ice drift retrieval from Sentinel-1 SAR imagery. *The Cryosphere*. **10**:(2), 913–925. doi:10.5194/tc-10-913-2016.

Muro, J., Canty, M., Conradsen, K., Hüttich, C., Nielsen, A., Skriver, H., Remy, F., Strauch, A., Thonfeld, F. and Menz, G. (2016) Short-Term Change Detection in Wetlands Using Sentinel-1 Time Series. *Remote Sensing*. **8**:(10), 795. doi:10.3390/rs8100795.

Musa, Z.N., Popescu, I. and Mynett, A. (2015) A review of applications of satellite SAR,

optical, altimetry and DEM data for surface water modelling, mapping and parameter estimation. *Hydrology and Earth System Sciences*. **19**:(9), 3755–3769. doi:10.5194/hess-19-3755-2015.

Naeimi, V., Paulik, C., Bartsch, A., Wagner, W., Kidd, R., Park, S.E., Elger, K. and Boike, J. (2012) ASCAT surface state flag (SSF): Extracting information on surface freeze/thaw conditions from backscatter data using an empirical threshold-analysis algorithm. *IEEE Transactions on Geoscience and Remote Sensing*. **50**:(7), 2566–2582. doi:10.1109/TGRS.2011.2177667.

Nakmuenwai, P., Yamazaki, F. and Liu, W. (2017) Automated extraction of inundated areas from multi-temporal dual-polarization RADARSAT-2 images of the 2011 central Thailand flood. *Remote Sensing*. **9**:(1), 78. doi:10.3390/rs9010078.

Nandi, I., Srivastava, P.K. and Shah, K. (2017) Floodplain Mapping through Support Vector Machine and Opyical/Infrared Images from Landsat 8 OLI/TIRS Sensors: Case Study from Varanasi. *Water Resource Management.* **31**, 1157-1171. doi:10.1007/s11269-017-1568-y.

NHMP (2016) *National Hydrological Monitoring Programme: Hydrological summary for the United Kingdom: December 2015*. [Online]. Available from: http://nora.nerc.ac.uk/512654/1/HS_201512 v2.pdf. Last Accessed 06/03/2019.

Nobre, A.D., Cuartas, L.A., Hodnett, M., Rennó, C.D., Rodrigues, G., Silveira, A., Waterloo, M. and Saleska, S. (2011) Height Above the Nearest Drainage - a hydrologically relevant new terrain model. *Journal of Hydrology*. **404**:(1–2), 13–29. doi:10.1016/j.jhydrol.2011.03.051.

O'Grady, D., Leblanc, M. and Gillieson, D. (2011) Use of ENVISAT ASAR Global Monitoring Mode to complement optical data in the mapping of rapid broad-scale flooding in Pakistan. *Hydrology and Earth System Sciences*. **15**:(11), 3475–3494. doi:10.5194/hess-15-3475-2011.

O'Grady, D., Leblanc, M. and Gillieson, D. (2013) Relationship of local incidence angle with satellite radar backscatter for different surface conditions. *International Journal of Applied Earth Observation and Geoinformation*. **24**:(1), 42–53. doi:10.1016/j.jag.2013.02.005.

O'Grady, D., Leblanc, M. and Bass, A. (2014) The use of radar satellite data from multiple incidence angles improves surface water mapping. *Remote Sensing of Environment*. **140**, 652–664. doi:10.1016/j.rse.2013.10.006.

Oberstadler, R., Honsch, H. and Huth, D. (1997) Assessment of the mapping capabilities of ERS-1 SAR data for flood mapping : a case study in Germany. *Hydrological Processes*. **11**, 1415–1425. doi:10.1002/(SICI)1099-1085(199708)11:10<1415::AID-HYP532>3.0.CO;2-2.

Ordnance Survey (2017) *OS TERRAIN 5: User guide and technical specification OS Terrain 5 User guide*. [Online]. Available from: https://www.ordnancesurvey.co.uk/docs/user-guides/os-terrain-5-user-guide.pdf. Last Accessed 22/05/2019

Ordnance Survey (2018) *OS VectorMap Local*. [Online]. Available from: https://digimap.edina.ac.uk/webhelp/os/osdigimaphelp.htm#data_information/os_products/vectormap_local.htm. Last Accessed 27/09/2019.

Orlowsky, B. and Seneviratne, S.I. (2012) Global changes in extreme events: regional and seasonal dimension. *Climatic Change*. **110**:(3–4), 669–696. doi:10.1007/s10584-011-0122-9.

Otsu, N. (1979) A Threshold Selection Method from Gray-Level Histograms. *IEEE Transactions on Systems, Man, and Cybernetics*. **9**:(1), 62–66.

doi:10.1109/TSMC.1979.4310076.

Owrangi, A.M., Lannigan, R. and Simonovic, S.P. (2014) Interaction between land-use change, flooding and human health in Metro Vancouver, Canada. *Natural Hazards*. **72**:(2), 1219–1230. doi:10.1007/s11069-014-1064-0.

Ozdemir, H. and Bird, D. (2009) Evaluation of morphometric parameters of drainage networks derived from topographic maps and DEM in point of floods. *Environmental Geology*. **56**:(7), 1405–1415. doi:10.1007/s00254-008-1235-y.

Pal, S.K. and Rosenfeld, A. (1988) Image enhancement and thresholding by optimization of fuzzy compactness. *Pattern Recognition Letters*. doi:10.1016/0167-8655(88)90122-5.

Park, J.W., Korosov, A.A., Babiker, M., Sandven, S. and Won, J.S. (2018) Efficient Thermal Noise Removal for Sentinel-1 TOPSAR Cross-Polarization Channel. *IEEE Transactions on Geoscience and Remote Sensing*. **56**:(3), 1555–1565. doi:10.1109/TGRS.2017.2765248.

Paul, A., Tripathi, D. and Dutta, D. (2018) Application and comparison of advanced supervised classifiers in extraction of water bodies from remote sensing images. *Sustainable Water Resource Management.* **4**, 905-919. doi:10.1007/s40899-017-0184-6.

Peduzzi, P., Dao, H., Herold, C. and Mouton, F. (2009) Assessing global exposure and vulnerability towards natural hazards: the Disaster Risk Index. *Natural Hazards and Earth System Science*. **9**:(4), 1149–1159. doi:10.5194/nhess-9-1149-2009.

Pekel, J.-F., Cottam, A., Gorelick, N. and Belward, A.S. (2016) High-resolution mapping of global surface water and its long-term changes. *Nature*. **540**:(7633), 418–422. doi:10.1038/nature20584.

Pham-Duc, B., Prigent, C. and Aires, F. (2017) Surface water monitoring within Cambodia and the Vietnamese Mekong Delta over a year, with Sentinel-1 SAR observations. *Water*. **9**:(6), 1–21. doi:10.3390/w9060366.

Pierdicca, N., Chini, M., Pulvirenti, L. and Macina, F. (2008) Integrating Physical and Topographic Information Into a Fuzzy Scheme to Map Flooded Area by SAR. *Sensors*. **8**:(7), 4151–4164. doi:10.3390/s8074151.

Pivot, F.C. (2012) C-band SAR imagery for snow-cover monitoring at Treeline, Churchill, Manitoba, Canada. *Remote Sensing*. **4**:(7), 2133–2155. doi:10.3390/rs4072133.

Plank, S., Jüssi, M., Martinis, S. and Twele, A. (2017) Mapping of flooded vegetation by means of polarimetric Sentinel-1 and ALOS-2 / PALSAR-2 imagery. *International Journal of Remote Sensing*. **38**:(13), 3831–3850. doi:10.1080/01431161.2017.1306143.

Porter, J. and Demeritt, D. (2012) Flood-risk management, mapping, and planning: Theinstitutional politics of decision support in England. *Environment and Planning A*. **44**:(10), 2359–2378. doi:10.1068/a44660.

Pradhan, B., Hagemann, U., Shafapour Tehrany, M. and Prechtel, N. (2014) An easy to use ArcMap based texture analysis program for extraction of flooded areas from TerraSAR-X satellite image. *Computers and Geosciences*. **63**, 34–43. doi:10.1016/j.cageo.2013.10.011.

Proietti, S., Lorenzon, F., Uttenhaler, A., Klaus, A. and Probeck, M. (2017) Overview of Global DEM: Assessment of the current global DEMs and requirements for an updated global DEM. [Online]. Available from: https://insitu.copernicus.eu/library/reports/OverviewofGlobalDEM_i0r7.pdf. Last Accessed 05/01/2020

Prudhomme, C., Giuntoli, I., Robinson, E.L., Clark, D.B., Arnell, N.W., Dankers, R., Fekete,

B.M., Franssen, W., Gerten, D., Gosling, S.N., Hagemann, S., Hannah, D.M., Kim, H., Masaki, Y., et al. (2014) Hydrological droughts in the 21st century, hotspots and uncertainties from a global multimodel ensemble experiment. *Proceedings of the National Academy of Sciences*. **111**:(9), 3262–3267. doi:10.1073/pnas.1222473110.

Pulvirenti, L., Pierdicca, N., Chini, M. and Guerriero, L. (2011) An algorithm for operational flood mapping from Synthetic Aperture Radar (SAR) data using fuzzy logic. *Natural Hazards and Earth System Science*. **11**:(2), 529–540. doi:10.5194/nhess-11-529-2011.

Pulvirenti, L., Pierdicca, N., Chini, M. and Guerriero, L. (2013) Monitoring flood evolution in vegetated areas using Cosmo-Skymed data: The Tuscany 2009 case study. *IEEE Journal of Selected Topics in Applied Earth Observations and Remote Sensing*. **6**:(4), 1807–1816. doi:10.1109/JSTARS.2012.2219509.

Pulvirenti, L., Marzano, F.S., Pierdicca, N., Mori, S. and Chini, M. (2014) Discrimination of Water Surfaces , Heavy Rainfall , and Wet Snow Using COSMO-SkyMed Observations of Severe Weather Events. *IEEE Transactions on Geoscience and Remote Sensing*. **52**:(2), 858–869. doi:10.1109/TGRS.2013.2244606.

Pulvirenti, L., Chini, M., Pierdicca, N. and Boni, G. (2016) Use of SAR Data for Detecting Floodwater in Urban and Agricultural Areas: The Role of the Interferometric Coherence. *IEEE Transactions on Geoscience and Remote Sensing*. **54**:(3), 1532–1544. doi:10.1109/TGRS.2015.2482001.

Raclot, D. (2006) Remote sensing of water levels on floodplains : a spatial approach guided by hydraulic functioning. *International Journal of Remote Sensing*. **27**:(12), 2553–2574. doi:10.1080/01431160600554397.

Rahman, S. and Di, L. (2017) The state of the art of spaceborne remote sensing in flood management. *Natural Hazards*. **85**:(2), 1223–1248. doi:10.1007/s11069-016-2601-9.

Rahmati, O., Kornejady, A., Samadi, M., Nobre, A.D. and Melesse, A.M. (2018) Development of an automated GIS tool for reproducing the HAND terrain model. *Environmental Modelling and Software*. **102**, 1–12. doi:10.1016/j.envsoft.2018.01.004.

Rakwatin, P., Sansena, T., Marjang, N. and Rungsipanich, A. (2013) Using multi-temporal remote-sensing data to estimate 2011 flood area and volume over Chao Phraya River basin, Thailand. *Remote Sensing Letters*. **4**:(3), 243–250. doi:10.1080/2150704X.2012.723833.

Rees, W.G. (2000) Simple masks for shadowing and highlighting in SAR images. *International Journal of Remote Sensing*. **21**:(11), 2145–2152. doi:10.1080/01431160050029477.

Rees, G. (2013) *Physical principles of remote sensing*. 3rd ed.. Cambridge ; New York: Cambridge University Press.

Refice, A., Capolongo, D., Pasquariello, G., DaAddabbo, A., Bovenga, F., Nutricato, R., Lovergine, F.P. and Pietranera, L. (2014) SAR and InSAR for Flood Monitoring: Examples With COSMO-SkyMed Data. *IEEE Journal of Selected Topics in Applied Earth Observations and Remote Sensing*. **7**:(7), 2711–2722. doi:10.1109/JSTARS.2014.2305165.

Rennó, C.D., Nobre, A.D., Cuartas, L.A., Soares, J.V., Hodnett, M.G., Tomasella, J. and Waterloo, M.J. (2008) HAND, a new terrain descriptor using SRTM-DEM: Mapping terra-firme rainforest environments in Amazonia. *Remote Sensing of Environment*. **112**:(9), 3469–3481. doi:10.1016/j.rse.2008.03.018.

Rignot, E. and Way, J.B. (1994) Monitoring freeze-thaw cycles along North-South Alaskan transects using ERS-1 SAR. *Remote Sensing of Environment*. **49**:(2), 131–137. doi:10.1016/0034-4257(94)90049-3.

Rodriguez, E., Morris, C.C. and Belz, J.J. (2006) A global assessment of the SRTM performance. *Photogrammetric Engineering and Remote Sensing*. **72**:(3), 249–260. doi:10.14358/PERS.72.3.249.

Rüetschi, M., Schaepman, M.E. and Small, D. (2017) Using Multitemporal Sentinel-1 C-band Backscatter to Monitor Phenology and Classify Deciduous and Coniferous Forests in Northern Switzerland. *Remote Sensing*. **10**:(2), 55. doi:10.3390/rs10010055.

Saatchi, S.S. and van Zyl, J.J. (1995) Estimation of canopy water content in Konza Prairie grasslands using synthetic aperture radar measurements during FIFE. *Journal of Geophysical Research*. **100**:(D12), 25481–25496. doi:10.1029/95jd00852.

Santoro, M. and Wegmüller, U. (2014) Multi-temporal synthetic aperture radar metrics applied to map open water bodies. *IEEE Journal of Selected Topics in Applied Earth Observations and Remote Sensing*. **7**:(8), 3225–3238. doi:10.1109/JSTARS.2013.2289301.

Satgé, F., Bonnet, M.P., Timouk, F., Calmant, S., Pillco, R., Molina, J., Lavado-Casimiro, W., Arsen, A., Crétaux, J.F. and Garnier, J. (2015) Accuracy assessment of SRTM v4 and ASTER GDEM v2 over the Altiplano watershed using ICESat/GLAS data. *International Journal of Remote Sensing*. **36**:(2), 465–488. doi:10.1080/01431161.2014.999166.

Scarpino, S., Albano, R., Cantisani, A., Mancusi, L., Sole, A. and Milillo, G. (2018) Multitemporal SAR Data and 2D Hydrodynamic Model Flood Scenario Dynamics Assessment. *International Journal of Geo-Information.* **7**, 105. doi:10.3390/ijgi7030105.

Schewe, J., Heinke, J., Gerten, D., Haddeland, I., Arnell, N.W., Clark, D.B., Dankers, R., Eisner, S., Fekete, B.M., Colón-González, F.J., Gosling, S.N., Kim, H., Liu, X., Masaki, Y., et al. (2014) Multimodel assessment of water scarcity under climate change. *Proceedings of the National Academy of Sciences*. **111**:(9), 3245–3250. doi:10.1073/pnas.1222460110.

Schlaffer, S., Matgen, P., Hollaus, M. and Wagner, W. (2015) Flood detection from multi-temporal SAR data using harmonic analysis and change detection. *International Journal of Applied Earth Observation and Geoinformation*. **38**, 15–24. doi:10.1016/j.jag.2014.12.001.

Schlaffer, S., Chini, M., Giustarini, L. and Matgen, P. (2017) Probabilistic mapping of flood-induced backscatter changes in SAR time series. *International Journal of Applied Earth Observation and Geoinformation*. **56**, 77–87. doi:10.1016/j.jag.2016.12.003.

Schumann, G., Hostache, R., Puech, C., Hoffmann, L., Matgen, P., Pappenberger, F. and Pfister, L. (2007) High-resolution 3-D flood information from radar imagery for flood hazard management. *IEEE Transactions on Geoscience and Remote Sensing*. **45**:(6), 1715–1725. doi:10.1109/TGRS.2006.888103.

Schumann, G.J.P., Matgen, P., Cutler, M.E.J., Black, A., Hoffmann, L. and Pfister, L. (2008a) Comparison of remotely sensed water stages from LiDAR, topographic contours and SRTM. *ISPRS Journal of Photogrammetry and Remote Sensing*. **63**:(3), 283–296. doi:10.1016/j.isprsjprs.2007.09.004.

Schumann, G., Matgen, P. and Pappenberger, F. (2008b) Conditioning Water Stages From Satellite Imagery on Uncertain Data Points. *IEEE Geoscience and Remote Sensing Letters*. **5**:(4), 810–813. doi:10.1109/LGRS.2008.2005646.

Schumann, G.J.P., Bates, P.D., Horritt, M.S., Matgen, P. and Pappenberger, F. (2009a) Progress in integration of remote sensing–derived flood extent and stage data and hydraulic models. *Reviews of Geophysics*. **47**:(4), RG4001. doi:10.1029/2008RG000274.

Schumann, G.J.P., Di Baldassarre, G. and Bates, P.D. (2009b) The Utility of Spaceborne

Radar to Render Flood Inundation Maps Based on Multialgorithm Ensembles. *IEEE Transactions on Geoscience and Remote Sensing*. **47**:(8), 2801–2807. doi:10.1109/TGRS.2009.2017937.

Schumann, G.J.P. and Moller, D.K. (2015) Microwave remote sensing of flood inundation. *Physics and Chemistry of the Earth*. **83**–**84**, 84–95. doi:10.1016/j.pce.2015.05.002.

Schumann, G.J.P. and Bates, P.D. (2018) The Need for a High-Accuracy , Open-Access Global DEM. *Frontiers in Earth Science.* **6**, 1–5. doi:10.3389/feart.2018.00225.

Shao, W., Zhang, Z., Li, X. and Li, H. (2016) Ocean wave parameters retrieval from Sentinel-1 SAR imagery. *Remote Sensing*. **8**, 707. doi:10.3390/rs8090707.

Skakun, S. (2010) A neural network approach to flood mapping using satellite imagery. *Computing and Informatics.* **29**, 1013-1024.

Small, D. and Schubert, A. (2008) Guide to ASAR Geocoding *Remote Sensing Laboratores, University of Zurich*. [Online]. Available from: http://www.geo.uzh.ch/microsite/rsl-documents/research/publications/other-sci-communications/2008_RSL-ASAR-GC-AD-v101-0335607552/2008_RSL-ASAR-GC-AD-v101.pdf.

Small, D. (2011) Flattening gamma: Radiometric terrain correction for SAR imagery. *IEEE Transactions on Geoscience and Remote Sensing*. **49**:(8), 3081–3093. doi:10.1109/TGRS.2011.2120616.

Smith, L.C. (1997) Satellite remote sensing of river inundation area, stage, and discharge: a review. *Hydrological Processes*. **11**:(10), 1427–1439. doi:10.1002/(SICI)1099-1085(199708)11:10<1427::AID-HYP473>3.0.CO;2-S.

Snapir, B., Momblanch, A., Jain, S.K., Waine, T.W. and Holman, I.P. (2019) A method for monthly mapping of wet and dry snow using Sentinel-1 and MODIS: Application to a Himalayan river basin. *International Journal of Applied Earth Observation and Geoinformation*. **74**:(October 2018), 222–230. doi:10.1016/j.jag.2018.09.011.

Sowter, A., Bin Che Amat, M., Cigna, F., Marsh, S., Athab, A. and Alshammari, L. (2016) Mexico City land subsidence in 2014–2015 with Sentinel-1 IW TOPS: Results using the Intermittent SBAS (ISBAS) technique. *International Journal of Applied Earth Observation and Geoinformation*. **52**, 230–242. doi:10.1016/j.jag.2016.06.015.

Stefanidis, S. and Stathis, D. (2013) Assessment of flood hazard based on natural and anthropogenic factors using analytic hierarchy process (AHP). *Natural Hazards*. **68**:(2), 569–585. doi:10.1007/s11069-013-0639-5.

Stephens, E., Schumann, G.J.P. and Bates, P. (2014) Problems with binary pattern measures for flood model evaluation. *Hydrological Processes*. **28**:(18), 4928–4937. doi:10.1002/hyp.9979.

Sun, G., Ranson, K.J., Kharuk, V.I. and Kovacs, K. (2003) Validation of surface height from shuttle radar topography mission using shuttle laser altimeter. *Remote Sensing of Environment*. **88**:(4), 401–411. doi:10.1016/j.rse.2003.09.001.

Sun A.Y. and Scanlon, B.R. (2019) How can Big Data and machine learning benefit environment and water management: a survey of methods, applications, and future directions. *Environmental Research Letters.* **14**, 073001. doi:10.1088/1748-9326/ab1b7d

Tachikawa, T., Kaku, M., Iwasaki, A., Gesch, D., Oimoen, M., Zhang, Z., Danielson, J., Krieger, T., Curtis, B., Haase, J., Abrams, M., Crippen, R. and Carabajal, C. (2011) *ASTER Global Digital Elevation Model Version 2 - Summary of Validation Reults*. [Online]. Available from: https://ssl.jspacesystems.or.jp/ersdac/GDEM/ver2Validation/Summary_GDEM2_validation_report_final.pdf.

Tadono, T., Nagai, H., Ishida, H., Oda, F., Naito, S., Minakawa, K. and Iwamoto, H. (2016) Generation of the 30 M-MESH global digital surface model by ALOS prism. *International Archives of the Photogrammetry, Remote Sensing and Spatial Information Sciences - ISPRS Archives*. **41**, 157–162. doi:10.5194/isprsarchives-XLI-B4-157-2016.

Tarpanelli, A., Barbetta, S., Brocca, L. and Moramarco, T. (2013) River Discharge Estimation by Using Altimetry Data and Simplified Flood Routing Modeling. *Remote Sensing*. **5**:(9), 4145–4162. doi:10.3390/rs5094145.

Teng, J., Jakeman, A.J., Vaze, J., Croke, B.F.W., Dutta, D. and Kim, S. (2017) Flood inundation modelling: A review of methods, recent advances and uncertainty analysis. *Environmental Modelling and Software*. **90**, 201–216. doi:10.1016/j.envsoft.2017.01.006.

Torbick, N., Chowdhury, D., Salas, W. and Qi, J. (2017) Monitoring rice agriculture across Myanmar using time series Sentinel-1 assisted by Landsat-8 and PALSAR-2. *Remote Sensing*. **9**, 119. doi:10.3390/rs90201019.

Torres, R., Snoeij, P., Geudtner, D., Bibby, D., Davidson, M., Attema, E., Potin, P., Rommen, B., Floury, N., Brown, M., Traver, I.N., Deghaye, P., Duesmann, B., Rosich, B., et al. (2012) GMES Sentinel-1 mission. *Remote Sensing of Environment*. **120**, 9–24. doi:10.1016/j.rse.2011.05.028.

Townsend, P. (2001) Mapping seasonal ooding in forested wetlands using multi-temporal Radarsat SAR. *Photogrammetric Engineering and Remote Sensing*. **67**:(7).

Trenberth, K. (2011) Changes in precipitation with climate change. *Climate Research*. **47**:(1), 123–138. doi:10.3354/cr00953.

Tsyganskaya, V., Martinis, S., Marzahn, P. and Ludwig, R. (2018) Detection of Temporary Flooded Vegetation Using Sentinel-1 Time Series Data. *Remote Sensing*. **10**:(8), 1286. doi:10.3390/rs10081286.

Twele, A., Cao, W., Plank, S. and Martinis, S. (2016) Sentinel-1-based flood mapping: a fully automated processing chain. *International Journal of Remote Sensing*. **37**:(13), 2990–3004. doi:10.1080/01431161.2016.1192304.

UK Authority (2018) *Environment Agency to extend LiDAR data to all of England*. [Online]. Available from: https://www.ukauthority.com/articles/environment-agency-to-extend-lidar-data-to-all-of-england/. Last Accessed 27/09/2018.

van der Sande, C.J., de Jong, S.M. and de Roo, A.P.J. (2003) A segmentation and classification approach of IKONOS-2 imagery for land cover mapping to assist flood risk and flood damage assessment. *International Journal of Applied Earth Observation and Geoinformation*. **4**:(3), 217–229. doi:10.1016/S0303-2434(03)00003-5.

Velotto, D., Bentes, C., Tings, B. and Lehner, S. (2016) First Comparison of Sentinel-1 and TerraSAR-X Data in the Framework of Maritime Targets Detection: South Italy Case. *IEEE Journal of Oceanic Engineering*. **41**:(4), 993–1006. doi:10.1109/JOE.2016.2520216.

Villadsen, H., Andersen, O.B., Stenseng, L., Nielsen, K. and Knudsen, P. (2015) CryoSat-2 altimetry for river level monitoring — Evaluation in the Ganges–Brahmaputra River basin. *Remote Sensing of Environment*. **168**, 80–89. doi:10.1016/j.rse.2015.05.025.

Voormansik, K., Praks, J., Antropov, O., Jagomagi, J. and Zalite, K. (2014) Flood mapping with TerraSAR-X in forested regions in Estonia. *IEEE Journal of Selected Topics in Applied Earth Observations and Remote Sensing*. **7**:(2), 562–577. doi:10.1109/JSTARS.2013.2283340.

Wang, Z., Lai, C., Chen, X., Yang, B., Zhao, S. and Bai, X. (2015) Flood hazard risk assessment model based on random forest. *Journal of Hydrology*. **527**, 1130–1141.

doi:10.1016/j.jhydrol.2015.06.008.

Wessel, B. (2016) TanDEM-X DEM Products Specification Document. [Online]. Available from: https://elib.dlr.de/108014/1/TD-GS-PS-0021_DEM-Product-Specification_v3.1.pdf. Last Accessed 05/01/2020

West, H., Horswell, M. and Quinn, N. (2018) Exploring the sensitivity of coastal inundation modelling to DEM vertical error. *International Journal of Geographical Information Science.* **32**:(6), 1172-1193. doi:10.1080/13658816.2018.1444165.

Westerhoff, R.S., Kleuskens, M.P.H., Winsemius, H.C., Huizinga, H.J., Brakenridge, G.R. and Bishop, C. (2013) Automated global water mapping based on wide-swath orbital synthetic-aperture radar. *Hydrology and Earth System Sciences*. **17**:(2), 651–663. doi:10.5194/hess-17-651-2013.

Winsemius, H.C., Aerts, J.C.J.H., van Beek, L.P.H., Bierkens, M.F.P., Bouwman, A., Jongman, B., Kwadijk, J.C.J., Ligtvoet, W., Lucas, P.L., van Vuuren, D.P. and Ward, P.J. (2016) Global drivers of future river flood risk. *Nature Climate Change*. **6**:(4), 381–385. doi:10.1038/nclimate2893.

Wood, M., de Jong, S.M. and Straatsma, M.W. (2018) Locating flood embankments using SAR time series: A proof of concept. *International Journal of Applied Earth Observation and Geoinformation*. **70**, 72–83. doi:10.1016/j.jag.2018.04.003.

Xu, H. (2006) Modification of normalised difference water index (NDWI) to enhance open water features in remotely sensed imagery. *International Journal of Remote Sensing*. **27**:(14), 3025–3033. doi:10.1080/01431160600589179.

Yamazaki, D., Ikeshima, D., Tawatari, R., Yamaguchi, T., O'Loughlin, F., Neal, J.C., Sampson, C.C., Kanae, S. and Bates, P.D. (2017) A high-accuracy map of global terrain elevations. *Geophysical Research Letters.* **44**:(11), 5844-5853. doi:10.1002/2017GL072874.

Yan, K., Di Baldassarre, G., Solomatine, D.P. and Schumann, G.J.P. (2015) A review of low-cost space-borne data for flood modelling: topography, flood extent and water level. *Hydrological Processes*. **29**:(15), 3368–3387. doi:10.1002/hyp.10449.

Yu, D. and Lane, S.N. (2006) Urban fluvial flood modelling using a two-dimensional diffusion-wave treatment, part 1: mesh resolution effects. *Hydrological Processes*. **20**:(7), 1541–1565. doi:10.1002/hyp.5935.

Yulianto, F., Sofan, P., Zubaidah, A., Sukowati, K.A.D., Pasaribu, J.M. and Khomarudin, M.R. (2015) Detecting areas affected by flood using multi-temporal ALOS PALSAR remotely sensed data in Karawang, West Java, Indonesia. *Natural Hazards*. **77**:(2), 959–985. doi:10.1007/s11069-015-1633-x.

Zhang, K., Gann, D., Ross, M., Biswas, H., Li, Y. and Rhome, J. (2019a) Comparison of TanDEM-X DEM with LiDAR Data for Accuracy Assessment in a Coastal Urban Area. *Remote Sensing.* **11**, 876. doi:10.3390/rs11070876.

Zhang, K., Gann, D., Ross, M., Robertson, Q., Sarmiento, J., Santana, S., Rhome, J. and Fritz, C. (2019b) Accuracy assessment of ASTER, SRTM, ALOS, and TDX DEMs for Hispaniola and implications for mapping vulnerability to coastal flooding. *Remote Sensing of Environment*. **225**, 290–306. doi:10.1016/j.rse.2019.02.028.

Zhou, C., Luo, J., Yang, C., Ll, B. and Wang, S. (2000) Flood Monitoring Using Multi-Temporal AVHRR and RADARSAT Imagery. *Photogrammeric Engineering & Remote Sensing*. **66**:(5), 633–638.

Zhu, Z. and Woodcock, C.E. (2012) Object-based cloud and cloud shadow detection in Landsat imagery. *Remote Sensing of Environment*. **118**, 83–94. doi:10.1016/j.rse.2011.10.028.

Zwenzner, H. and Voigt, S. (2009) Improved estimation of flood parameters by combining space based SAR data with very high resolution digital elevation data. *Hydrology and Earth System Sciences*. **13**, 567–576. doi:10.5194/hess-13-567-2009.

Appendix A: List of Sentinel-1 Images

Sentinel-1 Image	Date	Time	Ascending/Descending	Orbit Track
S1A_IW_GRDH_1SDV_20151111T061339_20151111T061404_008553_00C1EA_ED0E	11/11/2015	06:13	DESCENDING	81
S1A_IW_GRDH_1SDV_20151111T061404_20151111T061429_008553_00C1EA_2EAA	11/11/2015	06:14	DESCENDING	81
S1A_IW_GRDH_1SDV_20151112T180609_20151112T180634_008575_00C288_4D80	12/11/2015	18:06	ASCENDING	103
S1A_IW_GRDH_1SDV_20151112T180634_20151112T180659_008575_00C288_0CBA	12/11/2015	18:06	ASCENDING	103
S1A_IW_GRDH_1SDV_20151114T174942_20151114T175007_008604_00C35D_E3EE	14/11/2015	17:49	ASCENDING	132
S1A_IW_GRDH_1SDV_20151114T175007_20151114T175032_008604_00C35D_AA73	14/11/2015	17:50	ASCENDING	132
S1A_IW_GRDH_1SDV_20151116T062140_20151116T062205_008626_00C401_1F80	16/11/2015	06:21	DESCENDING	154
S1A_IW_GRDH_1SDV_20151116T062205_20151116T062230_008626_00C401_A2FD	16/11/2015	06:22	DESCENDING	154
S1A_IW_GRDH_1SDV_20151116T062230_20151116T062255_008626_00C401_F220	16/11/2015	06:22	DESCENDING	154
S1A_IW_GRDH_1SDV_20151119T175744_20151119T175809_008677_00C566_3F33	19/11/2015	17:57	ASCENDING	30
S1A_IW_GRDH_1SDV_20151119T175809_20151119T175834_008677_00C566_76DF	19/11/2015	17:58	ASCENDING	30
S1A_IW_GRDH_1SDV_20151119T175834_20151119T175859_008677_00C566_A3A0	19/11/2015	17:58	ASCENDING	30
S1A_IW_GRDH_1SDV_20151121T062955_20151121T063020_008699_00C610_E5E5	21/11/2015	06:29	DESCENDING	52
S1A_IW_GRDH_1SDV_20151121T063020_20151121T063045_008699_00C610_AA06	21/11/2015	06:30	DESCENDING	52
S1A_IW_GRDH_1SDV_20151123T061323_20151123T061357_008728_00C6D9_123F	23/11/2015	06:13	DESCENDING	81
S1A_IW_GRDH_1SDV_20151123T061406_20151123T061434_008728_00C6DA_49F3	23/11/2015	06:14	DESCENDING	81
S1A_IW_GRDH_1SDV_20151124T180609_20151124T180634_008750_00C76C_10EA	24/11/2015	18:06	ASCENDING	103
S1A_IW_GRDH_1SDV_20151124T180634_20151124T180659_008750_00C76C_4683	24/11/2015	18:06	ASCENDING	103
S1A_IW_GRDH_1SDV_20151126T174948_20151126T175013_008779_00C83F_0877	26/11/2015	17:49	ASCENDING	132
S1A_IW_GRDH_1SDV_20151126T175013_20151126T175038_008779_00C83F_DCC2	26/11/2015	17:50	ASCENDING	132
S1A_IW_GRDH_1SDV_20151128T062140_20151128T062205_008801_00C8E2_4EF9	28/11/2015	06:21	DESCENDING	154
S1A_IW_GRDH_1SDV_20151128T062205_20151128T062230_008801_00C8E2_DFD2	28/11/2015	06:22	DESCENDING	154
S1A_IW_GRDH_1SDV_20151128T062230_20151128T062255_008801_00C8E2_5590	28/11/2015	06:22	DESCENDING	154
Sentinel-1 Image	**Date**	**Time**	**Ascending/Descending**	**Orbit Track**
S1A_IW_GRDH_1SDV_20151201T175739_20151201T175804_008852_00CA54_B2A1	01/12/2015	17:57	ASCENDING	30
S1A_IW_GRDH_1SDV_20151201T175804_20151201T175829_008852_00CA54_A306	01/12/2015	17:58	ASCENDING	30
S1A_IW_GRDH_1SDV_20151201T175829_20151201T175854_008852_00CA54_808D	01/12/2015	17:58	ASCENDING	30
S1A_IW_GRDH_1SDV_20151203T062955_20151203T063020_008874_00CAF3_EAC9	03/12/2015	06:29	DESCENDING	52
S1A_IW_GRDH_1SDV_20151203T063020_20151203T063045_008874_00CAF3_FAA5	03/12/2015	06:30	DESCENDING	52
S1A_IW_GRDH_1SDV_20151205T061339_20151205T061404_008903_00CBC9_43AF	05/12/2015	06:13	DESCENDING	81
S1A_IW_GRDH_1SDV_20151205T061404_20151205T061429_008903_00CBC9_2323	05/12/2015	06:14	DESCENDING	81
S1A_IW_GRDH_1SDV_20151206T180609_20151206T180634_008925_00CC68_587A	06/12/2015	18:06	ASCENDING	103
S1A_IW_GRDH_1SDV_20151206T180634_20151206T180659_008925_00CC68_8584	06/12/2015	18:06	ASCENDING	103
S1A_IW_GRDH_1SDV_20151208T174942_20151208T175007_008954_00CD3E_349B	08/12/2015	17:49	ASCENDING	132
S1A_IW_GRDH_1SDV_20151208T175007_20151208T175032_008954_00CD3E_FEB2	08/12/2015	17:50	ASCENDING	132
S1A_IW_GRDH_1SDV_20151213T175743_20151213T175808_009027_00CF27_1B55	13/12/2015	17:57	ASCENDING	30
S1A_IW_GRDH_1SDV_20151213T175808_20151213T175833_009027_00CF27_4F38	13/12/2015	17:58	ASCENDING	30
S1A_IW_GRDH_1SDV_20151213T175833_20151213T175858_009027_00CF27_74BB	13/12/2015	17:58	ASCENDING	30
S1A_IW_GRDH_1SDV_20151215T062955_20151215T063020_009049_00CFCD_BE83	15/12/2015	06:29	DESCENDING	52
S1A_IW_GRDH_1SDV_20151215T063020_20151215T063045_009049_00CFCD_F652	15/12/2015	06:30	DESCENDING	52
S1A_IW_GRDH_1SDV_20151217T061322_20151217T061356_009078_00D09A_3C46	17/12/2015	06:13	DESCENDING	81
S1A_IW_GRDH_1SDV_20151217T061404_20151217T061433_009078_00D09B_ECA6	17/12/2015	06:14	DESCENDING	81
S1A_IW_GRDH_1SDV_20151218T180608_20151218T180633_009100_00D134_A692	18/12/2015	18:06	ASCENDING	103
S1A_IW_GRDH_1SDV_20151218T180633_20151218T180658_009100_00D134_5ADF	18/12/2015	18:06	ASCENDING	103
S1A_IW_GRDH_1SDV_20151220T174947_20151220T175012_009129_00D20A_C0F7	20/12/2015	17:49	ASCENDING	132
S1A_IW_GRDH_1SDV_20151220T175012_20151220T175037_009129_00D20A_24B0	20/12/2015	17:50	ASCENDING	132
S1A_IW_GRDH_1SDV_20151222T062139_20151222T062204_009151_00D2AF_8276	22/12/2015	06:21	DESCENDING	154
S1A_IW_GRDH_1SDV_20151222T062204_20151222T062229_009151_00D2AF_17F0	22/12/2015	06:22	DESCENDING	154
S1A_IW_GRDH_1SDV_20151222T062229_20151222T062254_009151_00D2AF_7270	22/12/2015	06:22	DESCENDING	154
S1A_IW_GRDH_1SDV_20151225T175738_20151225T175803_009202_00D428_9A5F	25/12/2015	17:57	ASCENDING	30
S1A_IW_GRDH_1SDV_20151225T175803_20151225T175828_009202_00D428_9464	25/12/2015	17:58	ASCENDING	30
S1A_IW_GRDH_1SDV_20151225T175828_20151225T175853_009202_00D428_8FD1	25/12/2015	17:58	ASCENDING	30
S1A_IW_GRDH_1SDV_20151227T062954_20151227T063019_009224_00D4C4_0147	27/12/2015	06:29	DESCENDING	52
S1A_IW_GRDH_1SDV_20151227T063019_20151227T063044_009224_00D4C4_F6E0	27/12/2015	06:30	DESCENDING	52
S1A_IW_GRDH_1SDV_20151229T061338_20151229T061403_009253_00D59B_F24A	29/12/2015	06:13	DESCENDING	81
S1A_IW_GRDH_1SDV_20151229T061403_20151229T061428_009253_00D59B_CC2A	29/12/2015	06:14	DESCENDING	81
S1A_IW_GRDH_1SDV_20151230T180608_20151230T180633_009275_00D635_8A92	30/12/2015	18:06	ASCENDING	103
S1A_IW_GRDH_1SDV_20151230T180633_20151230T180658_009275_00D635_A1CA	30/12/2015	18:06	ASCENDING	103

Sentinel-1 Image	Date	Time	Ascending/Descending	Orbit Track
S1A_IW_GRDH_1SDV_20160101T174941_20160101T175006_009304_00D70A_60DE	01/01/2016	17:49	ASCENDING	132
S1A_IW_GRDH_1SDV_20160101T175006_20160101T175031_009304_00D70A_D4B8	01/01/2016	17:50	ASCENDING	132
S1A_IW_GRDH_1SDV_20160103T062139_20160103T062204_009326_00D7AC_355B	03/01/2016	06:21	DESCENDING	154
S1A_IW_GRDH_1SDV_20160103T062204_20160103T062229_009326_00D7AC_C9F2	03/01/2016	06:22	DESCENDING	154
S1A_IW_GRDH_1SDV_20160103T062229_20160103T062254_009326_00D7AC_4BD4	03/01/2016	06:22	DESCENDING	154
S1A_IW_GRDH_1SDV_20160106T175742_20160106T175807_009377_00D920_544D	06/01/2016	17:57	ASCENDING	30
S1A_IW_GRDH_1SDV_20160106T175807_20160106T175832_009377_00D920_8394	06/01/2016	17:58	ASCENDING	30
S1A_IW_GRDH_1SDV_20160106T175832_20160106T175857_009377_00D920_BD87	06/01/2016	17:58	ASCENDING	30
S1A_IW_GRDH_1SDV_20160108T062954_20160108T063019_009399_00D9C6_850D	08/01/2016	06:29	DESCENDING	52
S1A_IW_GRDH_1SDV_20160108T063019_20160108T063044_009399_00D9C6_B8BA	08/01/2016	06:30	DESCENDING	52
S1A_IW_GRDH_1SDV_20160110T061321_20160110T061355_009428_00DA92_2DFD	10/01/2016	06:13	DESCENDING	81
S1A_IW_GRDH_1SDV_20160110T061404_20160110T061433_009428_00DA93_B5C5	10/01/2016	06:14	DESCENDING	81
S1A_IW_GRDH_1SDV_20160111T180608_20160111T180633_009450_00DB32_0CCD	11/01/2016	18:06	ASCENDING	103
S1A_IW_GRDH_1SDV_20160111T180633_20160111T180658_009450_00DB32_4FED	11/01/2016	18:06	ASCENDING	103
S1A_IW_GRDH_1SDV_20160113T174946_20160113T175011_009479_00DC0B_EB97	13/01/2016	17:49	ASCENDING	132
S1A_IW_GRDH_1SDV_20160113T175011_20160113T175036_009479_00DC0B_61B3	13/01/2016	17:50	ASCENDING	132
S1A_IW_GRDH_1SDV_20160115T062138_20160115T062203_009501_00DCAF_B4E4	15/01/2016	06:21	DESCENDING	154
S1A_IW_GRDH_1SDV_20160115T062203_20160115T062228_009501_00DCAF_D397	15/01/2016	06:22	DESCENDING	154
S1A_IW_GRDH_1SDV_20160115T062228_20160115T062253_009501_00DCAF_61F2	15/01/2016	06:22	DESCENDING	154
S1A_IW_GRDH_1SDV_20160118T175737_20160118T175802_009552_00DE25_F77D	18/01/2016	17:57	ASCENDING	30
S1A_IW_GRDH_1SDV_20160118T175802_20160118T175827_009552_00DE25_27C1	18/01/2016	17:58	ASCENDING	30
S1A_IW_GRDH_1SDV_20160118T175827_20160118T175852_009552_00DE25_433B	18/01/2016	17:58	ASCENDING	30
S1A_IW_GRDH_1SDV_20160120T062954_20160120T063019_009574_00DECB_BCE9	20/01/2016	06:29	DESCENDING	52
S1A_IW_GRDH_1SDV_20160120T063019_20160120T063044_009574_00DECB_7549	20/01/2016	06:30	DESCENDING	52
S1A_IW_GRDH_1SDV_20160122T061337_20160122T061402_009603_00DFAF_52C9	22/01/2016	06:13	DESCENDING	81
S1A_IW_GRDH_1SDV_20160123T180607_20160123T180632_009625_00E051_616A	23/01/2016	18:06	ASCENDING	103
S1A_IW_GRDH_1SDV_20160123T180632_20160123T180657_009625_00E051_1C89	23/01/2016	18:06	ASCENDING	103
S1A_IW_GRDH_1SDV_20160125T174940_20160125T175005_009654_00E129_B71B	25/01/2016	17:49	ASCENDING	132
S1A_IW_GRDH_1SDV_20160125T175005_20160125T175030_009654_00E129_777A	25/01/2016	17:50	ASCENDING	132
S1A_IW_GRDH_1SDV_20160127T062138_20160127T062203_009676_00E1D0_5EC0	27/01/2016	06:21	DESCENDING	154
S1A_IW_GRDH_1SDV_20160127T062203_20160127T062228_009676_00E1D0_343F	27/01/2016	06:22	DESCENDING	154
S1A_IW_GRDH_1SDV_20160127T062228_20160127T062253_009676_00E1D0_7F70	27/01/2016	06:22	DESCENDING	154
S1A_IW_GRDH_1SDV_20160130T175741_20160130T175806_009727_00E345_E92A	30/01/2016	17:57	ASCENDING	30
S1A_IW_GRDH_1SDV_20160130T175806_20160130T175831_009727_00E345_B6FD	30/01/2016	17:58	ASCENDING	30
S1A_IW_GRDH_1SDV_20160130T175831_20160130T175856_009727_00E345_EE89	30/01/2016	17:58	ASCENDING	30
Sentinel-1 Image	**Date**	**Time**	**Ascending/Descending**	**Orbit Track**
S1A_IW_GRDH_1SDV_20160201T062951_20160201T063016_009749_00E3EF_1469	01/02/2016	06:29	DESCENDING	52
S1A_IW_GRDH_1SDV_20160201T063016_20160201T063041_009749_00E3EF_F308	01/02/2016	06:30	DESCENDING	52
S1A_IW_GRDH_1SDV_20160201T063041_20160201T063106_009749_00E3EF_3DB4	01/02/2016	06:30	DESCENDING	52
S1A_IW_GRDH_1SDV_20160204T180607_20160204T180632_009800_00E561_75FD	04/02/2016	18:06	ASCENDING	103
S1A_IW_GRDH_1SDV_20160204T180632_20160204T180657_009800_00E561_40D5	04/02/2016	18:06	ASCENDING	103
S1A_IW_GRDH_1SDV_20160206T174945_20160206T175010_009829_00E633_C42C	06/02/2016	17:49	ASCENDING	132
S1A_IW_GRDH_1SDV_20160206T175010_20160206T175035_009829_00E633_3D29	06/02/2016	17:50	ASCENDING	132
S1A_IW_GRDH_1SDV_20160208T062141_20160208T062206_009851_00E6D3_581F	08/02/2016	06:21	DESCENDING	154
S1A_IW_GRDH_1SDV_20160208T062206_20160208T062231_009851_00E6D3_9F7B	08/02/2016	06:22	DESCENDING	154
S1A_IW_GRDH_1SDV_20160208T062231_20160208T062256_009851_00E6D3_C142	08/02/2016	06:22	DESCENDING	154
S1A_IW_GRDH_1SDV_20160211T175736_20160211T175801_009902_00E85C_D011	11/02/2016	17:57	ASCENDING	30
S1A_IW_GRDH_1SDV_20160211T175801_20160211T175826_009902_00E85C_7A7E	11/02/2016	17:58	ASCENDING	30
S1A_IW_GRDH_1SDV_20160211T175826_20160211T175851_009902_00E85C_B533	11/02/2016	17:58	ASCENDING	30

Appendix A. List of the 105 Sentinel-1 images used to derive flood extent in Chapter 5, along with key metadata.

Appendix B: Additional Catchment Flood Extent Results

River Tyne Catchment

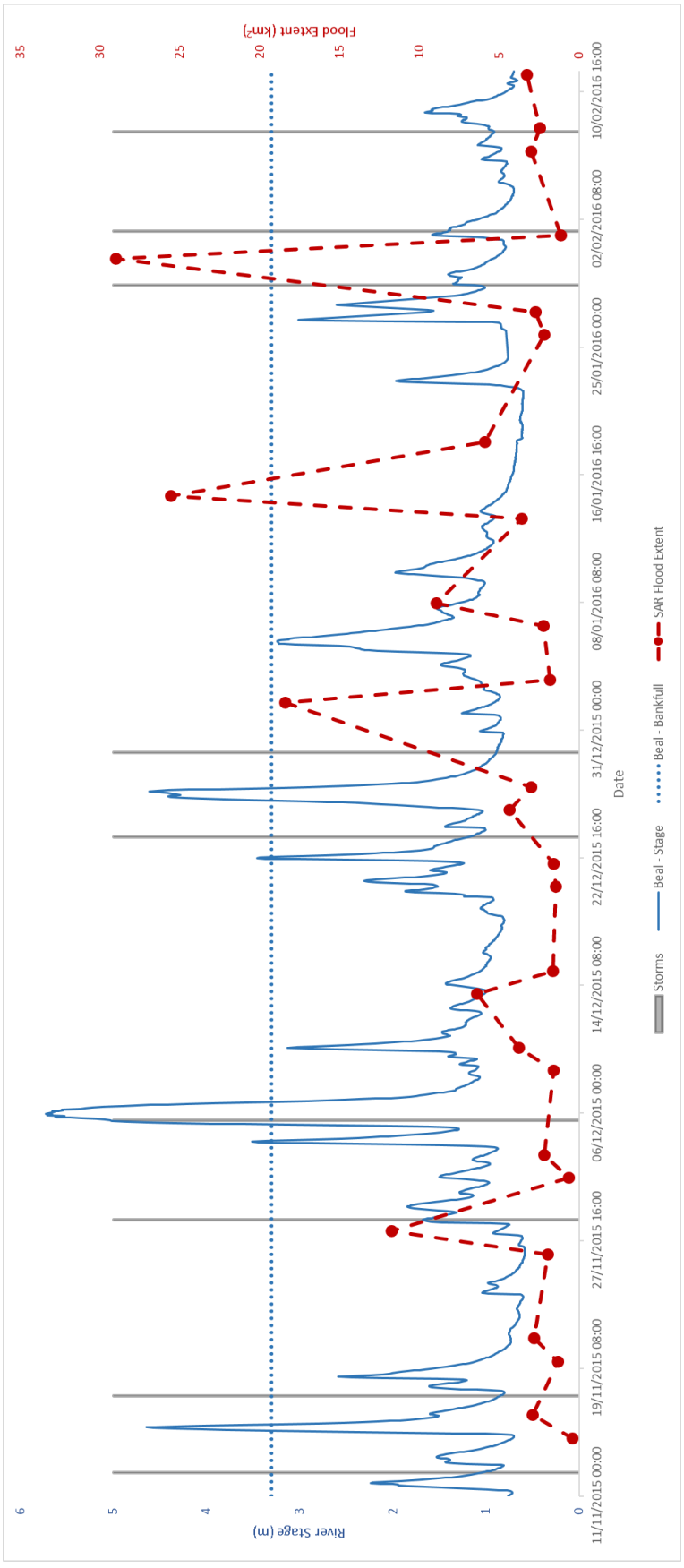

Appendix B: Tyne Catchment. Amount of flood extent identified in the Tyne catchment compared to river stage at the Corbridge gauge between 11th Nov 2015 and 11th Feb 2016. Low coverage (less than 70% of catchment) SAR images shown as unfilled data points. Approximate start period of named storms (from left, Abigail, Barney, Clodagh, Desmond, Eva, Frank, Gertrude, Henry and Imogen) shown for reference. Threshold for minor flooding occurrence taken from Environment Agency gauge information.

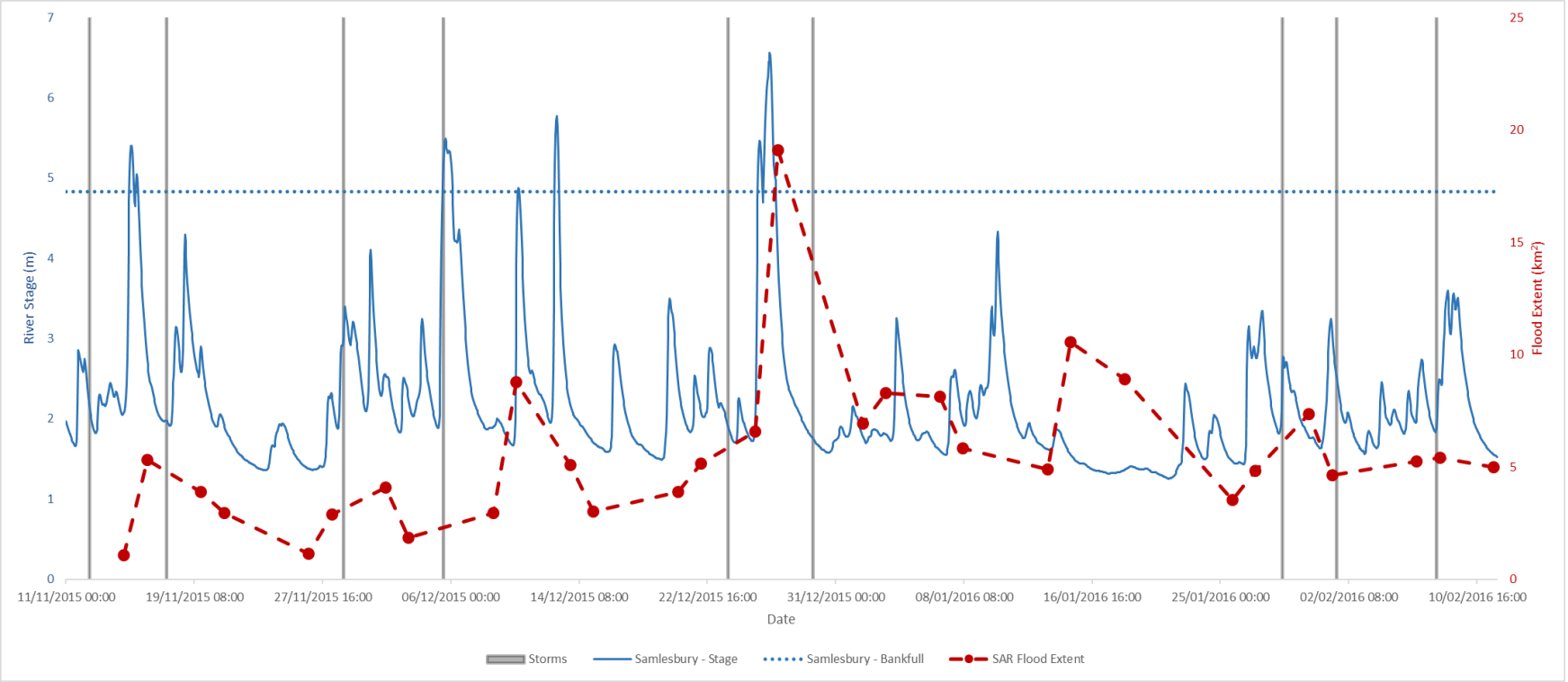

Appendix B: Ribble Catchment. Amount of flood extent identified in the Ribble catchment compared to river stage at the Samlesbury gauge between 11th Nov 2015 and 11th Feb 2016. Low coverage (less than 70% of catchment) SAR images shown as unfilled data points. Approximate start period of named storms (from left, Abigail, Barney, Clodagh, Desmond, Eva, Frank, Gertrude, Henry and Imogen) shown for reference. Threshold for minor flooding occurrence taken from Environment Agency gauge information.

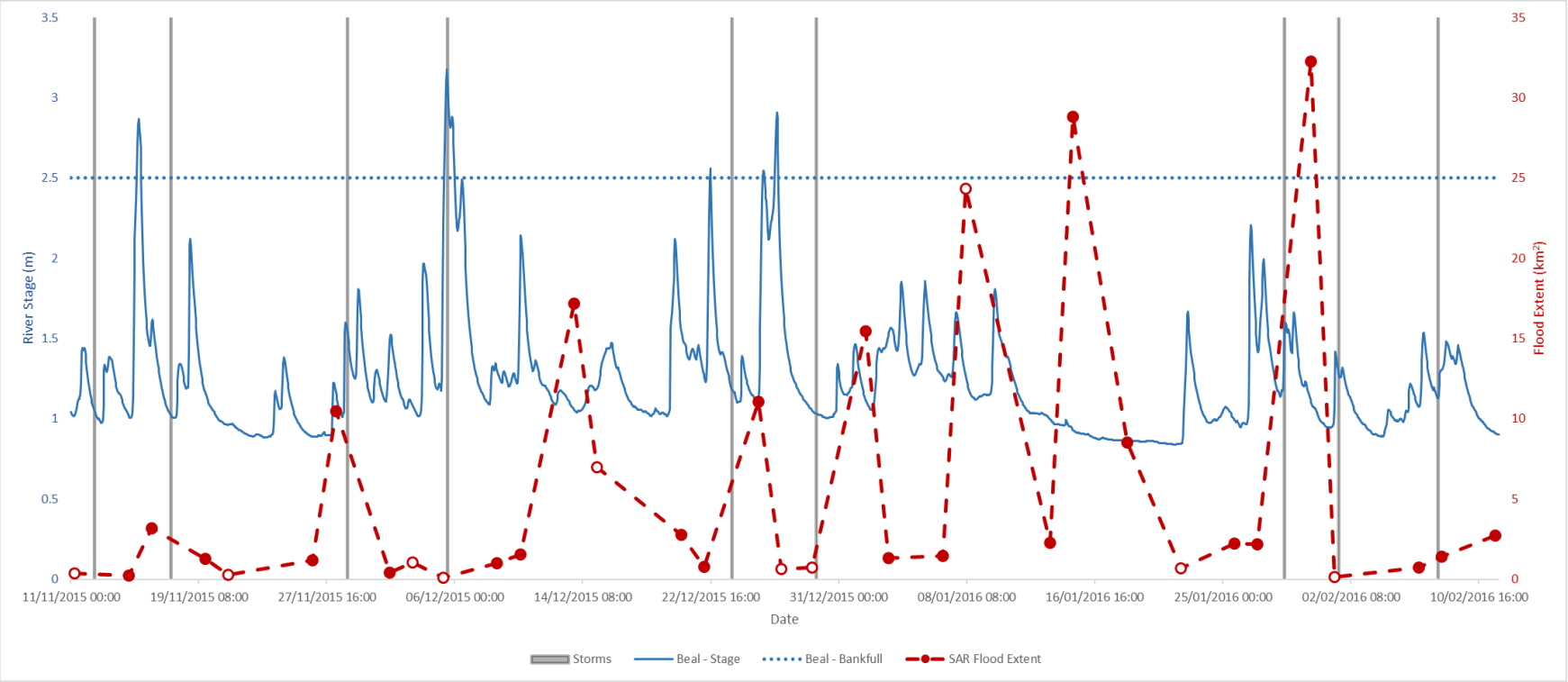

Appendix B: Tees Catchment. Amount of flood extent identified in the Tees catchment compared to river stage at the Darlington Broken Scar gauge between 11th Nov 2015 and 11th Feb 2016. Low coverage (less than 70% of catchment) SAR images shown as unfilled data points. Approximate start period of named storms (from left, Abigail, Barney, Clodagh, Desmond, Eva, Frank, Gertrude, Henry and Imogen) shown for reference. Threshold for minor flooding occurrence taken from Environment Agency gauge information.

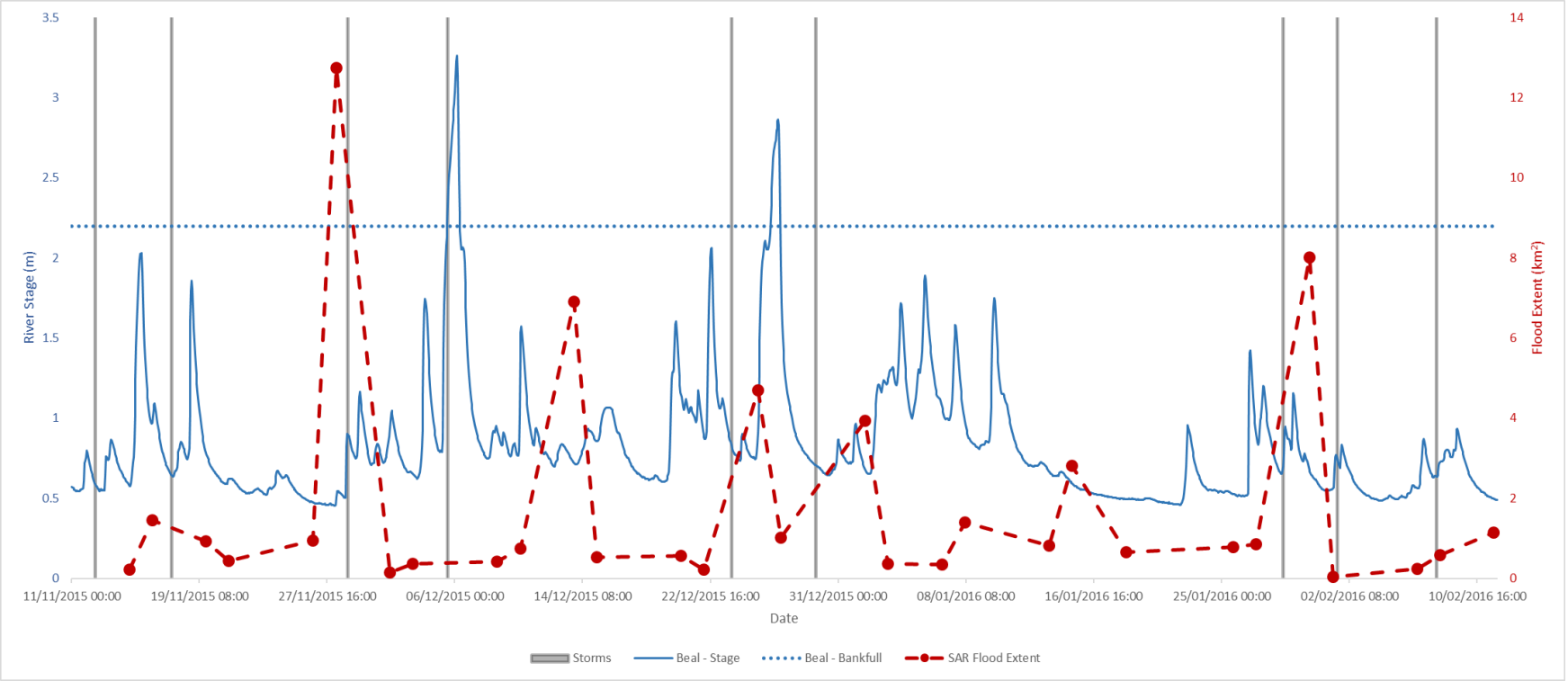

Appendix B: Wear Catchment. Amount of flood extent identified in the Wear catchment compared to river stage at the Sunderland Bridge gauge between 11th Nov 2015 and 11th Feb 2016. Low coverage (less than 70% of catchment) SAR images shown as unfilled data points. Approximate start period of named storms (from left, Abigail, Barney, Clodagh, Desmond, Eva, Frank, Gertrude, Henry and Imogen) shown for reference. Threshold for minor flooding occurrence taken from Environment Agency gauge information.

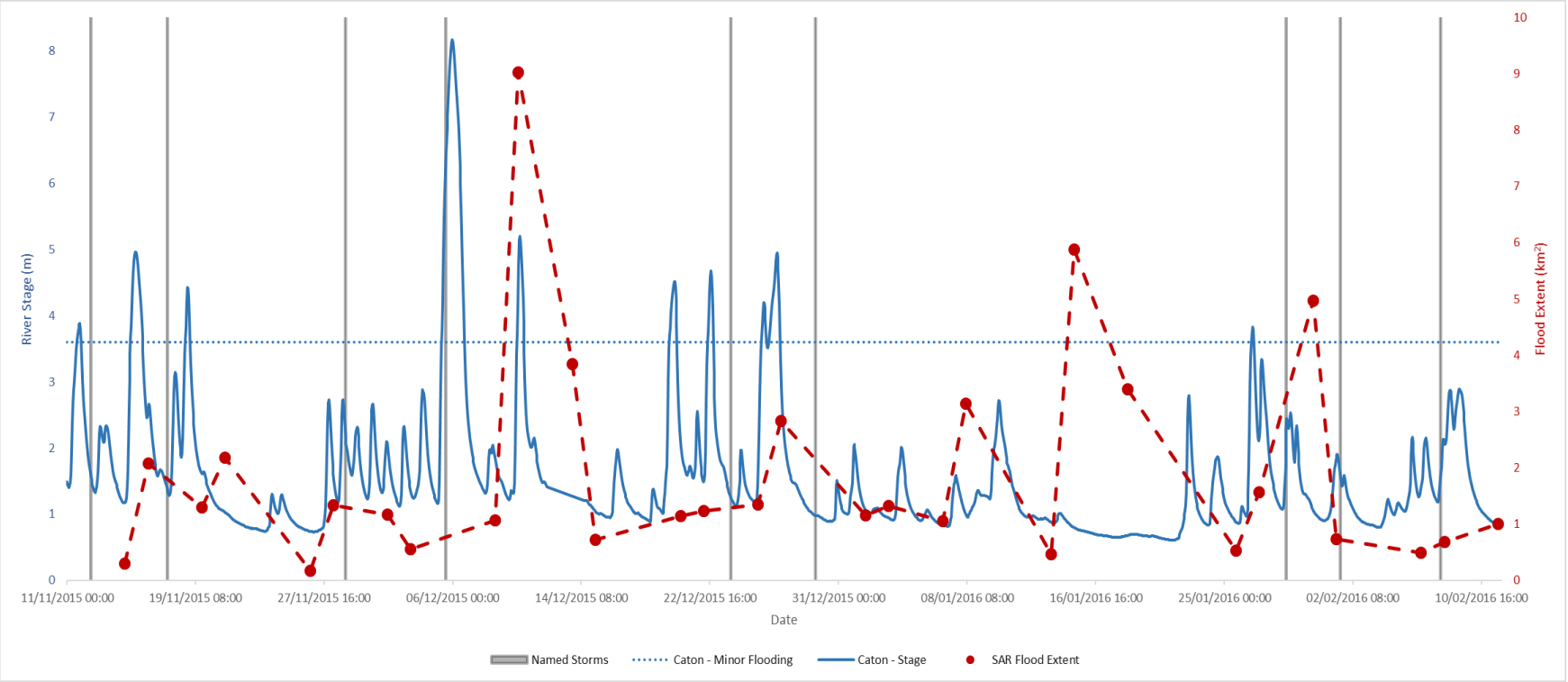

Appendix B: Lune Catchment. Amount of flood extent identified in the Lune catchment compared to river stage at the Caton gauge between 11th Nov 2015 and 11th Feb 2016. Low coverage (less than 70% of catchment) SAR images shown as unfilled data points. Approximate start period of named storms (from left, Abigail, Barney, Clodagh, Desmond, Eva, Frank, Gertrude, Henry and Imogen) shown for reference. Threshold for minor flooding occurrence taken from Environment Agency gauge information.

Appendix C: River Gauge Metadata

Gauge	River	Environment Agency		NRFA		Figures Data Shown
		Datum (m)	Flooding (m)	Datum (m)	Bankfull (m)	
Aldwark Bridge	Ure	8.56	3.00			6.9; 6.10
Beal	Aire	5.15	4.00	5.50	3.95	5.15; 5.21; 6.9; 6.10; 6.20
Bolton Percy	Bolton Percy Drain	0.00	6.00			6.9; 6.10
Bubwith	Derwent	0.00	5.50			6.9; 6.10
Carlton Bridge	Aire	1.47	4.50			6.9; 6.10
Caton	Lune	10.63	3.60	10.70	3.60	Appendix B
Cawood	Ouse	0.24	6.10			5.11; 5.21; 6.9; 6.10
Chapel Haddlesey	Aire	4.85	1.34			6.9; 6.10
Corbridge	Tyne	23.26	3.30			Appendix B
Crakehill Topcliffe	Swale	11.90	4.25	12.00	4.30	6.9; 6.10
Darlington	Tees	34.00	2.50	37.20	2.60	Appendix B
Elvington Sluices	Derwent	0.00	6.30			6.9; 6.10
Howe Bridge	Rye	15.20	4.00			6.9; 6.10
Kirby Wiske	Wiske	20.17	2.00	20.30	Unknown	6.9; 6.10
Knottingley Bank	Aire	5.02	4.50			6.9; 6.10
Low Marishes	Derwent	14.96	3.58	15.00	5.80	6.9; 6.10
Moor Monkton	Ouse	5.00	3.79			6.9; 6.10
Myton Bridge	Swale	8.19	3.75			5.11; 5.21; 6.9; 6.10; 6.19
Newton-on-Ouse	Kyle	5.75	3.32	5.70	Unknown	5.11; 6.9; 6.10
Portinscale	Derwent	72.47	Unknown	72.60	2.46	5.20;
Samlesbury	Ribble	6.00	4.83	9.50	5.90	Appendix B
Sedgwick	Kent	18.82	1.70	18.90	4.00	5.20;
Sheepmount	Eden	6.93	3.45	9.90	7.00	5.17;
Skelton	Ouse	4.57	3.00	4.60	6.96	6.9; 6.10
Skip Bridge	Nidd	7.58	3.01	8.20	Unknown	6.9; 6.10
Snaygill	Aire	89.02	4.00			5.15; 5.21;
Stamford Bridge	Derwent	0.00	9.00	5.10	Unknown	6.9; 6.10
Sunderland	Wear	40.20	2.20	40.20	2.28	Appendix B
Tadcaster	Wharfe	6.55	2.90	6.60	Unknown	6.9; 6.10
Tadcaster Sluices	Wharfe	-0.03	7.30			6.9; 6.10
Temple Sowerby	Eden	92.37	3.00	92.40	4.20	5.17; 5.21

Appendix C. River gauges and relevant metadata used throughout this thesis. NRFA refers to the National River Flow Archive.

Appendix D: GlobCover Example and Land Cover Classes

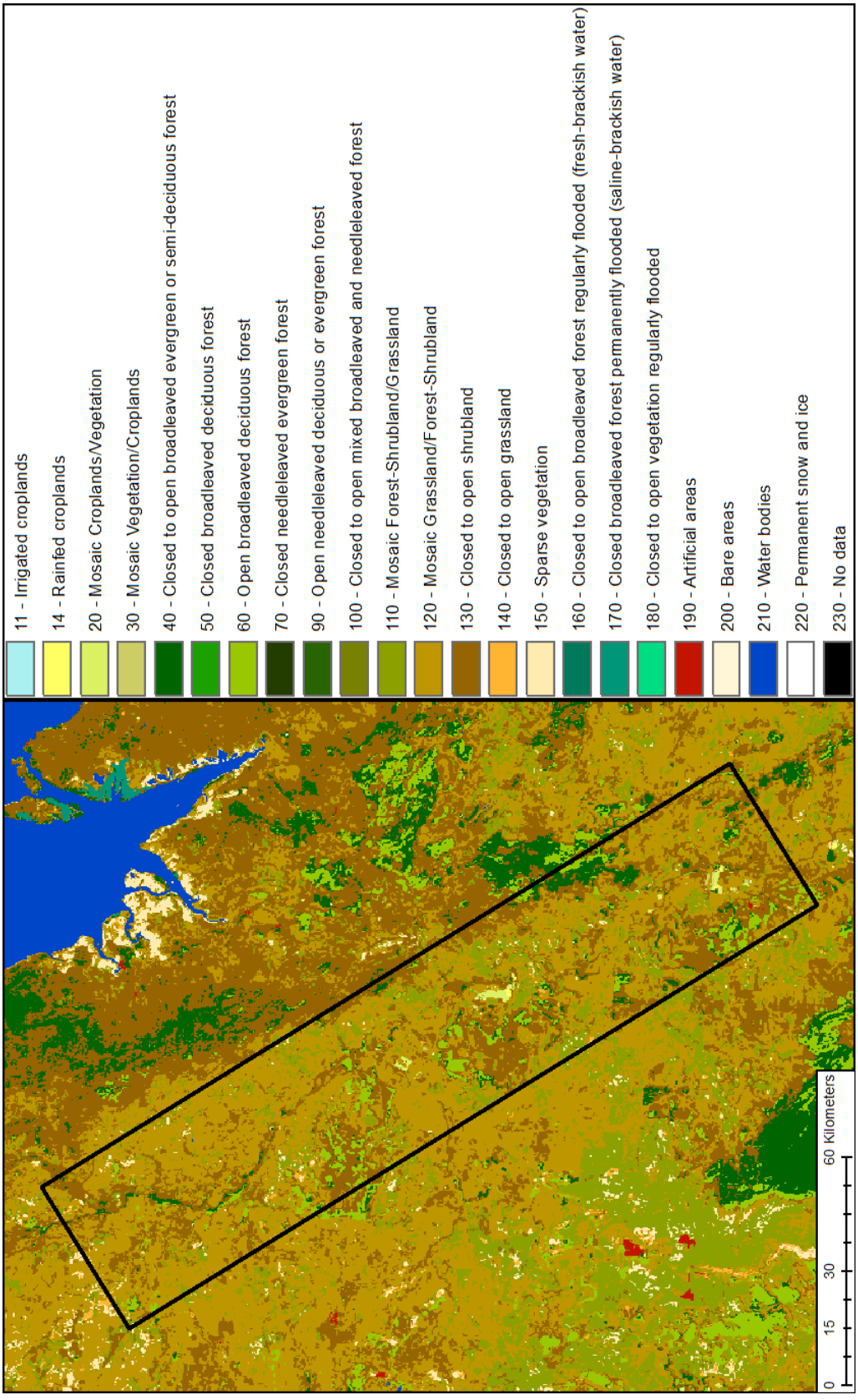

Appendix D. GlobCover land use map and land cover classes. Chapter 7 feature mask consists of land cover numbers; 40, 50, 60, 70, 90 and 100 (various types of woodland); 160 and 170 (regularly inundated woodland); 190 (artificial surfaces); 210 (water). Mosaic vegetation land covers, notably 110 and 120, are not included in this study as they form the majority of the study area. However, a case can be made for their inclusion given the woodland component of the vegetation mix.